# Image Analysis and Diffraction by the Myosin Lattice of Vertebrate Muscle

Chunhong Yoon

Department of Electrical and Computer Engineering

A thesis presented for the degree of
Doctor of Philosophy

University of Canterbury
Christchurch, New Zealand
August 2008

To my loving parents,
Jeonghwan and Gwiok

# Contents

# Acknowledgements

I would like to express my sincere gratitude to my supervisor, Prof. Rick Millane for his guidance, patience and friendship. Without your dedication and expertise, this thesis may never have been completed. I would also like to thank my co-supervisor, Prof. Phil Bones and overseas collaborators Prof. John Squire, University of Bristol and Dr. Pradeep Luther, Imperial College London for their contributions to this thesis.

I would also like to acknowledge the people involved in the examination of this thesis. I am grateful to Prof. Peter Doerschuk, Cornell University and Assoc. Prof. Alok Mitra, University of Auckland for their thorough reviews and suggestions for improvements. Thank you to Dr. Andrew Bainbridge-Smith for chairing the defense.

I am grateful to the Royal Society of New Zealand Marsden Fund for financial support.

Many thanks to my friends and colleagues in our Computational Imaging Group; Jeffrey Hsiao, Nic Blakeley, James Chen, Julian Maclaren and David Wojtas. Thank you to the technical staff in our department for their assistance. Special thanks to my long time buddies, Alan Wright, William Lee and Judy Zhou for the good memories during my years at UC.

It is my family that I have always relied on the most for love and support. I would like to thank my parents, Jeonghwan and Gwiok Yoon for their unconditional love. Mum and Dad, you have been my giving tree and for that I cannot thank you enough. A big thank you to my brother, Chunjin who has been my role model. Finally, I want to thank my sweetheart Jiyoung Kim for dating me. In all seriousness, thank you for your encouragement and thank you for waiting. *Saranghe*.

# Abstract

Closely packed myosin filaments are an example of a disordered biological array responsible for the contraction of muscle. X-ray fiber diffraction data is used to study these biomolecular assemblies but the inherent disorder in muscle makes interpretation of the diffraction data difficult. Limited knowledge of the precise nature of the myosin lattice disorder and its effects on X-ray diffraction data is currently limiting advances in studies on muscle structure and function.

This thesis covers theoretical and computational efforts to incorporate the myosin lattice disorder in X-ray diffraction analysis. An automated image analysis program is developed to rapidly and accurately quantitate the disorder from electron micrographs of muscle cross-sections. The observed disorder is modelled as an antiferromagnetic Ising model and the model verified using Monte Carlo simulations. Theory and methods are developed for efficient calculation of cylindrically averaged X-ray diffraction from two-dimensional lattices that incorporate this disorder.

# Preface

This project was initiated in an effort to ultimately determine the molecular structure of vertebrate muscle. X-ray fiber diffraction analysis is an essential tool for studying muscle structure. However, the presence of myosin filament disorder has prevented accurate analysis of X-ray diffraction data from many muscles. The disorder was first characterised by Luther and Squire [LS80] who observed that the myosin filaments adopt two rotations, or opposite orientations, "up" or "down" in a semi-systematical manner. Based on these findings, Millane and Goyal [MG00] endeavored to quantify the statistics of the disorder and generate lattices exhibiting similar statistics. This thesis is a progression from these studies.

The thesis addresses three topics related to the above problem: (1) Automatic analysis of muscle electron micrographs to classify filament orientations; (2) Modeling the myosin lattice disorder as a triangular Ising antiferromagnet (TIA) using Monte Carlo simulation. (3) Determining the effect of this kind of disorder on X-ray fiber diffraction patterns. Review material is presented in Chapter 1, and original work is presented in Chapters 2-5.

Parts of the programs used in this thesis were developed by the author's predecessors. In 2003, the first micrograph analysis program was developed by B. Bödvarsson, S. Klim, S. Mortensen and M. Mørkebjerg during their visit from Denmark. Monte Carlo simulations of antiferromagnetic triangular lattices in this thesis are performed using the program developed by A. Goyal and N. Blakeley. These programs have been extensively modified by the author to perform the specific tasks needed in this thesis.

Chapter 1 contains a review of background material relevant to this thesis. It covers muscle structure and the myosin lattice disorder, the Ising model, Monte Carlo simulation, X-ray crystallography, diffraction by disordered crystals, and X-ray fiber diffraction.

Chapter 2 describes an image analysis system for automated determination of the orientations of myosin filaments in electron micrographs of this muscle cross-sections. Results are presented from application to a number of micrographs and the precision of the system is accessed.

Chapter 3 describes an analysis of the myosin lattice disorder, i.e. the spatial distribution of the filament orientations. The chapter covers characterisation of the disorder, Monte Carlo simulation of the TIA and fitting to data derived from electron micrographs, and analytical approximations to the spatial correlation function.

In Chapter 4 the methods described in Chapters 2-3 are applied to a variety of muscle micrographs in order to characterise the myosin lattice disorder in different species.

In Chapter 5 the effect of the TIA disorder in two-dimensional lattices on X-ray diffraction patterns is studied. Analytical expressions for both the regular and cylindrically averaged diffraction are derived. Simulations are conducted to examine the characteristics of the diffraction and to assess the effect of the disorder on X-ray fiber diffraction patterns from muscle.

A summary of the key results of this work and suggestions for future research are briefly outlined in Chapter 6.

Some of the mathematical functions used in this thesis are briefly defined in the Appendix A and the electron micrographs used are shown in Appendix B.

Aspects of the work described in this dissertation have been published and presented. These are listed here in order of presentation:

B. Bödvarsson, S. Klim, S. Mortensen, M. Mørkebjerg, J. Chen, J. R. Maclaren, C. H. Yoon, P. K. Luther, J. M. Squire, A. Bainbridge-Smith, P. J. Bones, and R. P. Millane, "Determination of myosin filament positions and orientations in electron micrographs of muscle cross-sections", in Image Reconstruction from Incomplete Data III, P.J. Bones, M.A. Fiddy and R.P. Millane (Eds.), Proc. SPIE, 5562, pp. 97-108, 2004.

C.H. Yoon, J. Chen, J.R. Maclaren, B. Bödvarsson, S. Klim, S. Mortensen, M. Mørkebjerg, P.K. Luther, J.M. Squire, A. Bainbridge-Smith, P.J. Bones, and R.P. Millane, "Automated analysis of electron micrographs of muscle cross-sections", in Proc. IVCNZ, pp. 173-179, 2004.

C.H. Yoon, P.J. Bones, and R.P. Millane, "Recovery of myosin filament positions in muscle electron micrographs", in Proc. OSA Signal Recovery and Synthesis, 2005.

C.H. Yoon, P.J. Bones, and R.P. Millane, "Image Analysis for Electron Microscopy of Muscle Fibres", dicta, p. 79, Digital Image Computing: Techniques and Applications (DICTA'05), 2005.

R.P. Millane, C.H. Yoon, N.D. Blakeley, A. Goyal, "Analysis and modeling of substitution disorder in the myosin lattice of vertebrate muscle", in Image Reconstruction from Incomplete Data IV, P. J. Bones, M. A. Fiddy, R. P. Millane, eds., Proc. SPIE 6316, pp. 63160D, 2006.

C.H. Yoon, N.D. Blakeley, A. Goyal, and R.P. Millane, "Image Analysis and Modelling of Disorder in the Myosin Lattice of Vertebrate Muscle", in Proc. Image and Vision Computing New Zealand (IVCNZ), 2006

C.H. Yoon, R.P. Millane, N.D. Blakeley, and A. Goyal, "Statistical modeling of the myosin lattice in vertebrate muscle", in Computational Imaging V, C. A. Bouman, E. L. Miller, I. Pollak, eds., Proc. SPIE 6498, pp. 64981C, 2007.

B. Bödvarsson, S. Klim, S. Mortensen, M. Mørkebjerg, C.H. Yoon, J. Chen, J.R. Maclaren, P.K. Luther, J.M. Squire, P.J. Bones, and R.P. Millane, "A morphological image processing method for locating myosin filaments in muscle electron micrographs", Image and Vision Computing, 26, pp. 1073-1080, 2008.

C.H. Yoon, B. Bödvarsson, S. Klim, S. Mortensen, M. Mørkebjerg, J. Chen, J.R. Maclaren, P.K. Luther, J.M. Squire, P.J. Bones, and R.P. Millane, "Determination of myosin filament orientations in electron micrographs of muscle cross-sections", IEEE Trans. Image Process., in press, 2008.

I hope that the reader finds the thesis interesting and valuable.

# Chapter 1

# Introduction

Vertebrate muscle, Ising model, Monte Carlo simulation and X-ray diffraction are discussed in this chapter with an emphasis on information that will aid understanding of the work presented later in this thesis.

## 1.1 Muscle

The beauty and the wonders of evolution have lead to highly specialized and intricate biological structures and networks that test the limits of our comprehension. Muscle structure and its functions are no exceptions. The word muscle originates from the Latin musculus, diminutive of *mūs*,"little mouse." The reason being that some muscles were thought to be mouse-like in movement and shape in the time of the Ancient Greeks. This indicates that the mysterious inner workings of the muscle have intrigued man-kind for centuries. Even now, in the 21st century, the exact atomic details of the contraction mechanism of muscles remain unresolved.

### 1.1.1 Muscle Structure

It is convenient to classify the muscles of vertebrate animals according to the degree of structural order they possess; striated and non-striated. The striated muscles have a high degree of structural regularity, so much so that the fibers, of which the muscle is composed, display a regular transverse striation. Skeletal muscle is so named because it works on the skeleton and therefore is largely responsible for determining the external shape of a vertebrate. Typically about 40 per cent or more of the mass of an animal such as man is skeletal muscle. The alternative name, voluntary muscle, indicates that the contraction is under voluntary control. Heart muscle is involuntary and is very similar in structure to

skeletal muscle. In contrast, non-striated muscle (e.g. muscles of the walls of the gut and of blood vessels) has a much less regular structure, although it is now clear that it operates by a mechanism similar to that of skeletal and heart muscle [Off74].

Striated muscle is an intricate system of vascular, connective, nerve and muscle tissues. Every tissue plays an important role in the proper functioning of a muscle; muscle tissue is in charge of contraction, connective tissue provides support and protection, nerve tissue carries signals that trigger the muscle and vascular tissue carries blood and enzymes that are essential for muscle contraction.

Muscle tissue is a hierarchical assembly of *sarcomeres*, the basic contractile unit. Muscle tissue is composed of many bundles of muscle fasciculus enclosed in a layer of protective tissue called the epimysium. Each muscle fasciculus is in turn composed of thousands of muscle fibers, individually surrounded in a thin sheath of connective tissue, the endomysium. Muscle fiber is, in fact, a multinucleated muscle cell which is a fusion of numerous mononucleated myoblasts. It is called a fiber due to its highly elongated length ($\sim 10^{-1}$ m) in relation to its diameter ($\sim 10^{-5}$ m). The fiber's plasma membrane (outer wall) is called the sarcolemma, and the cytoplasm is the sarcoplasm. The sarcoplasm is tightly packed with contractile proteins termed myofibrils ($\sim$ 2 to 5 $\mu$m in diameter) running parallel to the fiber axis. The repeating unit of myofibrils is the sarcomere (Fig. 1.1).

The muscle sarcomere is approximately $2.2$ $\mu$m long in resting vertebrate muscles and contains the principal contractile proteins, *myosin* and *actin* which on their own can produce force and movement. The simultaneous shortening of sarcomeres is responsible for muscle contraction. Thus research on muscle structure and contraction can be focussed on investigating the structure and function of a single sarcomere [Squ97, CP04]. The sarcomere consists of highly organized overlapping arrays of myosin and actin filaments also known, respectively, as thick and thin filaments ( Fig. 1.2(a)). The myosin filaments lie on a triangular lattice with a spacing of $40$ $nm$. Each thick filament ($\sim 15$ $nm$ in diameter) is composed of about 250 myosin molecules [SLM90]. Actin filaments mainly consist of globular actin monomers and two types of regulatory proteins, *troponin* and *tropomyosin*.

Among many known varieties of myosin, vertebrate skeletal myosin is myosin type II [GH05]. The myosin II molecule is shown in Fig. 1.3(a). It has a long two-chain, parallel, coiled-coil, $\alpha$-helical rod about 1500 Å long and about 20 Å in diameter with a globular head on one end [SAKKL05]. The molecular weight of an intact myosin molecule is 480 $kDa$. It is made of two similar heavy chains (200 $kDa$ each) which interact along part of their length to give a two-chain coiled-coil $\alpha$-helical rod together with four light chains (20 $kDa$ each) which combine with the non-$\alpha$-helical parts of the heavy chains to form two globular heads called crossbridges. The rod which is part of the heavy chain weighs

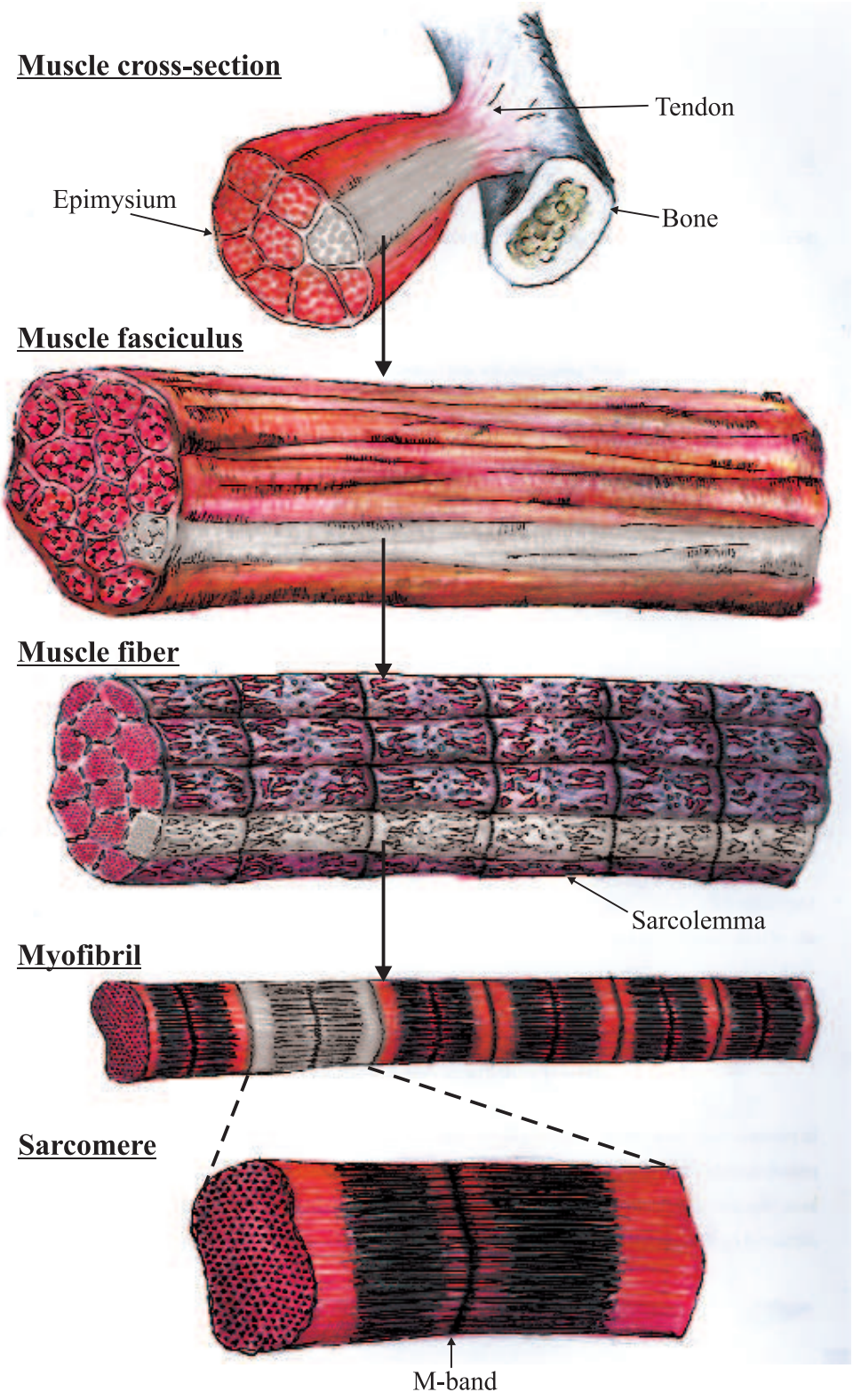


**Figure 1.1** Muscle tissue is a hierarchical assembly of sarcomeres. The shaded regions indicate the next component down the hierarchy (Not drawn to scale).

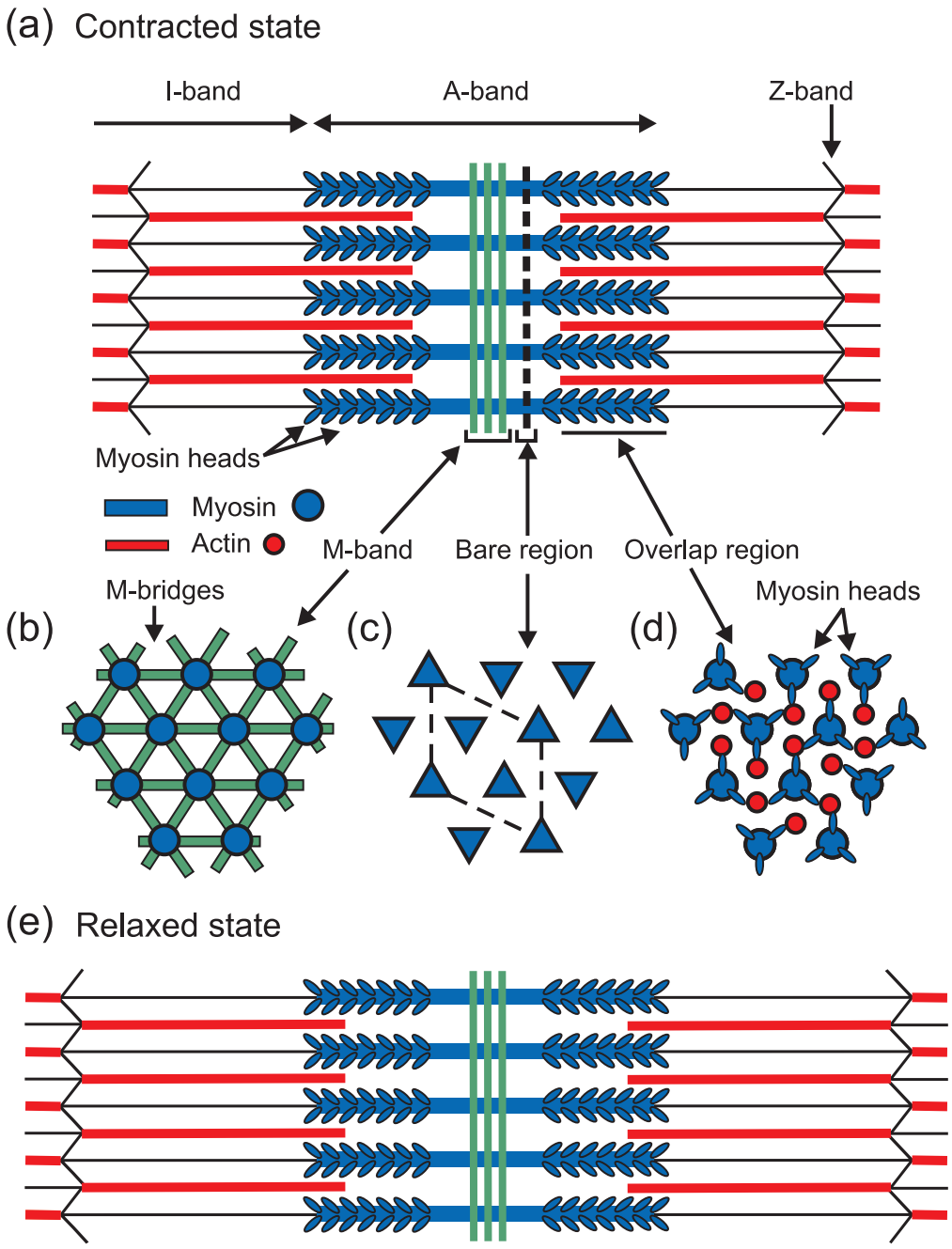


**Figure 1.2** Schematic diagram of a muscle sarcomere. (a) The overlapping myosin and actin filaments, the cross-linking of the myosin filaments at the M-band in the middle of the A-band and the location of the bare region (dashed lines) between the M-band and where the myosin head array starts on the myosin filaments. (b,c,d) Cross-sections through various parts of the sarcomere in (a), showing (b) the M-band where M-bridges cross-link the myosin filaments, (c) the bare region where the myosin filaments appear triangular (a superlattice cell is shown by the dashed lines) and (d) the crossbridge region where the myosin heads project from the myosin filament backbone, (e) sarcomere in relaxed state, tension generated is proportional to the amount of overlap of myosin and actin filaments. (Figures redrawn from [Squ81, LS80].)

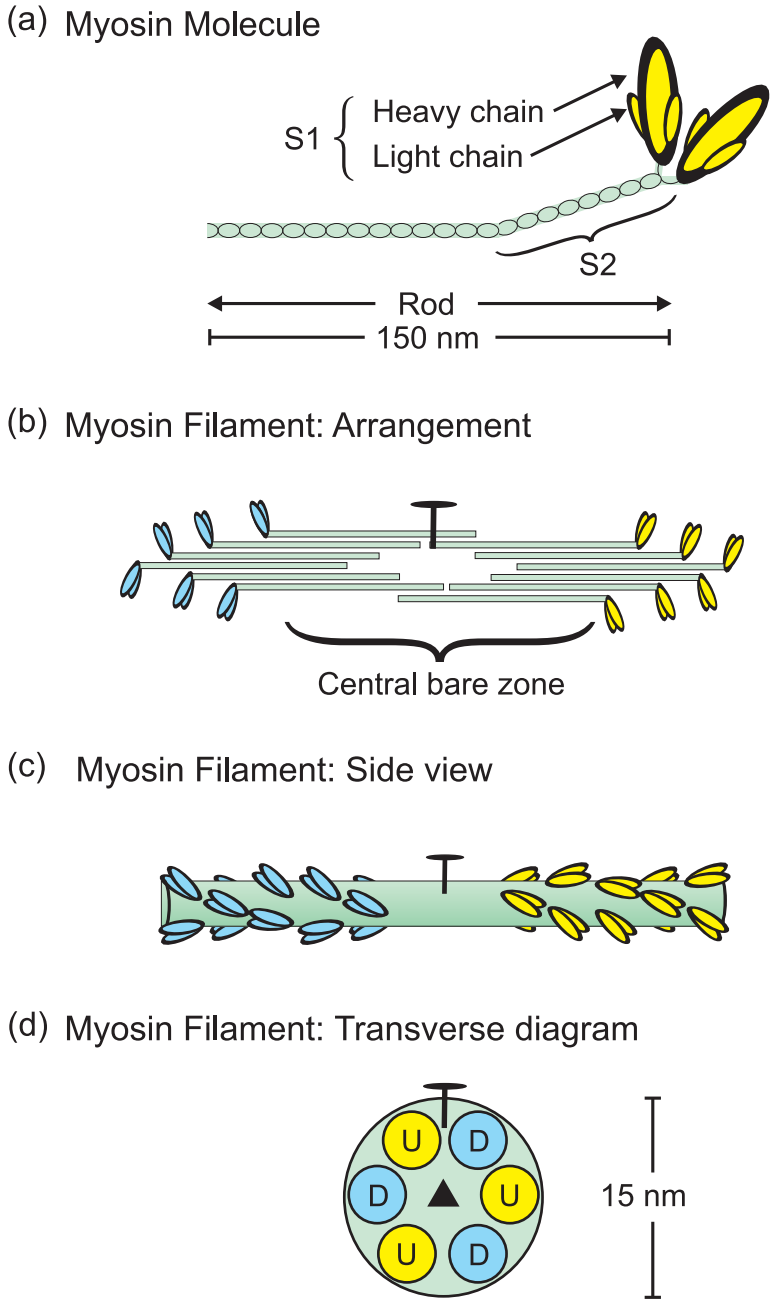


**Figure 1.3** Schematic diagram of the myosin filament. (a) The myosin molecule showing a long two-chain, parallel, coiled-coil, $\alpha$-helical rod and a globular head on one end. The binding sites for actin and two light chains are located on each subfragment 1 (S1) moiety. Subfragment 2 (S2) allows S1 to project a variable distance (up to 55 $nm$) from the filament backbone. (b) The bipolar packing of the myosin molecules showing the antiparallel arrangement giving rise to a heads-free bare zone region at the center of the filament. (c) Myosin filament composed of myosin molecules with the rod of the myosin molecules forming the backbone of the filament and the myosin heads are arranged on the surface of the filament backbone. The filament has two-fold symmetry (┬) perpendicular to the filament long axis. (d) View along the axis of the myosin filament shown in (c) has three-fold symmetry (▲) about the filament long axis. Polarity of the myosin molecules are labelled as up (U) and down (D). (Figures modified from [SAKKL05, Bag82].)

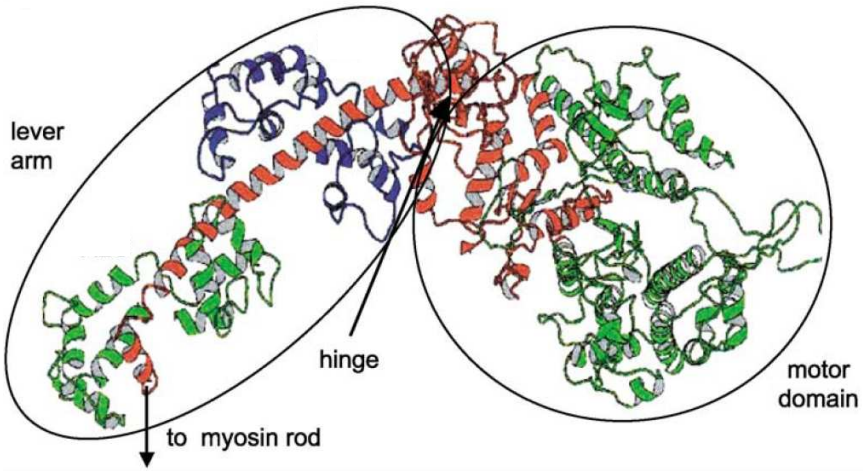


**Figure 1.4** The molecular assembly of the myosin head S1 (refer to Fig. 1.3(a)). The motor domain and the lever arm domain with a hinge in between that allows relative movement between the two domains [SAKKL05].

200 $kDa$. The molecular assembly of the myosin head subfragment is illustrated in Fig. 1.4. The myosin molecule is unusual in having a head which has the properties of an enzyme linked with a fibrous two-chain coiled-coil tail [Squ81]. The general arrangement of the myosin molecules within a myosin filament is shown in Fig. 1.3(b). The heads at opposite ends face in opposite directions (referred to as being bipolar), which explains the presence of a central bare zone. Around 250 myosin molecules aggregate to form the myosin filament which is illustrated in Fig. 1.3(c). The rods of individual myosin molecules form the shaft of the thick filament with the myosin heads protruding radially outwards toward neighbouring actin filaments. The molecular packing of the myosin molecules can be described as a three coaxial helices of subunit translation 143 Å and repeat 429 Å as shown in Fig. 1.5. The myosin filament has '32' dihedral point group symmetry. This is illustrated with a transverse diagram of the myosin filament showing antiparallel bundles of "up" (U) and "down" (D) myosin molecules in Fig. 1.3(d). It demonstrates three-fold symmetry about the filament long axis, i.e. 120° clockwise rotations of "up" myosin molecules, and two-fold symmetry perpendicular to the filament long axis, i.e. "up" molecules have symmetry with "down" molecules about the M-band.

### 1.1.2 Muscle Contraction

Muscle contraction occurs due to the "sliding" movement of actin and myosin filaments past each other [Hux57, Hux74]. A sarcomere in a relaxed state is shown in Fig. 1.2(e) compared to a contracted state in Fig. 1.2(a). The movement results from cycles in which myosin heads, which project from the myosin filament surface ( Fig. 1.2(a,d)), attach to actin, undergo a structural transition and are subsequently released from actin [Squ81].

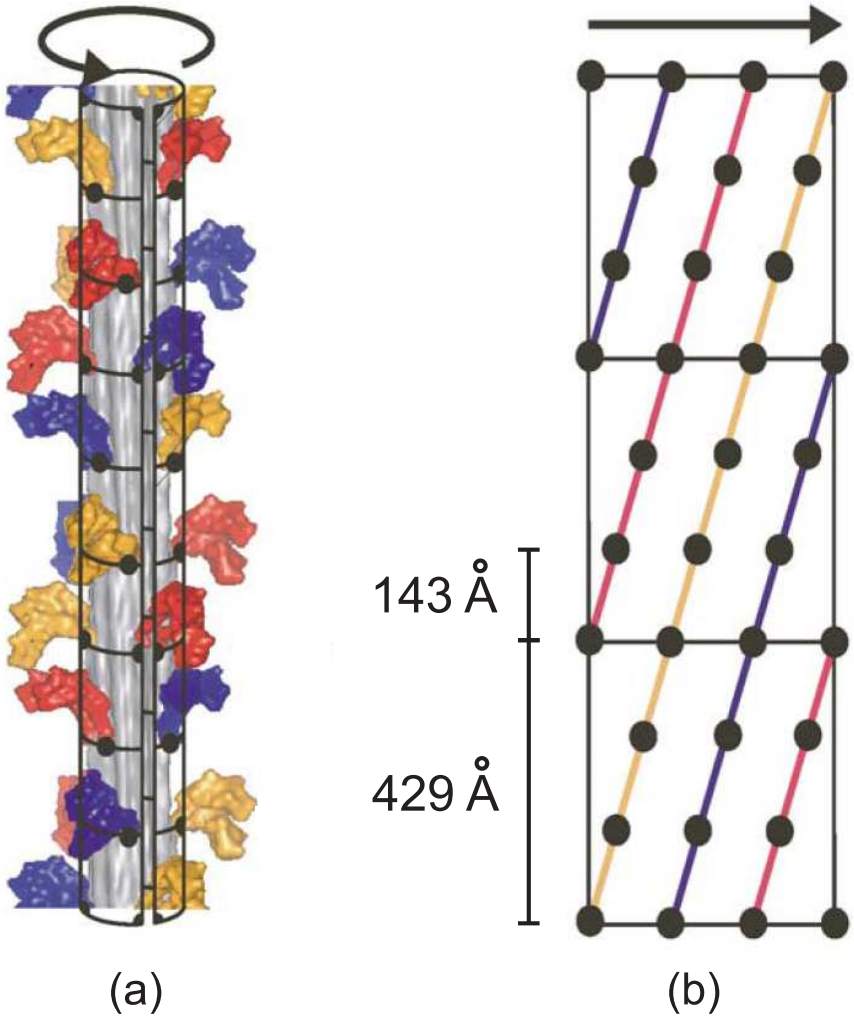


**Figure 1.5** Molecular packing in the myosin filament of vertebrate skeletal muscle. (a) The arrangement of the myosin heads on the surface of the myosin filament backbone lying approximately on three coaxial helices of subunit translation 143 Åand repeat 429 Å. The myosin head origins are labeled as black circles on a cylindrical net. (b) The net is spread out showing three helices of myosin head origins in different colours, red, blue, and yellow [Squ81, SAKKL05].

Calcium ions ($Ca^{2+}$) are the intracellular signal in the sequence of events connecting the nerve impulse to muscle contraction. The *sarcoplasmic reticulum* (SR) consists of flattened vesicles wrapped around the myofibrils like lace cuffs which stores $Ca^{2+}$. The transverse tubules, or *T-tubules*, are tubular invaginations of the muscle cell membrane, running perpendicularly to the fiber axis [ARDS03]. T-tubules are found at regular intervals along the length of the muscle fiber. In mammalian skeletal muscle they are found at each A-I junction as shown in Fig. 1.6. A T-tubule is in close contact with two lateral sacs of the SR called *terminal cisternae* (TC), forming a triad, the structural link between the nerve impulse and the resulting release of $Ca^{2+}$ from the SR.

When the brain sends nerve impulses in the form of action potentials, it causes depolari-

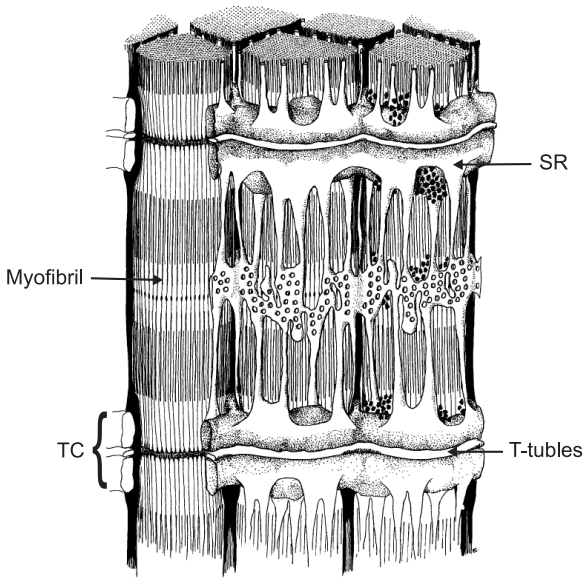


**Figure 1.6** A group of muscle myofibrils showing the T-tubules, which in turn interact with the TC of the SR to trigger the release of calcium ions locally into the adjacent myofibrils [Pea65].

sation of the T-tubules resulting in the rapid diffusion of $Ca^{2+}$ from the terminal cisternae into the myofibrillar lattice, where they are captured by troponin. This initiates a conformational change in the troponin-tropomyosin complex, which exposes actin's myosin-binding sites, allowing attachment-detachment cycles of the myosin heads to begin. First, the myosin heads charged with *adenosine triphosphate* (ATP), attach loosely to actin. The myosin head contains adenosine triphosphatase (ATPase), an enzyme that splits the high energy phosphate bond of ATP into adenosine diphosphate (ADP) and inorganic phosphate ($P_i$). The release of $P_i$ causes tight binding of the myosin head to actin and provides energy for the heads to undergo a conformational change that results in repositioning the angle of attachment (referred to as a power stroke), pulling the Z-discs in towards the M-band ( Fig. 1.2(a)). After pulling the actin, the head releases ADP and binds a new molecule of ATP. This results in the release of the head from actin and resumes its relaxed conformation and position, and the cycle is ready to repeat [GH05]. The myosin heads take turns at power stroking such that the tension generated is kept constant during muscle contraction.

### 1.1.3 Methods for Studying Muscle Structure

Our knowledge of muscle structure has increased significantly due to high resolution capabilities of modern equipment. Electron microscopy and X-ray fiber diffraction are used to resolve structures that are beyond the resolution capabilities of visible light. The intracellular components of muscle structures are viewed through optical (light) microscopy. For this reason, skeletal muscle is also known as striated muscle due to its distinct cross bands arising from aligned striated myofibrils under a polarising microscope. The striated

appearance is due to the proteins within the region responsible for its refraction not being distributed homogeneously, and the refractive index depends on the plane of polarisation of the light (birefringence). Resolution of these bands by refraction rather than by staining is important because it allows living muscle to be observed [Bag82].

To determine the fine structure of the muscle one must combine and integrate data obtained by electron microscopy, X-ray diffraction studies, and physical-chemical studies on the contractile proteins [CW74]. Although many biochemical and biophysical techniques are used to study muscle structure and function, the focus of this thesis is on methods for high resolution imaging of muscle. Brief introductions to the two main imaging techniques relevant to this thesis, X-ray diffraction and electron microscopy, are given here.

#### 1.1.3.1 X-ray Diffraction

X-ray diffraction techniques are a family of analytical techniques which reveal information about the geometric structure of materials based on observing the scattered intensity of an X-ray beam hitting a sample as a function of incident and scattered angle, polarization, and wavelength or energy. X-ray diffraction, whose traditional and most successful application is X-ray crystallography, has also been applied to studying the remarkable geometrical order of the contractile proteins of muscle [Hux71, WH81]. The advantage of X-ray diffraction is that the diffraction patterns contain higher resolution information than what can be obtained in an electron microscope. However, the interpretation of these patterns is often a difficult inverse problem. X-ray diffraction, and a variant called fiber diffraction analysis that is used to study fibrous specimens such as muscle are described in Sections 1.4 and 1.6, respectively.

#### 1.1.3.2 Electron Microscopy

Electron microscopy is an imaging technique whereby electrons rather than visible light are used to achieve higher magnification of the specimen. In particular, transmission electron microscopy (TEM) involves a high voltage electron beam emitted by a cathode and focused by electrostatic and electromagnetic lenses. The electron beam transmitted through the specimen is gathered and the image formed can be viewed in real time.

Electron microscopy allows direct observations of muscle components with a resolution limit of $\sim 1\ nm$. The structural components of the sarcomeres are visible as bands on an electron micrograph. Electron micrographs of longitudinal sections most clearly reveal the different bands (Fig. 1.7). Both ends of the sarcomere are defined by the Z-discs, membranes to which the actin filaments of the sarcomere are attached. The letter Z comes from German *zwischen*, which means "between," because the Z-discs divide the myofibril into sarcomere sections. The I-band contains only the thin filaments and is only weakly birefrin-

gent. The A-band contains the thick filaments. The letters I and A stand for isotropic and anisotropic, terminology still retained from light microscope studies of muscle. The dense A-band overlap region is strongly birefringent where the thin filaments appear alongside thick ones and small bridge-like structures can be seen (on the thick filaments extending toward the thin filaments) called *cross-bridges*. Sections through the so called bare region (H-zone) contain only thick filaments. H stands for Hensen, who first described it in 1868. The bare region lies between the M-band (the dark band down the middle), where adjacent myosin filaments are cross-linked by protein molecules (referred to as the M-bridges), and the start of the region where the myosin heads project out from the filament backbone. The letter M stands for *Mitteline*, German for midline.

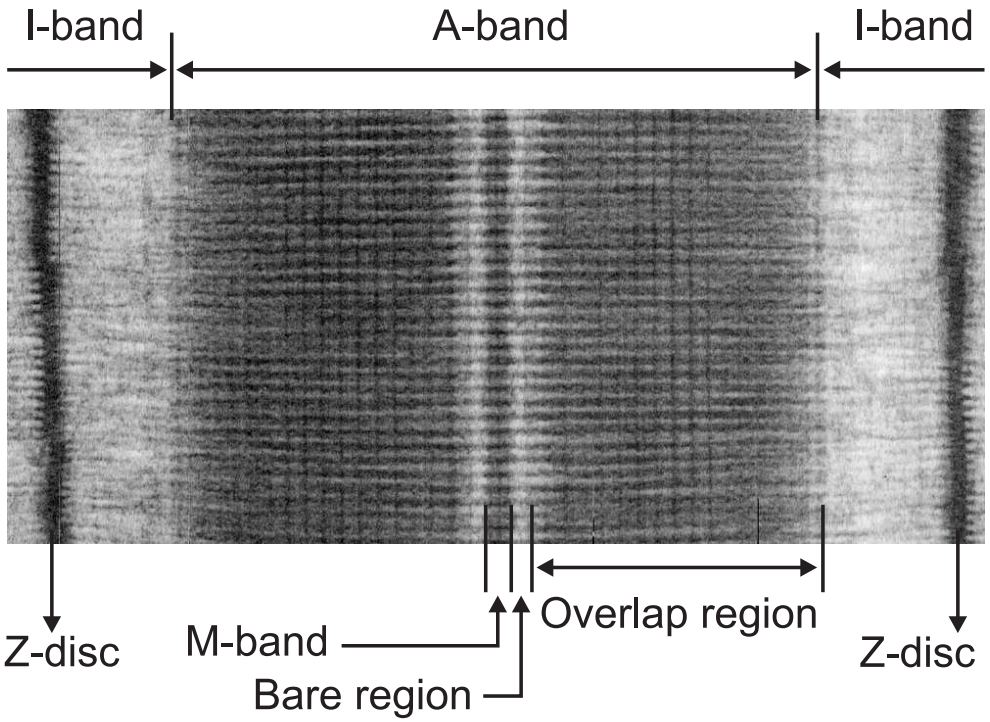


**Figure 1.7** Longitudinal section of the sarcomere. Typical length of a sarcomere is 2.4 $\mu$m. (Figure modified from [SAKKL05].)

Electron micrographs through transverse sections of the A-band show that the molecules pack on a hexagonal (or triangular) lattice (Fig. 1.2b-d). In particular, electron micrographs through the bare region clearly reveal the myosin lattice without interference from other molecular components (Fig. 1.8(a)). Direct observation of the 3-fold rotational symmetry is shown in Fig. 1.8(b). Careful inspection of such micrographs show that in most vertebrate striated muscles (except those in bony fish) the myosin filaments adopt one of two orientations, corresponding to a rotation of $\pm 60°$ (or $180°$ as a result of their 3-fold symmetry) about their long axis, and that the two orientations are distributed in a semi-random arrangement. The two orientations are referred to here as "up" and "down". This is referred to as the myosin lattice disorder. *A detailed study of the myosin lattice disorder is a primary*

*objective of this thesis.*

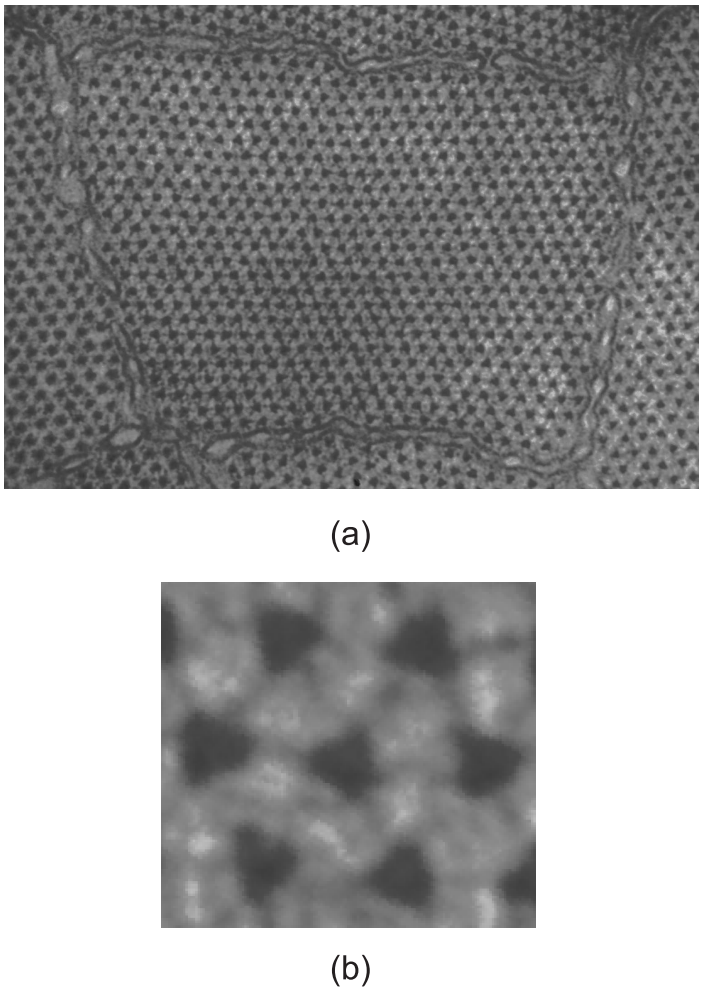


**Figure 1.8** Transverse section of the sarcomere. (a) Myosin filaments can be seen to lie on a hexagonal lattice, and (b) 3-fold rotational symmetry of myosin filaments about the fiber axis.

### 1.1.4 Myosin Lattice Disorder

The myosin lattice disorder refers to the semi-systematic distribution of orientations of the myosin filaments on the lattice. This naturally occurring phenomenon is directly observable and can be studied in most vertebrate muscles using electron micrographs of very thin and accurately cut transverse sections through the bare region (on each side of the M-band) where there can be between $200 \sim 1500$ filaments with each thick filament cross section being roughly triangular as described in Section 1.1.3.2. The A-band structure in fish muscle is different in that all the myosin filaments have only one orientation whereas the lattice observed in tetrapods exhibit substitution disorder of up and down filaments. Substitution disorder for the frog muscle in Fig. 1.8(a) is shown in Fig. 1.9.

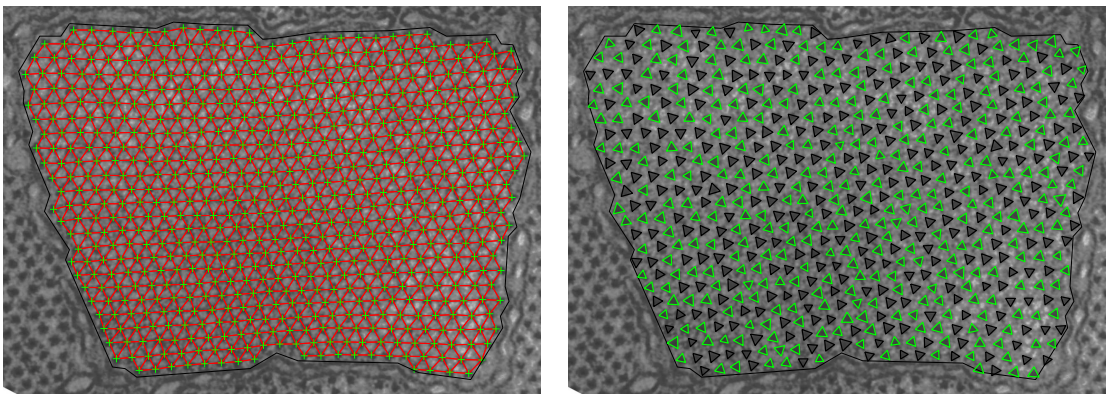

(a) (b)

**Figure 1.9** The myosin lattice disorder (a) the myosin filament positions deviate slightly from a regular hexagonal lattice, and (b) two filament orientations exist as indicated by the black and white triangles.

In 1980, Luther and Squire [LS80] determined, from studies of electron micrographs of frog sartorius muscles, that both up and down orientations are equally likely, however the distributions are not random. Some characteristics of the spatial distribution of the two orientations are described by using the so-called "no-three-alike" rules. These two rules define the way in which the neighbouring filaments tend to orientate with respect to each other (with some infrequent exceptions). Rule 1 states that no three mutually adjacent filaments in the hexagonal array of filaments in the A-band all have identical orientations; and rule 2 states that no three successive filaments along a row in the filament array have identical orientations. These rules are illustrated in Fig. 1.10.

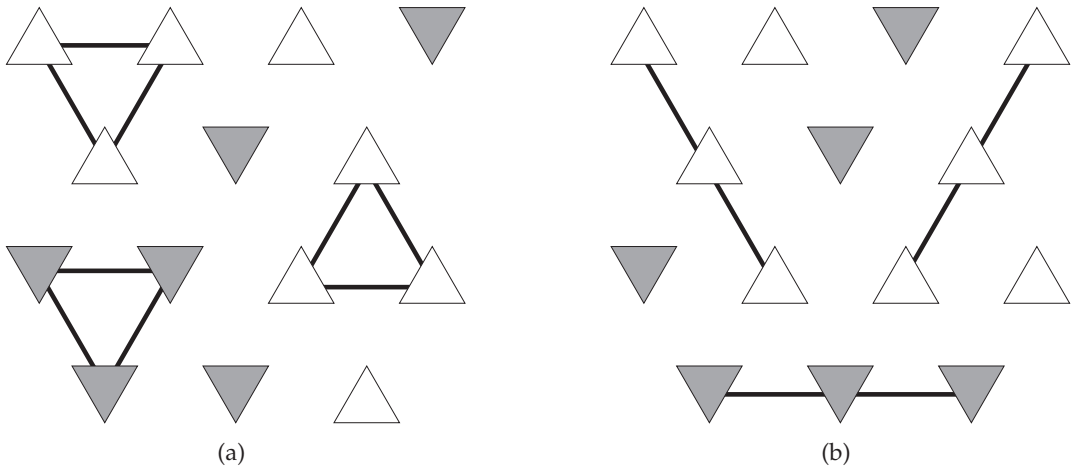

(a) (b)

**Figure 1.10** No-three-alike rule violations. (a) rule 1 and (b) rule 2.

The filaments which lie at the corners of a rhombus of side $\sim 81 \approx 47\sqrt{3}\, nm$, whose edges

join their second-nearest-neighbours, tend to have the same orientation and form the crystallographic pseudo-unit cell called the *superlattice* (Fig. 1.11) containing three myosin filaments and six actin filaments [LS80, HB67]. The existence of the superlattice structure was first conjectured by Huxley and Brown [HB67] from analysis of X-ray diffraction patterns of myosin lattice in the sartorius muscle of a frog. The no-three-alike rules are also called the superlattice rules since they appear to be related to the formation of superlattices. Understanding the disorder or the manifestation of the superlattices is important because it produces distinct peaks in the diffraction patterns of the muscle which must be taken into account for accurate diffraction analysis.

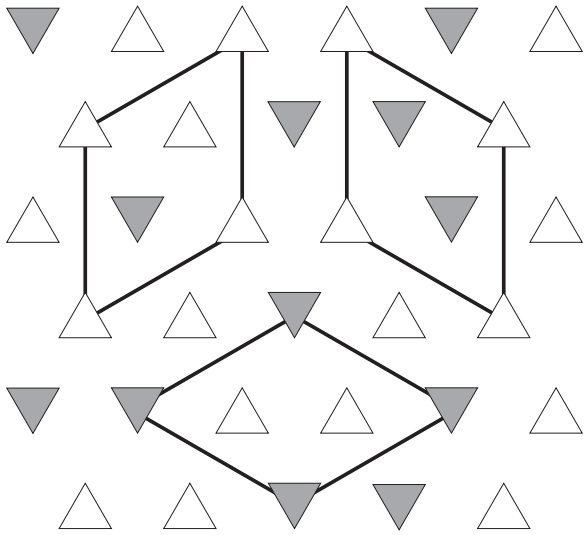

**Figure 1.11** Second-nearest-neighbours with the same orientation form superlattice cells.

As evidenced by reflections with spacings based on the $\sim$ 81 $nm$ lattice in X-ray fiber diffraction patterns, the same type of disorder is present in the myosin head arrangement [Hux74, LS80]. It is therefore expected that the disorder is related to the nature of the myosin head-actin interactions in the overlap region, and hence have implications for the mechanism of muscle contraction. It has been proposed that the superlattice structure leads to an efficient sharing of actin binding sites by myosin heads [LS80, LSF96]. The disorder in the superlattice places limitations on analysis and modelling of low-angle X-ray fiber diffraction data from higher vertebrate muscles because of so far undetermined effects on the diffracted X-ray intensities [Squ81]. Apart from its intrinsic interest, characterisation of the disorder would also open the door to rigorous analysis of X-ray fiber diffraction data from higher vertebrate muscles, as has been the case for other disordered systems [SM95a, ME02].

## 1.2 The Ising Model

### 1.2.1 General

The Ising model, named after Ernst Ising, is a simplified model of microscopic interactions of particles such as electrons, atoms and molecules which govern the macroscopic (physically measurable) quantities of a system. The model can be exactly solved to explain certain empirically observed facts about phase transitions in materials such as magnetising of cooling iron, boiling/freezing of water and superconductivity of materials at extremely low temperatures. In statistical mechanics, solving a model means being able to count the number of arrangements that add up to each energy level [Cip00]. It will be shown in Section 1.2.2 that this is equivalent to deriving the partition function of the system [WS98]. The real power of the Ising model comes from *universality*. Although the Ising model is an idealised representation of a real system, solving the model with the same dimensionality and symmetry of a real system, universality asserts that the exact critical exponents (physical quantities) of the real system will be obtained [MNE01, Cha87].

In 1924, in his Ph.D. thesis [Isi24], Ising solved the 1D case of a linear chain of particles that have magnetic moments (spins). He found that no phase transitions occur in the 1D case. A 2D case, the first of its kind, of a square lattice in the absence of an external magnetic field was analytically solved in 1944 by Onsager [Ons44]. The 2D case showed a phase transition which brought much attention to the subject. However, for extension of the model to 3D it turned out that the partition functions are no longer tractable [Ist00]. Despite this, a lot is known about 3D systems to high degrees of accuracy through the development of approximate methods and numerical methods such as Monte Carlo simulations.

The Potts model is a generalization of the Ising model where the spins are allowed to take $q$ different values. The 2D Ising model is the standard Potts model when $q = 2$. An Ising model postulates a lattice with a magnetic dipole or spin on each site, $s_i = \pm 1$. The states of the Ising system are the different sets of values that the spins can take, so that there are a total of $2^N$ possible states for a lattice with $N$ sites. The *Hamiltonian*, or the internal energy, for a general system is then

$$H = -\sum_{i,j} J_{ij} s_i s_j - B \sum_i s_i, \tag{1.1}$$

where $J_{ij} (= J_{ji})$ is the interaction energy between spins at sites $i$ and $j$, and $B$ is the external magnetic field strength applied to the system. The Hamiltonian system will tend to adopt configurations (arrangements of spins) that minimize the energy $H$.

For the remainder of the thesis, the discussion is restricted to Ising models in which only

nearest neighbour spins interact and the interaction is isotropic so that $J_{ij} = J$, and in the absence of an external field, so that $B = 0$. The Hamiltonian is then

$$H = -J \sum_{\langle i,j \rangle} s_i s_j, \tag{1.2}$$

where $\langle i, j \rangle$ denotes the set of nearest neighbours $(i, j)$. If $J > 0$ then identical adjacent spins have lower energy than opposite adjacent spins and the system is said to be *ferromagnetic*. If $J < 0$ then the system is said to be *antiferromagnetic* and opposite adjacent spins are preferred.

### 1.2.2 Elementary Statistical Thermodynamics

It was Gibbs [Gib02] who showed that for a system in state $\mu = (s_1, s_2, ..., s_N)$ with energy $E_\mu$ (given by Eq. (1.2)) in thermal equilibrium with an external thermal reservoir at temperature $T$, the equilibrium occupation probabilities are

$$p_\mu = \frac{e^{-E_\mu/k_B T}}{\sum_\mu e^{-E_\mu/k_B T}} = \frac{1}{Z} e^{-\beta E_\mu} \tag{1.3}$$

where $k_B$ is Boltzmann's constant, $1.38 \times 10^{-23} JK^{-1}$, $T$ is temperature, $e^{-E_\mu/k_B T}$ is the Boltzmann factor, $\beta = 1/(k_B T)$, and the normalising constant, $Z$ is called the *partition function* whose value is given by

$$Z = \sum_\mu e^{-\beta E_\mu}. \tag{1.4}$$

Consider the function for internal energy which is the ensemble average of the total energy of the system

$$\begin{aligned} U &= \sum_\mu p_\mu E_\mu \\ &= \frac{1}{Z} \sum_\mu (E_\mu e^{-\beta E_\mu}) \\ &= -\frac{\partial \ln Z}{\partial \beta}. \end{aligned} \tag{1.5}$$

The energy at a given temperature is therefore completely defined by the partition function. Also, the entropy can be expressed in terms of the partition function as

$$\begin{aligned} S &= -k_B \sum_\mu p_\mu \ln p_\mu \\ &= k_B \sum_\mu p_\mu (\beta E_\mu + \ln Z) \\ &= -k_B \beta \frac{\partial \ln Z}{\partial \beta} + k_B \ln Z. \end{aligned} \tag{1.6}$$

The Helmholtz free energy for a system is

$$\begin{aligned} A &= U - TS \\ &= -\frac{\partial \ln Z}{\partial \beta} - \Big( - k_B \beta T \frac{\partial \ln Z}{\partial \beta} + k_B T \ln Z \Big) \\ &= -k_B T \ln Z. \end{aligned} \tag{1.7}$$

Similarly other important critical exponents such as magnetization, specific heat and susceptibility can be derived from the partition function [Yeo92, BS96, NB99].

Expectation values can be regarded as the time average over many measurements of the same property of a single system, or measurements made for an ensemble of the replicated system at a single instant in time. Consider a physical system composed of $N$ identical particles confined to a space of volume $V$. Due to the statistical treatment, it is customary to perform the analysis in the so-called thermodynamic limit, $N \to \infty$ and $V \to \infty$ such that the ratio $N/V$, which represents the particle density, stays fixed at a preassigned value and fluctuations in the expected values vanish. In a typical case, $N$ would be an extremely large number - generally a mole, of order $10^{23}$ [Pat96].

Thermodynamics is based on experimental observations and hence describe the macroscopic properties of a system. Statistical mechanics affords quantitative insight at a microscopic level. On that note, the *spatial* (a.k.a. pair, spin-spin or two point connected) *correlation* function between sites $i$ and $j$, $\rho_{ij}$, is defined as

$$\begin{aligned} \rho_{ij} &= \frac{1}{Z} \sum_\mu x_i^\mu x_j^\mu e^{-\beta E_\mu} - \left[ \frac{1}{Z} \sum_\mu x_i^\mu e^{-\beta E_\mu} \right] \left[ \frac{1}{Z} \sum_\mu x_j^\mu e^{-\beta E_\mu} \right] \\ &= \langle x_i x_j \rangle - \langle x_i \rangle \langle x_j \rangle \\ &= \langle (x_i - \langle x_i \rangle)(x_j - \langle x_j \rangle) \rangle, \end{aligned} \tag{1.8}$$

where $x_i^\mu$ is the value of $x_i$ in state $\mu$. For a stationary system the statistics are independent of position so that $\rho_{ij}$ depends only on the geometric difference $\mathbf{d}_{ij}$ between sites $i$ and $j$.

### 1.2.3 The One-Dimensional Ising Model

Some of the key characteristics of the Ising model (without a phase transition) are easily illustrated by the one-dimensional model which is exactly solvable. The 1D model is therefore outlined here in detail.

Consider a magnet with $N$ spins laid out in a line equally spaced where each spin has a magnetic moment that is either up (represented by the value $+1$) or down ($-1$). Each spin only interacts with its nearest neighbours. In order to make the system translationally invariant, a periodic boundary condition is imposed on the system, i.e. $s_{N+1} \equiv s_1$ [Hua63, Bax82]. The thermodynamic limit is then obtained for $N \to \infty$. This system is illustrated in Fig. 1.12.

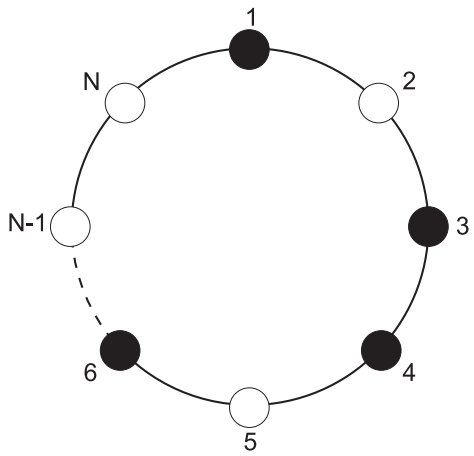


**Figure 1.12** One-dimensional Ising model. Black and white circles represent the spins, up and down, respectively.

Given the topology of the 1D chain in Fig. 1.12, the partition function is

$$Z = \sum_{s_1} \sum_{s_2} \sum_{s_3} \cdots \sum_{s_N} e^{-\beta J (s_1 s_2 + s_2 s_3 + \cdots + s_{N-1} s_N + s_N s_1)}. \tag{1.9}$$

Since

$$\sum_{s_i} e^{-\beta J s_i s_{i+1}} = e^{\beta J} + e^{-\beta J} = 2\cosh(\beta J), \tag{1.10}$$

the partition function is

$$Z = \{2\cosh(\beta J)\}^N. \tag{1.11}$$

Note that the second step in Eq. (1.10) is independent of $s_{i+1}$. The system is thus exactly solvable.

Substituting Eq. (1.11) into Eq. (1.5), the internal energy can be expressed explicitly as

$$U = -NJ \tanh(\beta J). \tag{1.12}$$

It is usual to express this as the internal energy per site, viz.

$$U/N = -J \tanh(\beta J). \tag{1.13}$$

Similarly, the entropy per site can be expressed explicitly using Eq. (1.11) and Eq. (1.6) as

$$S/N = k_B[\ln 2 + \ln(\cosh(\beta J)) - \beta J \tanh(\beta J)]. \tag{1.14}$$

Note that both Eqs. (1.13) and (1.14) are independent of the sign of $J$. The internal energy (normalised against J) and entropy are plotted in Fig. 1.13 versus temperature. Inspection of Fig. 1.13 shows the expected behaviour. At $T = 0$ (the ground state) the system settles into the minimum energy configuration with all bonds satisfied so that $U = -NJ$, which can also be seen from substituting $T = 0$ ($\beta \to \infty$) into Eq. (1.13). For the ferromagnetic system the ground state configuration is all spins identical, and for the antiferromagnetic system the spins are alternating. Since these are two such ground state configurations in either case, the entropy $S = k_B \ln(2)$, and the entropy per site $S/N$ vanishes at absolute zero. This can also be seen from substituting $T = 0$ ($\beta \to \infty$) into Eq. (1.14). For $T \to \infty$ thermal fluctuations dominate, the spin configurations become random, there is an equal number of satisfied and unsatisfied bonds and the energy averages to zero. This can also be seen from substituting $T \to \infty$ ($\beta = 0$) into Eq. (1.13). For large temperatures, all configurations, of which there are $2^N$, are equally likely, so that the entropy approaches $S = k_B \ln(2^N)$ and that the entropy per site approaches $k_B \ln(2) \approx 0.693 k_B$. This value is also obtained by substituting $\beta = 0$ into Eq. (1.14). As shown in Fig. 1.13 there is a smooth transition from $T = 0$ to $T \to \infty$, i.e. there is no phase transition.

The spatial correlation function clearly depends only on the distance $d$ between the sites $i$ and $j$, and is denoted $\Gamma(d)$. Using the transfer matrix method [KW41, WMC80, Yeo92] to simplify the partition function and substituting into Eq. (1.8) gives

$$\rho(d) = \tanh^d(\beta J). \tag{1.15}$$

The correlation function is plotted in Fig. 1.14 for both ferromagnetic and antiferromagnetic systems for the three cases $T = 0$, $T > 0$ and $T \to \infty$. At $T = 0$, all bonds are satisfied, there is long range order, and the correlation function reflects the identical and alternating ground states for the ferromagnetic and antiferromagnetic cases, respectively. For $T > 0$, thermal fluctuations result in these correlations decaying with distance and only short range order remains. As $T \to \infty$, all correlation vanishes as the sites have random spins.

Note that the decay is the same for both systems, but there is a sign change for odd $d$ when the system is antiferromagnetic.

This concludes the treatment of the one-dimensional Ising model and the fundamental theory supporting it. Now, the model is extended to the antiferromagnetic triangular lattice which exhibits geometric frustration.

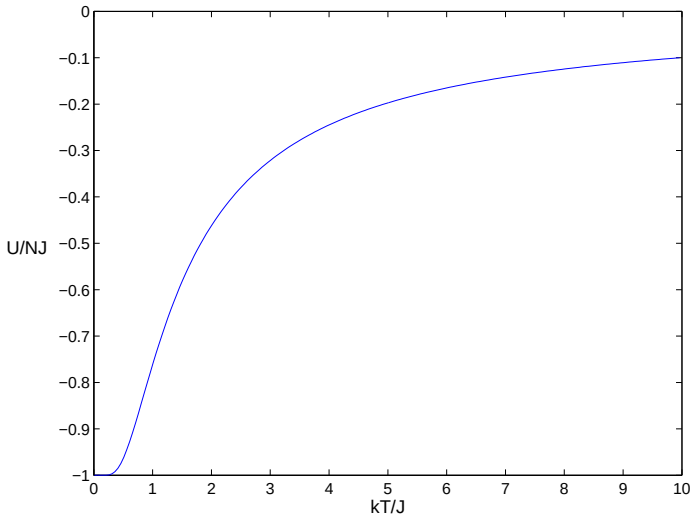


(a)

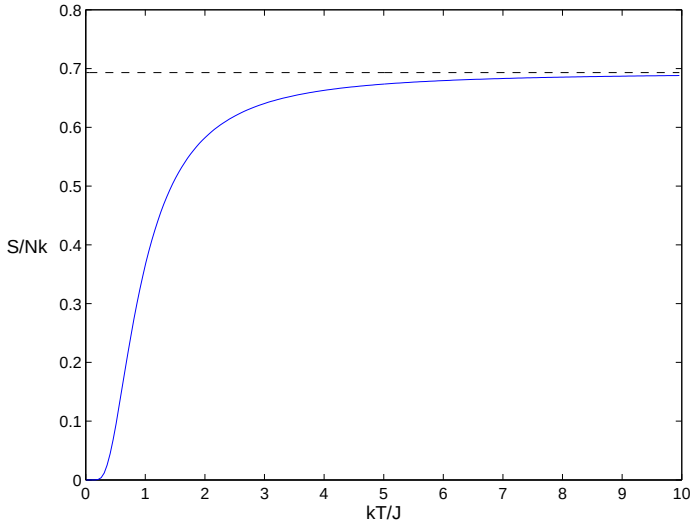


(b)

**Figure 1.13** (a) The internal energy and (b) the entropy of a one-dimensional Ising model system in zero field as a function of temperature.

### 1.2.4 Geometric Frustration on a Triangular Lattice

A spin system is frustrated if it cannot minimise the energy of each spin pair simultaneously. [AC97]. Frustration may arise in situations wherein a large fraction of spins in a

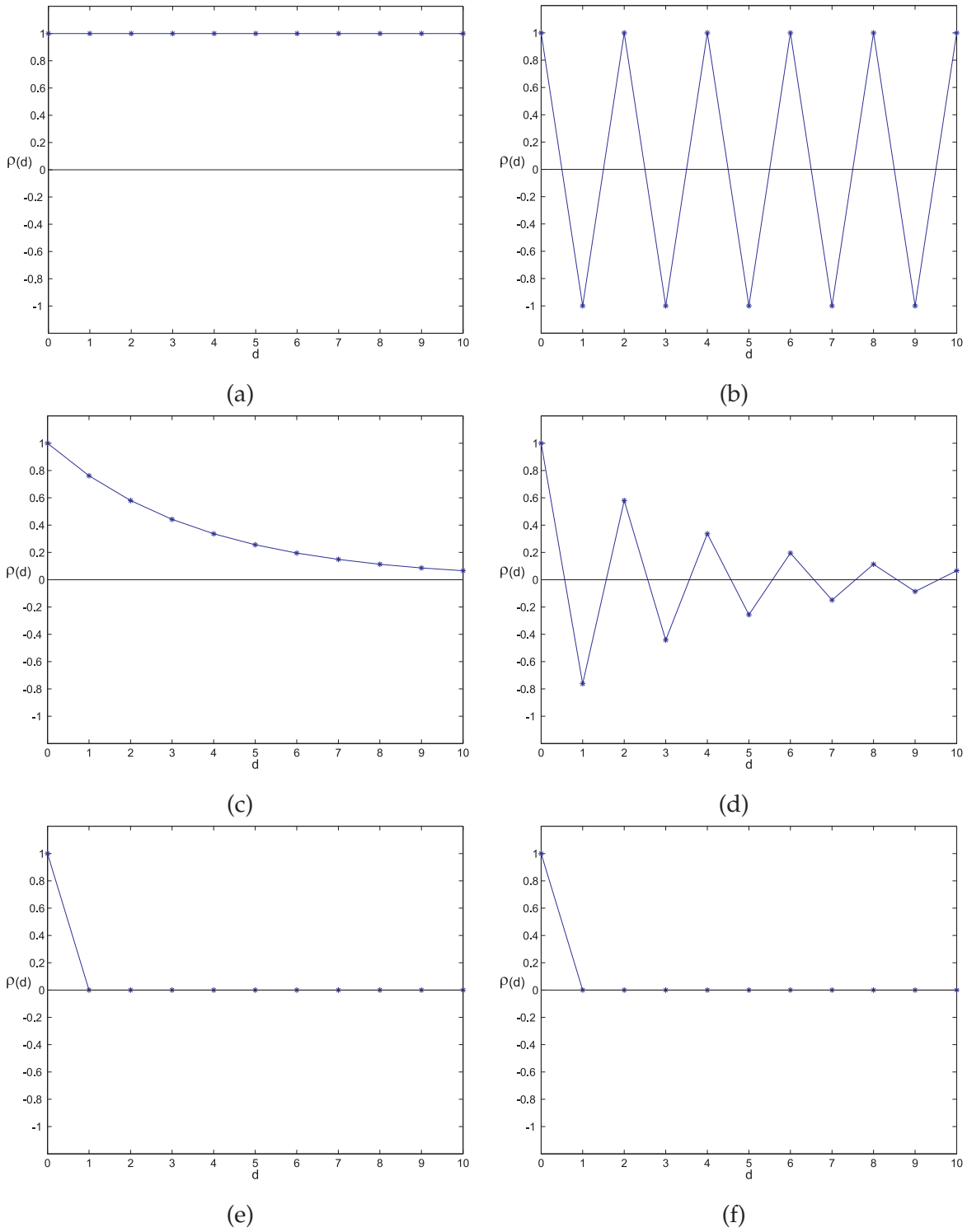


**Figure 1.14** Spatial correlation functions of a one-dimensional Ising model system in zero field as a function of spatial separation between two spins. Ferromagnetic and antiferromagnetic interactions are shown in the first and second columns, respectively, for (a, b) T = 0, (c, d) T = 1.0 and, (e, f) $T \rightarrow \infty$.

lattice are subject to competing or contradictory constraints [Gre01, Ram03]. As a result, even in the ground state all bonds are not fully satisfied, and it is highly degenerate (many states with equal energy). This phenomenon is important in a variety of systems from water ice to superconductivity [Pau35, Lie86]. Frustration became of interest to physicists almost 60 years ago when Wannier [Wan50] and Houtappel [Hou50] realised that the ground states are degenerate for an antiferromagetic Ising model on a triangular lattice, despite a naïve expectation of the third law of thermodynamics where one may expect the system to order down to a single minimum energy state [MS01]. That is, in the absence of frustration, an antiferromagnetic system would be expected to have all spins antialign to minimise the energy at $T = 0$. When frustration arises purely from the geometry or topology of the lattice it is termed geometric frustration [Gre01]. Geometric frustration has so far been observed in physical systems (e.g. magnetic materials, superconductors, spin ice) in which the elements are simple entities such as magnetic moments, atoms or small molecules [RHC$^+$99, Ram05].

Square and triangular lattices are used here to illustrate the concept of geometric frustration. Square lattices belong to the family of bipartite lattices. Bipartite lattices are not geometrically frustrated for an antiferromagnetic Ising system. A bipartite lattice is one that can be partitioned into two similar sublattices, $A$ and $B$, such that every site in $A$ has only nearest neighbours belonging to $B$ and vice versa [MNE01]. However, if only nearest neighbour interactions are present, it is clearly possible to assign one spin to sublattice $A$ and the other spin to sublattice $B$ so that all bonds are antiferromagnetic (Fig. 1.15).

On the other hand, a triangular lattice is a canonical example of a geometrically frustrated system for antiferromagnets. A triangular plaquette (Fig. 1.16) shows three mutual nearest neighbours. If antiferromagnetism is imposed on the lattice with opposite adjacent spins energetically preferred over identical adjacent spins, it is impossible to minimise the energy of all three interactions (Fig. 1.16), and if two spins have opposite orientations then the energy is independent of the orientation of the third spin leading to six (instead of two for ferromagnets) minimum energy configurations [MS01].

The fact that the antiferromagnetic triangular lattice is geometrically frustrated modifies particularly the low temperature behaviour because of the different set of ground states from the ferromagnetic case. For non-frustrated models, there are only two possible ground states and their minimum energy at absolute zero given by

$$U_0 = -\mathcal{N}J, \tag{1.16}$$

where $\mathcal{N}$ is the total number of interacting spin pairs (cardinality of the set $< i, j >$) [Wan50, MGP03]. In the thermodynamic limit, there are $3N$ bonds for a triangular lattice of size $N$. Ground state configurations admit a minimum energy configuration with energy -1 for

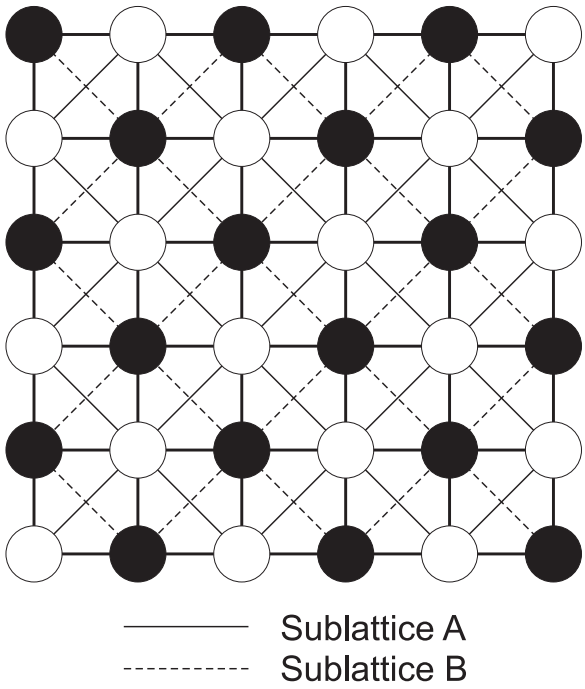


**Figure 1.15** A square lattice is bipartite. Two sublattices can take on separate spins, so that all bonds are antiferromagnetic on a square lattice. Black and white circles represent the spins, up and down.

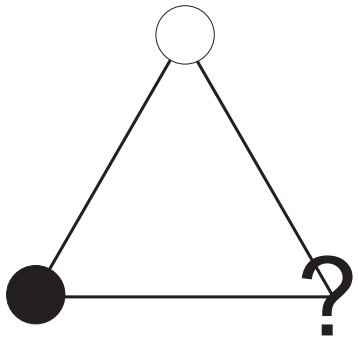


**Figure 1.16** Three mutual nearest neighbours on a triangular plaquette. The system is frustrated independent on the third spin. Black and white circles represent the spins, up and down.

each plaquette since only 2/3 of the interactions are favourable, so that the ground state energy is

$$U_0 = -\mathcal{N}J/3 = -NJ. \tag{1.17}$$

Wannier (1950) calculated the ground state entropy by counting the number of ground state configurations. Some of the classes of configurations are shown in Fig. 1.18. In Fig. 1.18a, rows of positive spins are placed in alteration with rows of negative spins. This simple arrangement contributes little to the entropy because there is only one such arrangement. Fig. 1.18b shows a configuration type where rows of alternating spins are stacked at random. Each row can be stacked independently, so there are $2^{\sqrt{N}}$ such configurations. This type is said to have a weight gain of $2^{\sqrt{N}}$. Since the entropy per site is proportional to $N^{-1}\ln(\text{weight gain})$, neither of these types of configuration contribute residual ground state entropy. The weight gain must grow exponentially as $\mathcal{O}(e^N)$ to contribute to the entropy. Fig. 1.18c shows the triangular lattice partitioned into three triangular sublattices of second-nearest neighbours with spacings of $\sqrt{3}$ (Fig. 1.17). Two sublattices have spins of fixed sign, but in the third, each sign can be assigned randomly. The weight gain is therefore $2^{N/3}$, and this does contribute to the entropy. Wannier considered all such contingencies and showed that the entropy per spin is finite at absolute zero [Wan50, JF97] and is given by

$$\frac{S_0}{N} = k_B \frac{2}{\pi} \int_0^{\pi/3} \ln(2\cos\omega)\mathrm{d}\omega \backsimeq 0.3231 k_B. \tag{1.18}$$

Note that the value of $\sim 0.3383$ given by Wannier (1950) is incorrect [MC06].

The spatial correlations of rectangular two-dimensional Ising lattice were first derived by the Onsager-Kaufman formulas [Ons44, Kau49]. In terms of Pfaffians, the correlations along a row was simplified as a single Toeplitz determinant which proved to be equivalent to the Onsager-Kaufman result [MPW63]. For the triangular Ising lattice at $T = 0$, the determinant is exactly solvable and Stephenson [Ste64] presented evidence that the asymptotic behaviour (i.e. as $d \to \infty$) of the spatial correlation along the lattice axis, to first order, is of the form

$$\rho(d) \backsim \epsilon_0 d^{-\frac{1}{2}} \cos(2\pi d/3), \tag{1.19}$$

where $\epsilon_0 = 2^{1/2}(E_0^T)^2 = 0.632226 \pm 2$, $E_0^T$ being the decay amplitude of the pair correlation at the Curie point (critical point) of an isotropic ferromagnetic triangular lattice. Eq. (1.19) is plotted in Fig. 1.19. Since $d$ takes integer values on the axis, the cosine takes the values $\{1, -\frac{1}{2}, -\frac{1}{2}, 1, -\frac{1}{2}, -\frac{1}{2}, \dots\}$. The correlation therefore decays as $d^{-1/2}$ weighted by $+1$ or $-1/2$ as shown in Fig. 1.19. The lattice can be partitioned into 3 sublattices (Fig. 1.17) such that positive correlations occur when the two sites are on the same sublattice and negative correlations when they are on different sublattices.

For a general off-axis separation, little is known on the precise form of the correlation.

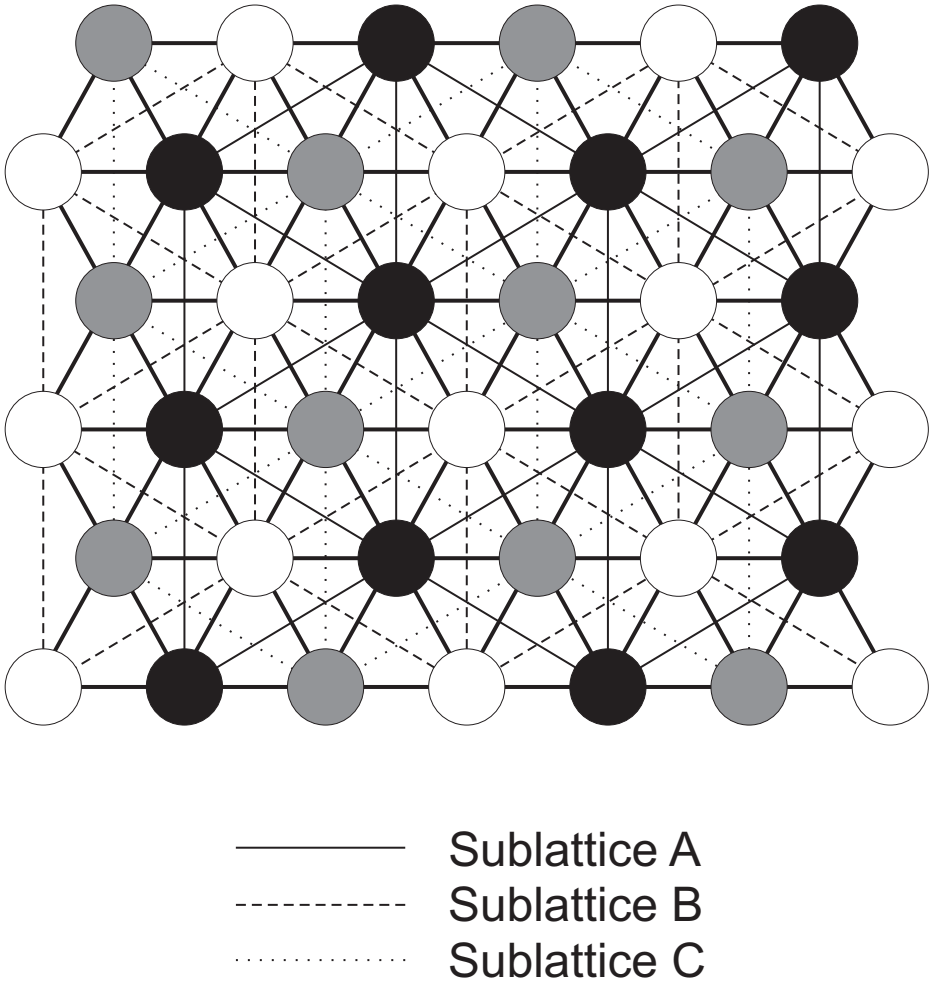


**Figure 1.17** Three triangular sublattices of second-nearest neighbours with spacings of $\sqrt{3}$.

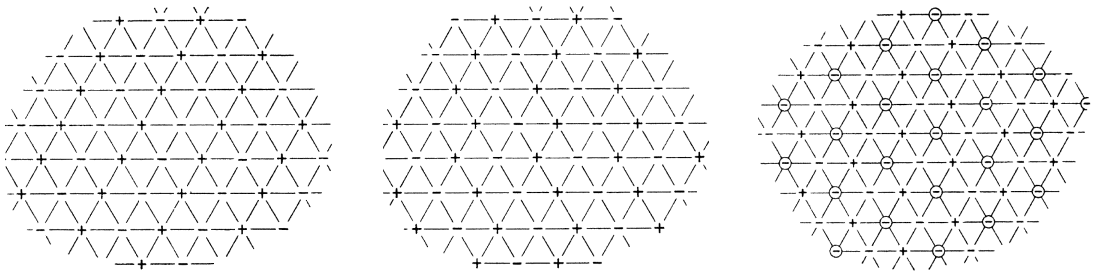


**Figure 1.18** Ground states of the antiferromagnetic Ising net. (a) A simple arrangement of minimum energy: Rows of positive spins placed in alteration with rows of negative spins. (b) An arrangement of minimum energy having medium-high weight: Rows of alternating spins stacked at random. (c) An arrangement of minimum energy having finite entropy: Two sublattices have spins of fixed sign, but in the third, each sign individually may be picked at random [Wan50].

However, there is evidence that it is approximated by Eq. (1.19) with cosine replaced by a factor equal to $+1$ if the two spins are on the same sublattice and $-1/2$ otherwise [Ste70, NHB84]. This implies that the correlation function is approximately (although probably not exactly) rotationally symmetric. Recent work shows that to higher order the correlation can be described in terms of three sublattices [WM08], however the above description is sufficient for the purposes of this thesis.

For $T > 0$, Stephenson (1970) derived an expression for the correlation using the asymptotic properties of the Toeplitz determinants [Wu66] as

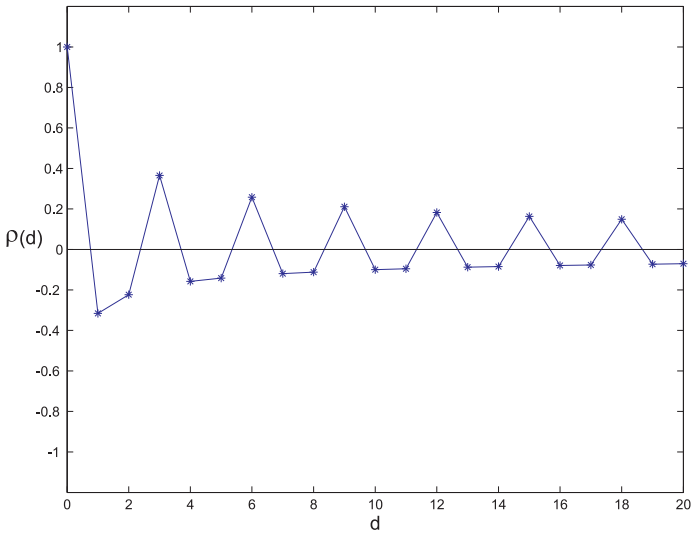


**Figure 1.19** Asymptotic behaviour of the spatial correlation along the triangular lattice axis at $T = 0$ calculated from Eq. (1.19).

$$\begin{aligned}\rho(d) \backsim & \left(\frac{\pi \sin\theta}{2}\right)^{-\frac{1}{2}} \nu^d d^{-1/2} \Big\{ \cos\left(d\theta + \frac{\theta}{2} - \frac{\pi}{4} - \phi\right) \\ & -(4d)^{-1}\Big[\frac{3}{2} + (2\sin\theta)^{-1}\cos\left(d\theta + \frac{3\theta}{2} + \frac{\pi}{4} - \phi\right) \\ & +\nu^2(1-\nu^2)^{-1}\cos(d\theta + \frac{\theta}{2} - \frac{\pi}{4} - \phi) \\ & +\nu^2\varrho^2\cos\left(d\theta + \frac{3\theta}{2} - \frac{\pi}{4} - 3\phi\right)\Big]\Big\}, \end{aligned} \tag{1.20}$$

where

$$\nu = \tanh(\beta J), \tag{1.21}$$

the real angle $\theta$ is defined by

$$\cos\theta = (1 + e^{4\beta J})/2, \quad 0 < \theta \leq \pi/3, \tag{1.22}$$

$$\varrho = (1 - 2\nu^2 \cos 2\theta + \nu^4)^{-1/4} \tag{1.23}$$

and

$$\phi = -\frac{1}{2} \arg(1 - \nu^2 \cos 2\theta + i\nu^2 \sin 2\theta). \tag{1.24}$$

It is easily verified that $-1 \leq \nu < 0$ from Eq. (3.30). Hence $\nu^d$ can be expressed as $(-1)^d|\nu|^d$. Then the essential features of the behaviour of the first term in Eq. (1.20) with $d$ are: (i) an exponential decay $|\nu|^d$ with alternating sign, (ii) a modulation by the cosine term and (iii) a decay amplitude of $(\frac{1}{2}\pi \sin\theta)^{-1/2}$. The first term of Eq. (1.20) is plotted in Fig. 1.20 for T = 1.0. Comparison with Fig. 1.19 shows similar behaviour but with a more rapid decay with $d$. This is as expected with increasing thermal disorder as the temperature increases. A more detailed analysis of Eq. (1.20) is given in Section 3.5.3

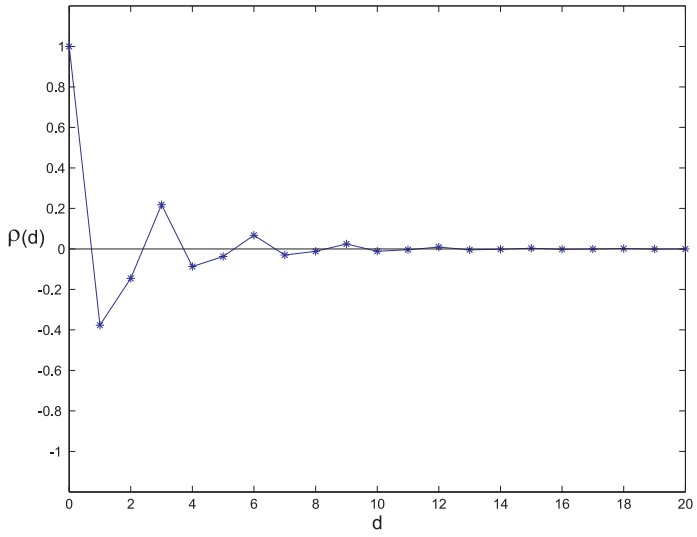


**Figure 1.20** Asymptotic behaviour of the spatial correlation along the triangular lattice axis at $T = 1.0$ calculated using the first term in Eq. (1.20).

Little is known analytically about the off-axis correlation function for $T > 0$ although, similar to the $T = 0$ case, it is believed to be approximately rotationally symmetric with relative weights of 1 and $-1/2$ for sites on the same and different sublattices, respectively.

## 1.3 Monte Carlo Simulation

### 1.3.1 Metropolis Algorithm

Monte Carlo simulation is a numerical method for simulating the random thermal fluctuation of a system from state to state where the expectations of the macroscopic properties can be regarded as the sample average over the states that the system passes through [MU,

NB99]. The Metropolis Monte Carlo algorithm was first published by Metropolis *et al* [MRR$^+$] for calculating the properties of any substance which may be considered as composed of interacting individual molecules. Metropolis Monte Carlo simulation is used to generate finite temperature states of the Ising model on a triangular lattice in Chapter 3 and the simulation method is outlined here.

The Metropolis algorithm works by simulating state transitions of the Ising model. The algorithm used and described here is referred to as having single-spin-flip dynamics meaning that transitions from one state to the next state is made by flipping the spin of a single site depending on its energy preferability. This is a Markov process since the next state is dependent on the current state regardless of the events that have occurred beforehand [GRS96]. The algorithm is constrained by ergodicity and detailed balance. Ergodicity requires only that all states of the lattice be reachable from the current state. A Markov process is said to obey detailed balance if

$$p_\mu P(\mu \to \nu) = p_\nu P(\nu \to \mu), \tag{1.25}$$

where $p_\mu$ and $p_\nu$ are the equilibrium occupation probabilities of being in states $\mu$ and $\nu$, respectively; and $P(\alpha \to \beta)$ is the short hand notation for $P(X_t = \beta | X_{t-1} = \alpha)$, the transition probability from the previous state $X_{t-1} = \alpha$ to the current state $X_t = \beta$.

Using single-spin-flip dynamics, the previous state $\mu$ and the current state $\nu$ differ by a single spin at $i^{th}$ site, $s_i$. Then the transition probability, $P(\mu \to \nu)$ is the product of two probabilities; the selection probability, $g(\mu \to \nu)$, the probability of the $i^{th}$ site $s_i$ being selected and the acceptance probability, $A(\mu \to \nu)$, the probability of accepting the flip of the $i^{th}$ site $s_i$, i.e.

$$P(\mu \to \nu) = g(\mu \to \nu) A(\mu \to \nu). \tag{1.26}$$

Given that the equilibrium distribution needs to be the Boltzmann distribution, the values of $p_\mu$ need to be the Boltzmann probabilities, Eq. (1.3). The transition probabilities satisfying the condition of detailed balance Eq. (1.25) is then

$$\frac{P(\mu \to \nu)}{P(\nu \to \mu)} = \frac{p_\nu}{p_\mu} = e^{-\beta(E_\nu - E_\mu)}. \tag{1.27}$$

Since the constraint only fixes the ratio

$$\frac{P(\mu \to \nu)}{P(\nu \to \mu)} = \frac{g(\mu \to \nu) A(\mu \to \nu)}{g(\nu \to \mu) A(\nu \to \mu)}, \tag{1.28}$$

there is complete freedom for choosing the selection probabilities and the acceptance probabilities.

The energies of systems in thermal equilibrium stay within a very narrow range - the energy fluctuations are small by comparison with the energy of the entire system. This allows us to narrow the search to a small subset of states that differ from the present state by only the flip of a single spin, i.e. single-spin-flip dynamics. Using single-spin-flip dynamics guarantees that the new state $\nu$ will have an energy $E_\nu$ differing from the current energy $E_\mu$ by at most $2J$ for each bond between the spin we flip and its neighbours. The maximum total energy change, $\Delta E_{max}$, is therefore $12J$ for the triangular lattice.

The selection probabilities $g(\mu \to \nu)$ for each of the possible states $\nu$ (the ones that only differ by a single-spin-flip) are all chosen to be equal, since there is no preference for selecting one site over the other. The selection probabilities for the rest (the states that differ by more than a single-spin-flip) are set to zero without violating the ergodicity constraint, since it is clearly possible to reach any state by flipping one site at a time. Hence

$$g(\mu \to \nu) = g(\nu \to \mu) = \frac{1}{N}. \tag{1.29}$$

Therefore, using Eqs. (1.27) and (1.28), the condition of detailed balance is simplified to

$$\frac{P(\mu \to \nu)}{P(\nu \to \mu)} = \frac{A(\mu \to \nu)}{A(\nu \to \mu)} = e^{-\beta(E_\nu - E_\mu)}. \tag{1.30}$$

The algorithm works by repeatedly choosing a new state $\nu$, and then accepting or rejecting it according to the chosen acceptance probability. If the state is accepted, the transition to the new state $\nu$ is made. If not, the state is left as it is, i.e. state $\mu$.

In taking a simple approach, one may set the acceptance ratios to

$$A(\mu \to \nu) = e^{-\beta(E_\nu - E_\mu + \Delta E_{max})/2} \tag{1.31}$$

and

$$A(\nu \to \mu) = e^{\beta(E_\nu - E_\mu - \Delta E_{max})/2}, \tag{1.32}$$

so that Eq. (1.30) is satisfied. Note that the term $\Delta E_{max}$ is added to constrain the acceptance probabilities between 0 and 1. As shown in Fig. 1.21, the vast majority of the moves are rejected and the system is idle for most of the flips. The Metropolis algorithm is efficient in the sense that the acceptance probabilities are maximised. The way to maximise the acceptance probabilities is always to give the larger of the two acceptance probabilities $A(\mu \to \nu)$ or $A(\nu \to \mu)$ the largest value possible - namely 1- and then adjust the other to satisfy the constraint Eq. (1.30). To see how that works out in this case, suppose that of the two states $\mu$ has the lower energy and $\nu$ the higher, i.e., $E_\mu < E_\nu$. Then the larger of the two acceptance probabilities $A(\nu \to \mu)$ is set to one. In order to satisfy Eq. (1.30), $A(\mu \to \nu)$ must then take the value $e^{-\beta(E_\nu - E_\mu)}$ [NB99]. Thus the acceptance probabilities are given

by

$$A(\mu \to \nu) = \begin{cases} e^{-\beta(E_\nu - E_\mu)} & \text{if } E_\nu - E_\mu > 0 \\ 1 & \text{otherwise.} \end{cases} \tag{1.33}$$

This is shown in Fig. 1.21. This states that if the flip would result in the decrease of the total energy of the system, then it is always accepted. Otherwise, the move is accepted with a probability that decreases, proportional to the Boltzmann factor, as the energy gain of the system increases. This is the essence of the Metropolis algorithm. Successive states are generated by repeatedly applying single-spin-flip dynamics. After convergence at a particular temperature, the algorithm produces a sequence of states in equilibrium at that temperature.

The Metropolis algorithm near the critical temperature can suffer from critical slowing down. This phenomena arises as the system prepares for a phase transition and the correlation length increases forming large clusters. Since the clusters are already in the favourable state, the acceptance probability $A(\mu \to \nu)$ drops dramatically as the temperature approaches the critical temperature requiring a huge number of flips to reach equilibrium, making it very inefficient and inaccurate. Alternative cluster-flipping dynamics are used in the Wolff, Swendsen-Wang and Niedermayer's algorithms that perform considerably better than the Metropolis algorithm near the critical temperature. The reader is referred to the details in [Wol89, SW87, Nie88]. However, the Metropolis algorithm is the most efficient algorithm away from the critical temperature [NB99] which is the case considered in this thesis. The number of flips required for the system to reach equilibrium at a particular temperature is discussed next.

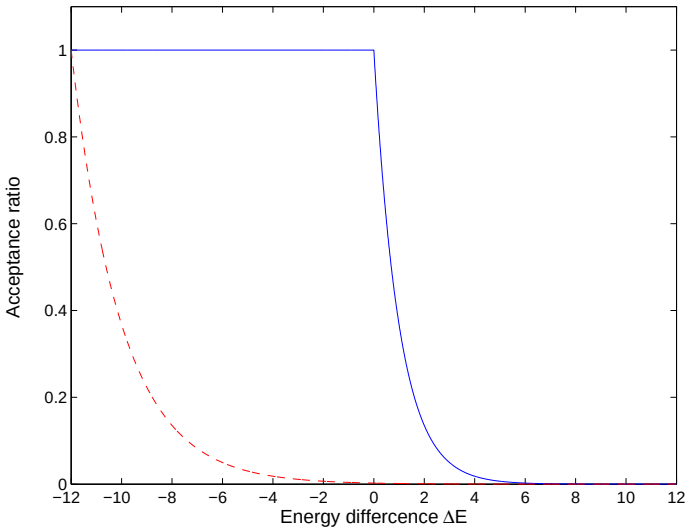


**Figure 1.21** Plot of the acceptance ratios $A(\mu \to \nu)$ against the energy difference. The acceptance ratio in Eq. (1.31) (dashed line) and the Metroplis acceptance ratio (solid line). Figure based on [NB99].

### 1.3.2 Equilibration and Decorrelation

Analogous to a hot apple pie cooling on a window sill, a system in thermal exchange with an external thermal reservoir gradually reaches the same temperature as its surroundings. Then the system is said to be in thermal equilibrium which means that parameters such as the internal energy, entropy and spatial correlation etc. have stabilised and the average probability of finding the system in any particular state $\mu$ is proportional to the Boltzmann weight $e^{-\beta E_\mu}$ of that state. Ideally, one should wait an infinite amount of time for the system to come to equilibrium with its surroundings. However in reality, this is not possible and for all intents and purposes, the time to reach equilibrium will be taken to be finite which is referred to as the *equilibration time*, $\tau_{eq}$. Note that time in Monte Carlo simulations is measured in *sweeps*, a sweep being $N$ attempted flips where $N$ is the number of sites on the lattice. Hence $\tau_{eq}$ is defined to be the number of sweeps required for some parameter value to close within one standard deviation of the parameter mean.

Once equilibrium is reached, the system configurations can be sampled to compute ensemble averages to compute macroscopic quantities. Independent samples are needed to compute an unbiased average. For single-spin-flip dynamics subsequent states are highly correlated however, and it takes many transitions to generate a new system that is significantly different from the former sample. The *decorrelation time* $\tau_{decorr}$ measures the number of sweeps required for a sufficiently independent state to be obtained. The decorrelation time is calculated using the time-displaced autocorrelation [NB99], given by

$$\mathcal{X}[j] = \frac{1}{n-j}\sum_{i=0}^{n-j} x[i]x[i+j] - \frac{1}{(n-j)^2}\sum_{i=0}^{n-j} x[i]\sum_{i=0}^{n-j} x[i+j], \tag{1.34}$$

where $x[i]$ is the value of some parameter after $i$ sweeps, $n$ is the number of sweeps, and $\mathcal{X}[j]$ is the time-displaced autocorrelation with a displacement of $j$ sweeps. The decorrelation time $\tau_{decorr}$ is then determined by running a simulation for a sufficiently large number of sweeps $n$, calculating the time-displaced autocorrelation for some parameter, and then finding the displacement such that the autocorrelation falls to $e^{-1} \approx 0.37$ of its zero-displacement value. i.e.,

$$\tau_{decorr} = \text{argmin}_j\{\mathcal{X}[j] \leq e^{-1}\} \qquad \text{for } j \in [0, n-1]. \tag{1.35}$$

Note that when $j$ gets close to $n$, there are few terms in the sums in Eq. (1.34) and the statistical errors become large, hence it is important to keep $n >> j$. Typically, $n > 2j$ is sufficient. States that are spaced by more than $\tau_{decorr}$ sweeps are considered to be sufficiently independent for averaging to obtain estimates of macroscopic parameters. Typically a spacing of $2\tau_{decorr}$ is used and the expected number of samples $\eta$ per simulation is

then given by

$$\eta = \frac{n - \tau_{eq}}{2\tau_{decorr}}. \tag{1.36}$$

## 1.4 X-ray Crystallography

X-ray crystallography is a collection of experimental techniques that are used to determine the arrangement of atoms within a crystal at atomic, or near atomic, resolution [WHf95]. In an experiment, a crystalline specimen is irradiated by a monochromatic beam of X-rays where the electrons in the specimen interact and scatter the incident beam (Fig. 1.22(a)) producing a diffraction pattern of regularly spaced intensity peaks, called reflections. The diffracted intensities are recorded by a detector at various orientations where spacing and symmetry information can be derived directly. A three-dimensional electron density map can be built up by constraining the molecular model with knowledge of the primary structure and the stereochemical information. Considering that 38,914 of the 45,744 structures (11 Sept. 2007) contained in the Protein Data Bank (PDB) were determined using X-ray diffraction, it is the most predominant tool for studying molecular structures and structure/function relationships.

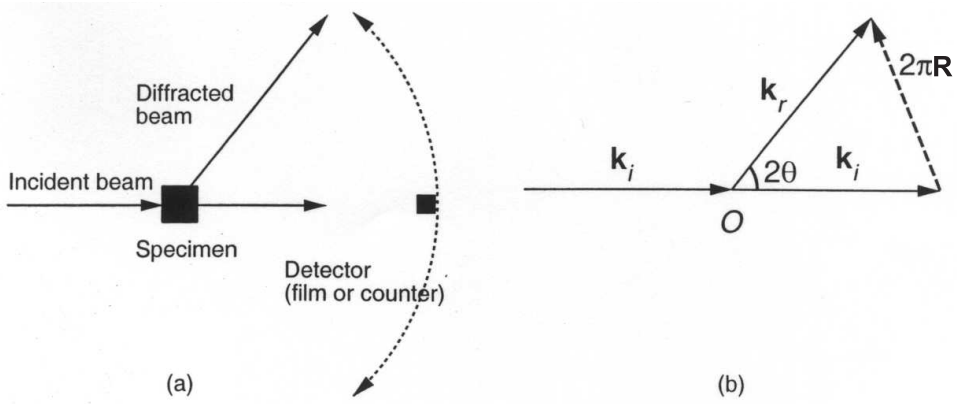


**Figure 1.22** (a) The experimental setup for an X-ray crystallography experiment, and (b) the relationship between the wavevectors $\mathbf{k}_i$ and $\mathbf{k}_r$ and scattering angle $2\theta$. [Ead01]

### 1.4.1 Diffraction of X-rays

X-rays used in crystallography have a wavelength of approximately 1Å (0.1nm) [Gui63]. This is the ideal wavelength for producing significant diffraction in crystals that typically possess interatomic distances on the same scale. Consider an incident wavevector $\mathbf{k}_i = 2\pi/\lambda \mathbf{s}_i$ where $\lambda$ is the wavelength and $\mathbf{s}_i$ is a unit vector in the direction of propagation (Fig. 1.22(b)). When this wave impinges on a scatterer positioned at $\mathbf{r}_0$, with scattering factor (the scattering pattern if the scatterer is located at the origin) $f_0$, the complex ampli-

tude of the scattered X-rays is

$$A(\mathbf{R}) = f_0 \exp(i2\pi\mathbf{R}\cdot\mathbf{r}_0), \tag{1.37}$$

where $\mathbf{R}$ is the scattering vector defined by $\mathbf{R} = (\mathbf{k}_r - \mathbf{k}_i)/2\pi$ and $\mathbf{k}_r$ is the unit vector in the direction of the diffracted X-ray beams (Fig. 1.22(b)). The diffraction amplitude is formed in reciprocal space also known as inverse or Fourier space. For a group of $n$ scatterers, located at positions $\mathbf{r}_j$, and each with scattering factor $f_j$, the scattered amplitude is the sum of that due to each scatterer, i.e.

$$A(\mathbf{R}) = \sum_{j=1}^{n} f_j \exp(i2\pi\mathbf{R}\cdot\mathbf{r}_j). \tag{1.38}$$

Extending this relationship to diffraction by a continuous medium of scatterers with electron density $\rho(\mathbf{r})$, then

$$A(\mathbf{R}) = \int_{-\infty}^{\infty} \rho(\mathbf{r}) \exp(i2\pi\mathbf{R}\cdot\mathbf{r})\mathrm{d}\mathbf{r}. \tag{1.39}$$

The integral Eq. (1.39) is the Fourier transform relationship [Appendix A.3] between the electron density of constituent atoms $\rho(\mathbf{r})$ and the complex scattered amplitude of the X-rays $A(\mathbf{R})$. The electron density of a diffracting region can be reconstructed from the complex amplitude by inversion of the Fourier transform as

$$\rho(\mathbf{r}) = \int_{-\infty}^{\infty} A(\mathbf{R}) \exp(-i2\pi\mathbf{R}\cdot\mathbf{r})\mathrm{d}\mathbf{R}. \tag{1.40}$$

In practice, only the intensity $|A(\mathbf{R})|^2$ can be measured, and the phase of the complex amplitude is unknown. This is known as "the phase problem". A number of different methods exist for obtaining estimates of the phases of the complex amplitude diffracted by the crystals [Mil90].

### 1.4.2 Diffraction by Crystals

For specimens with no structural order, determination of the positions of the individual atoms is impossible due to the huge number of variables to be determined. However, if a specimen is crystalline (i.e. periodic) the electron density of the specimen is completely characterised by a single repeating unit cell which is a more feasible task. An unbounded perfect crystal lattice can be described as an array of delta functions located at the crystal sites,

$$l_\infty(\mathbf{r}) = \sum_m \sum_n \sum_p \delta(\mathbf{r} - \mathbf{r}_{mnp}), \tag{1.41}$$

where $\mathbf{r}_{mnp}$ is the periodic repetition of the unit cell along vectors,

$$\mathbf{r}_{mnp} = m\mathbf{a} + n\mathbf{b} + p\mathbf{c}, \tag{1.42}$$

where $m$, $n$, and $p$ are integers, and **a**, **b**, and **c** are vectors which form the edges of the unit cell (Fig. 1.23(a)). The periodic electron density of a crystal, $\rho(\mathbf{r})$, is then written as the convolution of a function that is equal to the electron density in a single unit cell, $\rho_{cell}(\mathbf{r})$, and the crystal lattice, viz.

$$\rho(\mathbf{r}) = \rho_{cell}(\mathbf{r}) \otimes l_{\infty}(\mathbf{r}). \tag{1.43}$$

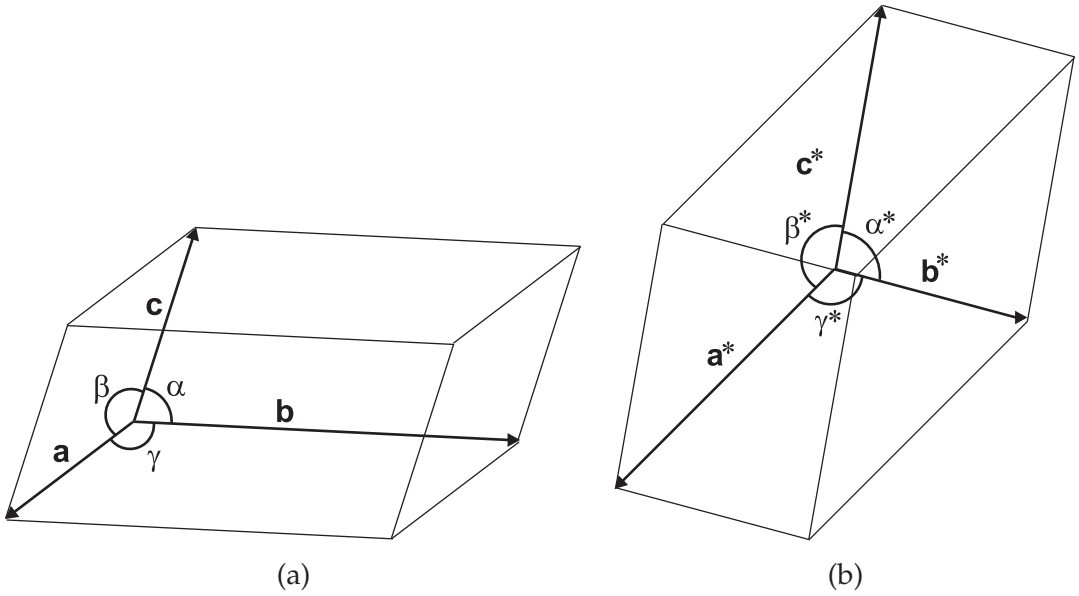


**Figure 1.23** Definition of the unit cell vectors and parameters (a) in real space, and (b) in reciprocal space.

Using the convolution theorem for Fourier transforms, the complex amplitude diffracted by the crystal can be written as

$$A(\mathbf{R}) = F(\mathbf{R})L_{\infty}(\mathbf{R}), \tag{1.44}$$

where $F(\mathbf{R})$ is the scattering from one unit cell

$$F(\mathbf{R}) = \int \rho_{cell}(\mathbf{r}) \exp(i2\pi\mathbf{r}\cdot\mathbf{u})\mathrm{d}\mathbf{r}, \tag{1.45}$$

and $L_{\infty}(\mathbf{R})$ is the Fourier transforms of $l_{\infty}(\mathbf{r})$. The Fourier transform of an infinite periodic lattice is also a lattice

$$L_{\infty}(\mathbf{R}) = \sum_h \sum_k \sum_l \delta(\mathbf{R} - \mathbf{R}_{hkl}), \tag{1.46}$$

referred to as the reciprocal lattice, that has sites at the positions

$$\mathbf{R}_{hkl} = h\mathbf{a}^* + k\mathbf{b}^* + l\mathbf{c}^*, \tag{1.47}$$

where

$$\begin{aligned} \mathbf{a}^* &= \frac{\mathbf{b} \times \mathbf{c}}{V_{cell}} \\ \mathbf{b}^* &= \frac{\mathbf{c} \times \mathbf{a}}{V_{cell}} \\ \mathbf{c}^* &= \frac{\mathbf{a} \times \mathbf{b}}{V_{cell}} \end{aligned} \tag{1.48}$$

are the vectors defining the lattice and $V_{cell}$ is the volume of the unit cell of the lattice in real space (Fig. 1.23(b)), given by

$$V_{cell} = |\mathbf{a} \cdot \mathbf{b} \times \mathbf{c}| \,. \tag{1.49}$$

Referring to Eqs. 1.44 and 1.46, the Fourier transform of the unit cell is *sampled* at the reciprocal lattice points. The diffraction is therefore *discrete* and is denoted by

$$F_{hkl} = F(\mathbf{R}_{hkl}) \tag{1.50}$$

which are called the *structure factors*.

The electron density in the unit cell can be calculated from the structure factors, using Eqs. 1.40 and 1.50, by

$$\rho(\mathbf{r}) = \sum_{\mathbf{h}} F_{\mathbf{h}} \exp(-i2\pi\mathbf{r} \cdot \mathbf{h}) \tag{1.51}$$

where $\mathbf{h} = (h, k, l)$. This can not be done directly since only the magnitude $|F_{\mathbf{h}}|$ is measured. A variety of methods are used to solve this problem. These are not described here and the reader is referred to texts on crystallography, such as [Dre94], for the details.

The reciprocal lattice vectors $\mathbf{R}_{hkl}$ have simple geometric interpretations; each vector $\mathbf{R}_{hkl}$ is perpendicular to the family of planes in real space that are parallel to the plane passing through the points $(\mathbf{a}/h, 0, 0)$, $(0, \mathbf{b}/k, 0)$, and $(0, 0, \mathbf{c}/l)$, that contain lattice points, and are spaced by a distance $\mathbf{d}_{hkl}$ given by

$$\mathbf{d}_{hkl} = \frac{1}{|\mathbf{R}_{hkl}|}. \tag{1.52}$$

The indices $hkl$ that identify the set of planes are referred to as the Miller indices [Bal71]. An example of two-dimensional triangular lattice plane spacings and corresponding Miller

indices are shown in Fig. 1.24. The lattice and the resulting reciprocal lattice are shown in Fig. 1.25. Note that in this case the reciprocal lattice spacing is 1.155 (3 d.p).

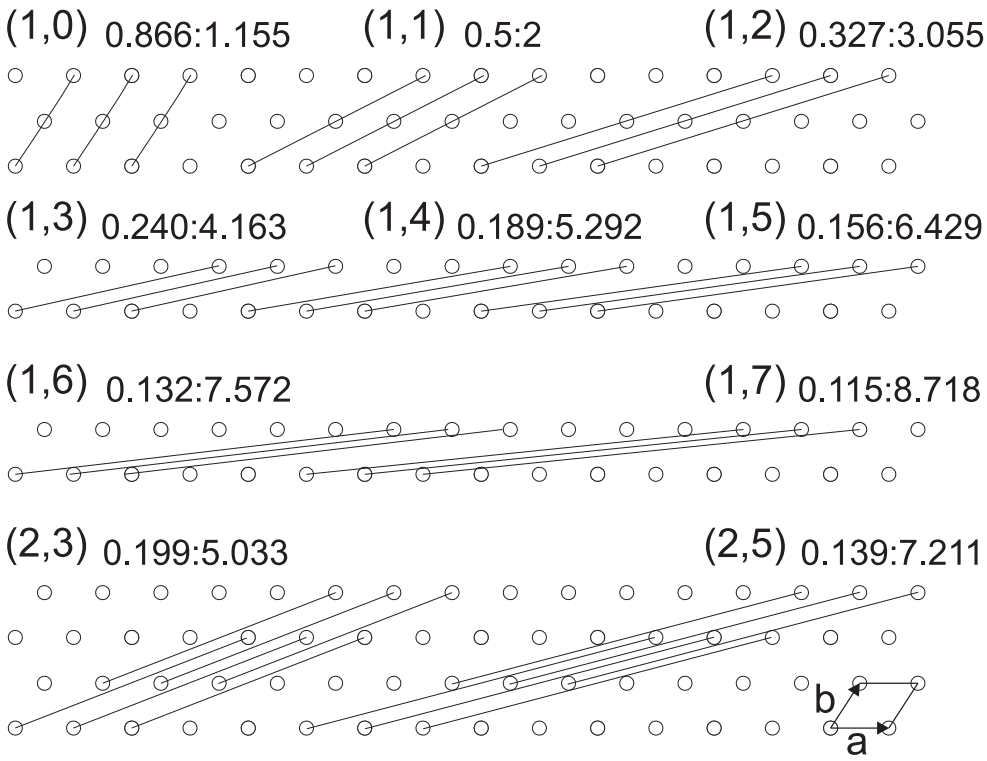


**Figure 1.24** Lattice planes indicated by the Miller indices $(h, k)$ on a triangular lattice with $a = b = 1$. Plane spacings in real and reciprocal space are shown as $d_{hkl} : R_{hkl}$ (3 d.p).

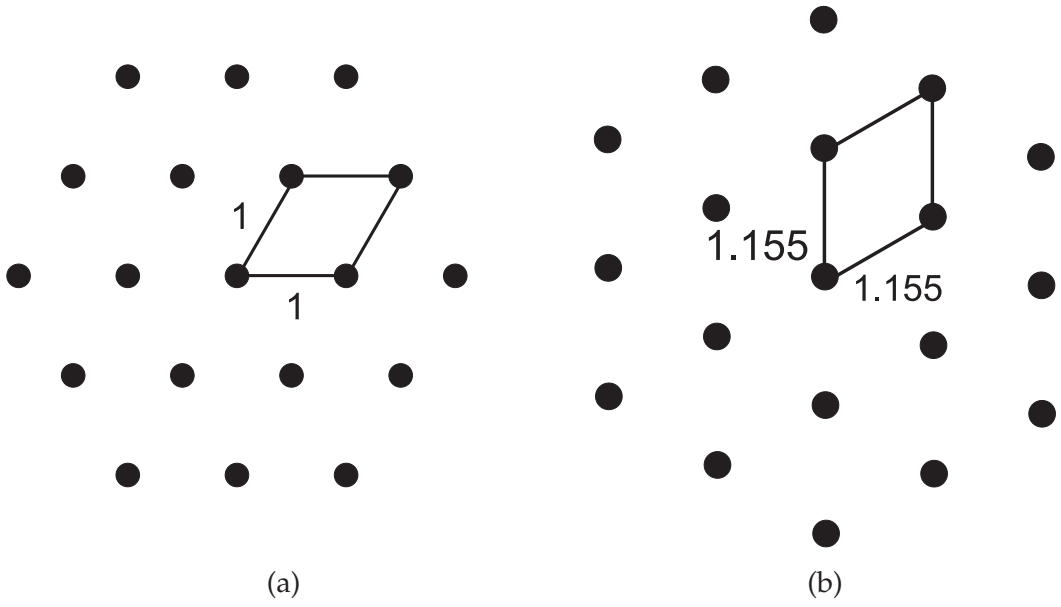


**Figure 1.25** (a) Triangular lattice and (b) its reciprocal triangular lattice.

A real crystal has a finite boundary that can be described by a shape function, $s(\mathbf{r})$, defined as

$$s(\mathbf{r}) = \begin{cases} 1 & \text{inside the boundary} \\ 0 & \text{otherwise.} \end{cases}$$

Using this function, the electron density of the finite crystal (Fig. 1.26) can be written as

$$\rho(\mathbf{r}) = [\rho_{cell}(\mathbf{r}) \otimes l_{\infty}(\mathbf{r})]s(\mathbf{r}). \tag{1.53}$$

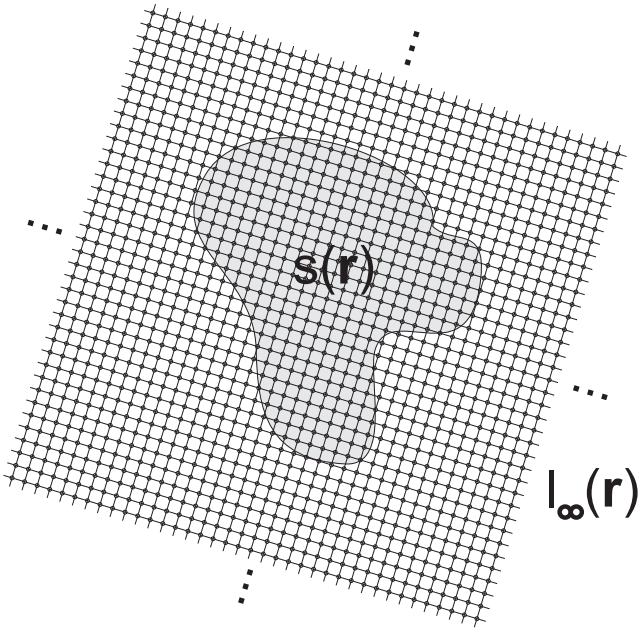


**Figure 1.26** A real crystal has a boundary described by a shape function, $s(\mathbf{r})$ on an infinite lattice, $l_{\infty}(\mathbf{r})$.

The complex amplitude diffracted from the finite crystal is obtained by substituting Eq. (1.53) into Eq. (1.39) giving

$$A(\mathbf{R}) = [F(\mathbf{R})L_{\infty}(\mathbf{R})] \otimes S(\mathbf{R}), \tag{1.54}$$

where $S(\mathbf{R})$ is the Fourier transform of $s(\mathbf{r})$. Each sharp reflection is therefore convolved with, or blurred by, $S(\mathbf{R})$, leading to finite size reflections.

## 1.5 Diffraction by Disordered Crystals

The perfect crystalline state is only likely to be observed in substances of low molecular weight where incipient distortions are corrected under the equilibration of the interparticle forces within the specimen [KK05]. In larger polymers, it is highly probable that the crystalline molecular assemblies exhibit disorder in the way that the molecules pack together. If the disorder is not too severe, so that the specimen still has an approximately

regular crystalline structure, then diffraction data can still be used for structure determination. However, in order to do this, the effect of the disorder on the diffracted amplitudes must be taken into account. This requires one to develop models of different types of disorder and expressions for the diffraction from such models [WB95, SM95b].

### 1.5.1 Types of Disorder

Disorder can be divided into two types; disorder involving displacements and occupancies of the constituent molecules. These are referred to as displacive and occupancy disorder [Wel04] or lattice and substitution disorder [Str93] (Fig. 1.27). Lattice disorder consists only of deviations in the positions of the molecules away from the positions in a regular periodic lattice. Therefore, lattice distortion in a crystalline material can be completely characterized by considering only distortions in the underlying lattice, without reference to the molecules themselves. In the simplest kind of lattice disorder, the distortions at different lattice sites are independent. This type of lattice disorder is often referred to as thermal disorder, disorder of the first kind [HB62], or uncorrelated disorder [SM96b]. It is easy to see that in close-packed systems, as a result of steric exclusion, the distortions at one lattice site may affect the distortions at neighboring sites [WB95]. If this effect is significant, the distortions at neighboring sites are correlated, and this is referred to as correlated disorder. The effect of correlations is to complicate the model of disorder and calculation of the diffraction.

Two principal models have been developed to describe lattice disorder in crystalline materials, the paracrystal [HB62] and the perturbed lattice [WMC80]. Such models have been used extensively to analyse diffraction from disordered materials such as polymers, glasses and alloys [HH95, WB95]. The paracrystalline model is perhaps more intuitively satisfying in that each position of the molecules are built up with respect to the existing lattice one by one. The paracrystal describes cumulative disorder that results in large deviations from a periodic lattice and is ill-defined in two- and three-dimensions [EM01]. The perturbed lattice model describes the distortion as having random deviations from regular lattice sites. Since the disorder is anchored to a periodic lattice, the model is well-behaved even in high dimensions.

Substitution disorder consists of variations in the kinds, rather than in the positions, of the scattering units at each lattice site, i.e. variations in the scattering factor $F(\mathbf{R})$ of the unit cell. It encompasses a wide variety of disorder such as mixture, vacancy, interstitial, rotation and dislocation disorder. Substitution disorder may also be correlated or uncorrelated. Various kinds of correlated and uncorrelated disorder have been studied by a number of authors [Str93, Ead01, Wel04].

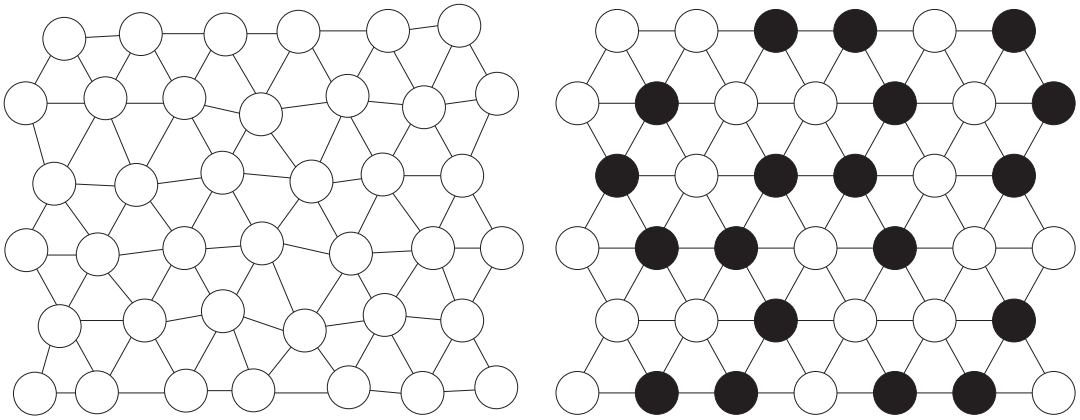

(a) (b)

**Figure 1.27** Two types of disorder. (a) lattice disorder and (b) substitution disorder. Black and white circles represent two different constituent units.

### 1.5.2 Diffraction by Disordered Lattices

Both lattice and substitution disorder are often present in disordered crystalline materials, although one of these may dominate. The complex amplitude diffracted from a perfect lattice with shape function $s(\mathbf{r})$ that has electron densities $\rho_{jk}(\mathbf{r})$ at positions $\mathbf{r}_{jk}$ of a two-dimensional lattice is given, using Eqs. 1.39 and 1.53, as

$$A(\mathbf{R}) = \sum_j \sum_k \int_r \rho(\mathbf{r} - \mathbf{r}_{jk}) \exp(i2\pi\mathbf{R} \cdot \mathbf{r}) s(\mathbf{r}_{jk}) \mathrm{d}\mathbf{r}, \tag{1.55}$$

which is equivalent to

$$A(\mathbf{R}) = \sum_j \sum_k F_{jk}(\mathbf{R}) \exp(i2\pi\mathbf{R} \cdot \mathbf{r}_{jk}) s(\mathbf{r}_{jk}), \tag{1.56}$$

where $F_{jk}(\mathbf{R})$ is the structure factor of the scatterer occupying site $(j, k)$. Introducing lattice disorder in the form of a perturbed lattice gives

$$A(\mathbf{R}) = \sum_j \sum_k F_{jk}(\mathbf{R}) \exp(i2\pi\mathbf{R} \cdot [\mathbf{r}_{jk} + \mathbf{d}_{jk}]) s(\mathbf{r}_{jk}), \tag{1.57}$$

where $\mathbf{d}_{jk}$ is the random vector with zero mean that describes the displacement of the scatterer away from the mean position $\mathbf{r}_{jk}$. The average intensity diffracted from an ensemble

of crystallites with identical shapes and orientations can be written as [Str93]

$$\begin{aligned}\langle I(\mathbf{R})\rangle_d &= \langle A(\mathbf{R})A^*(\mathbf{R})\rangle_d \\ &= \sum_j\sum_k\sum_{j'}\sum_{k'}\Big[s(\mathbf{r}_{j+j',k+k'})s(\mathbf{r}_{j',k'})\exp(i2\pi\mathbf{R}\cdot[\mathbf{r}_{jk}-\mathbf{r}_{j'k'}]) \\ &\quad\times\langle F_{jk}(\mathbf{R})F^*_{j'k'}(\mathbf{R})\exp(i2\pi\mathbf{R}\cdot[\mathbf{d}_{jk}-\mathbf{d}_{j'k'}])\rangle_d\Big]. \qquad (1.58)\end{aligned}$$

It is assumed that the variations in both the occupancies and the displacements are described by statistics that are stationary over the lattice and the notation $\langle\rangle_d$ is used to denote averaging over all states of disorder. Suppose that the type of molecule occupying one site has no bearing on its displacement, i.e. the lattice and substitution disorders are uncorrelated, then Eq. (1.58) can be written as

$$\begin{aligned}\langle I(\mathbf{R})\rangle_d &= \sum_j\sum_k\sum_{j'}\sum_{k'}\Big[s(\mathbf{r}_{j+j',k+k'})s(\mathbf{r}_{j',k'})\exp(i2\pi\mathbf{R}\cdot[\mathbf{r}_{jk}-\mathbf{r}_{j'k'}]) \\ &\quad\times\langle F_{jk}(\mathbf{R})F^*_{j'k'}(\mathbf{R})\rangle_d\langle\exp(i2\pi\mathbf{R}\cdot[\mathbf{d}_{jk}-\mathbf{d}_{j'k'}])\rangle_d\Big]. \qquad (1.59)\end{aligned}$$

The effects of lattice and substitution disorder on the diffracted intensity are expressed through $\langle\exp(i2\pi\mathbf{R}\cdot[\mathbf{d}_{jk}-\mathbf{d}_{j'k'}])\rangle_d$ and $\langle F_{jk}(\mathbf{R})F^*_{j'k'}(\mathbf{R})\rangle_d$, respectively.

### 1.5.3 Diffraction by the Myosin Superlattice

Diffraction by simple lattice muscles give rise to a hexagonal reciprocal lattice as shown in Fig. 1.28(a) and (b). For higher vertebrate muscles, the myosin disorder results in a superlattice as described in Section 1.1.4 and illustrated in Fig. 1.28(c). This leads to superlattice reflections in the diffraction pattern that belong to a hexagonal reciprocal lattice with a smaller lattice spacing as shown in Fig. 1.28(d). The intensity of these superlattice reflections are a function of the disorder, and this relationship is clearly relevant to the interpretation of such diffraction patterns.

## 1.6 X-ray Fiber Diffraction

Polymers are macromolecules composed of repeating units that form molecular chains. Polymer fibers are composed of usually long and slender molecules that exhibit a preferred orientation and align approximately parallel with each other. This common axis is called the molecular axis and the direction of preferred orientation is called the fiber axis. The degree of order in the lateral plane (the plane perpendicular to the molecular axis) is used to categorise the fiber specimen into three kinds; noncrystalline, polycrystalline and disordered fibers. Noncrystalline fibers have no order in the lateral plane. The cross-sections of noncrystalline fibers contain randomly positioned and randomly rotated molecular seg-

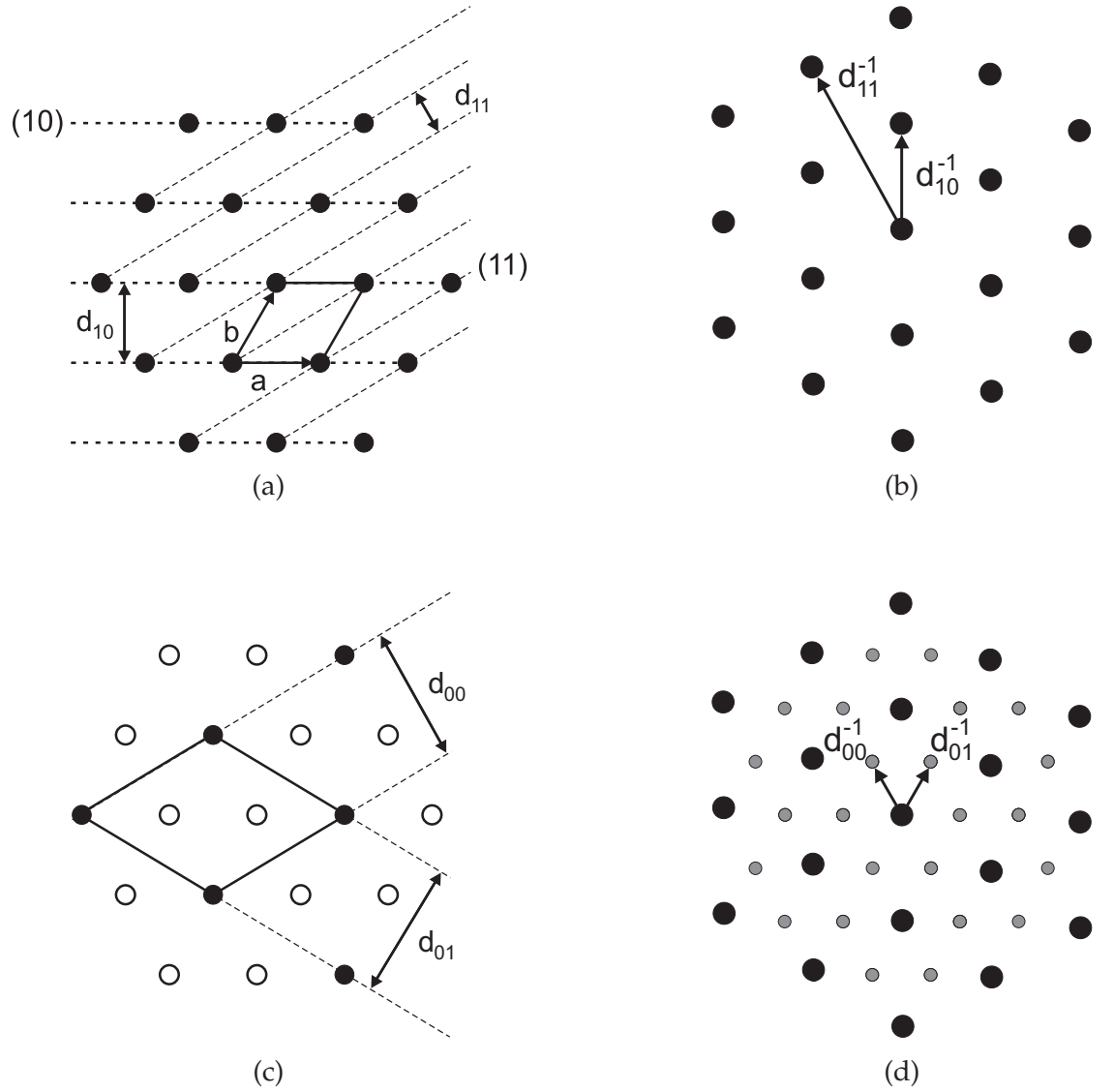


**Figure 1.28** Schematic diagrams of real lattices ((a), (c)) and their respective reciprocal lattices ((b), (d)). (a) Shows a hexagonal lattice with a unit cell with $a = b = 1$ as outlined. The equatorial X-ray diffraction pattern (b) arises from $(10)$ and $(11)$ planes. The corresponding reflections are perpendicular to these planes and at positions from the center of the diffraction pattern which are inversely proportional to the plane separation. In diagram (c), two types of scatterers are represented by $\circ$ and $\bullet$. Its diffraction pattern (d) comprises the fundamental lattice reflections and, in addition, the superlattice reflections denoted by grey markers that lie on a lattice reciprocal to the superlattice cell shown in (c). (Figure modified from [LS80, Bag82])

ments. However, in polycrystalline fibers the molecular segments crystallise to form well ordered microcrystallites in the lateral plane. These microcrystallites are randomly positioned in the lateral plane and randomly rotated about the molecular axis. Disordered fibers possess intermediate order in the lateral plane.

Using cylindrical polar coordinates $(R, \psi, Z)$ in reciprocal space, and choosing the $Z$ axis parallel to the fiber axis then, assuming perfect orientation in this direction, the intensity $I(R, Z)$ diffracted by a fiber is the cylindrical average of a single crystallite, or molecule, given by

$$I(R, Z) = \left(\frac{1}{2\pi}\right) \int_0^{2\pi} I_c(R, \psi, Z) \mathrm{d}\psi, \tag{1.60}$$

where $I_c(R, \psi, Z)$ is the intensity diffracted by a single crystallite or molecule.

### 1.6.1 Helical Structures

Molecules or assemblies in polymer fibers often adopt an extended periodic helical structure that is made up of a large number of identical, or nearly identical, residues, or subunits that in an oriented specimen are distributed along an axis [MD01]. Even a periodic structure with no helical symmetry can be described as a one-fold helix, so that helical structures are a general description of oriented molecules.

The repeating distance of the helical structure is referred to as the $c$-repeat, denoted by $c$, and the projected length of one helical turn is called the pitch, $P$ (Fig. 1.29). The ordered structure is generated from a subunit (a.k.a. residue or asymmetric unit) by repeated application of a rotation about an axis, referred to as the helix axis, together with a translation parallel to this axis. Hence it is most convenient to adopt a cylindrical-polar coordinate system, $(r, \phi, z)$. If in one $c$-repeat there are $u$ repetitions of the subunit, so that adjacent units are related by a translation of

$$\Delta z = \frac{c}{u} \tag{1.61}$$

and a rotation of

$$\Delta\phi = 2\pi\frac{\nu}{u}, \tag{1.62}$$

where $\nu$ is the number of turns in one $c$-repeat. Therefore, if the electron density of an atom in the helix has coordinates $f(r, \phi, z)$, then same atoms can be found at $f(r, \phi + m\Delta\phi, z + m\Delta z)$ where $m$ is any integer, i.e.

$$f(r, \phi, z) = f(r, \phi + m\Delta\phi, z + m\Delta z), \tag{1.63}$$

The structure is said to have $u_\nu$ helix symmetry. A helix with 7 residues in 2 turns is illustrated in Fig. 1.29.

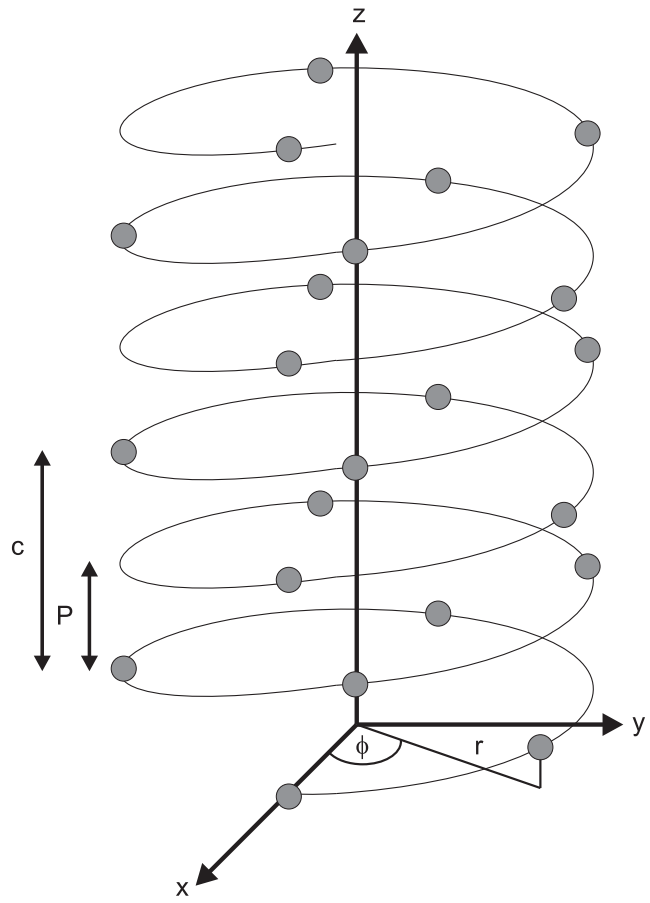


**Figure 1.29** A helix with $7_2$ symmetry and one atom in the helical repeat unit (○). Cartesian (x,y,z) and cylindrical-polar $(r, \phi, z)$ coordinates are shown. The c-repeat (c) and pitch (P) are also shown.

### 1.6.2 Diffraction by Helical Structures

The equation describing diffraction by a helical polymer, with helix symmetry $u_\nu$, is derived by considering diffraction from atoms on a helical wire [CCV52, KCW58] as shown in Fig. 1.29. The origin of the coordinate system in real space may be chosen so that one of the atoms, has cylindrical coordinates ($r_0$,0,0), where $r_0$ is the distance of the atom from the helix axis. The complex amplitude diffracted from this atomic helix is restricted to a set of planes spaced $1/c$ along the $Z$ axis of reciprocal space (i.e. the helix forms a one-dimensional crystal), and with the omission of a factor of $(1/c)$ can be written as a function of cylindrical polar coordinates $(R, \psi, Z)$ as [CCV52]

$$F(R, \psi, Z) = \sum_l F_l(R, \psi)\delta(Z - l/c) \tag{1.64}$$

where

$$F_l(R, \psi) = f_0(\rho) \sum_n \exp(in[\psi + \pi/2])J_n(2\pi r_0 R), \tag{1.65}$$

$\rho = (R^2 + l^2/c^2)^{1/2}$, $f_0(\rho)$ is the atomic scattering factor, and $J_n$ is the Bessel function of the first kind of order $n$ (see Appendix A.1). The summation is Eq. (1.65) is over all Bessel orders $n$ that satisfy the helix selection rule

$$l = n\nu + mu \tag{1.66}$$

where $m$ is any integer.

A helical polymer can be decomposed into a set of atomic helices, one for each atom in the asymmetric unit. The transform of the polymer is then equal to the sum of the transforms of the individual atomic helices. If $(r_j, \psi_j, z_j)$ is the position of an atom in the asymmetric unit, then using the translation and rotation properties of the Fourier transform, the Fourier transform of the molecular helix is

$$F_l(R, \psi) = \sum_n G_{nl}(R) \exp(in[\psi + \pi/2]) \tag{1.67}$$

where $G_{nl}$ are the *Fourier-Bessel structure factors* defined as

$$G_{nl}(R) = \sum_{j \in \mathcal{H}} f_j(\rho) J_n(2\pi r_j R) \exp(i[2\pi z_j l/c - n\psi_j]) \tag{1.68}$$

where the $f_j$ are the scattering factors of the atoms in the asymmetric unit, and $\mathcal{H}$ denotes the set of all atoms in one asymmetric unit. On any layer line, the helix selection rule has an infinite number of solutions, but at any radius $R$ only those orders satisfying

$$|n| \leq n_{max} = 2\pi r_{max} R + 2 \tag{1.69}$$

where $r_{max}$ is the maximum radius of the molecule, are of significant value [CDK70, Mak82]. Hence, when Fourier-Bessel structure factors are calculated for model polymer structures, the Fourier-Bessel series can be truncated at the Bessel order $\pm n_{max}$ calculated using Eq. (1.69) with $R$ equal to the maximum reciprocal radius for which the Fourier-Bessel coefficients are required. Since $J_n(0)$ equals 0 for $n \neq 0$, but equals 1 for $n = 0$, the Fourier-Bessel structure factors are on the $Z$ axis for all layers whose index $l$ is not a multiple of $u$. Hence the helix symmetry parameter $u$ can be determined from a simple inspection of the diffraction pattern.

Using Eqs. 1.60 and 1.67 shows that the measured, cylindrically averaged, fiber diffraction pattern intensity is given by

$$I_l(R) = I(R, l/c) = \sum_n |G_{nl}|^2 . \tag{1.70}$$

The structure determination problem in fiber diffraction is to determine the electron den-

sity $\rho(r, \phi, z)$ from the data $I_l(R)$. The electron density can be written in terms of the Fourier-Bessel structure factors as [Str93]

$$\rho(r, \phi, z) = \frac{2\pi}{c} \sum_n \sum_l \exp[(i(n\phi - 2\pi z l/c))] \int_0^\infty G_{nl}(R) J_n(2\pi R r) R \, \mathrm{d}R. \tag{1.71}$$

The phase problem in fiber diffraction is then to determine the complex $G_{nl}(R)$ from the intensities $I_l(R)$. The reader is referred to the details in [MD01]. An alternative approach to structure determination is to model the helical molecule with adjustable parameters, calculate the diffraction, and optimise the parameters by matching the calculated diffraction to the measured diffraction $I_l(R)$. For complex structures such as muscle, this is the method of choice. Clearly, the effect of any disorder in the fiber specimen must be taken into account when calculating the diffraction.

### 1.6.3 Muscle Fiber Diffraction

An example of an X-ray fiber diffraction pattern from muscle is shown in Fig. 1.30. The main contractile proteins of muscle, the myosin and actin filaments, align parallel to the fiber axis and are arranged in a regular hexagonal lattice. The myosin filament is a three-stranded helix with an axial repeat of $42.9\ nm$ [Squ72, LK02]. The axial translation of the actin monomers along the filament is $\sim 5.5\ nm$ where one troponin complex and a tropomyosin rod are associated with 7 actin monomers, giving an axial repeat of about $7 \times 5.5\ nm$ or $38.5\ nm$ [SEO69]. The different periodicities of these interdigitated filaments result in two sets of layer lines along the meridional axis, spaced by the corresponding reciprocals of the axial repeats, in fiber diffraction patterns. Close inspection of Fig. 1.30 shows the separate myosin and actin layer lines as indicated. Digital processing techniques can be used to separate out the layer lines due to the myosin and actin filaments. Therefore, at least in principle, the diffraction due to myosin alone can be analysed.

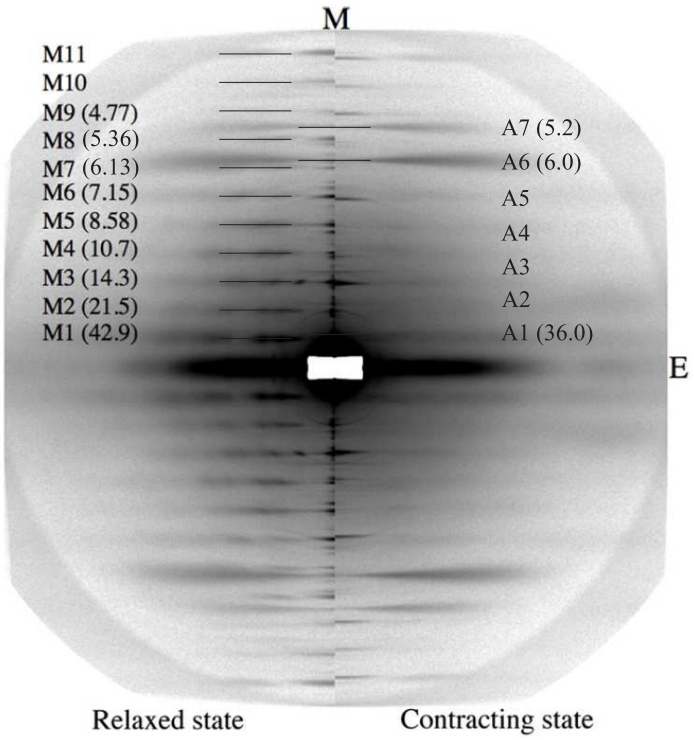


**Figure 1.30** X-ray diffraction patterns in the relaxed and contracting states of frog skeletal muscles [OTS+07]. The background intensity was subtracted. The left side is the relaxed state and the right side is the contracting state with the meridional axes (M) and the equatorial axes (E) coincident. The fiber axis is vertical. M1 to M11 denote the first to the 11th-order myosin layer lines with a crystallographic period of 42.9 $nm$ (the relaxed state) or 43.5 $nm$ (the contracting state). The values in parentheses are axial spacings in real space. Similarly, A1 to A7 denote the actin layer lines with a crystallographic period $\sim 36.0\ nm$. Note that this figure is used here only to illustrate the myosin and actin layer lines, and not anything concerning the relaxed and contracted states.

# Chapter 2

# Automatic Analysis of Muscle Micrographs

## 2.1 Introduction

The primary experimental source of information on the muscle myosin lattice disorder is electron micrographs of thin cross sections. To extract this information in a convenient and quantitative fashion requires an automatic method of analysing the micrographs. This chapter describes an algorithm for this purpose together with implementation, results, and an assessment of the accuracy of the algorithm.

As detailed in Section 1.1.1, a single micrograph usually intersects a number of myofibrils (Fig. 2.1a) and a part of a micrograph that shows a single sarcomere cross-section of the bare region is shown in Fig. 2.1b. The myofibril is the region that contains the regular lattice bounded by the amorphous SR, and the myosin filaments are the dark regions that are seen to lie on an approximately regular triangular lattice. There are large variations between the images in terms of contrast, background, noise level and extraneous features. The micrographs also vary from sample to sample as a result of structural differences between different muscles and different species.

Analysis of the micrographs involves locating the individual myosin filaments within a myofibril, determining their orientations about the myofibril axis and then classifying the orientations into two groups, namely up or down. Once all the filaments are classified, the disorder can be analysed statistically. Inspection of Fig. 2.1 shows that the filament profiles are indistinct as they deviate from the idealised triangular shape. This makes both manual and automatic analysis difficult.

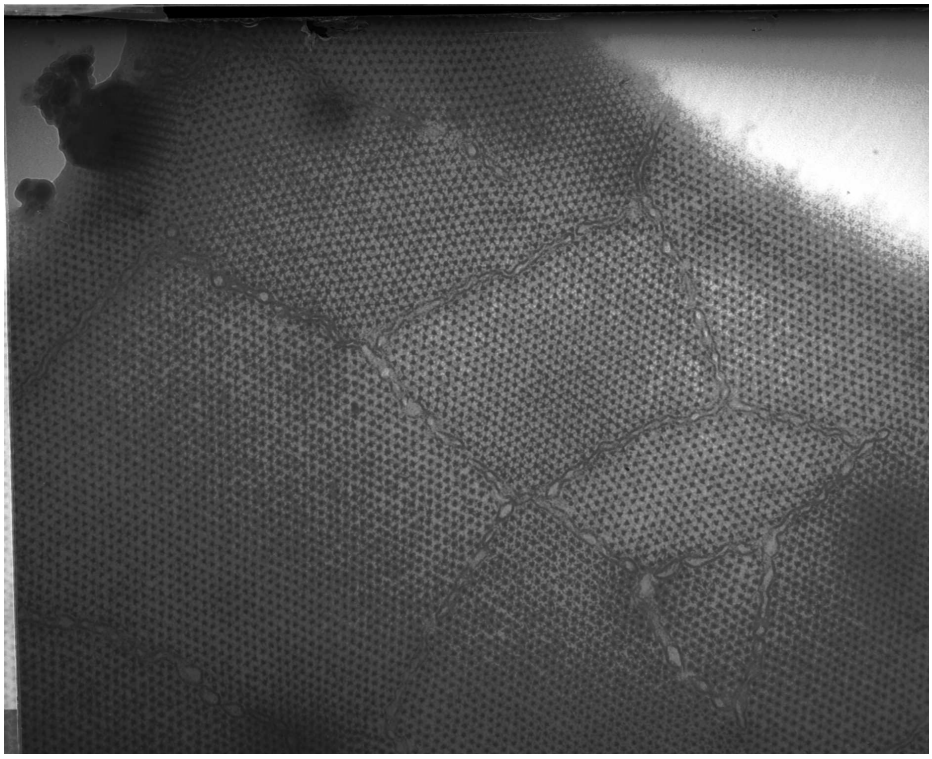

(a)

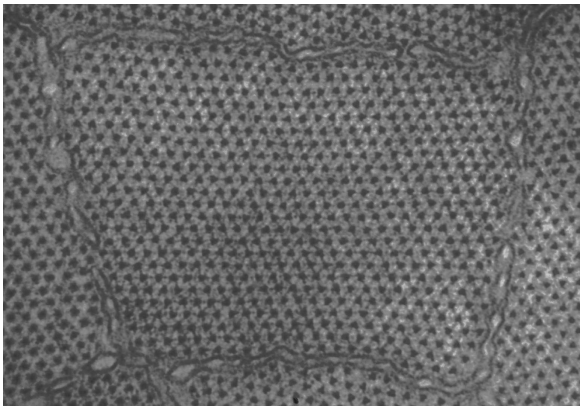

(b)

**Figure 2.1** Electron micrograph of a frog sartorius muscle. (a) A cross section of the frog muscle fiber shows the bare regions (see Fig. 1.2a) of the tightly packed myofibrils. (b) The bare region of a single myofibril bounded by SR.

Currently used manual methods for analysing these micrographs are tedious and not suitable for obtaining consistent data. Thus development of an automated method for fast and accurate determination of the myosin filament orientations in these micrographs is described here. The overall approach is to first locate the filaments by filtering the image with a point spread function (psf) that incorporates the local hexagonal symmetry. The orientation of each filament is then determined by template matching with a template that contains the salient features of the filament cross-sections. The orientations are then classified using a Gaussian mixture model. The algorithm is assessed by comparison of the results with those from manual analysis.

## 2.2 Location of the Filaments

The first step is to locate the filaments in a micrograph. An approach to locating the filaments that uses linear filtering with a psf that incorporates the filament size and lattice symmetry is developed [YBK+08]. This is an improvement on a previously described algorithm that uses grayscale morphology to locate the filaments [BKM+08]. The latter algorithm uses $h$-dome extraction [Vin93] coupled with a neighbour analysis and use of lattice symmetry to optimise the threshold value, followed by further processing to correct erroneous locations. Although, this algorithm was effective, it is complex and does not use the lattice symmetry in the most efficient manner. *The objective of the new algorithm described here is to combine the detection of local maxima and the lattice symmetry into a single step.* This simplifies the algorithm and avoids the iterative determination of the threshold level in the previous method.

Some generalisations can be made about the muscle micrographs. The myosin filaments stain darker than the surrounding material. The triangular lattice on which the filaments lie is very regular on a local scale, and the variation in the lattice is rather small over an entire myofibril. Also, the filament widths are approximately half the spacing between the filament neighbours. The filament size and local lattice symmetry are used to generate a psf that can be used to filter the whole micrograph image, i.e. the psf mathematically approximates a local section of the myosin lattice.

The approach is to estimate the filament locations by matched filtering with a psf that approximates the filament size and the positions of the nearest neighbours. The psf is generated as follows. Let the grayscale on a micrograph image be denoted $f(x, y)$. The user selects a clear area on the micrograph and defines the approximate coordinates of the center of one filament and its six nearest neighbours. These center coordinates do not need to be particularly accurate. This is the only manual step in the algorithm. Two parameters are computed from this initial step. These are the lattice spacing, denoted $d$,

and the angle of the lattice, denoted $\theta$. The twelve nearest neighbour spacings between the seven selected filaments are calculated and averaged to give $d$. The orientations between the twelve nearest neighbour vectors are calculated and averaged modulo $60^\circ$ to give $\theta$.

A single myosin filament, $p(x, y)$, at the origin is modelled at low resolution as a disk, i.e.

$$p(x,y) = \begin{cases} 1, & \text{if } x^2 + y^2 \leq c^2 \\ 0 & \text{otherwise,} \end{cases} \tag{2.1}$$

where $c = d/4$ is the approximate radius of the myosin filaments. Since a single myosin filament generally has six nearest neighbours, disposed with approximately hexagonal symmetry, the psf, $h(x, y)$ consists of a central filament with six hexagonally arranged neighbours at the appropriate spacing and orientation, i.e.

$$h(x,y) = p(x,y) + \sum_{m=0}^{5} p\Big(x - d\cos\Big(\theta + \frac{m\pi}{3}\Big), y - d\sin\Big(\theta + \frac{m\pi}{3}\Big)\Big). \tag{2.2}$$

The psf is illustrated in Fig. 2.2.

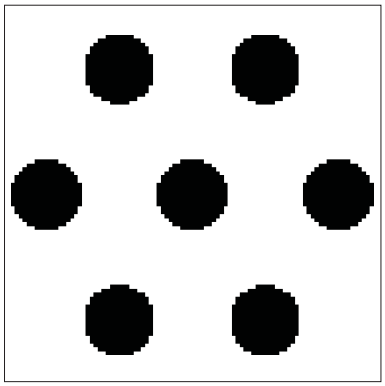

**Figure 2.2** The filter point spread function used to determine the filament positions.

The psf is convolved with the micrograph image producing a filtered image $g(x, y)$ where

$$g(x,y) = f(x,y) \otimes h(x,y). \tag{2.3}$$

The correlation is calculated by multiplying the discrete Fourier transform (DFT) of the image, $F(u, v)$ and the psf, $H(u, v)$ and calculating the inverse DFT. The filtered image contains distinct intensity peaks at the filament positions and a considerably reduced noise level compared to the original image.

The advantage of this approach over the morphological approach is that the constraints of

local maxima and local hexagonal symmetry are incorporated into a single step. The result is that a cleaner estimate of the peaks corresponding to the filaments is obtained much more easily.

The grayscale regional maxima image, denoted $m(x, y)$ of the filtered image $g(x, y)$ is determined where the regional maxima are connected components of pixels (based on an 8-neighbourhood) with the same intensity value whose boundary pixels external to the region have strictly smaller values [Vin93]. The grayscale regional maxima image is then converted to a binary maxima image, $w(x, y)$ and the centroids of the maxima are taken as the estimates of the filament positions.

Application of the algorithm to a number of micrographs showed that it was effective in most cases. However, in particularly noisy micrographs some false positives were detected. Most false positives are eliminated by running the algorithm a second time using a psf with spacings $d + 1$ pixels, and retaining only those filaments that are within 2 pixels of those initially determined. The algorithm then locates almost all of the filaments with sufficient accuracy for subsequent processing in all micrographs studied.

Examples showing the application of this algorithm are presented in Section 2.5.

## 2.3 Determination of Filament Orientations

Having determined the approximate locations of the filaments, the next step is to estimate the azimuthal rotation of each filament, henceforth referred to as the orientation. This is achieved by template matching. The myosin filament cross-sections have three-fold rotational symmetry, and inspection of many filaments in different micrographs shows that they have an approximate equilateral triangular shape. In addition to the triangular shape, two relevant characteristics of the filaments in the micrographs are that they do not have sharp outer edges and that the interior of the filaments is variable with some filaments appear to have less mass in the center. We therefore use a template consisting of a hollow equilateral triangle with soft edges. The core template matching uses, with modifications, a program developed by B. Bödvarsson, S. Klim, S. Mortensen and M. Mørkebjerg.

The orientation of each filament is estimated by finding the orientation of the template that gives the largest correlation with the image of the filament. The most accurate estimate of the filament orientation is obtained if the template size and position accurately correspond to the size and position of the filament in the image. Since the filament sizes and positions are known only approximately, the best orientation is obtained by conducting a search over, in addition to the orientation $\theta$ of the template, the size $s$ (defined as the edge length of the triangle) and the position $(x, y)$ relative to the initial filament positions determined

as described above. To allow fast calculation of the correlations, a family of templates of various sizes and orientations is precomputed and stored for later use. The range of sizes used is $d/4 < s < 3d/4$ with $\triangle s = 0.5$ pixels. As a result of the triangular shape, the unique set of orientations belongs to the interval $0 \leq \theta < 120^\circ$ and typically $\triangle\theta = 4^\circ$. Each template is constructed as an equilateral triangle of side length $s$ and with the values of the boundary pixels being proportional to the fraction of the pixel within the triangle. This is blurred with a square of $5 \times 5$ pixels, an interior triangle of edge length $s - 2$ pixels is set to zero, and it is then rotated by the set of angles $\theta$. An example template is shown in Fig. 2.3.

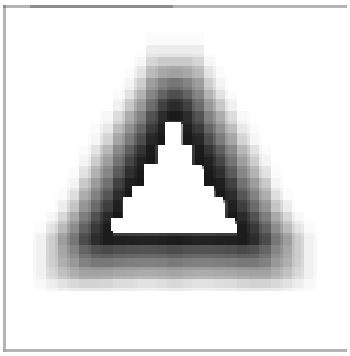

**Figure 2.3** Example template used to determine filament orientations.

Each filament in the micrograph image is correlated with each template for each position (relative to the initially determined filament position) in the range $-3 < x, y < 3$ pixels in steps of 0.5 pixels, and the correlation coefficient

$$r(x, y, s, \theta) = \frac{1}{n-1} \sum_{i=1}^{n} \left[ \frac{t(x, y, s, \theta, i) - \mu_t}{\sigma_t} \cdot \frac{f(i) - \mu_f}{\sigma_f} \right] \tag{2.4}$$

calculated. In Eq. (2.4), $t(x, y, s, \theta, i)$ and $f(i)$ are the template and filament values, respectively, at pixel *i*, $\mu$ and $\sigma$ are the mean and standard deviation respectively, and the sum is over the $n$ pixels that overlap in the filament image and the template. The estimate of each filament orientation, $\theta$, is that which maximises the correlation, i.e.

$$\theta = \arg\max_{\theta'} \left[ \max_{x,y,s} r(x, y, s, \theta') \right]. \tag{2.5}$$

For each filament, the larger the maximum correlation, the more reliable is the estimate of the orientation. Filaments that are particularly noisy or are less triangular in shape give smaller correlation coefficients and therefore less reliable orientations. The mean correlation coefficient over all the filaments, denoted $\overline{r}$, is calculated and is used as a measure of the overall quality of the image in terms of determining the filament orientations. Filaments that give correlation coefficients less than a chosen threshold value, denoted $r_{min}$,

are considered to have estimated orientations that are too unreliable and their orientations are therefore marked as being unknown. Filaments marked as unknown are not used in the subsequent classification stage. A suitable threshold value varies from image to image although a value of 0.75 was found to be suitable in many cases.

## 2.4 Classification of Orientations

As described in Section 1.1.4, the *myosin filaments in most vertebrate muscles adopt one of two orientations* and it is the spatial distribution of these two orientations that is of interest. Since the filament orientations determined as described above belong to the interval (0,120°), the difference in orientations of oppositely oriented filaments is approximately $\pm 60^\circ$. As a result of imperfections in the muscle and errors in determining the orientations, the measured orientations are not exactly $60^\circ$ apart, but fall into two narrow distributions whose means are approximately $60^\circ$ apart. The objective then is to classify each filament whose orientation is determined as belonging to one of two populations which we refer to as *up* and *down*. The underlying distribution of orientations is modelled as a Gaussian mixture consisting of two normal distributions. Since the orientations exist on the finite interval $(0, 120^\circ)$, each normal distribution is wrapped on this interval and the resulting distribution is denoted by $f(\mu, \sigma, \theta)$, where $\mu$ and $\sigma$ are the mean and standard deviation of each original normal distribution. The model distribution of the filaments orientations $f_{model}(\theta)$ is then given by

$$f_{model}(\theta) = p_{up} f(\mu_{up}, \sigma_{up}, \theta) + (1 - p_{up}) f(\mu_{down}, \sigma_{down}, \theta), \tag{2.6}$$

where $p_{up}$ is the fraction of filaments classified as up. The parameters $\mu_{up}, \mu_{down}, \sigma_{up}, \sigma_{down}$, and $p_{up}$ are determined by fitting $f_{model}(\theta_i)$ to the histogram of estimated filament orientations $h(\theta_i)$ over the whole image by minimising the sum of squared errors (SSE), where

$$SSE(\mu_{up}, \mu_{down}, \sigma_{up}, \sigma_{down}, p_{up}) = \sum_{\theta_i} [N f_{model}(\theta_i) - h(\theta_i)]^2, \tag{2.7}$$

and $N$ is the number of measured filament orientations. The minimization is performed using the Matlab function *fminsearch*. Ideally, the two populations will be separated by $60^\circ$, there will be a small spread of the orientations within each population, and the numbers of filaments in each population will be approximately equal. We therefore expect that $\triangle\mu = |\mu_{up} - \mu_{down}| \approx 60^\circ, \sigma_{up} \ll 60^\circ, \sigma_{down} \ll 60^\circ$ and $p_{up} \approx 0.5$. If these conditions are not satisfied then the orientation data are not consistent with the kind of distribution we expect. This could be due to a noisy image in which the filament orientations cannot be accurately estimated, or to the filament orientations not belonging to two populations. The latter case may occur if the lattice contains dislocations (leading to different pairs of orientations in

different regions of the image), or if the specimen contains only one filament orientation (as occurs in teleost muscles). The quantities $\triangle\mu$, $\sigma_{up}$, $\sigma_{down}$, and $p_{up}$ are therefore used to assess the quality of the specimen and of the analysis.

After fitting the model distribution, each orientation is assigned to either population using

$$\theta_i \in \begin{cases} \pi_{up} & \text{if} \quad p_{up} f(\mu_{up}, \sigma_{up}, \theta_i) \geq p_{down} f(\mu_{down}, \sigma_{down}, \theta_i) \\ \pi_{down} & \text{otherwise,} \end{cases} \tag{2.8}$$

where $\pi_{up}$ and $\pi_{down}$ represent two populations. This classification minimises the expected number of misclassifications. With each filament orientation assigned to one of the two populations, the analysis is complete.

## 2.5 Applications

The algorithms described above were implemented in Matlab (MathWorks, Natick, Massachusetts) and run on a 2.8GHz Pentium 4 PC with 1GB of RAM. Results are presented here for applications to three muscle micrographs. Dissected muscle fibers were fixed, dehydrated and embedded in Araldite, and thin transverse sections cut with an ultramicrotome and stained. Micrographs were obtained in a JEOL 1200CX electron microscope at a nominal 20,000$\times$ magnification. Images were digitized at 8 bits with a $20\ \mu m$ raster spacing on a Leafscan 45 film scanner. Transverse sections were selected as those showing little or no evidence of the M-band in the micrographs. To assess the precision of the algorithm, the automatic classification of the orientations was compared with a classification based on manually determined orientations. For the manual analysis, a program was used which allows the user to visually fit an equilateral triangle with adjustable position, angle and size to each filament displayed on a computer monitor. The manually determined orientations are then classified automatically as described above. Orientations that cannot be reliably estimated manually are marked as unknown and are not used in the classification.

The first micrograph is of a cross-section of frog sartorius muscle is shown in Fig. 3.5 and the region of one myofibril (inside the white border) was analysed. The raster spacing for this image is about $1\ nm/pixel$. A careful, although tedious, manual analysis of this image was performed and located 820 filaments. The filament location algorithm described in Section 2.2 was run. The algorithm took less than one minute to run and located 818 filaments. A subimage (corresponding to the region outlined in black in Fig. 3.5) is shown in Fig. 2.5, together with the region used to define the psf, the psf, the filtered image, the regional maxima image, and the final filament positions. The mean distance between the automatically and manually determined filaments was 1.4 pixels which corresponds to $1.4\ nm$. This is small compared to the filament dimensions ($15\ nm$) and is within the

precision needed to determine the filament orientations.

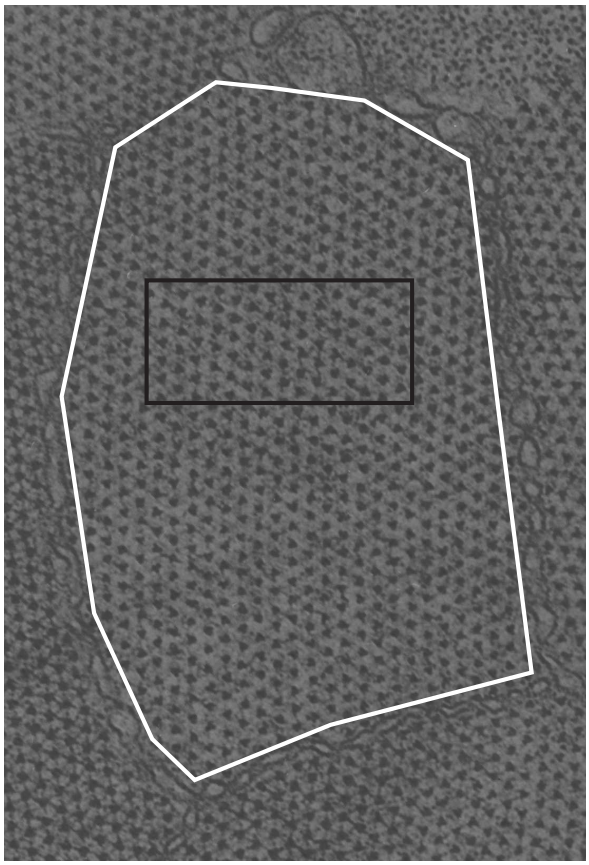

**Figure 2.4** Part of an electron micrograph of frog sartorius muscle. The white border denotes the region of one myofibril which was analysed. The black border denotes the subimage shown in Figs. 2.5 and 2.6.

The filament orientations were determined automatically as described in Section 2.3 and took two minutes. The mean correlation coefficient for the orientation of all filaments was $\overline{r} = 0.80$, and 738 (90%) of the filaments have reliable orientations ($r > r_{min} = 0.75$). The fitted templates for the subimage are shown in Fig. 2.6. The distribution of orientations is shown in Fig. 2.7, and two populations are evident. The mixture model gave a good fit to the histogram (Fig. 2.7). The parameters shown in Table 2.1 indicate that the data are consistent with two populations of filament orientations. On the basis of the mixture model, the orientations were classified into two populations as described above, and the classifications for the subimage are illustrated in Fig. 2.6.

The filament orientations were also determined manually and classified automatically as described above. The manual analysis found 720 (88%) reliable orientations. A comparison of the results of the manual and automatic classifications is shown in Table 2.2. As seen in the table, the automatically determined orientations are consistent overall with the manual

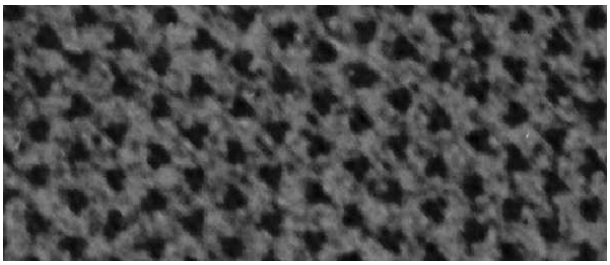

(a)

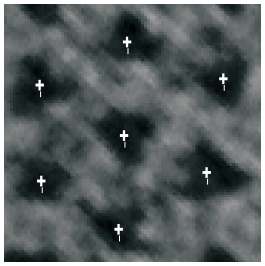

(b)

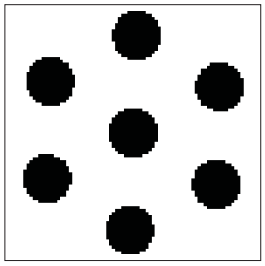

(c)

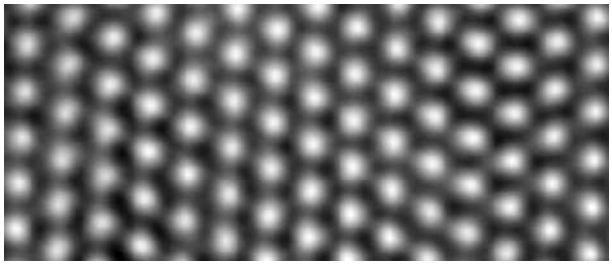

(d)

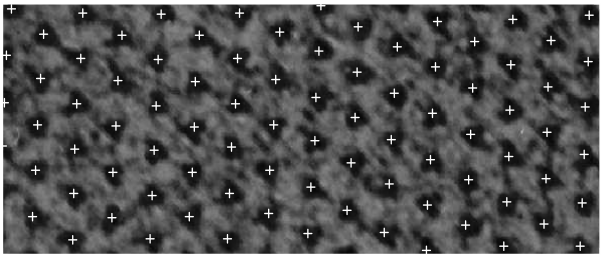

(e)

**Figure 2.5** (a) A part of the image shown in Fig. 2.5, (b) manually located filament position used to determine the psf, (c) the psf, (d) the filtered subimage, and (e) the determined filament positions.

**Table 2.1** Parameters for the example micrographs.

| Parameter | Image | | | | |
|---|---|---|---|---|---|
| | frog | turtle | poly | poly A | poly B |
| $\overline{r}$ | 0.80 | 0.80 | 0.81 | 0.81 | 0.81 |
| $\triangle\mu$ (°) | 60 | 62 | 55 | 61 | 58 |
| $\sigma_{up}$ (°) | 11 | 15 | 35 | 7 | 12 |
| $\sigma_{down}$ (°) | 10 | 15 | 10 | 15 | 13 |
| $p_{up}$ | 0.52 | 0.54 | 0.84 | 0.44 | 0.50 |

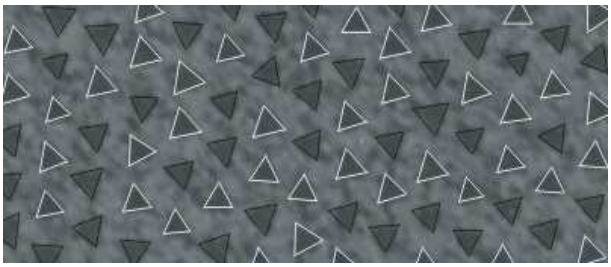

**Figure 2.6** Templates fitted to the filaments in the frog sartorius muscle image. The white and black triangles denote the classification into up and down orientations.

determinations. Of the 738 automatically determined orientations, 653 ($88\%$) agree with the manually determined orientations, only 16 ($2\%$) have the opposite orientation, and the remaining 69 ($20\%$) could not be determined manually. As expected, there is more variation in the manual classification of the orientations that could not be reliably determined automatically. Overall, the algorithm appears to perform well on this (relatively high quality) micrograph. The results obtained are consistent with manual classification, and the automatic method gives a higher proportion of reliable classifications than does the manual method.

The second micrograph analysed is from turtle leg muscle (Fig. 2.8) and a manual analysis of this image identified 339 filaments. The raster spacing is about $1.5\ nm/pixel$. This image is noisier than the frog sartorius muscle (Fig. 3.5). The myosin filaments do not have clearly defined triangular profiles and the myofibril contains many small features (possibly parts of the actin filaments) between the myosin filaments, making both manual and automated analysis more difficult. The noisy nature of the image is more apparent in the subimage shown in Fig. 2.9a.

The filament location algorithm located 334 filaments with only 1 false positive and 6 false

**Table 2.2** Comparison of the automatic and manually determined orientations from the frog sartorius muscle micrograph.

| Classification | | Automatic orientations | | | |
|---|---|---|---|---|---|
| | | up | down | unknown | total |
| Manual orientations | up | 335 | 9 | 25 | 369 |
| | down | 7 | 318 | 22 | 347 |
| | unknown | 32 | 37 | 30 | 99 |
| | total | 374 | 364 | 77 | 815 |

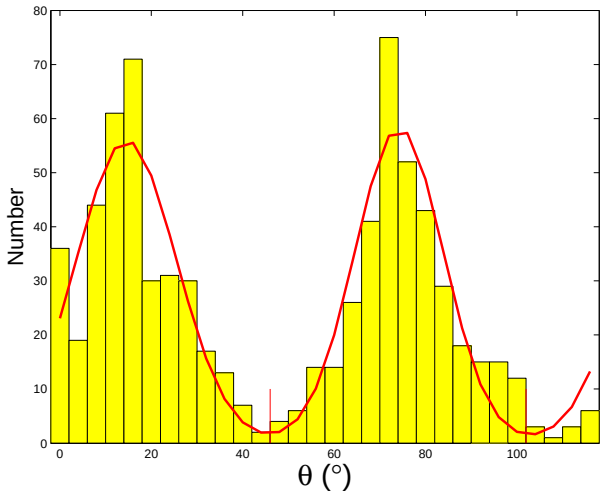


**Figure 2.7** The histogram and mixture model for the frog sartorius muscle image.

negatives compared to a manual analysis. The filament location is illustrated for the subimage in Fig. 2.9b. The filament orientations were determined automatically giving a mean correlation coefficient of 0.80. Using a correlation threshold of 0.75, 281 of the orientations (84%) were above the threshold. Fitting the Gaussian mixture model gave the parameters listed in Table 2.1, indicating a good classification. The results of the classification for the subimage are shown in Fig. 2.9c. The orientations were also determined manually as described above and classified automatically. A comparison of the manual and automatic classifications are shown in Table 2.3. Of the automatically determined orientations, 200 (71%) agree with the manually determined classifications and 19 (7%) have the opposite classification. The proportion of opposite manually and automatically determined orientations is larger than in the first example as a result of the higher level of noise in this image. However, comparison of two manual analyses of this micrograph by two individuals results in a similar percentage of filaments being labelled with opposite classifications,

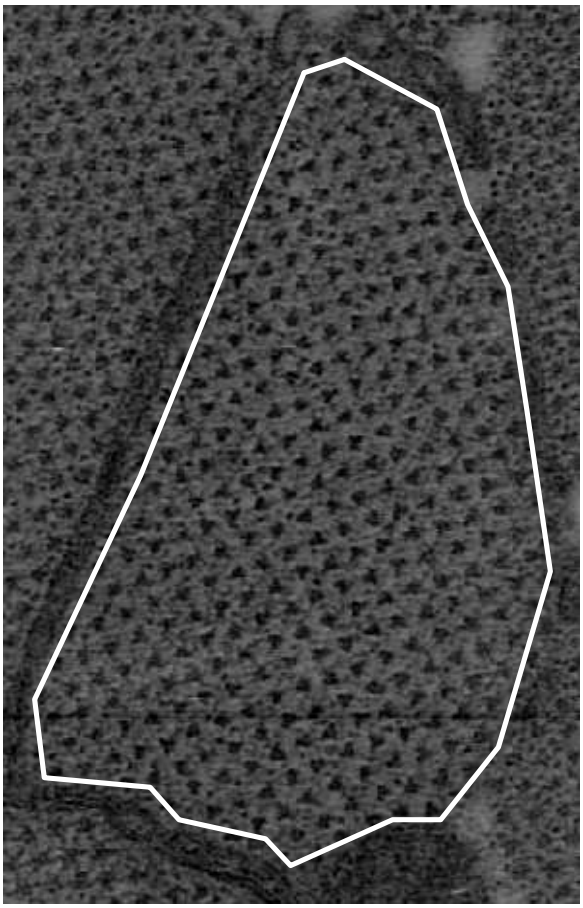

**Figure 2.8** Electron micrograph of turtle muscle.

indicating that the automatic method is at least as good as a manual analysis.

The third example is a micrograph from polypterus muscle is shown in Fig. 2.11 and the raster spacing is about $1.5\ nm/pixel$. Automatic analysis of this micrograph located 1044 filaments and the orientations of 986 $(94\%)$ of these were reliably determined using a correlation threshold of 0.75. The histogram of orientations is shown in Fig. 2.12a and the parameters listed in Table 2.1. Inspection of the histogram, however, shows no evidence of two populations as expected. The large values of $\sigma_{up}$ and $p_{up}$ are diagnostic of a problem.

The histogram in Fig. 2.12 shows evidence of peaks at $15^\circ$ and $75^\circ$. A possible explanation is that a region with orientation means of ($15^\circ$, $75^\circ$) coexists with other region(s) inside the same myofibril with different orientation means. In order to investigate this possibility, the

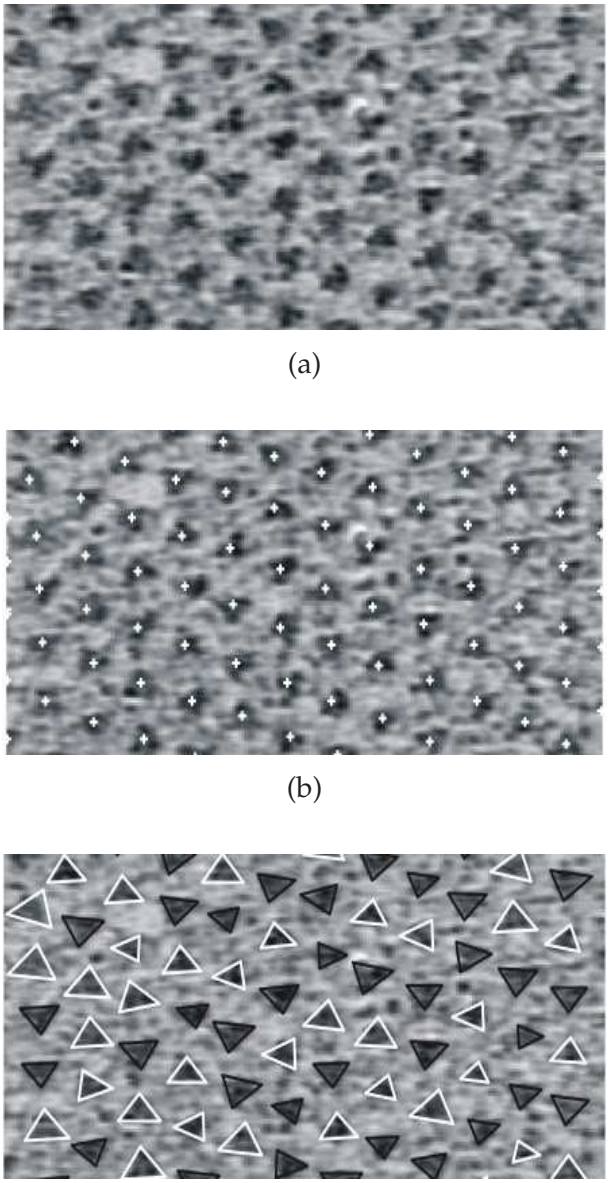

(a)

(b)

(c)

**Figure 2.9** (a) A subimage of the turtle muscle micrograph, (b) filament location and (c) the classification of filament orientations.

**Table 2.3** Comparison of the automatic and manually determined orientations from the turtle leg muscle micrograph.

| Classification | | Automatic orientations | | | |
|---|---|---|---|---|---|
| | | up | down | unknown | total |
| Manual orientations | up | 96 | 7 | 12 | 115 |
| | down | 12 | 104 | 18 | 134 |
| | unknown | 21 | 40 | 22 | 83 |
| | total | 129 | 151 | 52 | 332 |

orientations $\theta$ were colour coded as

$$\theta \in \begin{cases} red & \text{if } \theta \in \mu \pm \phi \\ cyan & \text{if } \theta \in (\mu + \psi) \pm \phi \\ blue & \text{if } \theta \in (\mu + 2\psi) \pm \phi \\ yellow & \text{if } \theta \in (\mu + 3\psi) \pm \phi \\ black & \text{otherwise,} \end{cases} \tag{2.9}$$

where $\mu = 15°, \psi = 30°$ and $\phi = 10°$ and shown in Fig. 2.10. The lower left of the myofibril is seen to be dominated by yellow and cyan markers and the remainder by red and blue. On this basis a border is defined in the transition region between two regions which are labelled A and B as shown in Fig. 2.11. In principle it may be possible to do this segmentation automatically based on differences in the texture, however this would probably be quite difficult in practice. Each region was then analysed separately. This gave the histograms shown in Fig. 2.12b and Fig. 2.12c and the parameters listed in Table 2.1. The values of the parameters indicate good classifications in each region, which is also evident in the histograms. The means of the orientations are $(44°, 106°)$ and $(15°, 73°)$ in regions A and B, respectively, showing that the pairs of orientations in the two regions are rotated by $30°$ relative to each other. The regions A and B contain 335 and 704 filaments, respectively, with 317 and 663, respectively, orientations reliably determined. Evidently then, the myofibril is segregated into two regions with a high degree of orientational order within each region. It is perhaps not surprising that such "dislocations" occur in large myofibrils.

## 2.6 Summary

The algorithm described in this chapter allows effective and rapid analysis of noisy micrographs to determine the spatial distribution of filament orientations. Comparison with

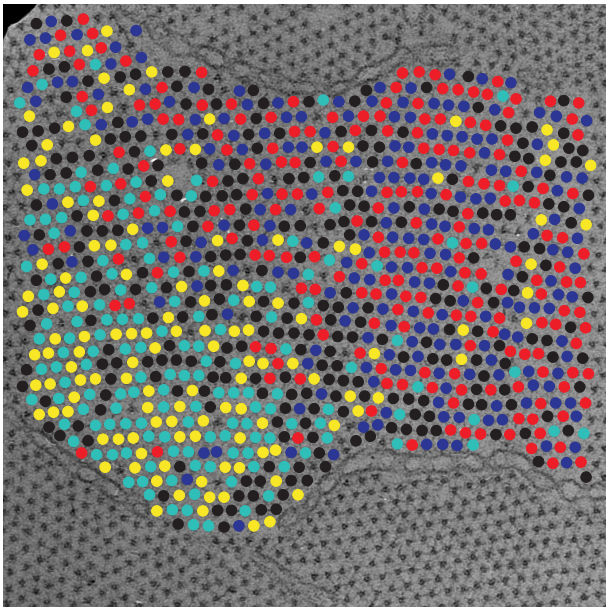

**Figure 2.10** Chart used to segregate the regions shown in Fig. 2.11. Yellow, cyan, red and blue markers represent four groups of orientations in Eq. (2.9). A cluster of yellow and cyan markers is dominant on the left and red and blue markers clustered on the right side of the lattice.

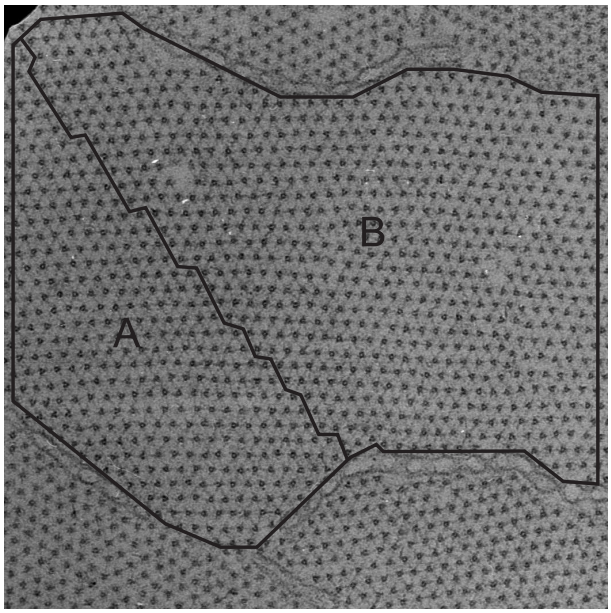


**Figure 2.11** Electron micrograph of polypterus muscle. Two regions (A and B) represent the dislocated regions.

manually classified orientations shows a good consistency, indicating that the automatic analysis is at least as accurate as, and probably more accurate than, manual analysis. Data on the distribution of orientations obtained using this algorithm are used in later Chapters to analyse this distribution.

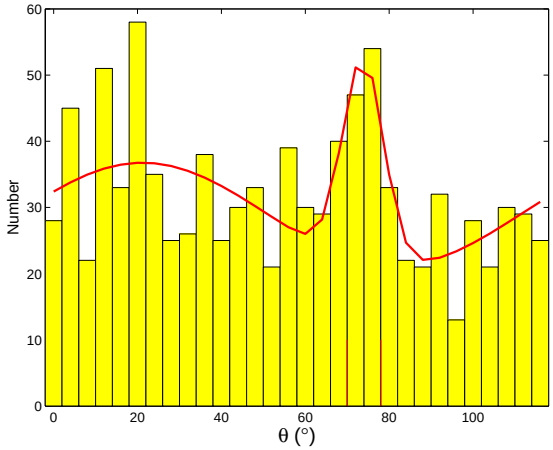


(a)

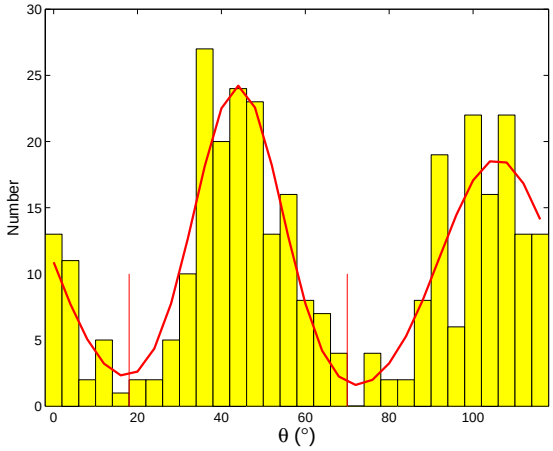


(b)

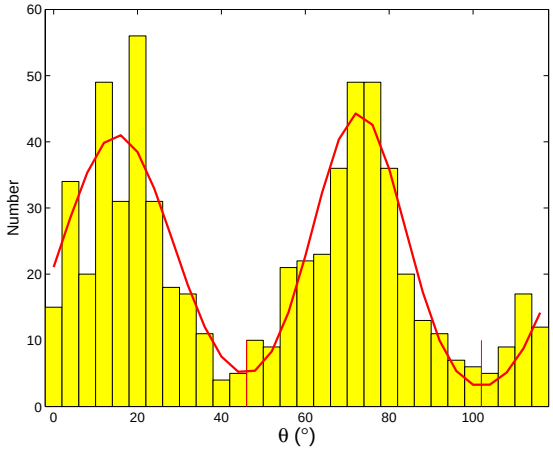


(c)

**Figure 2.12** (a) The histogram and mixture model for the polypterus muscle lattice, (b) the histogram and mixture model for the polypterus muscle lattice region A and (c) the histogram and mixture model for the polypterus muscle lattice region B.

# Chapter 3

# Analysis of the Myosin Lattice Disorder

## 3.1 Introduction

The myosin lattice disorder is believed to be a result of the preference for adjacent filaments to adopt opposite orientations in order to maximise the number of binding sites with the surrounding actin filaments. It is probable that the disorder is driven by the energetics of intermolecular interactions, and it is further likely that these interactions are dominated by those between nearest neighbours. A natural question therefore is whether the observed spatial distribution of the filament orientations is a consequence of such nearest neighbour interactions. This question is investigated in this chapter.

Representing the filament orientations by a binary variable indicates that a possible model is the triangular Ising antiferromagnet (TIA) described in Chapter 1. In order to determine if the Ising model quantitatively explains the myosin orientation disorder, it is necessary first to define suitable parameters that quantitate the disorder. Then, Monte Carlo simulations of the TIA are conducted, and the various disorder parameters are calculated and compared to those calculated from the myosin lattice. The degree of disorder of the TIA increases with temperature as described in Section 1.2.4. Thus the simulations are conducted at different temperatures to find the temperature which produces the best fit to the myosin lattice disorder. A set of simulation results are presented that indicates that the TIA is indeed a good model for the myosin lattice disorder.

## 3.2 Myosin Lattice Disorder Parameters

Various statistical parameters can be used to describe the disorder. Here particular parameters that describe the short-range and long-range statistics are defined that are used to characterise the myosin lattice disorder. The disorder parameters involve relationships between the orientations at $n$ sites ($n$th-order statistics).

First, parameters are defined that are used to quantitate the no-three-alike rules described in Section 1.1.4, followed by parameters to quantitate the superlattice content. These are short-range parameters, and a more usual long-range parameter, the correlation function, is then described.

### 3.2.1 No-Three-Alike Rules

The two "no-three-alike" rules observed in the myosin lattice put forward by Luther and Squire [LS80] are not obeyed without exception. Hence, the frequencies with which the two rules are violated are defined as parameters of the disorder. This frequency is calculated by locating all sets of three filaments corresponding to a rule (referred to as cliques) and counting the number of cliques on which the rule is violated. The frequencies of rule violation are then given by

$$f_{rv1} = \frac{N_{rv1}}{N_{c1}} \qquad f_{rv2} = \frac{N_{rv2}}{N_{c2}} \tag{3.1}$$

where $N_{rv1}$ and $N_{rv2}$ are the number of rule violations and $N_{c1}$ and $N_{c2}$ are the number of cliques. For a large lattice with random orientations at each site, the rule violation frequencies are $f_{rv} = 1/4$. Luther and Squire point out that both rules are quite strong but the second rule is not as strong as the first.

Both of the rules imply that opposite orientation of adjacent (nearest-neighbour) filaments is preferred, since violation of the rules reduces the number of such adjacent orientations within the clique. For a rule 1 clique, violating the rule decreases the number of "desirable" interactions, i.e. opposite adjacent orientations, by two. For a rule 2 clique however, violating the rule decreases the number of desirable interactions by one or two with respect to configurations for which the rule is obeyed. This may account, in part, for rule 2 being violated more often than rule 1, although this is an approximation since the influence of the local configurations extends beyond the clique. However, the key point to note is that a ground state is defined as all the rule 1 cliques being satisfied on the lattice, hence $f_{rv1}$ is a measure of the lattice disorder away from the ground state whereas no restrictions are imposed on the value of $f_{rv2}$.

### 3.2.2 Superlattice Content

A key characteristic of the myosin lattice disorder is the tendency of the filament orientations to form a superlattice; rhombi formed by second-nearest-neighbour filaments that all have the same orientation. One way to characterise the degree of superlattice is to count the proportion of superlattice cells for which the orientations at the vertices are identical. The fractional superlattice cell content, $f_s$, is therefore defined by

$$f_s = \frac{N_s}{N_{ts}} \tag{3.2}$$

where $N_s$ is the number of superlattice cells with identical orientations and $N_{ts}$ is total number of superlattice cells. Note that the superlattice cells have to be counted over the three possible directions of the superlattice as described in Section 1.1.4. For a large lattice with random orientations at each site, the superlattice content is $f_s = (1/2)^3 = 1/8$.

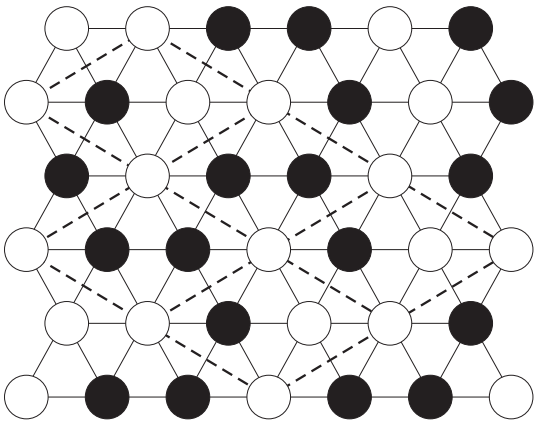

**Figure 3.1** An example of a superlattice clump which is a contiguous formation of superlattice cells (dashed).

An important feature of the superlattice structure is the extent to which the superlattice cells form contiguous domains which are referred to here as "clumps" (shown in Fig. 3.1). A clump is defined as a set of superlattice cells such that each shares at least one edge with the clump. Let $N_{sc}^i$ denote the number of superlattice cells that comprise the *i*th superlattice clump. Then, the mean and standard deviation of the superlattice clump size are defined as

$$\overline{N}_{sc} = \frac{\sum_{i=1}^{N_{sc}} N_{sc}^i}{N_{sc}} = \frac{N_s}{N_{sc}} \tag{3.3}$$

$$\sigma_{sc} = \sqrt{\frac{\sum_{i=1}^{N_{sc}} (N_{sc}^i - \overline{N}_{sc})^2}{N_{sc}}}, \tag{3.4}$$

where $N_{sc}$ is the number of superlattice clumps.

### 3.2.3 Correlation Function

As noted above, the most fundamental characteristic of the myosin lattice is that adjacent filaments prefer to have opposite orientations, i.e. nearest neighbour pairs (+1,-1) and (-1,+1) occur more frequently than (+1,+1) and (-1,-1). A natural measure is therefore the fraction of oppositely oriented nearest neighbour bonds (or pairs) $x_o$ defined by $x_o = N_o/N$ where $N_o$ is the number of oppositely oriented adjacent pairs and $N$ is the total number of pairs. In the context of magnetism, $x_o$ varies from 1 for a maximally antiferromagnetic system to $1/2$ for a random system to 0 for a maximally ferromagnetic system. A more symmetric parameter is the bond order $\sigma$ [DKR+97, Zim79] defined by

$$\sigma = 1 - \frac{2N_o}{N} = 1 - 2x_o. \tag{3.5}$$

The bond order varies between -1 for a maximally antiferromagnetic system (although this is not possible for a triangular lattice as a result of geometric frustration) to zero for a random system to +1 for a maximally ferromagnetic system. The symmetric parameter $\sigma$ is therefore used.

The sites on a triangular lattice are indexed by the integer $(m, n)$ in the oblique coordinate system with internal angle $\gamma = 60°$ as shown in Fig. 3.2. For stationary disorder, the origin can be chosen to be anywhere on the lattice.

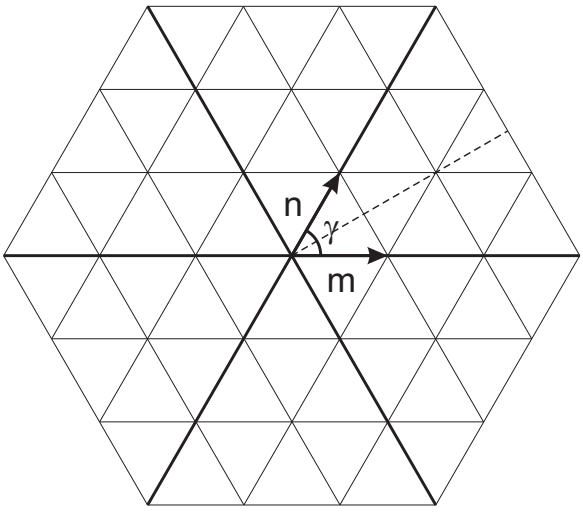


**Figure 3.2** Oblique coordinate system with $\gamma = 60°$. It has mirror line symmetry (dashed) within a six-fold rotational symmetry (bold).

The short- and long-range second-order statistics can be described using the spatial correlation coefficient. The correlation coefficient varies between -1 for fully anti-correlated random variables and +1 for fully correlated random variables. This follows the properties of the bond order defined above in terms of the site orientations if the definition is

extended to any two sites as opposed to nearest neighbours. For disorder that is stationary (independent of position in the lattice), the correlation coefficient depends only on the vector difference $(m, n)$ between the sites $(p, q)$ and $(p + m, q + n)$ where $p$ and $q$ are any integers. A tentative definition for the correlation coefficient is therefore

$$\rho_{mn} = 1 - 2x^o_{mn} \tag{3.6}$$

where $x^o_{mn}$ is the fraction of pairs of sites spaced by $(m, n)$ that have opposite orientations.

The correlation coefficient between two random variables $x$ and $y$ is defined by

$$\rho_{xy} = \frac{\langle (x - \overline{x})(y - \overline{y})\rangle}{\sqrt{\langle (x - \overline{x})^2\rangle \langle (y - \overline{y})^2\rangle}}. \tag{3.7}$$

For application to the problem at hand, the filament orientations are assigned a random variable that takes the value +1 for one orientation and -1 for the other orientation. This random variable is denoted $s_{pq}$ for the site $(p, q)$. The correlation coefficient is then given by

$$\rho_{mn} = \frac{\langle (s_{pq} - \overline{s}_{pq})(s_{p+m,q+n} - \overline{s}_{p+m,q+n})\rangle_{p,q}}{\sqrt{\langle (s_{pq} - \overline{s}_{pq})^2\rangle_{p,q} \langle (s_{p+m,q+n} - \overline{s}_{p+m,q+n})^2\rangle_{p,q}}}. \tag{3.8}$$

Assuming that the lattice is large enough that each orientation occurs with frequency $1/2$, $\overline{s}_{pq} = 0$, and Eq. (3.8) simplifies to

$$\rho_{mn} = \langle s_{pq} s_{p+m,q+n}\rangle. \tag{3.9}$$

Note that this can also be easily derived from Eq. (1.8). Then Eq. (3.9) can be written as

$$\rho_{mn} = (1 - x^o_{mn}) - x^o_{mn} = 1 - 2x^o_{mn} \tag{3.10}$$

so that, indeed, this corresponds to the tentative definition above. In particular, $\rho_{01} = \rho_{10} = \sigma$.

The triangular lattice has six-fold rotational symmetry and the correlation coefficient must have the same symmetry. Furthermore, the lattice has mirror symmetry about a line inclined at $30^\circ$ to one of the axes, and the correlation coefficient must have the same symmetry (Fig. 3.2). The correlation coefficient is therefore uniquely defined by its behaviour on the sector $m \geq 0$ and $0 \leq n \leq m$.

### 3.2.4 Normalisation and the Effect of Unknown Orientations

It is desirable to use normalised, or unit-free, parameters to describe the disorder. For example, the normalised energy of a configuration is given by

$$\begin{aligned} E^{\text{Norm}} &= \frac{E}{E_{max}} \\ &\approx \frac{E}{3JN} = \frac{3JN(1-2x_{01}^{o})}{3JN} = \rho_{01}, \end{aligned} \tag{3.11}$$

where $E_{max}$ is the lattice with all ferromagnetic interactions, $N$ is the number of sites, and the approximation in Eq. (3.11) applies when $N \to \infty$. All of the parameters defined above, except $\overline{N}_{sc}$ and $\sigma_{sc}$ related to the superlattice clump sizes, are normalised and, in particular, they are independent of the size of the lattice.

It is evident from the work reported in Chapter 2 that the orientation at all sites cannot be determined from a micrograph. The effect of this on calculation of the parameters described above needs to be considered. It is desirable to estimate these parameters for the whole lattice, including the sites for which the orientation is unknown. The parameters $f_{rv1}$, $f_{rv2}$, $f_s$ and $\rho_{mn}$ are unaffected by the presence of sites with unknown orientations as a result of the way they are normalised. However, the mean clump size $\overline{N}_{sc}$ (and, although to a lesser extent, $\sigma_{sc}$) will be reduced substantially by the presence of unknown orientations, since the latter will break up what would have been larger clumps. The fraction of sites for which the orientation is unknown is defined as

$$f_u = \frac{N_u}{N} \tag{3.12}$$

where $N_u$ is the number of unknown orientations and $N$ is the total number of sites. Clearly, this quantity also serves as an indicator of the quality of a micrograph. The effect of unknown orientations is discussed further in Section 3.3.

## 3.3 Monte Carlo Simulation of the Antiferromagnetic Ising Model

Metropolis Monte Carlo simulation (Section 1.3) is used to simulate equilibrium configurations of the TIA at different temperatures. The aim of the Monte Carlo simulation is to calculate how the disorder parameters change with temperature and determine whether at a specific temperature the TIA and the myosin lattice exhibit similar disorder. Monte Carlo simulations are performed on lattices that have identical shapes to the myosin lattices observed in micrographs. Initial spins are randomly oriented with the free boundary condition applied. By using a size and shape identical to that of a particular myofibril, finite

size effects are eliminated. As noted previously, the myosin lattice will generally contain sites for which the orientations are unknown. This is simply accounted for by conducting the MC simulation with the full lattice but calculating the parameters using only the sites that correspond to known sites in the micrograph. The parameters from the simulation then correspond exactly to those calculated from the micrograph.

The simulations are conducted in terms of a reduced temperature $T$, where

$$T' = k_B T / \Delta e, \tag{3.13}$$

$T'$ is absolute temperature and $\Delta e$ is the difference in interaction energy between identical and opposite nearest neighbour orientations. A set of simulations is conducted for a range of temperatures between $T_{min}$ and $T_{max}$ in steps of $\Delta T$ to probe the behaviour of the model at varying temperature. The simulation is started at $T = T_{max}$ and at the end of the simulation at temperature $T$, the final state of the simulation is used as the initial state for the simulation at $T - \Delta T$. This is referred to as simulated annealing and has the advantage that the system should come to equilibrium faster than starting from a random configuration ($T = \infty$) each time.

The state transitions have single-spin-flip dynamics and the acceptance rate depends on the energy difference $E_\nu - E_\mu$ between the current state $\mu$ and the proposed next state $\nu$. By recognising that only the local interactions with the flipped spin contribute to the change in energy, the energy difference is simplified as

$$E_\nu - E_\mu = 2 J s_k^\mu \sum_{<i,k>} s_i^\mu, \tag{3.14}$$

where $s_k^\mu$ is the $k$th site in the current state proposed for flipping [NB99].

At each temperature step, $\tau_{eq}$ sweeps are made and then measurements are taken at every $\tau_{\text{decorr}}$ sweeps, i.e. the mean and the standard deviation calculated. An efficient method for calculating the averages is to update the mean and the standard deviations during each measurement and discard the large data set. The updated mean $\overline{x}'$ and standard deviation $\sigma_x'$ at the next step are

$$\overline{x}' = \frac{m^2 \overline{x} + x}{m^2 + 1},$$

$$\sigma_x'^{\,2} = \frac{\sigma_x^2 (m+1)}{m} + \frac{(x - \overline{x})^2}{m^2 + 1}, \tag{3.15}$$

where $x$ is the parameter calculated at the current step, $m$ is the current number of steps, and $\overline{x}$ and $\sigma_x$ are the previous mean and standard deviation [Han75].

### 3.3.1 Free Boundary Conditions and Edge Effects

Calculation of the parameters as described above is suitable for comparison with micrographs. However, if one is interested in values for an infinitely large lattice then the effect of a finite simulation needs to be considered. The simulated TIA system has a finite number of sites, $N$ with an imposed free boundary condition which results in the sites on the boundary of the lattice having fewer than six nearest neighbour interactions. The disorder is then not strictly stationary. The significance of this is illustrated by the calculation of the expected bond order parameter on a finite lattice with free boundary conditions.

For simplicity, let the triangular lattice be an $n$ by $n$ rhombus with $N$ sites so that $N = n^2$. Clearly, there are then $n_o = 4(n-1)$ sites on the boundary and the rest, $n_i = N - n_o$, internal. It is conjectured that the sites on the boundary are less frustrated and the proportion of antiferromagnetic bonds per site may differ. For a triangular lattice, there are three bonds associated with one site and a change of a bond is weighted $1/3$, so it may be reasonable to expect the outer edge bond order, $\sigma_o$ to deviate as much as $-1/3$ from $\sigma_i$. If the outer edge bond order, $\sigma_o$, is defined as

$$\sigma_o = 1 - 2\chi_o^o, \tag{3.16}$$

where $\chi_o^o$ is number of oppositely oriented adjacent pair of sites that both have strictly less than six nearest neighbour bonds and similarly, $\sigma_i$ is defined as

$$\sigma_i = 1 - 2\chi_o^i, \tag{3.17}$$

where $\chi_o^i$ is number of oppositely oriented adjacent pair of sites that have at least one site with six nearest neighbour bonds, then the expected bond order for sites on the boundary could range between $-1/3 \geq \sigma_o \geq -2/3$. Note that substituting a bond order of $-2/3$ into Eq. (3.10) corresponds to $5/6$ of the bonds being antiferromagnetic. The bond order for the whole lattice is the sum of the two expected bond orders each weighted accordingly by the number of respective sites

$$\sigma = \frac{n_i\sigma_i + n_o\sigma_o}{N}. \tag{3.18}$$

The edge effect on the bond order for various $\sigma_o$ calculated using Eq. (3.18) are shown in Fig. 3.3.

By consideration of the triangular plaquette, the bond order is bounded below by $-1/3$ for an infinite size TIA system. However, Fig. 3.3 shows that the bond order of a finite size TIA system is less than $-1/3$. Indeed, Monte Carlo simulations of TIA system $(N = 704)$ shows that the bond order, $\sigma$, drops below $-1/3$ for low temperatures as shown in Fig. 3.4, although comparison with Fig. 3.3 show that $\sigma_o$ is close to $-1/3$.

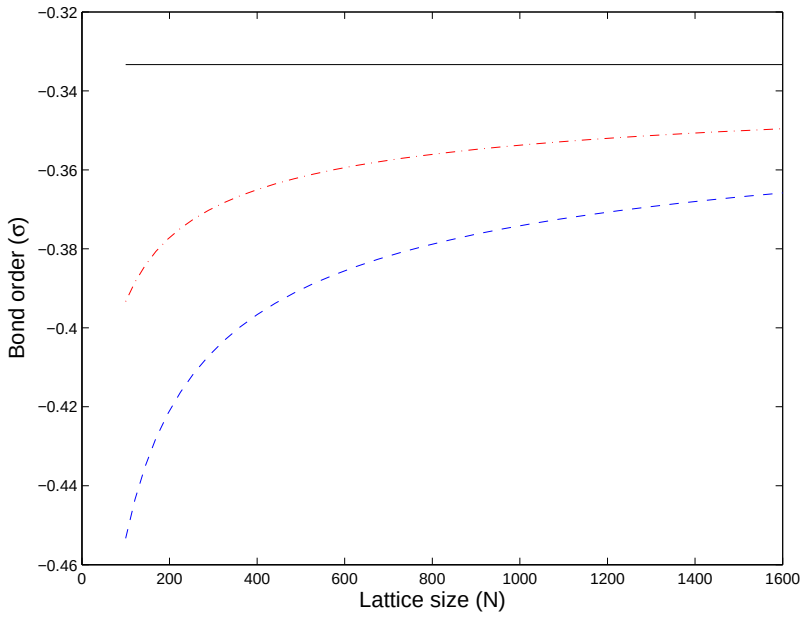


**Figure 3.3** Edge effect on bond order range for $\sigma_o = -\frac{1}{3}$ (—), $-\frac{1}{2}$ $(- \cdot -)$, and $-\frac{2}{3}$ $(--)$.

## 3.4 Results

### 3.4.1 Simulation Results

A set of simulation results is presented in this section that is based on the micrograph of the frog myosin lattice shown in Fig. 3.5. The myosin lattice analysis algorithm described in Chapter 2 was applied to this micrograph and located 805 filaments, of which 704 orientations could be reliably determined, i.e. there are 101 unknown orientations. Energy minimisations of the TIA model were conducted on a finite lattice with the same shape and dimensions of the myosin lattice in the micrograph and with free boundary conditions. The sites were initialised with random spins, and simulation temperatures began at $T_{max} = 1.00$ reduced to $T_{min} = 0.20$ in steps of $\Delta T = 0.01$. The core Monte Carlo simulation uses a program developed by Dr. Nic Blakeley.

As described in Section 1.3.2, average equilibration and decorrelation times were calculated for the simulation by running 3 preliminary simulations at $T_{min}$ using different seeds, which gave 19.0 (6.1) and 3.7 (0.6) sweeps for the equilibration and decorrelation times, respectively. The equilibration time can be seen to be about 20 sweeps in Fig. 3.6. Based on these preliminary calculations, the equilibration and decorrelation times used in the simulation were 20 and 10 sweeps at all temperatures, respectively. At each temperature, 10020 sweeps are performed, i.e. 20 sweeps for equilibration followed by $10^4$ sweeps allowing

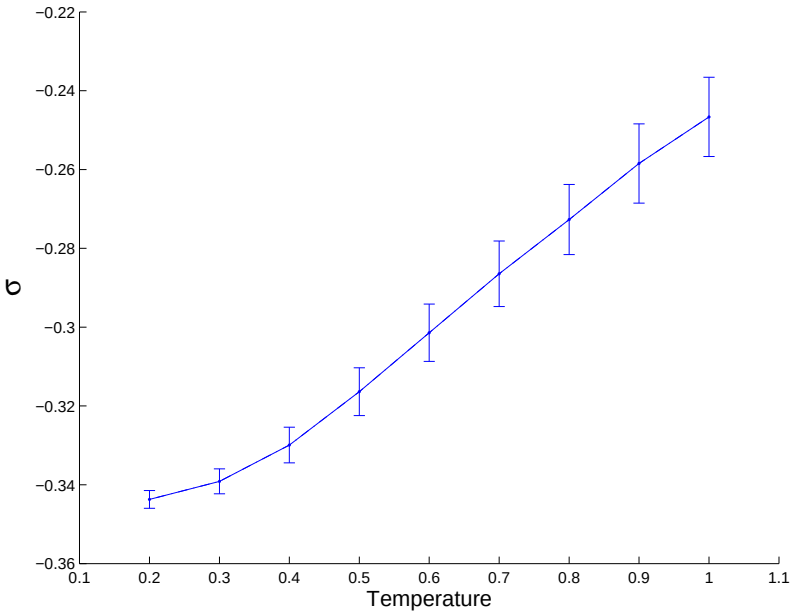


**Figure 3.4** Bond order versus temperature for Monte Carlo simulations of TIA system $(N = 704)$.

$10^3$ configurations to be sampled every 10 sweeps, and the disorder parameters averaged over the $10^3$ samples. Standard deviations of the parameters were also calculated from the $10^3$ samples.

The resulting mean and standard deviations of various parameters versus temperature are shown in Fig. 3.7. The normalised energy, $E^{\text{norm}}$ (Fig. 3.7(a)) shows that the MC simulation reduces the energy of the system as temperature decreases. At $T_{min}$, the energy is approximately $1/3$ of the corresponding fully ferromagnetic lattice as expected (Eq. (1.17)). The acceptance ratio, $\alpha$ decreases steadily from approximately $1/2$ to $1/4$ as temperature is decreased from $T_{max}$ to $T_{min}$ as shown in Fig. 3.7(d). This indicates that the state transitions are frequent enough at all temperatures studied, and the simulation does not suffer from critical slowing. The proportion of positively oriented spins is always close to $1/2$ as shown in Fig. 3.7(c) indicating no bias. The bond order, $\sigma$ decreases to about -0.34 at $T_{min}$ with small standard deviations (Fig. 3.7(b)). For an infinite lattice, the bond order is bound below by -1/3 and the slightly smaller value obtained is due to finite size effects as discussed in Section 3.3.1.

The third- and fourth-order statistics for characterising the disorder described in Section 3.2 are plotted against temperature in Fig. 3.8. The frequency of rule 1 violations, $f_{rv1}$ vanishes to almost zero at $T_{min}$ (Fig. 3.8(a)). The frequency of rule 2 violations, $f_{rv2}$ decreases to about 0.04 for low $T$ (Fig. 3.8(b)). Inspection of Fig. 3.8(c) shows that the frequency of superlattice cells, $f_s$ varies between about $1/4$ to $1/2$ which is well above that for a random

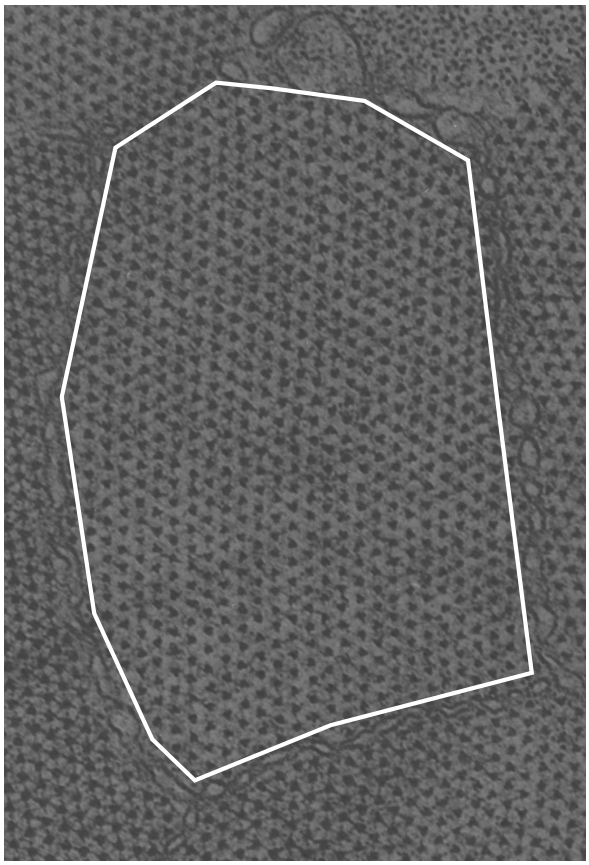

**Figure 3.5** Part of an electron micrograph of frog sartorius muscle. The white border denotes the region of one myofibril which was analysed.

lattice (1/8). As expected, the number of superlattice clumps $N_{sc}$ decreases as the mean size of the superlattice clumps $\overline{N}_{sc}$ increase, as temperature decreases (Figs. 3.8(d)-(e)). The standard deviation of the superlattice clump size increases with decreasing temperature (Fig. 3.8(f)).

The spatial correlation function calculated from the TIA simulations is shown versus $d$ for different temperatures in Fig. 3.9(a). Note the larger correlations at lower temperatures as expected. The triangular lattice (Fig. 3.10(a)) can be partitioned into three sublattices. All three sublattices are rhombic lattices formed from joining the second nearest neighbours (Fig. 3.10(b)). A honeycomb lattice is formed by combining the two sublattices that do not contain the origin (Fig. 3.10(c)). As mentioned in Section 1.2.4, if the pair of sites are on the same sublattice, then the correlation function is positive. However, if the pair of sites are on different sublattices, then the correlation function is negative. Hence, the correlation function shown in Fig. 3.9(a) is replotted in Fig. 3.9(b) as two separate curves for pair separations, $d$, either on the same sublattice or on different sublattices. This shows the behaviour of the correlation function more clearly.

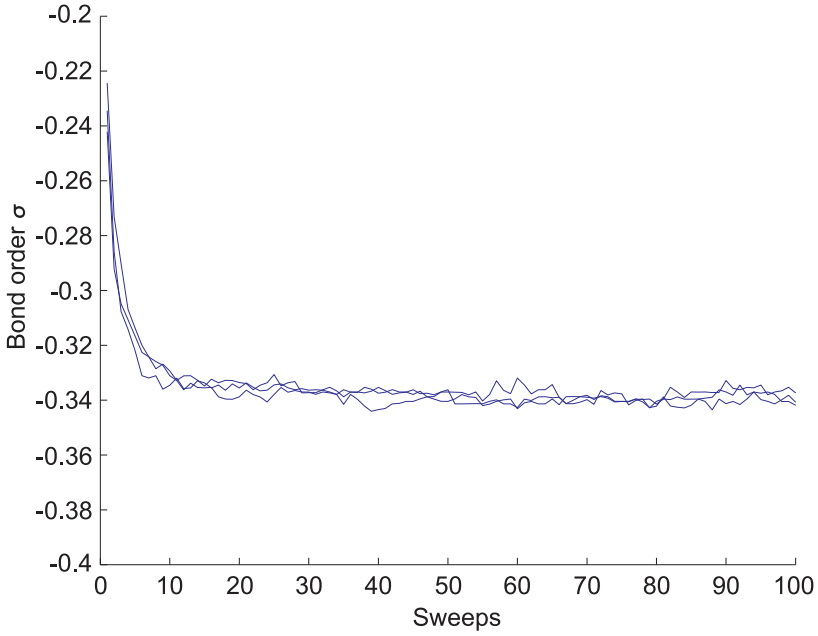


**Figure 3.6** Equilibration for the myosin lattice shown in Fig. 3.5.

### 3.4.2 Comparison with Data from Micrograph

To assess if the TIA is a good model of the myosin disorder, the parameters from the simulation are compared to those from the micrograph. However, this first involves determining the temperature that gives the best fit between the simulations and the data. This is referred to as the effective temperature, $T_{\text{eff}}$, of the myosin lattice. The effective temperature is estimated by performing a search over a wide range of temperatures for which the correlation function matches the values derived from the myosin lattice. At each temperature step, the weighted root mean square error (RMSE) between the spatial correlations of the TIA ($\rho^{sim}_{m,n}(T)$) and the myosin lattice ($\rho^{data}_{m,n}$) is calculated. The effective temperature is then given by

$$\begin{aligned} T_{\text{eff}} &= \underset{T'}{\text{argmin}} \Big\{ RMSE \Big\} \\ &= \underset{T'}{\text{argmin}} \Big\{ \frac{1}{N} \sum_{m,n} \sqrt{\frac{(\rho^{sim}_{m,n}(T') - \rho^{data}_{m,n})^2}{\sigma^{sim}_{m,n}(T')^2}} \Big\}, \end{aligned} \tag{3.19}$$

where $N$ is the number of samples $(m, n)$. The resulting RMSE gives a measure of how well the TIA fits the myosin lattice in terms of the correlation function. The values of the other parameters from the simulations at $T_{\text{eff}}$ are also compared with those calculated from the micrograph.

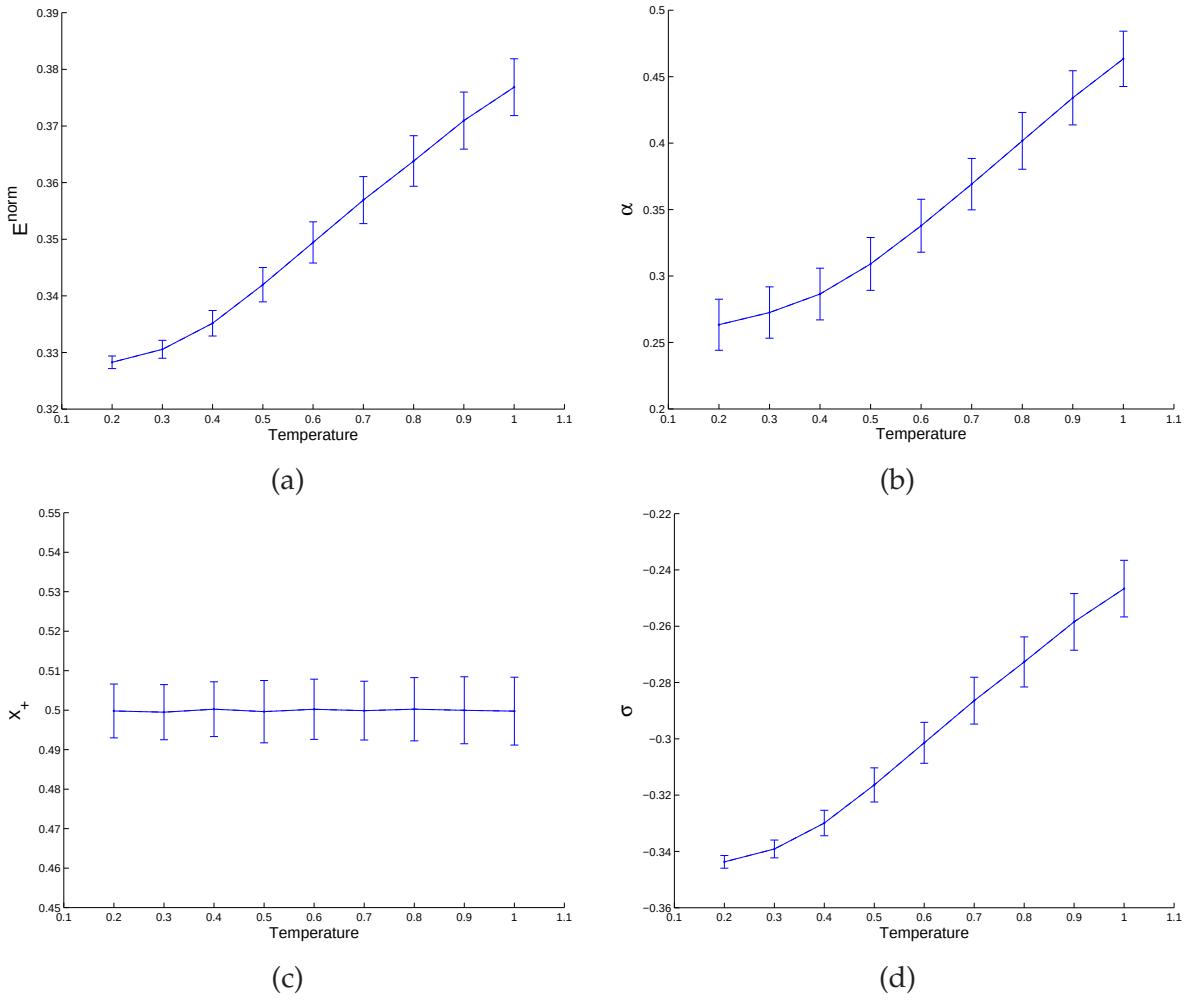


**Figure 3.7** Plot of various parameters verses temperature.

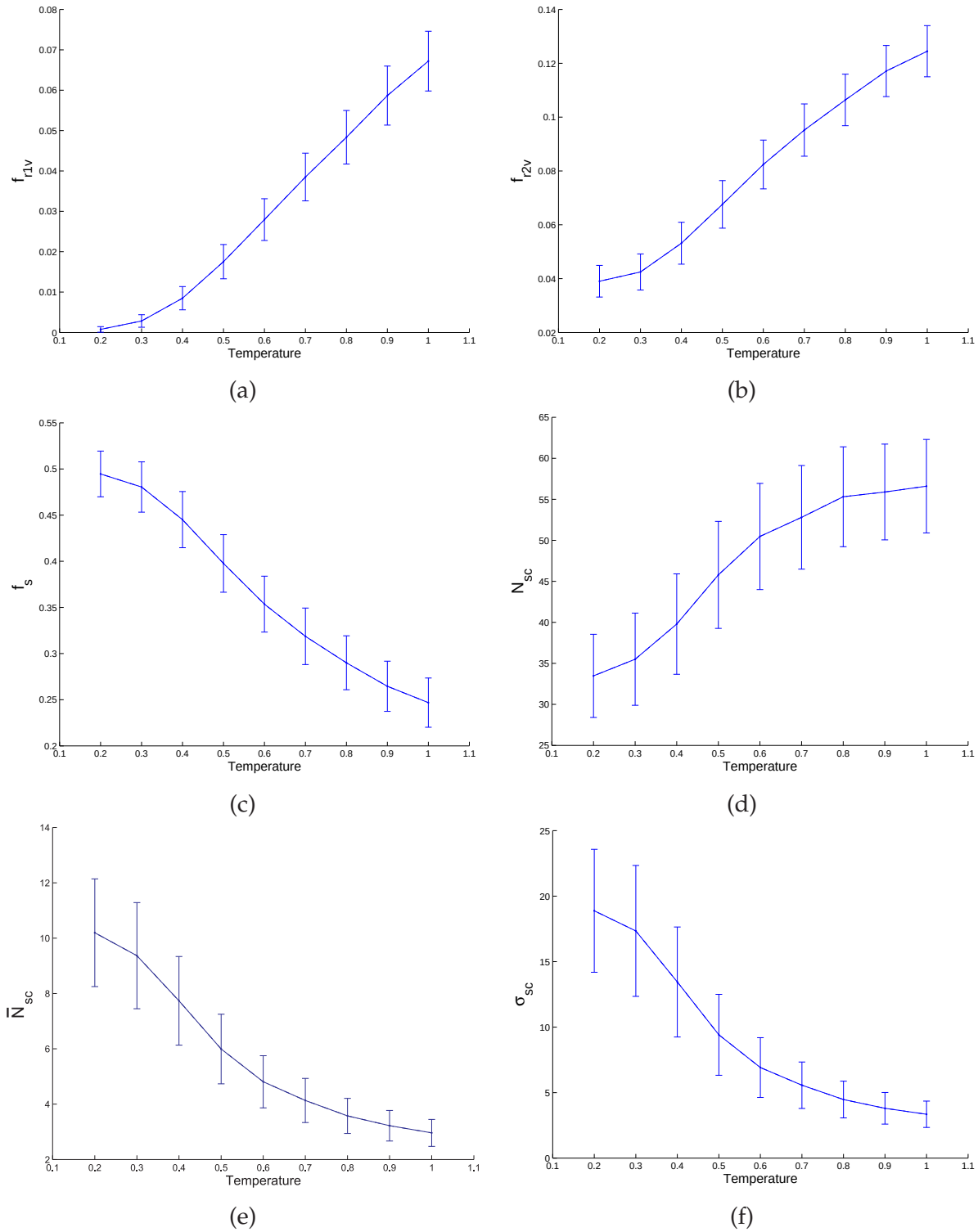


**Figure 3.8** Plot of the disorder parameters verses temperature.

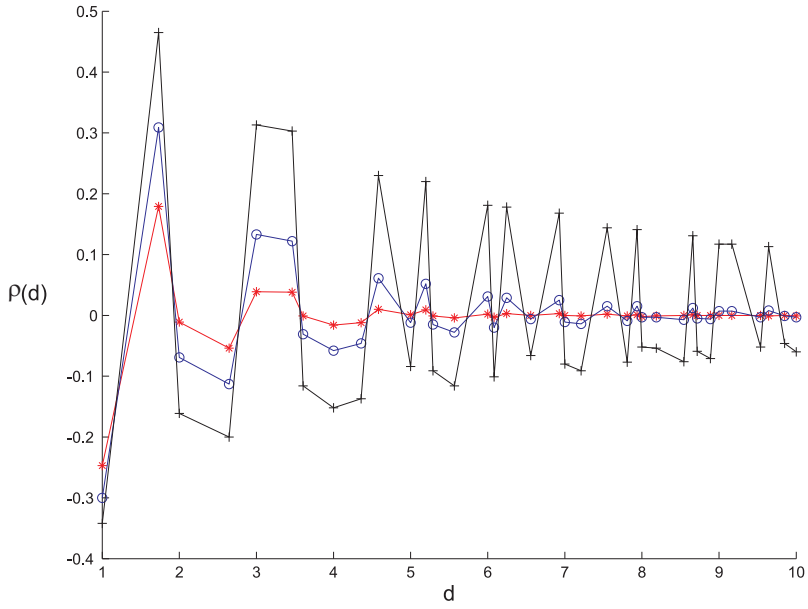


(a)

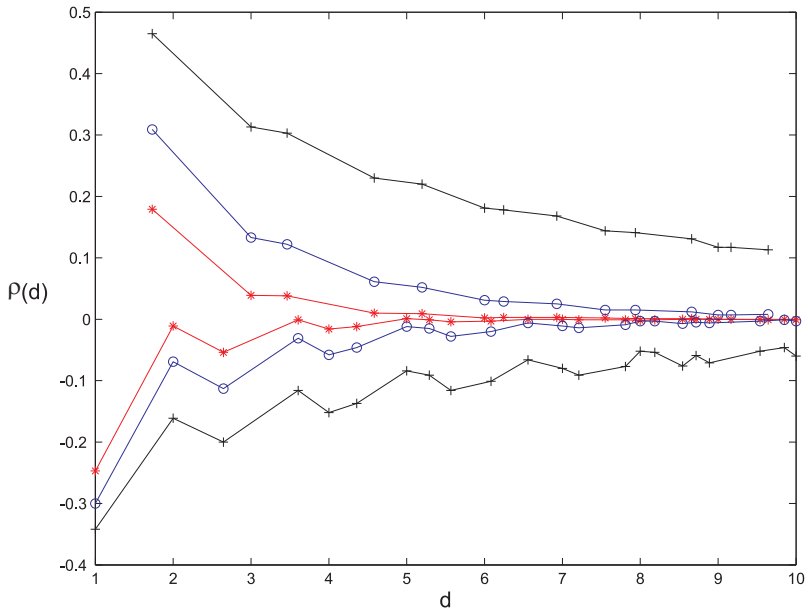


(b)

**Figure 3.9** Plot of spatial correlation against general pair separations. (a) Spatial correlation of the Monte Carlo simulated TIA at $T = 1.00$ (*), $T = 0.60$ (o) and $T = 0.20$ (+). (b) Spatial correlation separated into two curves for pair of sites either on the same sublattice (positive correlation) or on a different sublattice (negative correlation) for $T_{max} = 1.00$ (*), $T = 0.60$ (o) and $T_{min} = 0.20$ (+).

Before calculating the error as a function of temperature, the correlation coefficients from the micrograph are plotted in Fig. 3.11 and compared to the TIA at $T = 0.2, 0.6$ and $1.0$. This indicates a good match at a temperature near 0.6. A plot of the RMSE versus temperature (in steps of $\Delta T = 0.01$) is shown in Fig. 3.12. The minimum for this particular myosin

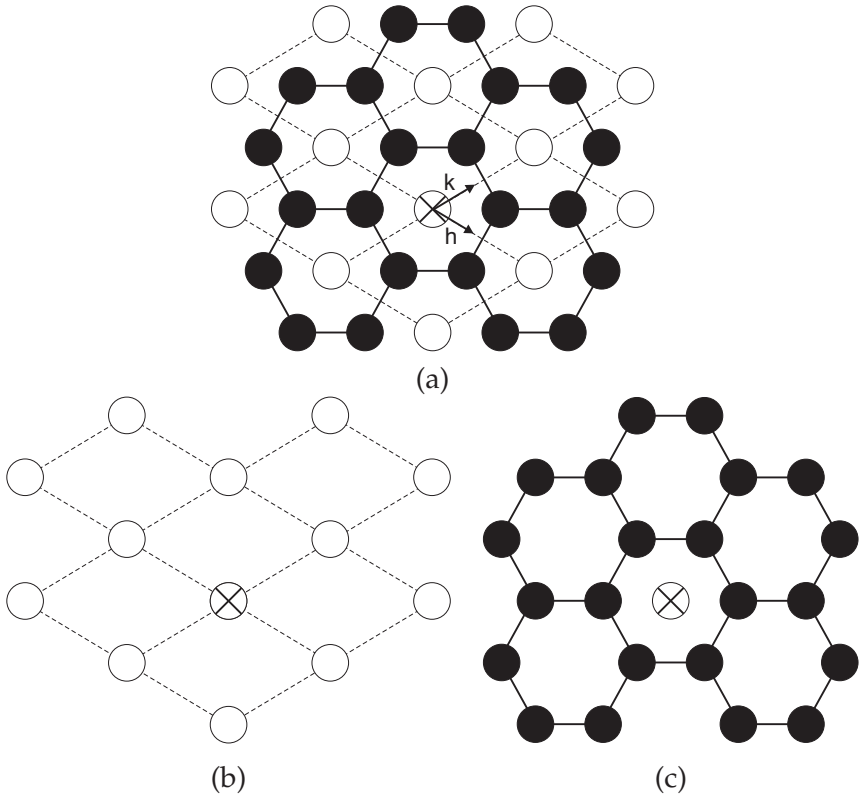


**Figure 3.10** The triangular lattice contains three sublattices. The rhombic lattice (containing the origin labelled $\otimes$) is a sublattice formed from second nearest neighbours also referred to as the superlattice. The honeycomb lattice is a combination of the other two sublattices. (a) The triangular lattice can be partitioned into (b) the rhombic lattice and (c) the honeycomb lattice.

lattice is at $T = 0.56$, so that $T_{\text{eff}} = 0.56$. The correlation function from the simulation is compared with that from the myosin lattice in Fig. 3.13 and good agreement, within the error bars, is evident.

A comparison between the parameters for the myosin lattice and the MC simulated lattice at $T_{\text{eff}} = 0.56$ is given in Table 3.1. Two sets of parameters are listed for the simulations, masked and unmasked. The sites on $\text{TIA}^{\text{mask}}$ correspond to sites on the myosin lattice with unknown orientations. $\text{TIA}_{\text{eff}}^{\text{unmask}}$ simulates the myosin lattice as if all orientations can be reliably determined. The realisations of these lattices with rule violations 1 and 2 are shown in Fig. 3.14 and Fig. 3.15, respectively. All disorder parameters of $\text{TIA}_{\text{eff}}$ match well against the myosin lattice except for the larger values of $\overline{N}_{sc}$ and $\sigma_{sc}$ for $\text{TIA}_{\text{eff}}^{\text{unmask}}$. The presence of unknown orientations in the lattice reduce the number of superlattice cells and break up the superlattice clumps, so the larger values for $\overline{N}_{sc}$ and $\sigma_{sc}$ are expected. This is evident in Fig. 3.16.

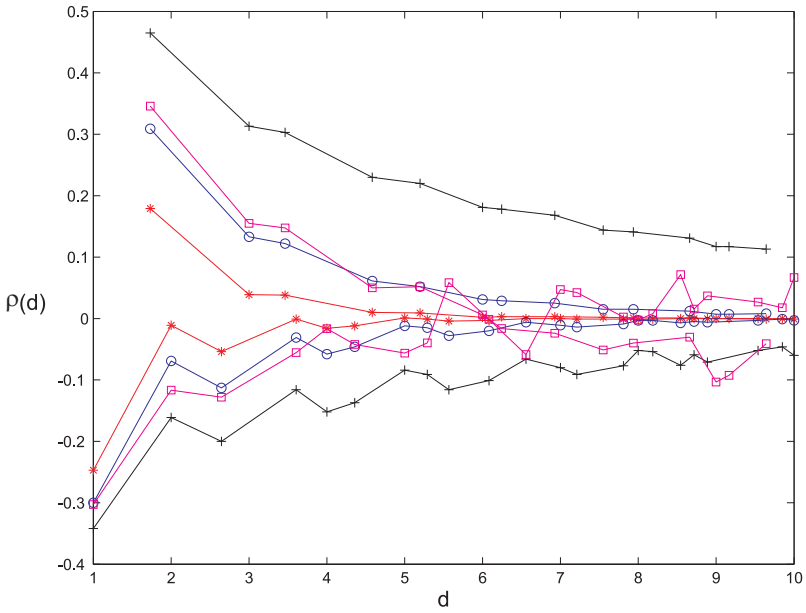


(a)

**Figure 3.11** Plot of spatial correlation against separation. (a) Spatial correlation of the Monte Carlo simulated TIA at $T_{max} = 1.00$ (*), $T = 0.60$ (o), $T_{min} = 0.20$ (+), and the myosin lattice (□).

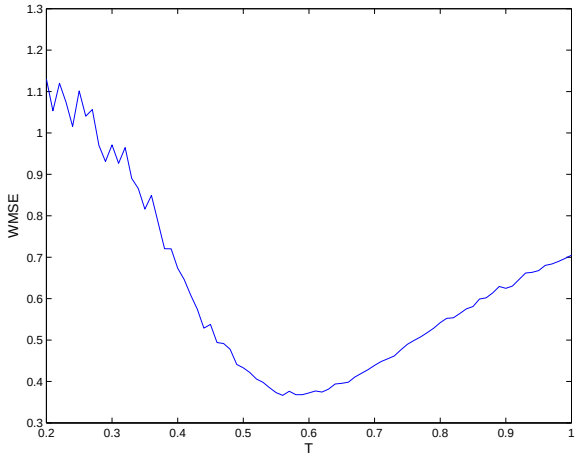


**Figure 3.12** RMSE versus temperature.

### 3.4.3 Discussion of the Results

*The results described above provide very good quantitative evidence that the structure of the disordered myosin lattice is a direct result of an antiferromagnetic type of interaction between neighbouring myosin filaments, resulting in a frustrated system.* For an equilibrium system, the difference in the interaction energy $\Delta e$ between adjacent filaments with like and unlike orientations can be estimated using Eq. (3.13). The frog sartorius muscle at room temperature

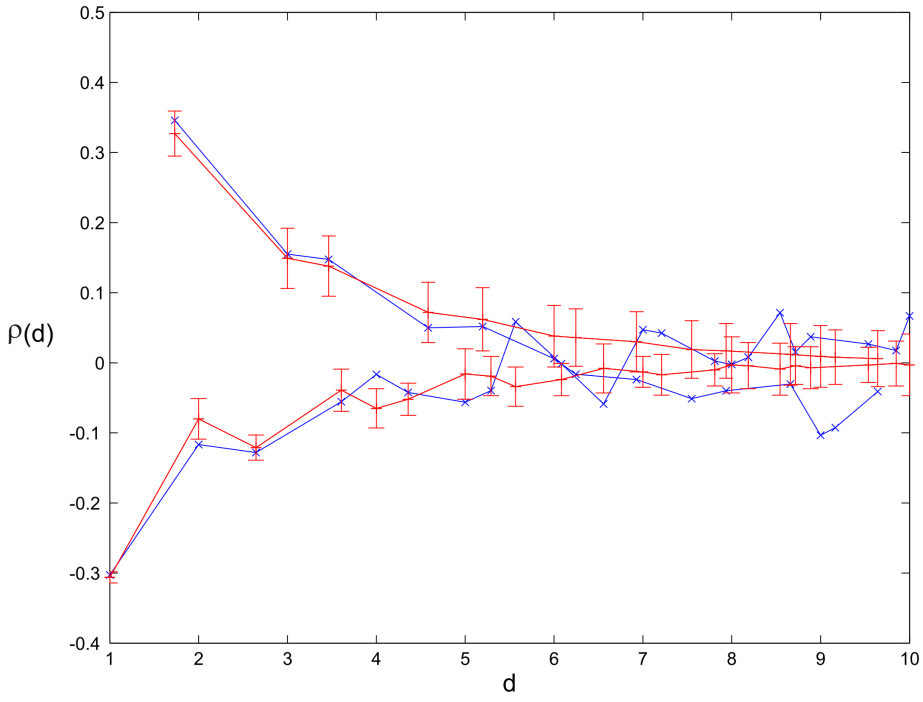


**Figure 3.13** Spatial correlation of the myosin lattice (·) and TIA at $T_{\text{eff}} = 0.56$ (x). Simulation error bars ($\pm\sigma^{sim}$) are also plotted.

$T' = 300K$ with $T_{\text{eff}} = 0.56$ implies that $\Delta e = 4.5kJ/mol$ for two adjacent myosin filaments. This value is close to the stabilization energies contributed by hydrogen bonds and other weak protein-protein interactions. The myosin filament at the M-band is made up of six bundles, each bundle containing parallel myosin molecules [LS80], with three bundles pointing up and three pointing down as shown in Fig. 3.17. A consideration of the symmetry within the filament (Fig. 3.17) shows that the preferred M-bridge interactions must be between parallel, rather than antiparallel, myosin molecules (up to up and down to down (Fig. 3.17)). Thus one may conclude that the energy gain per M-bridge interaction (probably mediated primarily by the protein component myomesin (Fig. 3.18) between parallel, rather than antiparallel, myosin molecules is about $4.5kJ/mol$. This value is comparable to those known to be sufficient to disrupt protein-protein binding [DUdVW00]. The resulting configurations of the myosin heads approaching the actin filaments (Fig. 3.19) are believed to generate more tension in the contracting muscle [LSF96].

## 3.5 Analytical Approximations to the Spatial Correlation Function

As described in Section 1.2.4, various analytical approximations have been derived for the correlation function of the TIA. Some insight into the ordering of frustrated systems can

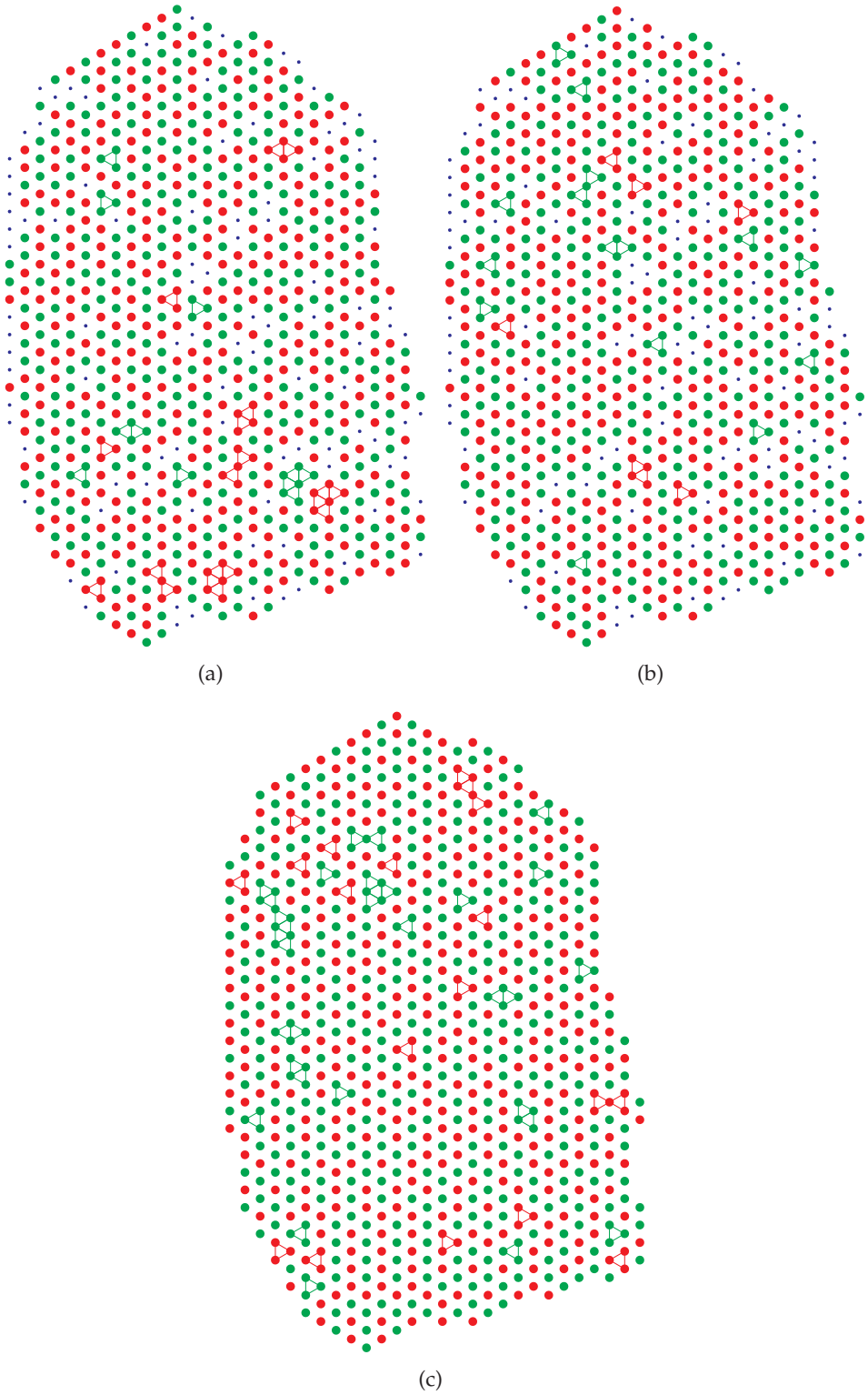


**Figure 3.14** "No-three-alike" rule 1 violations (Fig. 1.10) are shown for (a) the myosin lattice, (b) the $\mathrm{TIA}_{\mathrm{eff}}^{\mathrm{mask}}$ and (c) the $\mathrm{TIA}_{\mathrm{eff}}^{\mathrm{unmask}}$. Two possible orientations at a site are represented by light and dark circles. Unknown and masked sites are represented by dots.

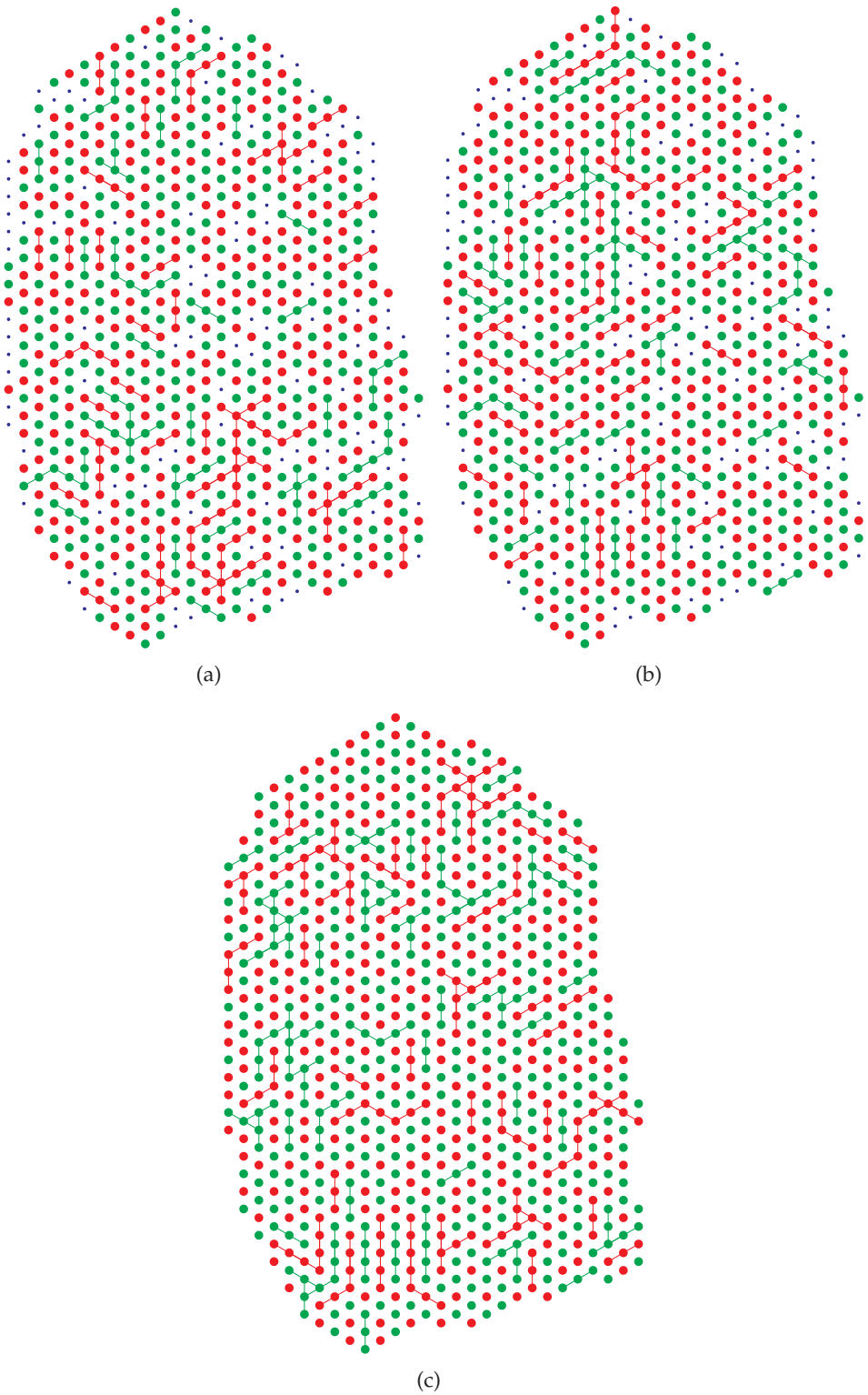


**Figure 3.15** "No-three-alike" rule 2 violations (Fig. 1.10) are shown for (a) the myosin lattice, (b) the $\mathrm{TIA}_{\mathrm{eff}}^{\mathrm{mask}}$ and (c) the $\mathrm{TIA}_{\mathrm{eff}}^{\mathrm{unmask}}$. Two possible orientations at a site are represented by light and dark circles. Unknown and masked sites are represented by dots.

**Table 3.1** Comparison of the disorder parameters between the myosin lattice $\text{TIA}_{\text{eff}}^{\text{mask}}$ and $\text{TIA}_{\text{eff}}^{\text{unmask}}$.

| | Myosin lattice | $\text{TIA}_{\text{eff}}^{\text{mask}}$ | $\text{TIA}_{\text{eff}}^{\text{unmask}}$ |
|---|---|---|---|
| $x+$ | 0.51 | 0.51 | 0.49 |
| $\sigma$ | -0.30 | -0.31 | -0.29 |
| $E^{\text{norm}}$ | -0.30 | -0.30 | -0.29 |
| $f_{rv1}$ | 0.03 | 0.02 | 0.03 |
| $f_{rv2}$ | 0.07 | 0.07 | 0.08 |
| $f_s$ | 0.36 | 0.36 | 0.34 |
| $\overline{N}_{sc}$ | 3.49 | 2.91 | 4.20 |
| $\sigma_{sc}$ | 3.52 | 3.45 | 6.73 |

be gained from these expressions. The utility of these approximations is examined here by comparison with Monte Carlo calculations.

### 3.5.1 Nature of the Superlattice

The triangular lattice has six-fold rotational symmetry and mirror symmetry through the line $h = k$ (Fig. 3.2). The correlation function must have the same symmetry so it is uniquely defined by its behaviour on the sector $h > 0$ and $k \leq h$. The correlation function has already been shown to have different behaviour depending on whether the two points are on the same or different sublattices. The distances between two sites that are on the same or different sublattices is first investigated. Placing the origin on the site of one sublattice, the coordinates of any other site on that sublattice can be written $(\sqrt{3}h, \sqrt{3}k)$ where $h$ and $k$ are integers (Fig. 3.10). Therefore, the distance $d_{hk}$ to any site on that sublattice is

$$\begin{aligned} d_{hk}^2 &= (\sqrt{3}h)^2 + (\sqrt{3}k)^2 + \sqrt{3}h\sqrt{3}k \\ &= 3(h^2 + k^2 + hk) \\ &= 3c, \end{aligned} \tag{3.20}$$

so that $d_{hk}^2$ is a multiple of 3.

Referring to Fig. 3.20 shows that the coordinates of any site on one of the other sublattices is $(\sqrt{3}h, \sqrt{3}k) \pm (1/\sqrt{3}, 1/\sqrt{3})$. The distance $d'_{hk}$ from the origin to any site on one of the

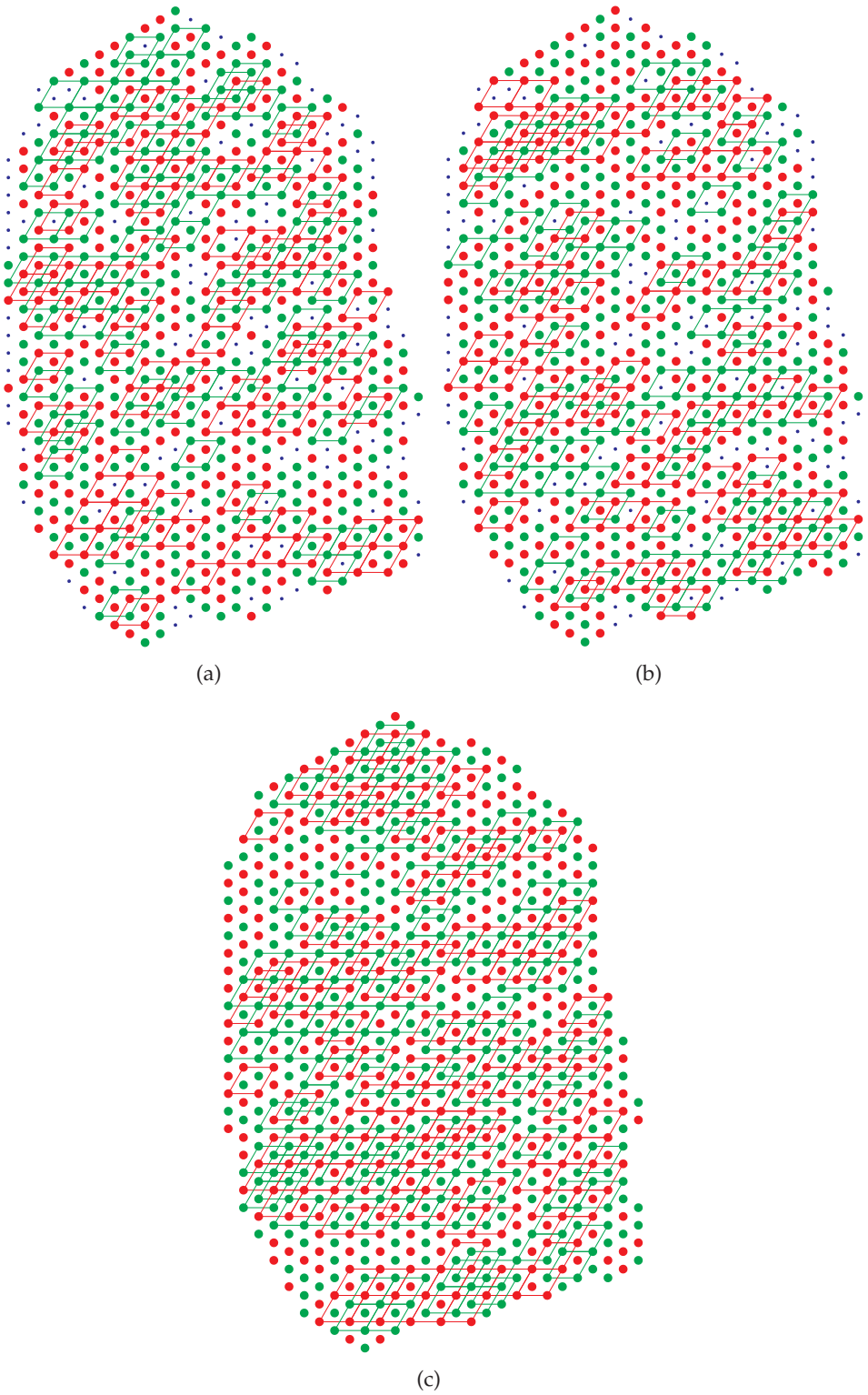


**Figure 3.16** Formation of superlattice cells on (a) the myosin lattice, (b) the $TIA_{eff}^{mask}$ and (c) the $TIA_{eff}^{unmask}$. Two possible orientations at a site are represented by light and dark circles. Unknown orientation and masked sites are represented by dots.

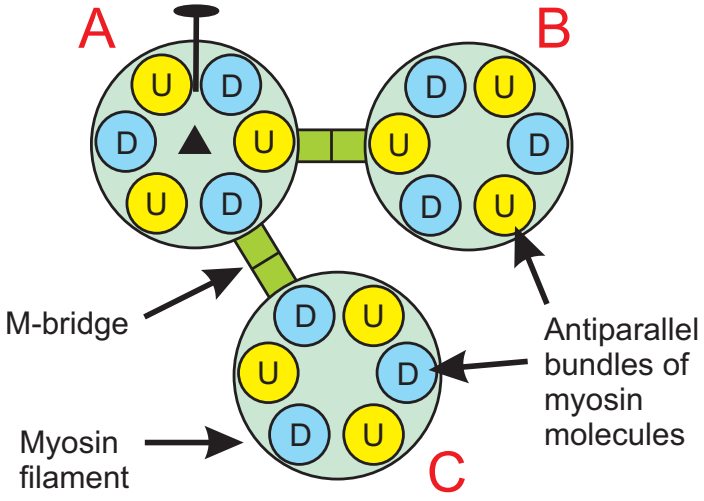


**Figure 3.17** Illustration of the interaction between three adjacent myosin filaments $(A, B, C)$, where $B$ and $C$ have the same orientation which is different to that of $A$. Each filament has '32' dihedral point group symmetry, which relates up $(U)$ and down $(D)$ bundles of parallel myosin molecules via three 2-fold axes perpendicular to the filament long axis, each 2-fold axis being related by 3-fold symmetry about the long axis. Filament pairs $A$ and $B$ and $A$ and $C$ can make the preferred M-bridge interactions (M4 bridges of myomesin [OGWF97] (Fig. 3.18) between parallel $U$ to $U$ or $D$ to $D$ myosin molecules, whereas the $B$ to $C$ interaction is energetically unfavourable.

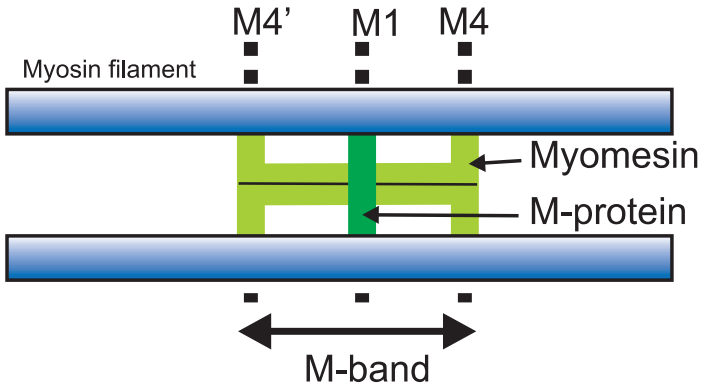


**Figure 3.18** Illustration of the three main M-bridge lines in the frog muscle M-band (M4', M1 and M4, where M4 is symmetry related to M4' [SS77]), and the likely protein components of these bridges, namely myomesin mainly forming M4 and M4', and M-protein forming M1 [OGWF97]. Since the M1 bridge level is missing on some muscle types [PJLS94, SAKKL05], it is presumed that the interactions at M4 and M4' dominate in defining the A-band myosin filament lattice.

other sublattices is therefore

$$\begin{aligned} d_{hk}^2 &= \left(\sqrt{3}h \pm \frac{1}{\sqrt{3}}\right)^2 + \left(\sqrt{3}k \pm \frac{1}{\sqrt{3}}\right)^2 + \left(\sqrt{3}h \pm \frac{1}{\sqrt{3}}\right)\left(\sqrt{3}k \pm \frac{1}{\sqrt{3}}\right) \\ &= 3(h^2 + k^2 \pm h \pm k) + 1 \\ &= 3c + 1. \end{aligned} \tag{3.21}$$

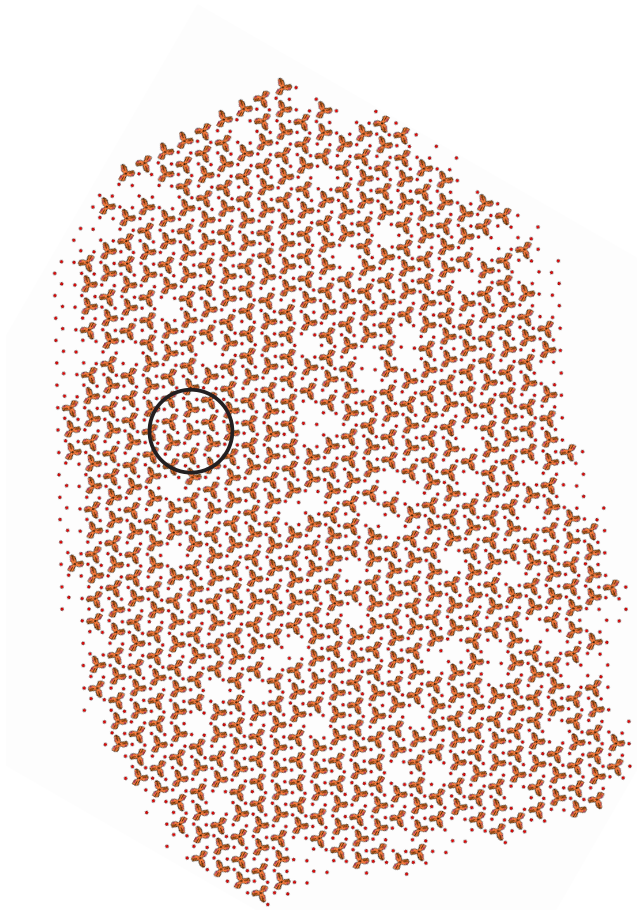

**Figure 3.19** The binary variables for TIA are replaced with up and down filaments each with three protruding myosin heads. The resulting myosin heads are evenly distributed amongst the actin filaments (encircled).

which is not a multiple of 3. To summarise:

$$\begin{aligned} d_{hk}^2 &= 3c \quad \text{on the superlattice} \\ &\neq 3c \quad \text{off the superlattice} \end{aligned} \tag{3.22}$$

Therefore, the distance between two sites uniquely specifies whether the two sites are on the same or different sublattices. However, two different pairs of sites on the same sublattice may still have the same distance between them so that the distance does not necessarily uniquely define the correlation function.

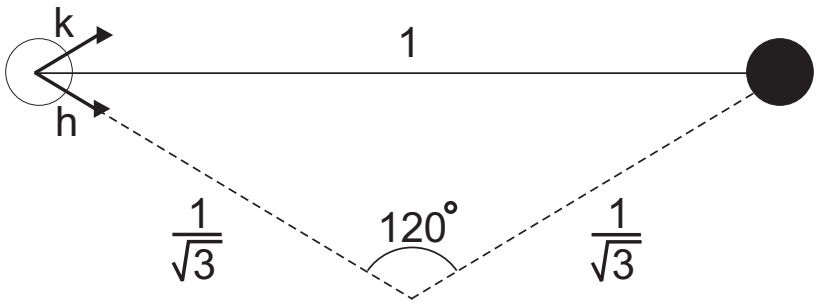


**Figure 3.20** The coordinates of any site on one of the other sublattices is given by $(\sqrt{3}h, \sqrt{3}k) \pm (1/\sqrt{3}, 1/\sqrt{3})$.

## 3.5.2 Ground State Behaviour

### 3.5.2.1 On-Axis

The correlation function is largest at $T = 0$ (ground state) and decreases as the temperature increases as thermal fluctuations become more dominant. Recall from Section 1.2.4 that the asymptotic zero-temperature behaviour of the pair correlation along a lattice axis is of the form [Ste70]

$$\rho(d) \sim \epsilon_0 d^{-1/2} \cos\left(2\pi \frac{d}{3}\right), \tag{3.23}$$

where $d = |\mathbf{d}|$ is the spin separation and $\epsilon_0 = 2^{1/2}(E_0^T)^2 \approx 0.632$, where $E_0^T$ is the decay amplitude of the pair correlation at the Curie point (critical point) of an isotropic ferromagnetic triangular lattice. The oscillatory term has period 3 and is +1 when the pairs are on the same sublattice (multiples of 3) and -1/2 when on different sublattices. Monte Carlo simulation at $T = 0$ suffers from critical slowing since the acceptance ratio is zero for $E_\nu > E_\mu$ which has the effect of freezing the lattice configuration in a small subset of the ground states. Instead, the correlation function from a Monte Carlo simulation near the ground state ($T = 0.01$) is compared to Eq. (3.23) in Fig. 3.21. Agreement is seen to be fairly good although not exact.

### 3.5.2.2 Off-Axis

No rigorous results are available for the behaviour of the correlation function of the TIA when the two sites are not on-axis. However, Nienhuis *et al* (1984) used spin-wave operators to formulate the critical behaviour of Triangular Ising Solid-on-solid (TISOS) models and the results suggest that Eq. (3.23) describes the $T = 0$ correlation function off-axis where $d$ is the distance between the sites and the cosine term is replaced by 1 if the sites are on the same sublattice and by $-1/2$ if they are on different sublattices. On this basis then the correlation function is rotationally invariant, i.e. depends only on the distance $d$ between sites and the sublattice. The correlation coefficient is calculated by MC for three

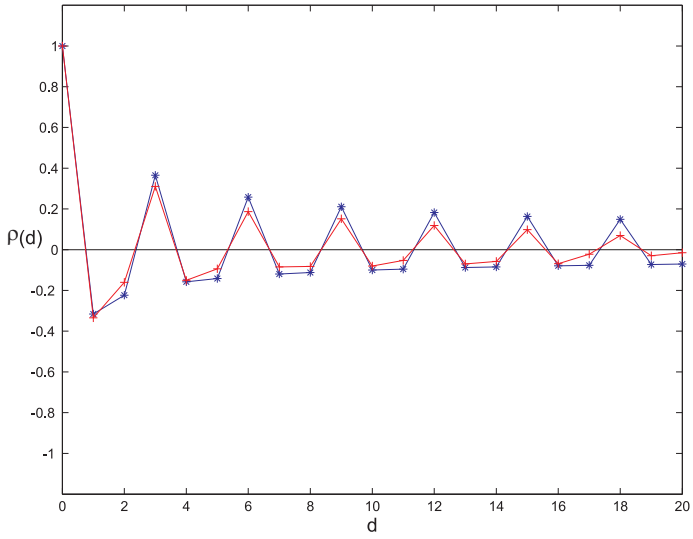


**Figure 3.21** Plot of the asymptotic correlation behaviour along an axis at $T = 0$ (*) and Monte Carlo correlation function near the ground state $T = 0.01$.

different off-axis lattice directions at $T = 0.01$ and compared those calculated by Eq. (3.23) in Fig. 3.22. Good agreement is evident, supporting both approximate rotational invariance and reasonable accuracy of Eq. (3.23) for off-axis separations.

## 3.5.3 $T > 0$ Behaviour

### 3.5.3.1 On-Axis

Stephenson (1970) has derived the approximate asymptotic behavior of the on-axis pair correlation for $T > 0$ as an asymptotic expansion in $d$. The two leading terms are given in Section 1.2.4 are repeated here for convenience

$$\begin{aligned}\rho(d) \sim \left(\frac{\pi}{2}\sin\theta\right)^{-\frac{1}{2}}\nu^d \cdot d^{-\frac{1}{2}}\Big\{ &\cos\left(d\theta + \frac{\theta}{2} - \frac{\pi}{4} - \phi\right) \\ &-(4d)^{-1}\Big[\frac{3}{2} + (2\sin\theta)^{-1}\cos\left(d\theta + \frac{3\theta}{2} + \frac{\pi}{4} - \phi\right) \\ &+\nu^2(1-\nu^2)^{-1}\cos\left(d\theta + \frac{\theta}{2} - \frac{\pi}{4} - \phi\right) \\ &+\nu^2\varrho^2\cos\left(k\theta + \frac{5\theta}{2} - \frac{\pi}{4} - 3\phi\right)\Big]\Big\}. \end{aligned} \tag{3.24}$$

where

$$\nu = \tanh(\beta J). \tag{3.25}$$

The real angle $\theta$ is defined by

$$\cos\theta = (1 + e^{4\beta J})/2, \quad 0 < \theta \leq \pi/3, \tag{3.26}$$

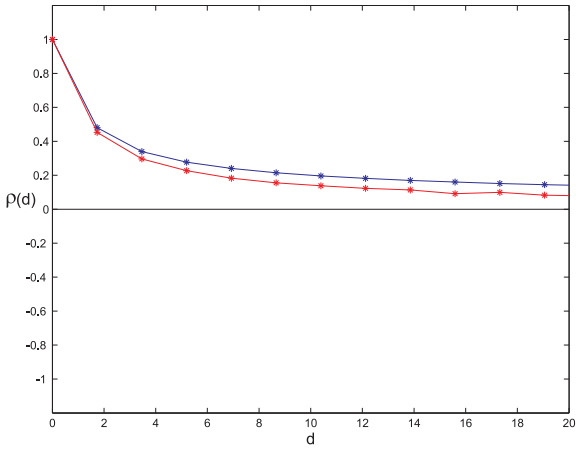


(a)

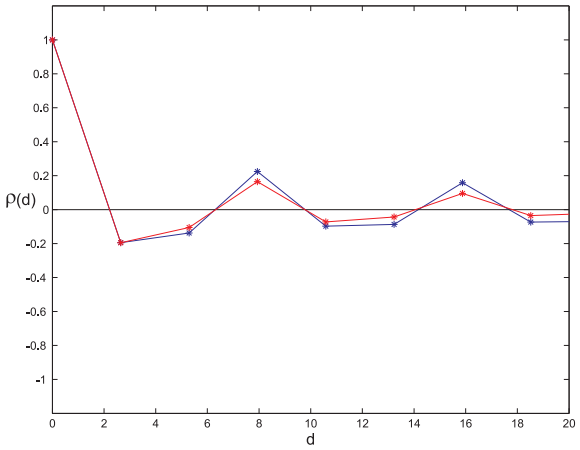


(b)

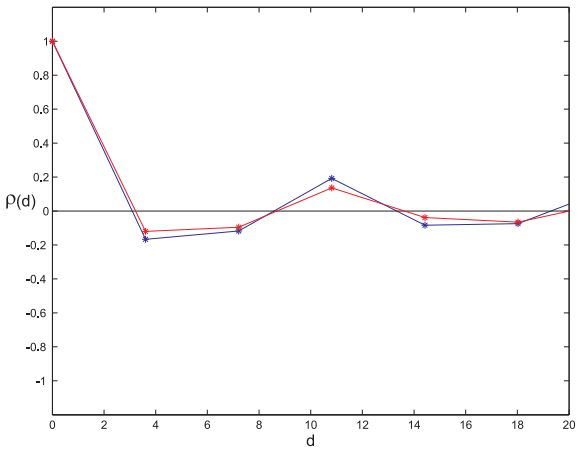


(c)

**Figure 3.22** Plot of the asymptotic correlation behaviour and correlation function obtained from Monte Carlo at $T = 0.01$ along (a) (1,1) (b) (2,1) and (c) (3,1) axis.

$$\varrho = (1 - 2\nu^2 \cos 2\theta + \nu^4)^{-1/4} \tag{3.27}$$

and

$$\phi = -\frac{1}{2} \arg(1 - \nu^2 \cos 2\theta + i\nu^2 \sin 2\theta). \tag{3.28}$$

The first term of the correlation function given in Eq. (3.24) is compared with that calculated by Monte Carlo simulations for various temperatures in Fig. 3.23. The agreement is seen to be reasonably good for $T \geq 0.3$.

The first order term in Eq. (3.24) is

$$\rho(d) \sim \left(\frac{\pi}{2} \sin\theta\right)^{-\frac{1}{2}} \nu^d \cdot d^{-\frac{1}{2}} \cos\left(d\theta + \frac{\theta}{2} - \frac{\pi}{4} - \phi\right). \tag{3.29}$$

Since the interaction energy $J$ is negative, $-1 \geq \nu \geq 0$ so that

$$\nu^k = (-1)^k \left|\nu\right|^k, \tag{3.30}$$

and substituting Eq. (3.30) into Eq. (3.29) gives

$$\rho(d) \sim \left(\frac{\pi}{2} \sin\theta\right)^{-\frac{1}{2}} (-1)^d \left|\nu\right|^d \cdot d^{-\frac{1}{2}} \cos\left(d\theta + \frac{\theta}{2} - \frac{\pi}{4} - \phi\right). \tag{3.31}$$

At $T = 0$, $\theta = \pi/3$ and $\phi = -\pi/12$n and the oscillatory term becomes

$$\cos\left(d\theta + \frac{1}{2}\theta - \frac{1}{4}\pi - \phi\right) \simeq \cos\left(\pi\frac{d}{3}\right). \tag{3.32}$$

This approximation is used for small $T$. Noting that

$$\cos\left(2\pi\frac{d}{3}\right) = (-1)^d \cos\left(\pi\frac{d}{3}\right), \tag{3.33}$$

for all integers and using Eq. (3.31) and Eq. (3.32), the asymptotic behaviour is simplified to

$$\rho(d) \simeq \left(\frac{1}{2}\pi \sin\theta\right)^{-\frac{1}{2}} \left|\nu\right|^d \cdot d^{-\frac{1}{2}} \cos\left(2\pi\frac{d}{3}\right). \tag{3.34}$$

Eq. (3.34) will be referred to as simplified spatial correlation function. Eq. (3.34) resembles the form of Eq. (3.23) for $T = 0$, but with a different decay factor and an additional decay term, $|\nu|^d$. Both decay terms are functions of temperature. This approximation is plotted for various temperatures and compared with the first term of the asymptotic correlation function in Fig. 3.24. They are seen to be almost identical for $T < 1.0$

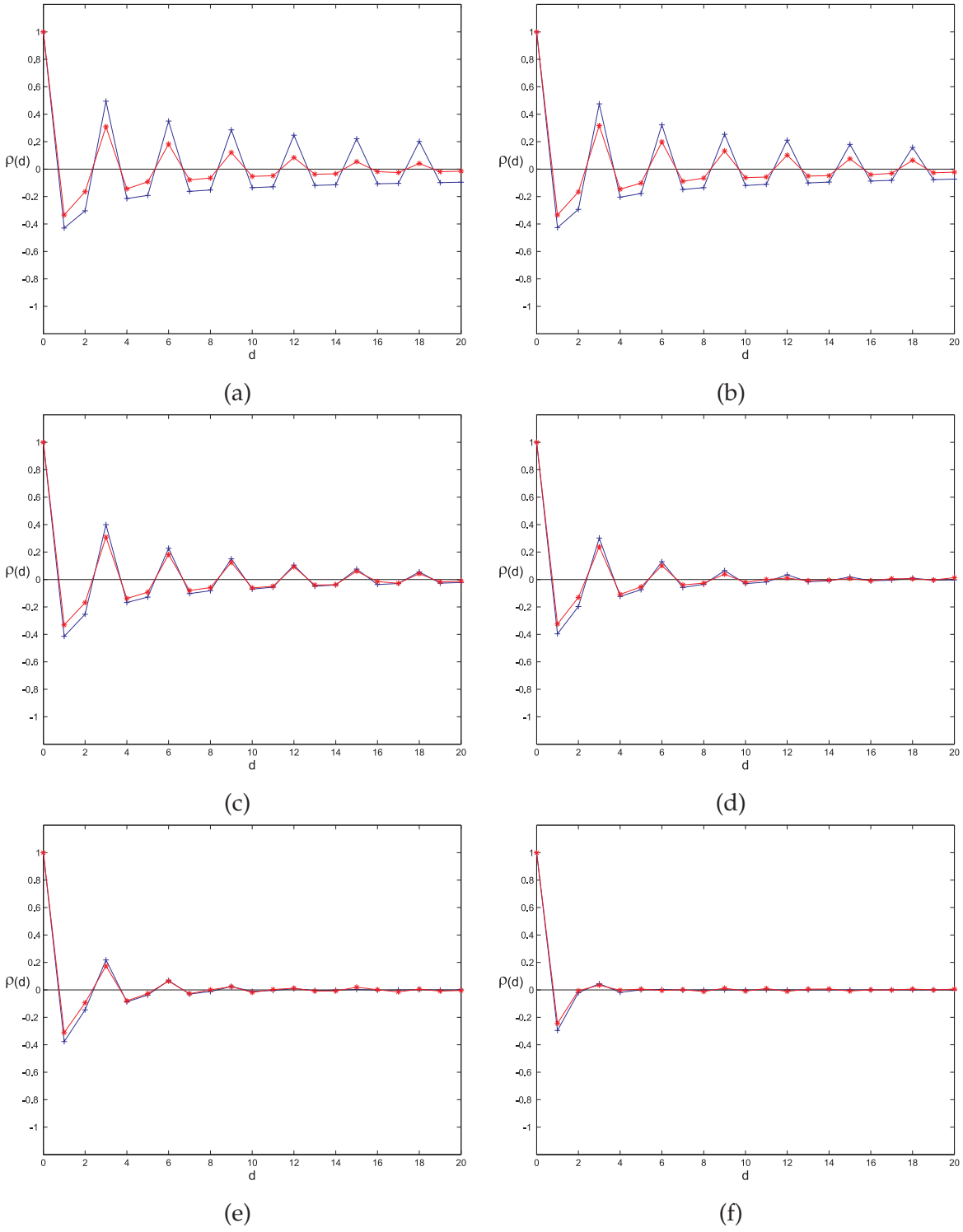


**Figure 3.23** The first term of the correlation function given in Eq. (3.24) (+) is compared with the correlation function obtained from Monte Carlo simulations (*) for various temperatures (a) $T = 0.1$, (b) $T = 0.2$, (c) $T = 0.3$, (d) $T = 0.4$, (e) $T = 0.5$, and (f) $T = 1.0$.

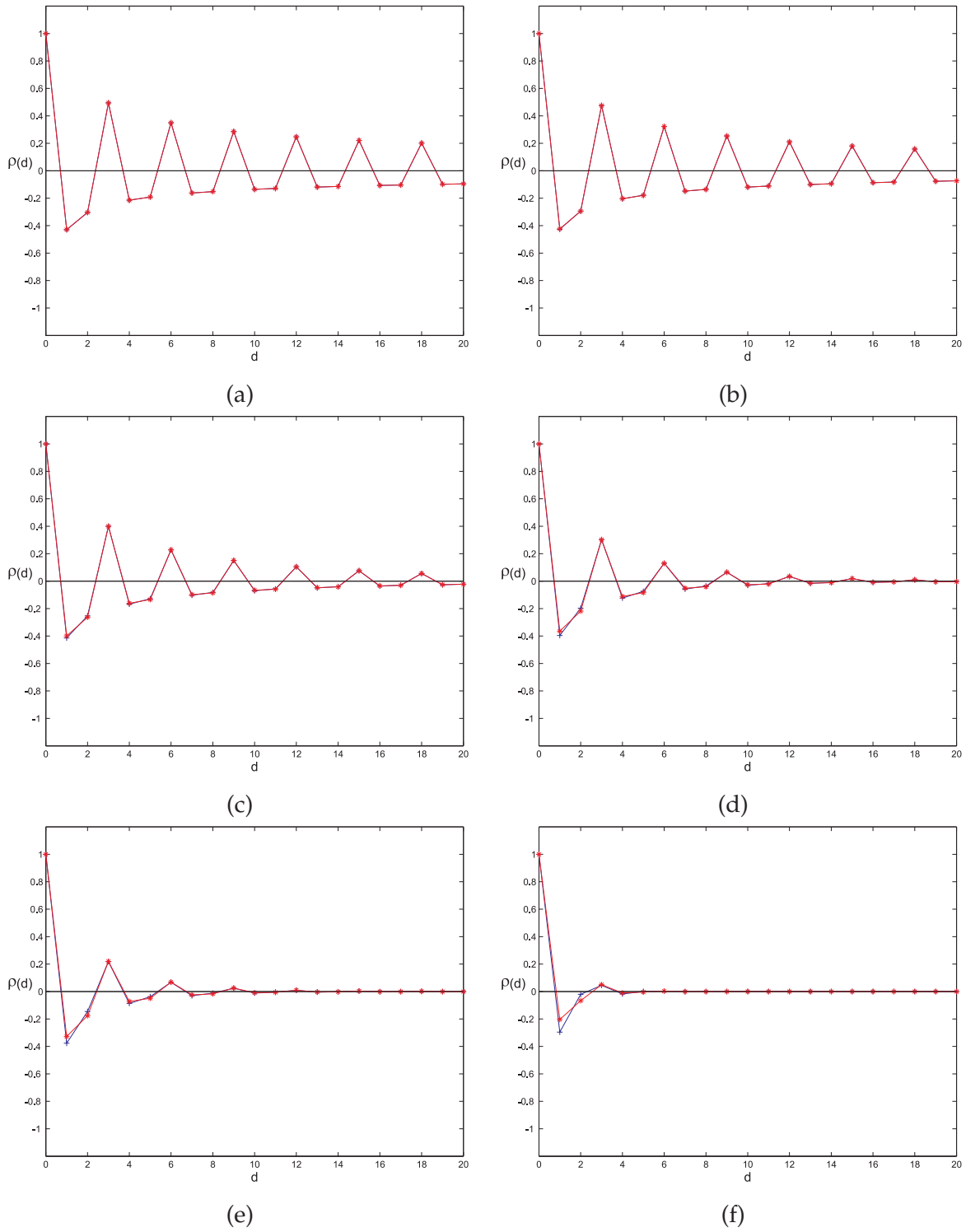


**Figure 3.24** The correlation function given in Eq. (3.29) (+) is compared with the correlation function in Eq. (3.34) (*) for various temperatures (a) $T = 0.1$, (b) $T = 0.2$, (c) $T = 0.3$, (d) $T = 0.4$, (e) $T = 0.5$, and (f) $T = 1.0$.

#### 3.5.3.2 Off-Axis

The on-axis correlation function in Eq. (3.34) is now generalised here to the off-axis case. As with the off-axis correlation function for the ground state, the off-axis pair correlation function is assumed to be rotationally invariant, i.e.

$$\rho(d) \sim \left(\frac{\pi}{2}\sin\theta\right)^{-\frac{1}{2}} |\nu|^d \, d^{-\frac{1}{2}} \cos\left(2\pi\frac{d}{3}\right). \tag{3.35}$$

Again, the oscillatory term is a function equal to 1 if the pair are on the same sublattice and -1/2 otherwise. This is compared with Monte Carlo simulations at various temperatures in Fig. 3.25.

Equation 3.35 and the Monte Carlo results match reasonably well for $T \geq 0.3$. Below this temperature, the difference between the two correlation functions are pronounced. In summary, Eq. (3.35) provides a reasonably good analytical approximation to the correlation function, both on- and off-axis, for $T \geq 0.3$.

### 3.5.4 Discussion

The effective temperature of the frog sartorius muscle is greater than 0.3 and the simplified correlation function is therefore useful for the frog myosin lattice. The correlation functions obtained from the frog muscle (Fig. 3.5), and the Monte Carlo and simplified correlation functions at $\text{TIA}_{\text{eff}} = 0.56$ are shown in Fig. 3.26. Both correlation functions from the Monte Carlo TIA and Eq. (3.35) approximates the correlation function of the myosin lattice closely for $d \leq 5$. This justifies the use of the simplified correlation function for the diffraction calculations in Chapter 5.

## 3.6 Conclusions

Compelling evidence is presented that the disorder in the frog sartorius myosin lattice is a direct result of an antiferromagnetic type of interaction between neighbouring myosin filaments resulting in a frustrated system. Significantly, identification of the disorder with the Ising model makes the large body of results on this model available for analysis of the myosin lattice and its X-ray fiber diffraction data. Of course the results presented here are for only one myofibril from frog sartorius muscle. Although compelling, they cannot be generalised to superlattice muscles in general without examining more myofibrils and more species. This is addressed in the next chapter.

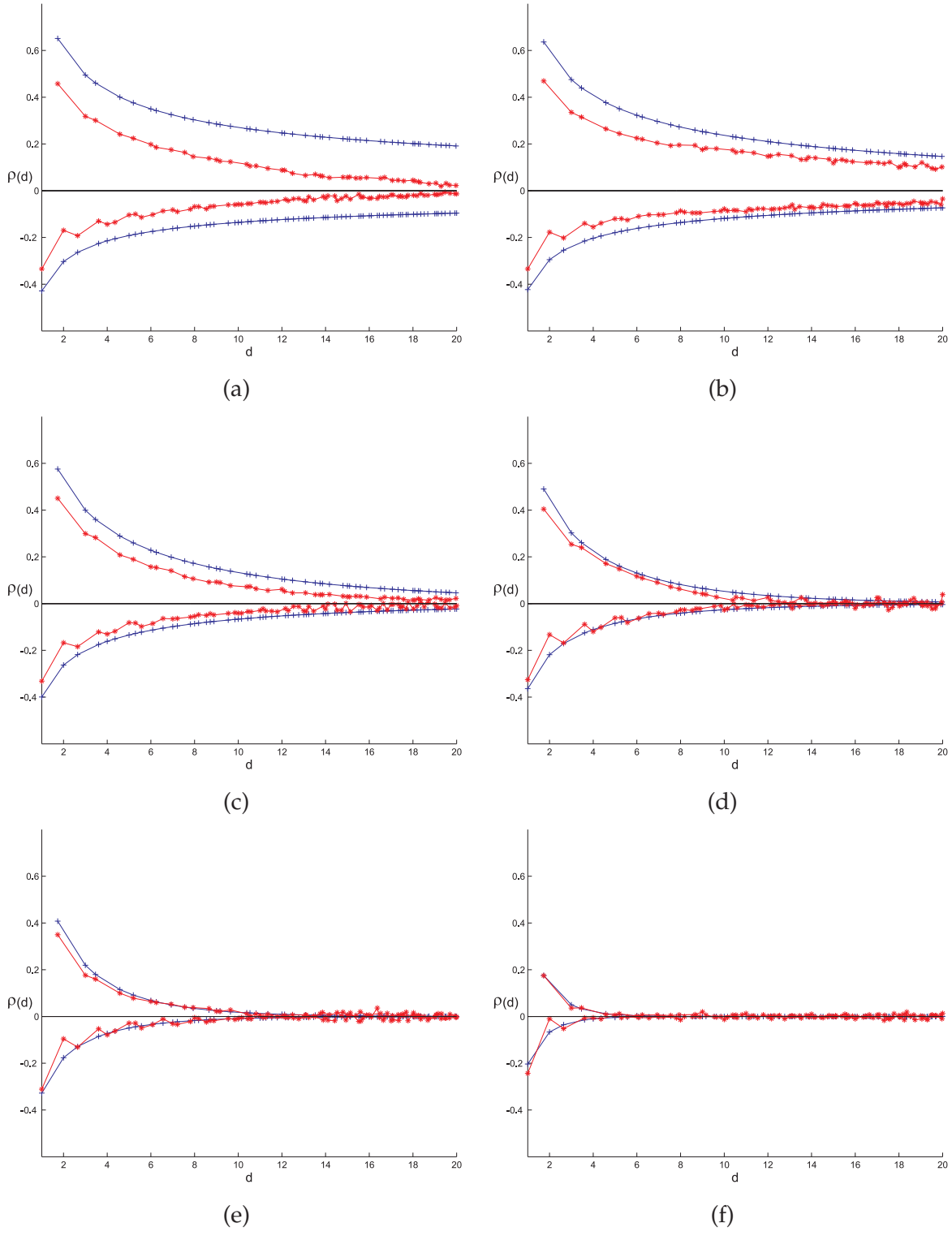


**Figure 3.25** The correlation function given in Eq. (3.35) (+) compared with the correlation function obtained from Monte Carlo simulations (*) for various temperatures (a) $T = 0.1$, (b) $T = 0.2$, (c) $T = 0.3$, (d) $T = 0.4$, (e) $T = 0.5$, and (f) $T = 1.0$.

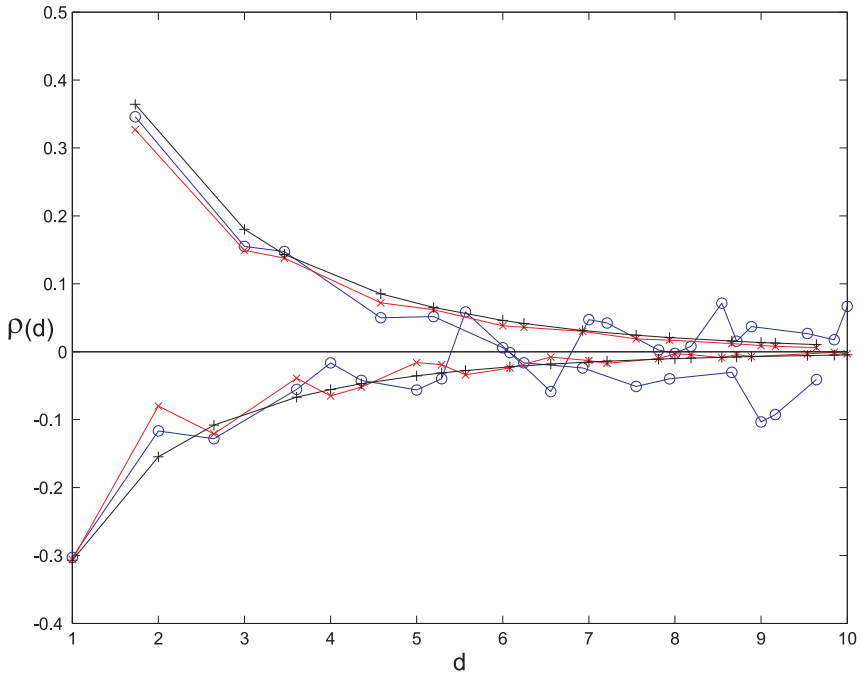


**Figure 3.26** Plots of the correlation functions of the myosin lattice (o), Monte Carlo $\mathrm{TIA}_{\mathrm{eff}}$ $(\times)$ and the simplified correlation function at $T_{\mathrm{eff}}$(+).

# Chapter 4

# Myosin Lattice Disorder in a Variety of Muscles

## 4.1 Introduction

The myosin lattice disorder affects the way in which the myosin heads interact with actin filaments. A study of the evolutionary pathway of vertebrate muscle [LSF96] has shown that even the earliest vertebrates that came into existence possess the myosin lattice disorder (superlattice). Perhaps more significantly, the study of the myosin lattice disorder is motivated by the fact that it applies to human muscle structure and function. The automated muscle micrograph analysis program and the model for the lattice disorder described in Chapters 2 and 3 allows rapid analysis of data from electron micrographs of various species to study the variability in the myosin lattice disorder.

The results presented in Chapter 3 show that the Ising model provides a good model of the myosin lattice disorder in a single frog sartorius muscle micrograph with an effective temperature of 0.56. However, this is a single myofibril. *To verify this model in general, it is necessary to apply it to a number of micrographs from different species, and if a good fit is obtained, to determine their effective temperatures*. A compilation of data extracted from analysing a number of micrographs and modeling of the disorder using Monte Carlo simulations of the TIA is presented in this chapter. In Section 4.2, the micrographs used in the survey are shown. In Section 4.3, the parameters used to summarise the results are listed. Results for a simple lattice muscle are presented in Section 4.4. Results for a variety of superlattice micrographs are presented in Section 4.5 that include myofibrils within a single fiber, different fibers for a single species, and different species. In addition to the parameters, histograms of filament orientations, superlattice cell distributions, and plots of the correlation function

are presented. The results are summarised and discussed in Section 4.6.

## 4.2 Micrographs Used

The myosin lattice disorder of five different species are presented in this chapter namely, mudskipper, shark, Polypterus, frog and turtle. These species are chosen to give a broad representation of the vertebrate family (Fig. **??**) which includes the cartilaginous fish (Chondrichthyes), the ray-finned fish (Actinopterygii) and the amphibious tetrapods. It is noted that the shark white muscle is classified as having a superlattice structure while the shark red muscle has simple lattice structure [LSF96]. The micrographs were kindly provided by Dr. Pradeep K. Luther, National Heart and Lung Institute, Imperial College of Science and Technology, London. The original images can be found in Appendix B.

A total of 23 myofibrils were analysed using the methods described in Chapter 2 to determine the filament orientations and the methods of Chapter 3 to fit the Ising model and determine the effective temperature. Five regions were analysed from the mudskipper (simple lattice) micrograph (Fig. 4.1). The most abundant source of myofibril images were from frog muscles and the quality of these micrographs was higher, and 13 myofibrils from 3 micrographs shown in Figs. 4.2-4.4 were analysed. The remaining 5 myofibrils were from shark, turtle and polypterus muscles as shown in Fig. 4.5.

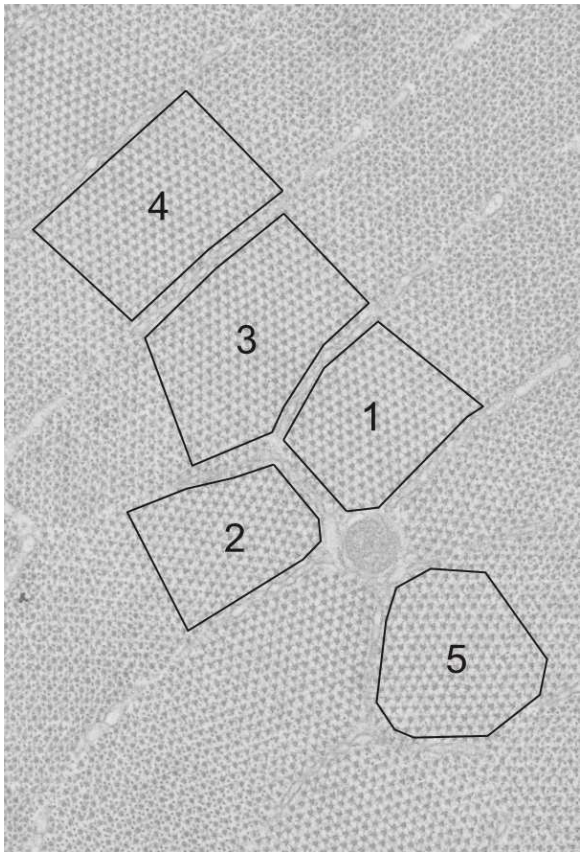


**Figure 4.1** Electron micrograph of a mudskipper muscles. The myofibrils analysed are outlined and labelled.


**Figure 4.2** First electron micrograph of a frog sartorius muscles. The myofibrils analysed are outlined and labelled.

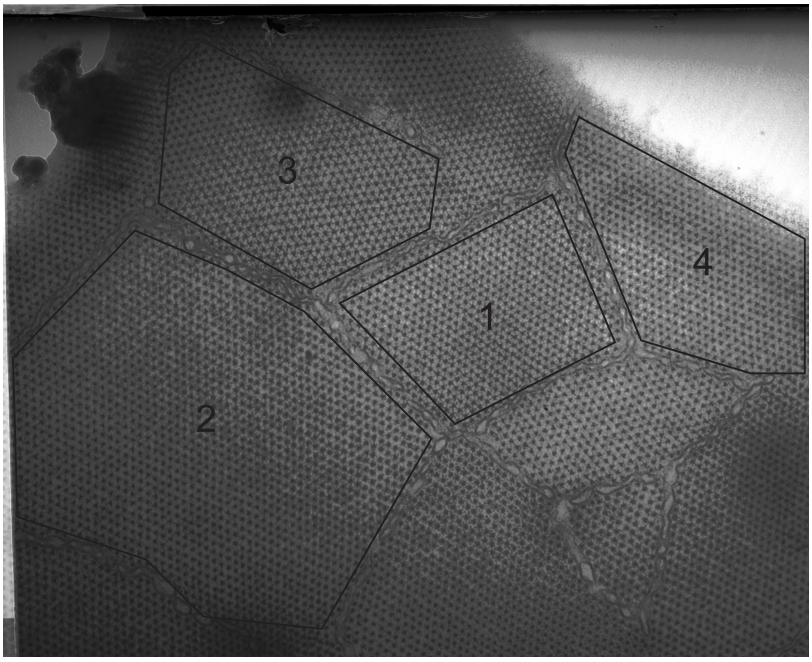


**Figure 4.3** Second electron micrograph of a frog sartorius muscles. The myofibrils analysed are outlined and labelled.

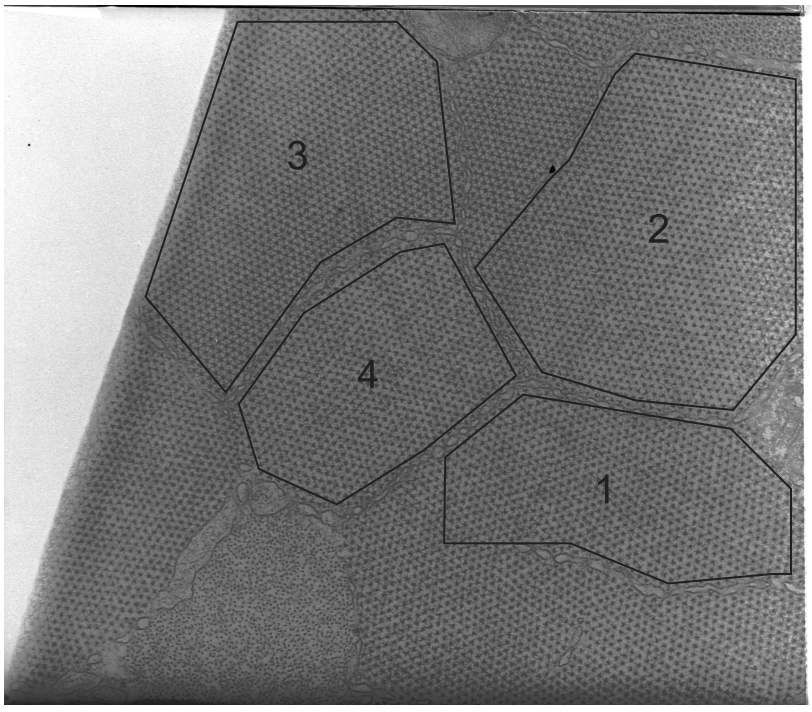


**Figure 4.4** Third electron micrograph of a frog sartorius muscles. The myofibrils analysed are outlined and labelled.

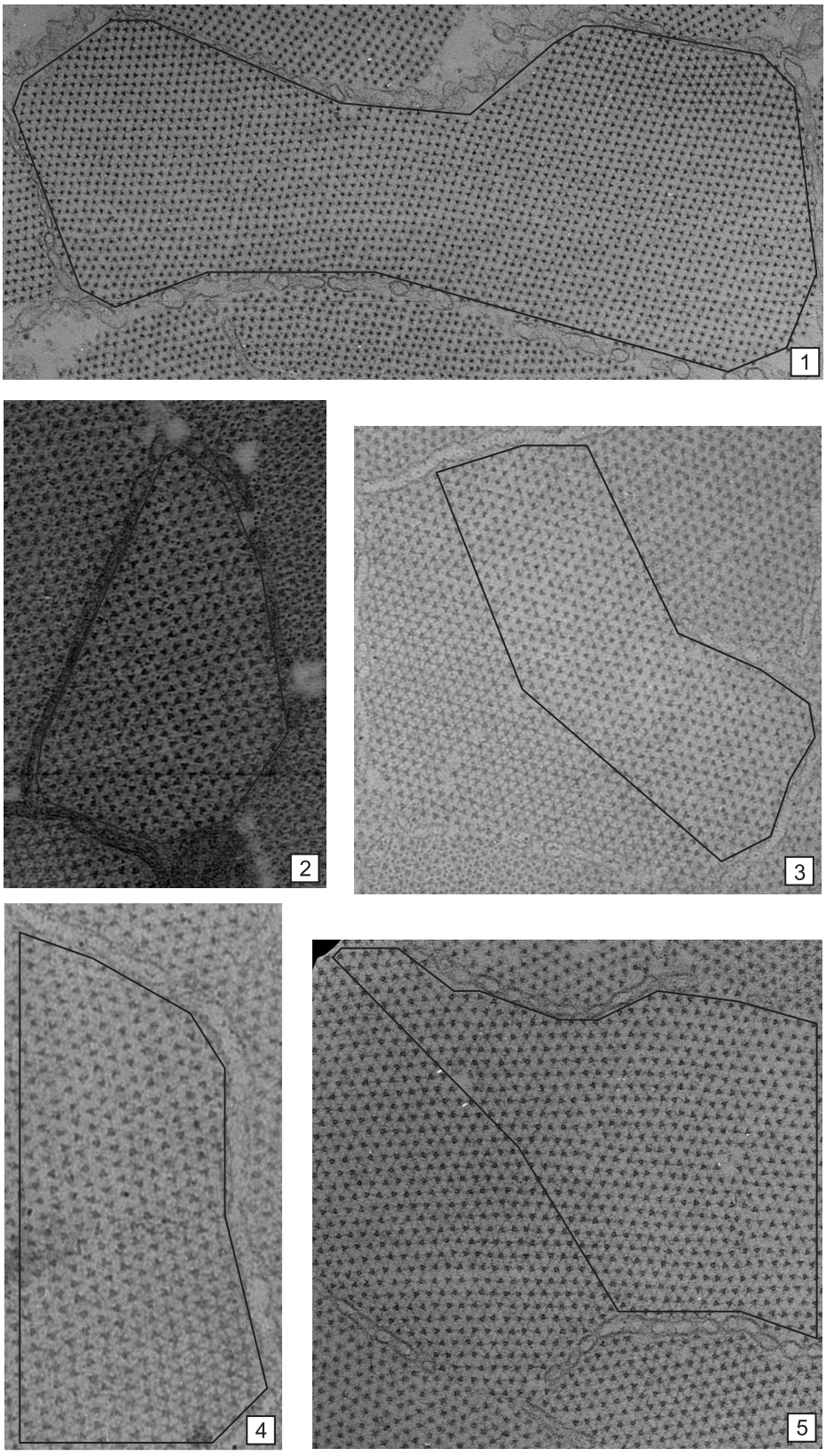


**Figure 4.5** Electron micrographs of vertebrate muscles. The myofibrils (or parts thereof) analysed are outline for 1) the shark myotomal muscle, 2) the turtle leg muscle, and 3-5) the polypterus white muscle.

## 4.3 Summary of Parameters

The results are presented as 13 parameters as well as various plots and figures. These parameters are all described in Chapters 2 and 3 but are summarised here for convenience. These parameters are divided into three categories. The first 7 parameters $(N - p_{up})$ describe characteristics of the micrographs and their analysis. The next 4 parameters $(f_{rv1} - \sigma)$ describe the disorder parameters of the lattice. The remaining 2 parameters ($RMSE_{min}$ and $T_{\text{eff}}$) describe the fit of the correlation function of the TIA and the degree of disorder.

**Table 4.1** Myosin lattice disorder parameters.

| | |
|---|---|
| $N$ | Total number of filaments. |
| $\overline{r}$ | Mean correlation coefficient for the best fit triangular templates to the myosin filaments. |
| $f_u$ | Fraction of unknown filament orientations. The correlation coefficient threshold is set to 0.75 for all analyses. |
| $\triangle\mu$ $(^\circ)$ | Angular separation between the means of the up and down orientations. |
| $\sigma_{up}$ $(^\circ)$ | Standard deviation of rotations of up filaments. |
| $\sigma_{down}$ $(^\circ)$ | Standard deviation of rotations of down filaments. |
| $p_{up}$ | Fraction of filaments classified as up. |
| $f_{rv1}$ | Frequency of violation of superlattice rule 1. |
| $f_{rv2}$ | Frequency of violation of superlattice rule 2. |
| $f_s$ | Fractional superlattice content. |
| $\sigma$ $(= \rho_{01})$ | Bond order or nearest neighbour correlation coefficient. |
| $RMSE_{min}$ | Minimum root mean square error over temperature between the simulated and measured spatial correlations out to distance of 10 lattice spacings. |
| $T_{\text{eff}}$ | Effective temperature of the myosin lattice. |

## 4.4 Mudskipper Muscle

Regions of a mudskipper muscle micrograph (Fig. 4.1) were analysed using the method described in Chapter 2. Inspection of the micrograph shows that it is not accurately cut across the bare region with evidence of actin filaments. Five small sections of the myofibrils that include only the bare region were carefully selected and analysed. The image is fairly noisy, the myosin profiles are not ideally triangular and the proportion of unknown filament orientations is quite high except for one region (Table 4.2). Histograms of the orientations are shown in Fig. 4.6. It is evident that in regions 1 and 2, there is only a single orientation whereas in regions 3 to 5, there appear to be two orientation populations approximately $30^\circ$ apart. Hence a single Gaussian model and mixture models were fitted as shown in Fig. 4.6. The fit to the histograms is reasonably good and the derived standard

deviations and difference in orientations are shown in the table. The orientations in region 4 are shown in Fig. 4.7, and the two populations are seen to be segregated into two regions. The mudskipper muscle thus shows a simple lattice although dislocations in the orientations may be present.

**Table 4.2** Myosin lattice disorder parameters for the mudskipper muscle.

| | Region 1 | Region 2 | Region 3 | Region 4 | Region 5 |
|---|---|---|---|---|---|
| $N$ | 196 | 171 | 281 | 264 | 199 |
| $\overline{r}$ | 0.77 | 0.76 | 0.77 | 0.77 | 0.76 |
| $f_u$ | 0.33 | 0.37 | 0.24 | 0.05 | 0.43 |
| $\sigma_{up}$ (°) | 21 | 10 | 10 | 7 | 7 |
| $\sigma_{down}$ (°) | - | - | 8 | 11 | 9 |
| $\triangle\mu$ (°) | - | - | 35 | 34 | 32 |

## 4.5 Superlattice Muscles

Results for the superlattice micrographs are presented here. Four types of data are presented for the regions analysed; 1) tables of the disorder parameters, 2) histograms and the mixture models for the filament orientation, 3) the myosin lattices showing the classified filament orientations and the superlattice, and 4) the spatial correlation plots for the myosin lattice and the TIA at the effective temperatures.

### 4.5.1 Frog

The five myofibrils shown in the micrograph shown in Fig. 4.2 were analysed and the results are summarised in Table 4.3. The last column shows the means. Histograms of the filament orientations are shown in Fig. 4.8 and the bimodal distribution is evident. The derived filament orientations and superlattices for the five myofibrils are shown in 4.9. The up and down filaments are shown as light and dark circles and undetermined filament orientations are shown as black dots. Superlattice cells in one of the three orientations are shown. The spatial correlation functions for the five myofibrils and for the Monte Carlo simulations at the effective temperature are shown in Fig. 4.10. Error bars show one standard deviation.

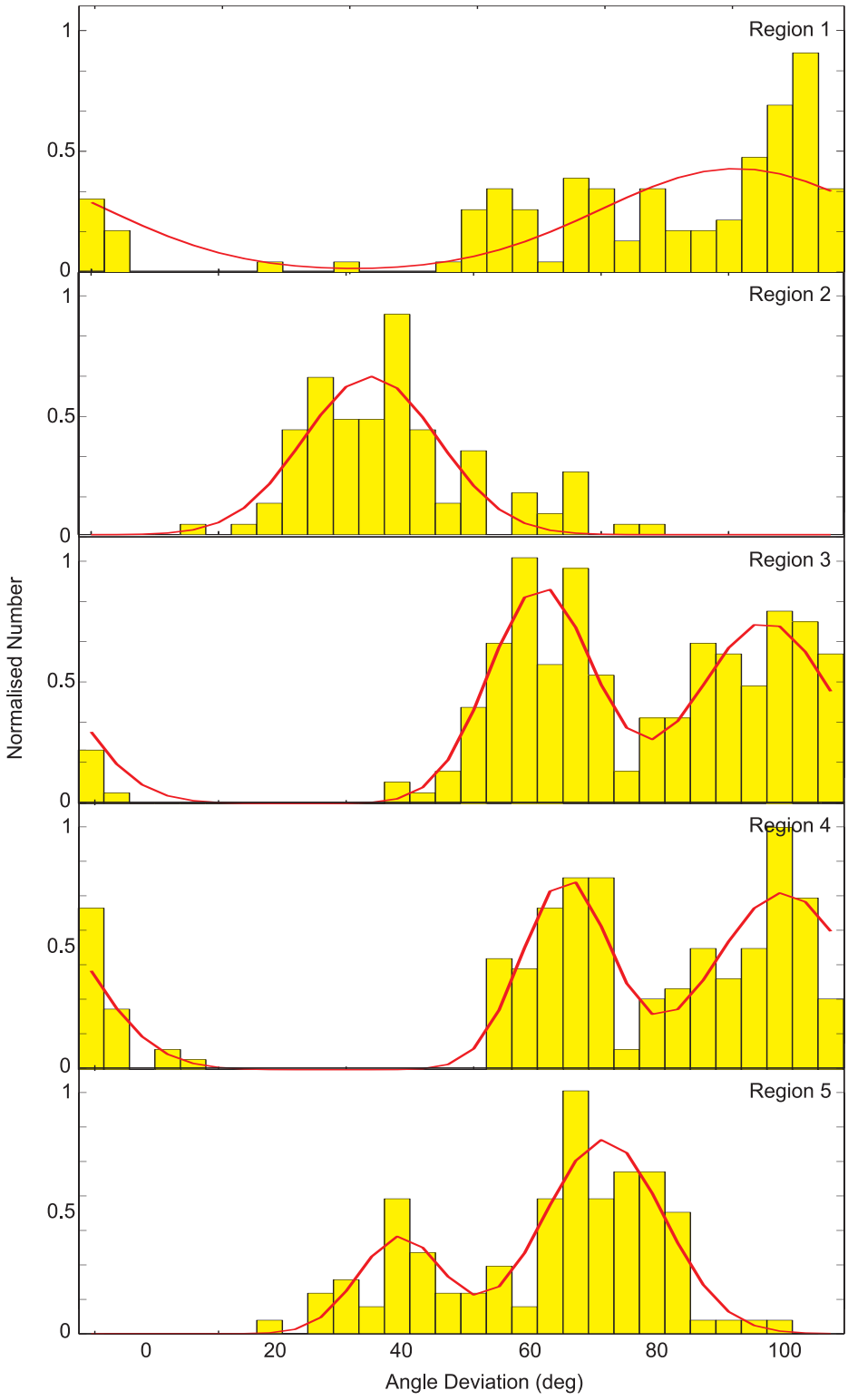


**Figure 4.6** The histogram and mixture model for the mudskipper muscle regions in Fig. 4.1.

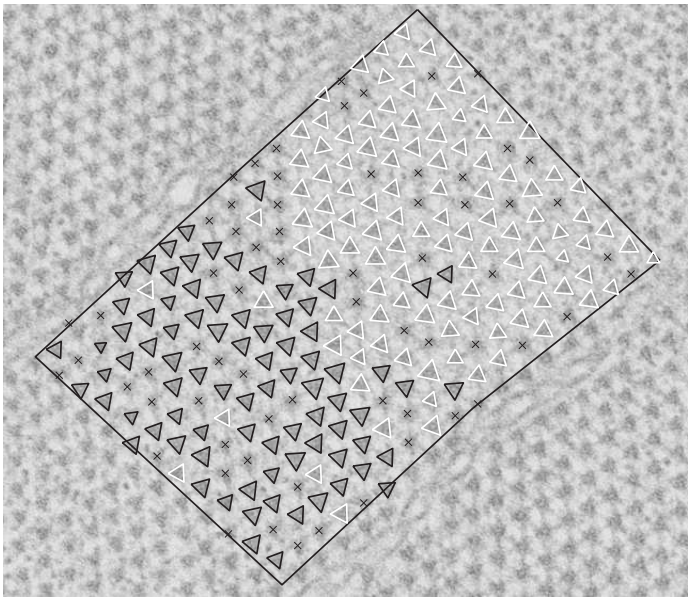

**Figure 4.7** Fitted triangles for the mudskipper region 4. Two orientation populations are shown as white and black triangles.

**Table 4.3** Myosin lattice disorder parameters of the frog sartorius muscle in Fig. 4.2.

| | Region 1 | Region 2 | Region 3 | Region 4 | Region 5 | Average |
|---|---|---|---|---|---|---|
| $N$ | 577 | 724 | 566 | 932 | 512 | 662 |
| $\overline{r}$ | 0.79 | 0.78 | 0.81 | 0.80 | 0.78 | 0.79 |
| $f_u$ | 0.17 | 0.25 | 0.12 | 0.16 | 0.27 | 0.19 |
| $\triangle\mu$ (°) | 59 | 60 | 62 | 60 | 59 | 60 |
| $\sigma_{up}$ (°) | 10 | 11 | 12 | 11 | 11 | 11 |
| $\sigma_{down}$ (°) | 10 | 11 | 10 | 11 | 11 | 11 |
| $p_{up}$ | 0.50 | 0.50 | 0.51 | 0.49 | 0.49 | 0.50 |
| $f_{rv1}$ | 0.03 | 0.03 | 0.03 | 0.04 | 0.04 | 0.03 |
| $f_{rv2}$ | 0.06 | 0.08 | 0.08 | 0.07 | 0.07 | 0.07 |
| $f_s$ | 0.45 | 0.37 | 0.38 | 0.44 | 0.34 | 0.40 |
| $\sigma$ | -0.30 | -0.30 | -0.29 | -0.29 | -0.29 | -0.29 |
| $RMSE_{min}$ | 0.20 | 0.17 | 0.16 | 0.19 | 0.27 | 0.20 |
| $T_{\text{eff}}$ | 0.48 | 0.55 | 0.47 | 0.54 | 0.61 | 0.53 |

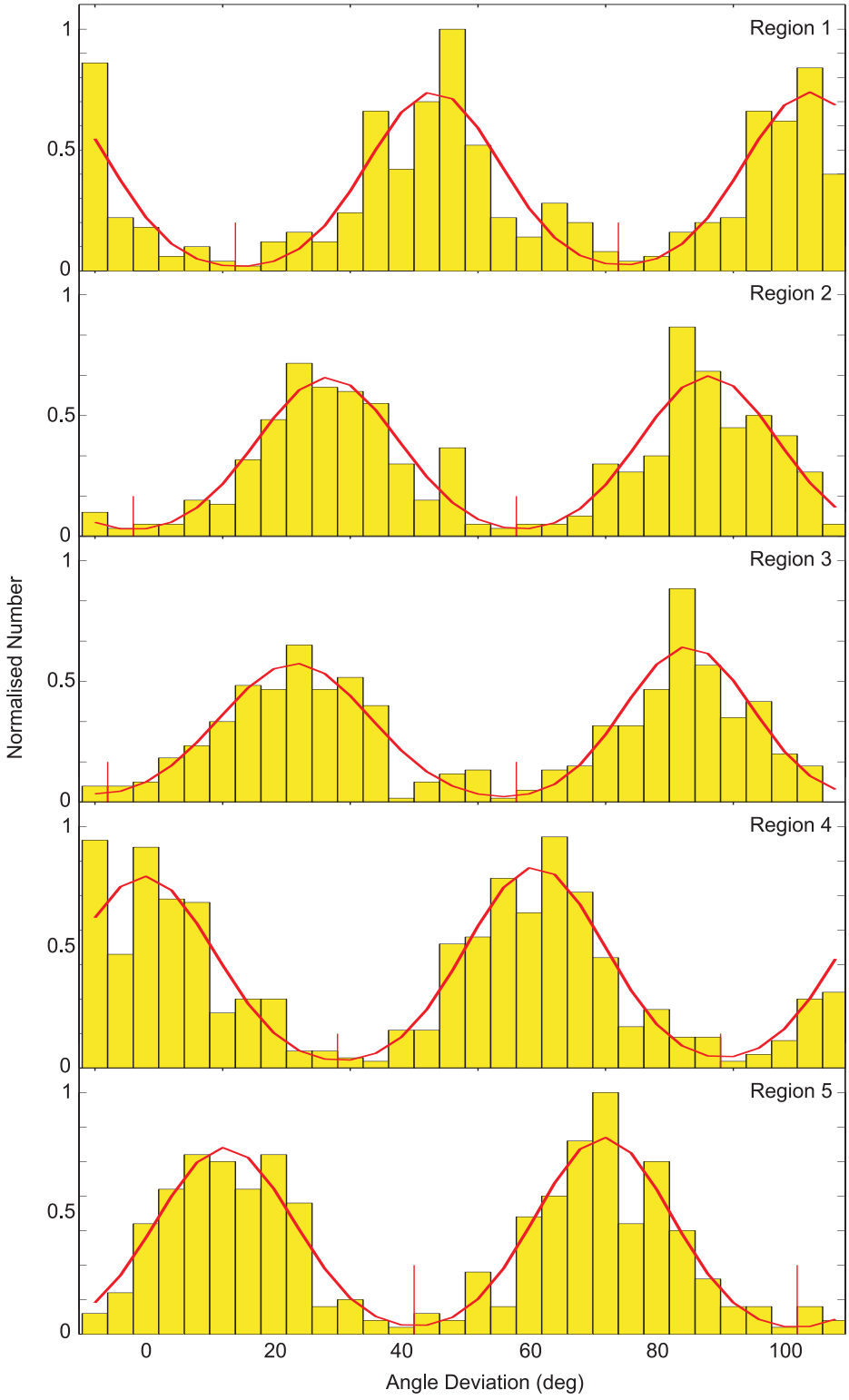


**Figure 4.8** Histograms and mixture models for the frog sartorius muscle regions shown in Fig. 4.2.

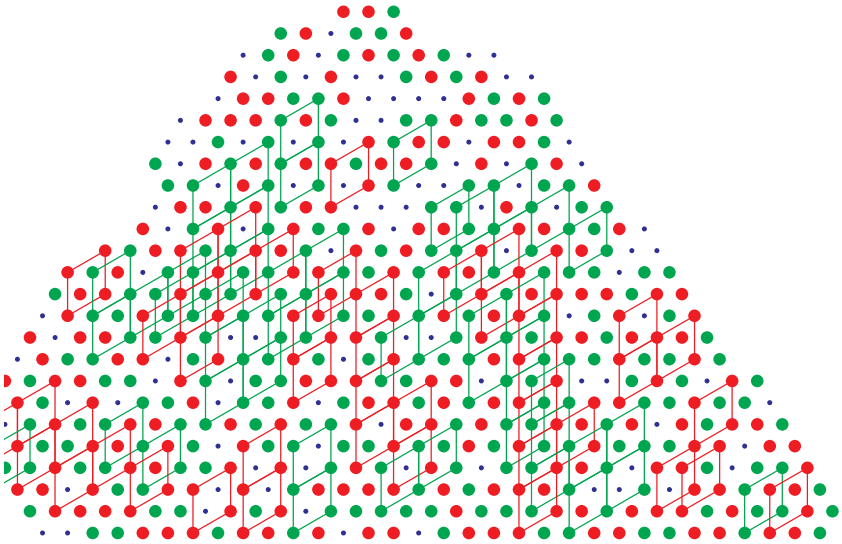

(a)

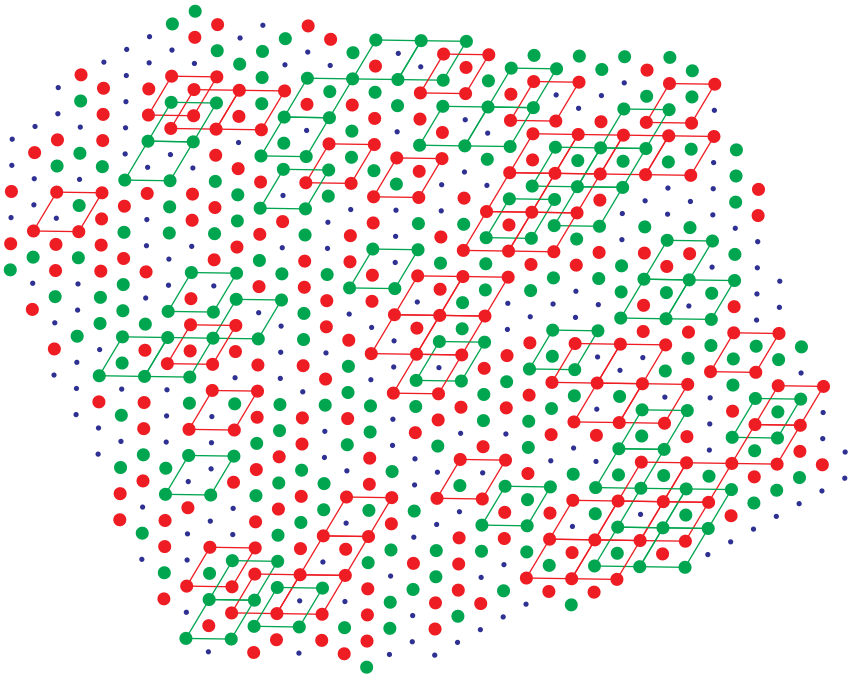

(b)

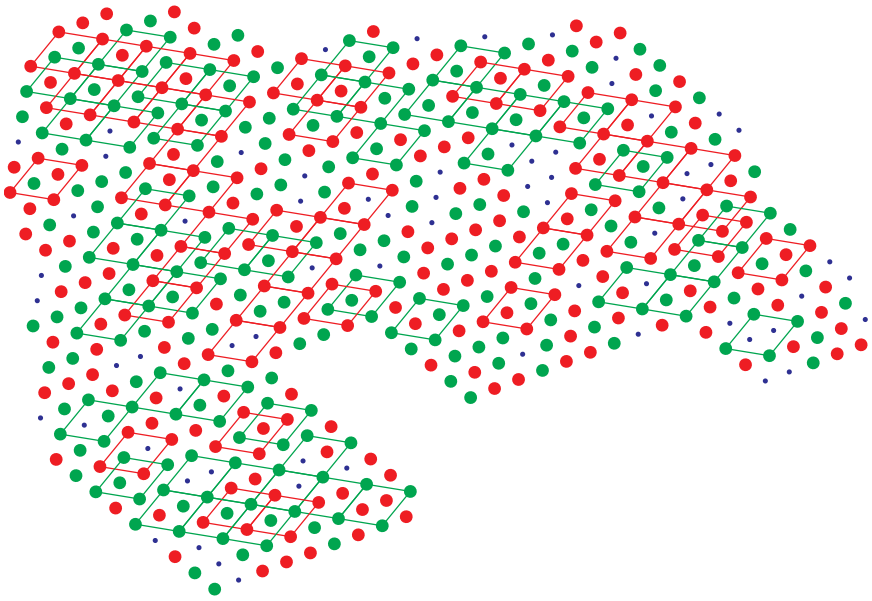

(c)

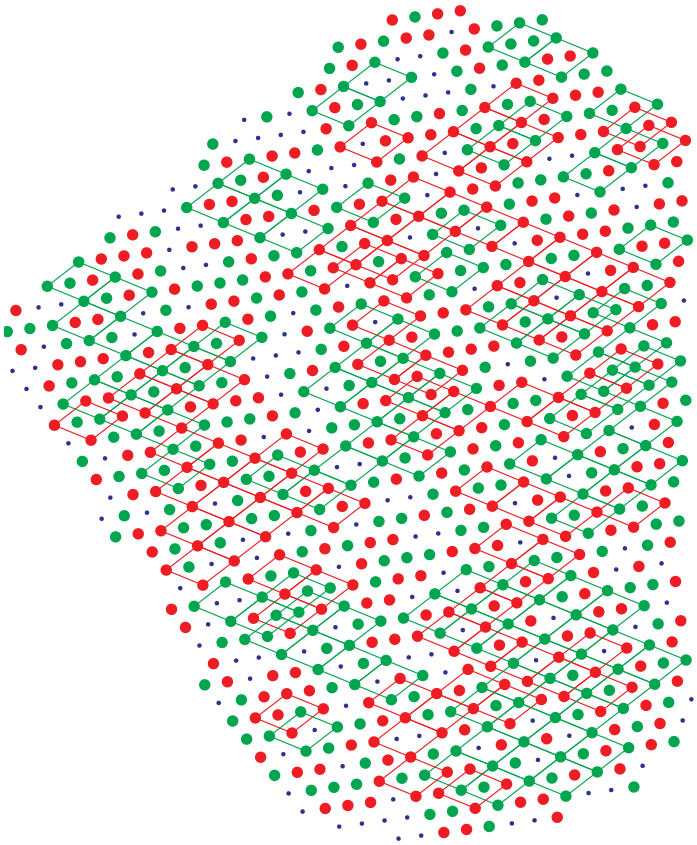

(d)

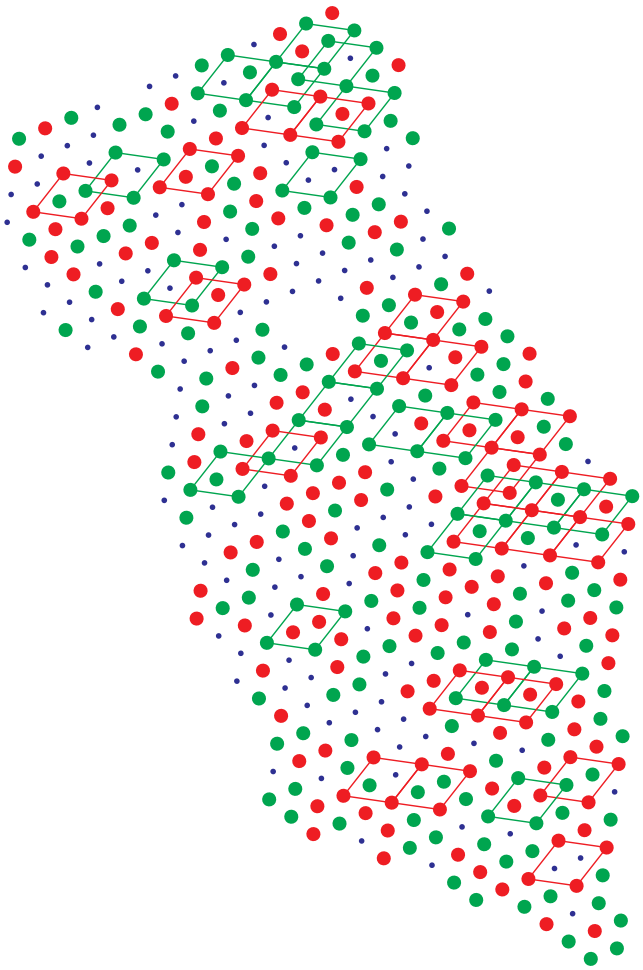

(e)

**Figure 4.9** Myosin lattice disorder in the A-band of frog sartorius muscle shown in Fig. 4.2. The up and down filaments are shown as light and dark circles and undetermined filament orientations are shown as black dots. Superlattice formations are shown as rhombi. (a) Regions 1, (b) region 2, (c) region 3, (d) region 4, and (e) region 5.

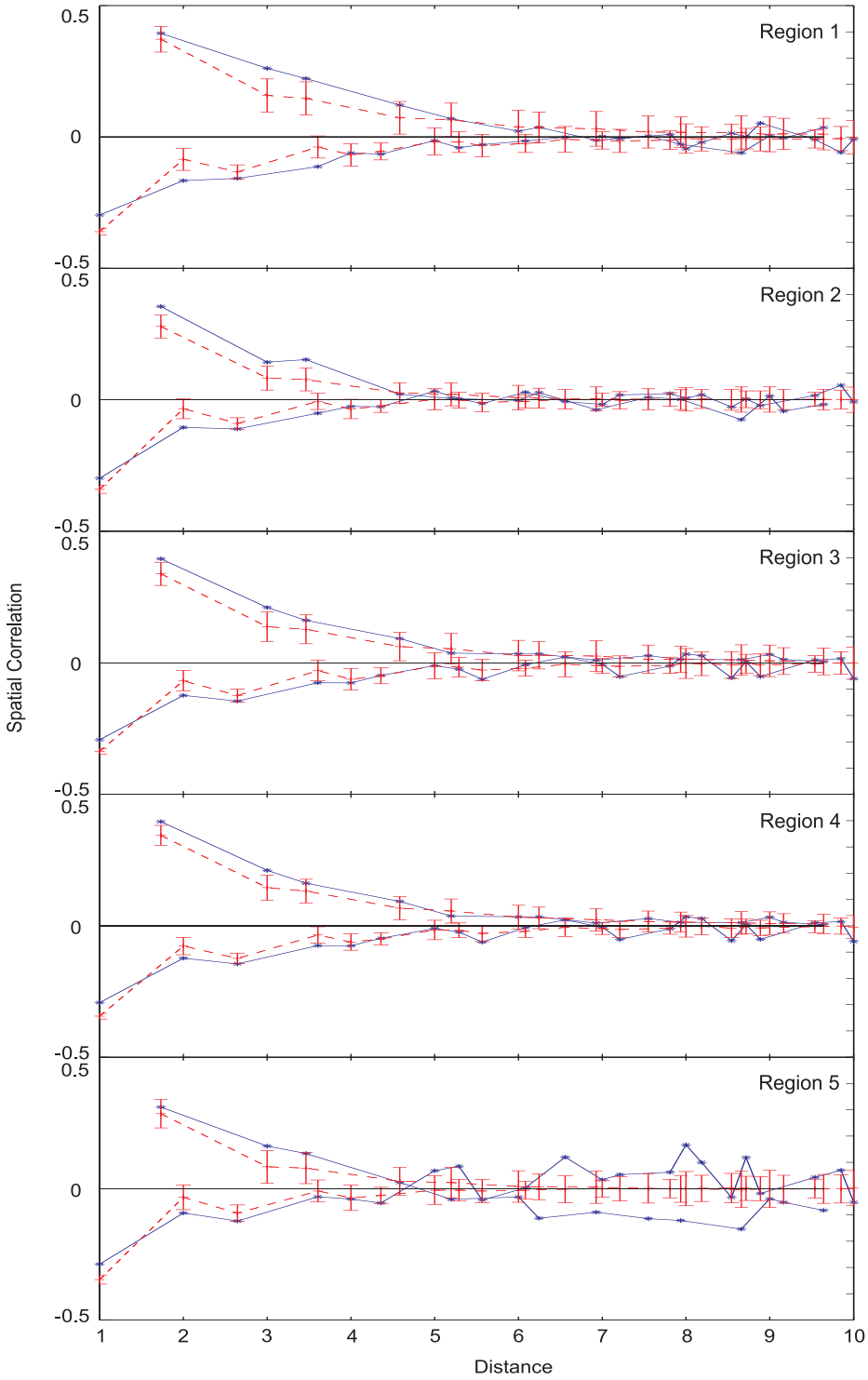


**Figure 4.10** Spatial correlation functions of the regions (solid lines) shown in Fig. 4.2 with Monte Carlo simulations (dashed lines) at the effective temperatures. The error bars are one standard deviation from the mean.

The second frog sartorius muscle micrograph shown in Fig. 4.3 was analysed in the same way. The results are summarised in Table 4.4 and the orientation histograms, distribution of orientations and correlation functions are shown in Figs. 4.11, 4.12 and 4.13, respectively.

**Table 4.4** Myosin lattice disorder parameters of the frog sartorius muscle in Fig. 4.3.

| | Region 1 | Region 2 | Region 3 | Region 4 | Average |
|---|---|---|---|---|---|
| $N$ | 653 | 1714 | 680 | 531 | 895 |
| $\overline{r}$ | 0.80 | 0.84 | 0.80 | 0.83 | 0.82 |
| $f_u$ | 0.15 | 0.03 | 0.15 | 0.07 | 0.08 |
| $\triangle\mu$ (°) | 61 | 60 | 60 | 61 | 60 |
| $\sigma_{up}$ (°) | 6 | 16 | 8 | 10 | 10 |
| $\sigma_{down}$ (°) | 9 | 10 | 9 | 10 | 9 |
| $p_{up}$ | 0.46 | 0.55 | 0.48 | 0.51 | 0.50 |
| $f_{rv1}$ | 0.04 | 0.09 | 0.03 | 0.03 | 0.05 |
| $f_{rv2}$ | 0.09 | 0.12 | 0.08 | 0.07 | 0.09 |
| $f_s$ | 0.37 | 0.35 | 0.39 | 0.40 | 0.38 |
| $\sigma$ | -0.28 | -0.21 | -0.28 | -0.30 | -0.27 |
| $RMSE_{min}$ | 0.26 | 0.41 | 0.21 | 0.17 | 0.26 |
| $T_{\text{eff}}$ | 0.59 | 0.57 | 0.58 | 0.62 | 0.59 |

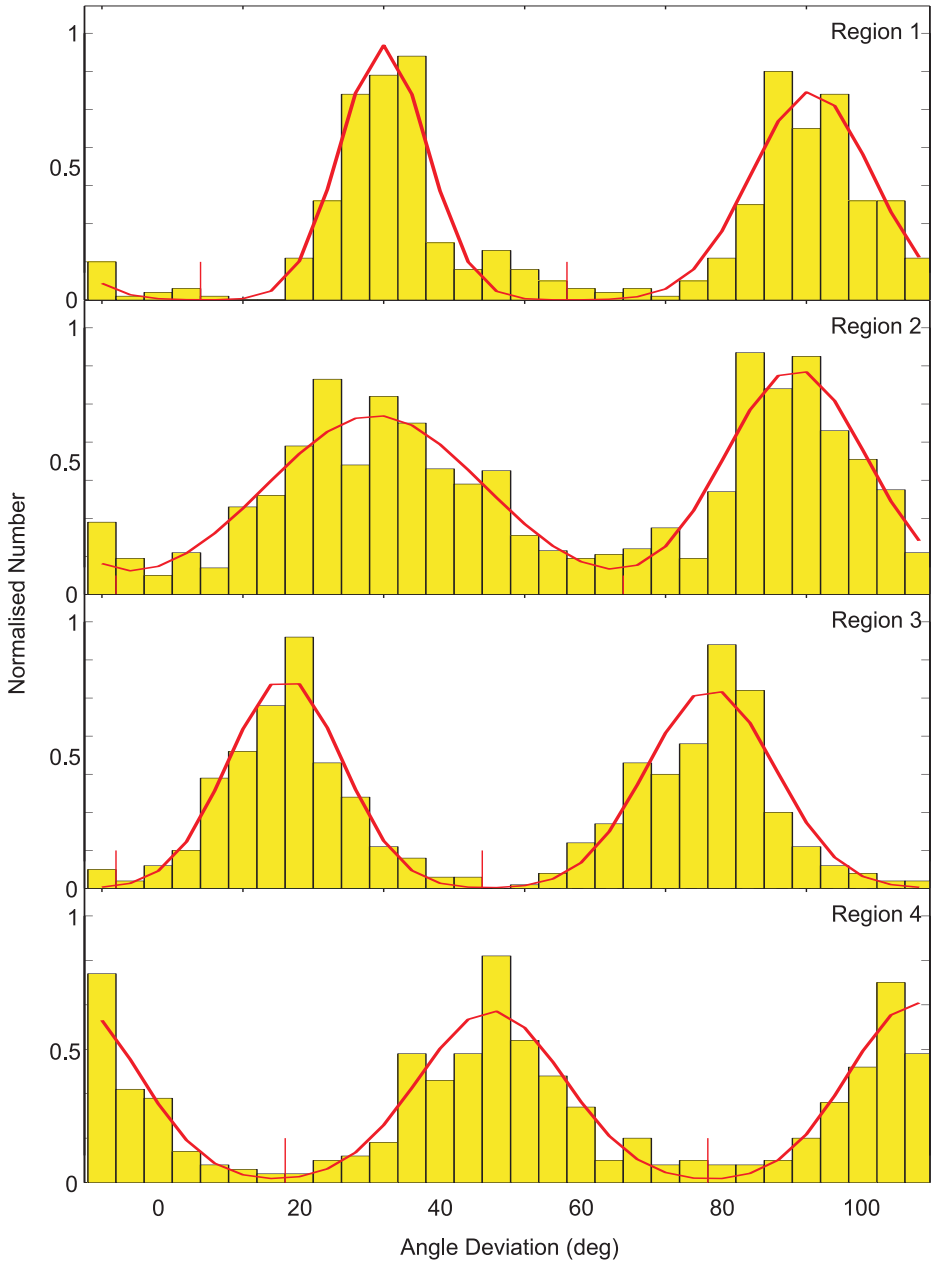


**Figure 4.11** The histogram and mixture model for the frog sartorius muscle regions in Fig. 4.3.

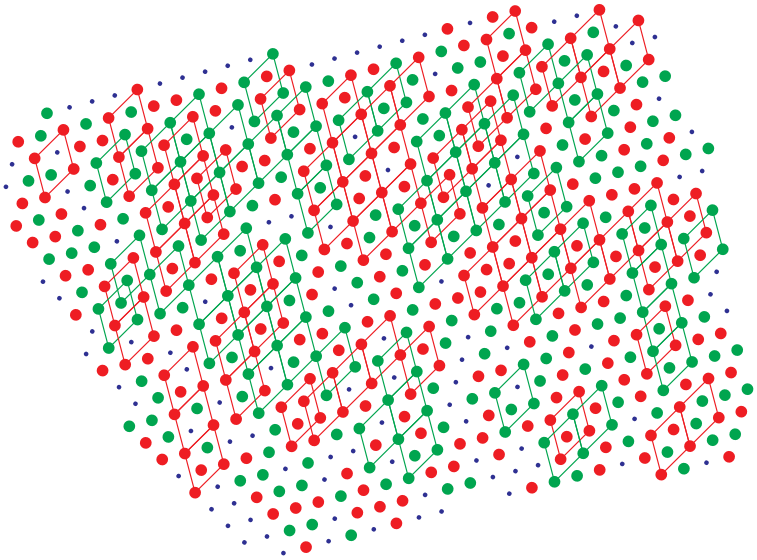

(a)

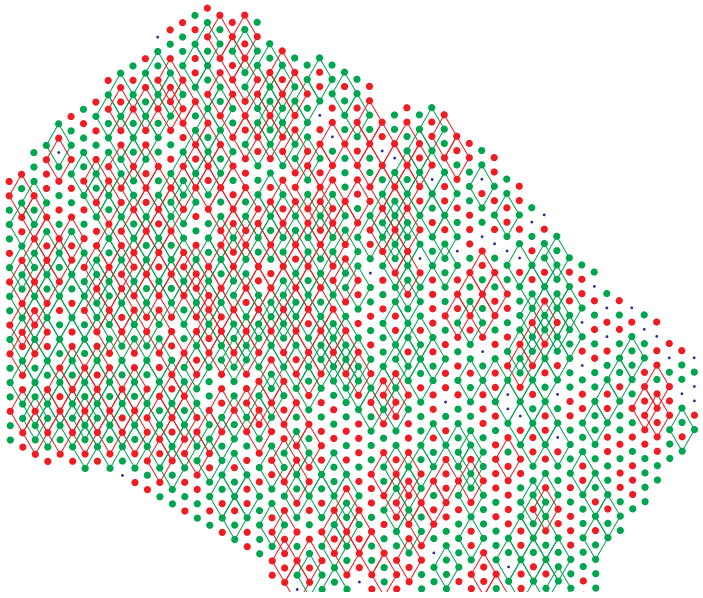

(b)

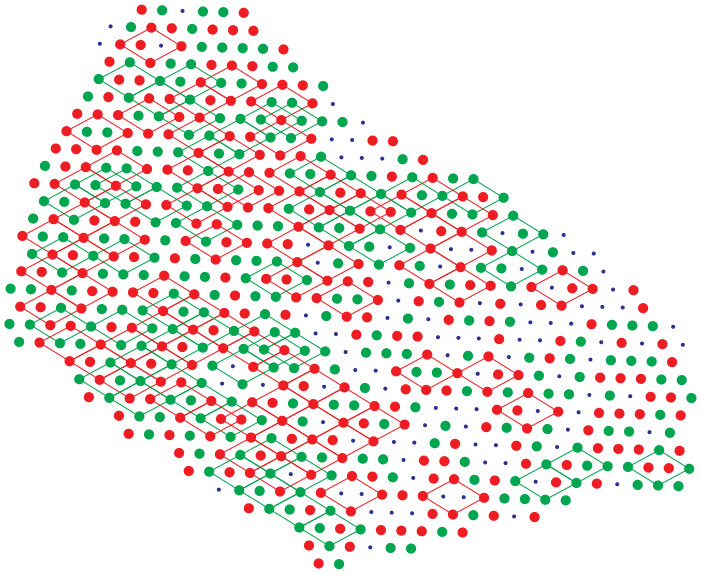

(c)

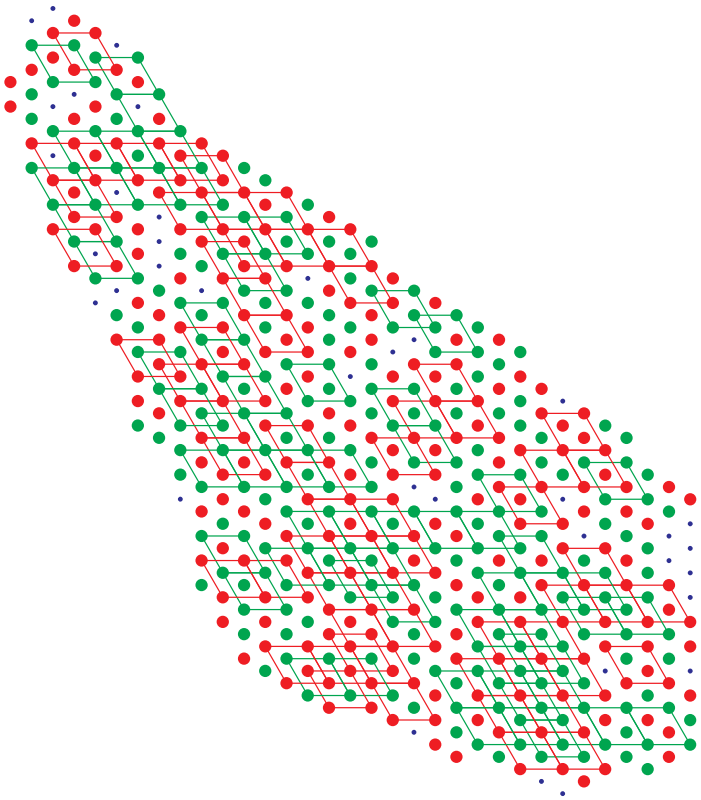

(d)

**Figure 4.12** Myosin lattice disorder in the A-band of frog sartorius muscle shown in Fig. 4.3. The up and down filaments are shown as light and dark circles and undetermined filament orientations are shown as black dots. Superlattice formations are shown as rhombi. (a) Region 1, (b) region 2, (c) region 3, and (d) region 4.

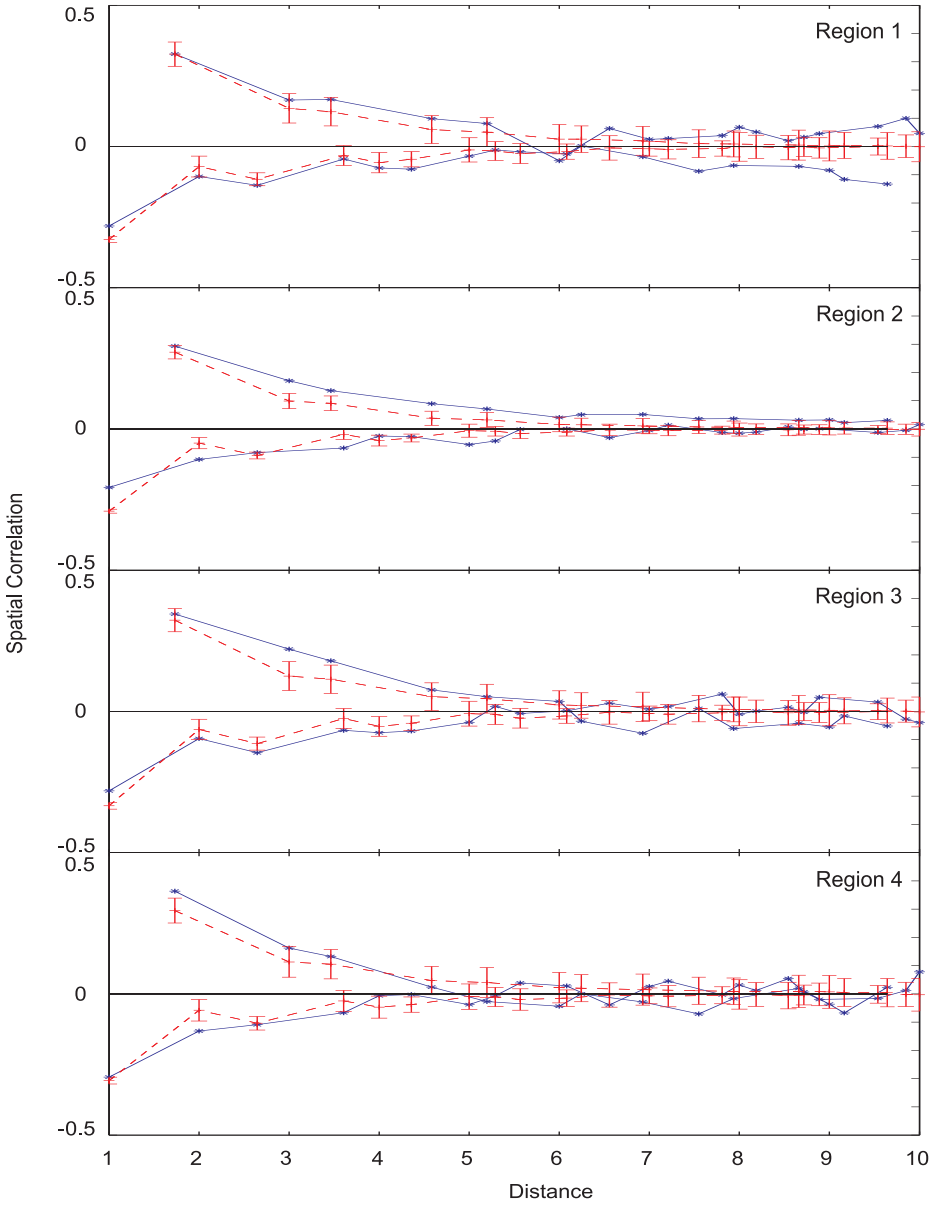


**Figure 4.13** Spatial correlation of the regions (solid) shown in Fig. 4.3 with Monte Carlo simulations (dashed) at the effective temperatures. The error bars are one standard deviation from the mean.

The third frog sartorius muscle micrograph shown in Fig. 4.4 was analysed in the same way. The results are summarised in Table 4.5 and the orientation histograms, distribution of orientations and correlation functions are shown in Figs. 4.14, 4.15 and 4.16, respectively.

**Table 4.5** Myosin lattice disorder parameters of the frog sartorius muscle in Fig. 4.4.

| | Region 1 | Region 2 | Region 3 | Region 4 | Average |
|---|---|---|---|---|---|
| $N$ | 756 | 1372 | 1208 | 808 | 1036 |
| $\overline{r}$ | 0.79 | 0.84 | 0.80 | 0.80 | 0.81 |
| $f_u$ | 0.19 | 0.06 | 0.17 | 0.13 | 0.13 |
| $\triangle\mu$ (°) | 59 | 60 | 64 | 60 | 61 |
| $\sigma_{up}$ (°) | 12 | 10 | 7 | 11 | 10 |
| $\sigma_{down}$ (°) | 14 | 11 | 9 | 9 | 11 |
| $p_{up}$ | 0.49 | 0.51 | 0.49 | 0.52 | 0.50 |
| $f_{rv1}$ | 0.11 | 0.03 | 0.03 | 0.03 | 0.05 |
| $f_{rv2}$ | 0.13 | 0.07 | 0.07 | 0.07 | 0.09 |
| $f_s$ | 0.285 | 0.388 | 0.389 | 0.364 | 0.357 |
| $\sigma$ | -0.19 | -0.30 | -0.30 | -0.30 | -0.27 |
| $RMSE_{min}$ | 0.30 | 0.25 | 0.34 | 0.37 | 0.32 |
| $T_{\text{eff}}$ | 0.64 | 0.67 | 0.68 | 0.56 | 0.64 |

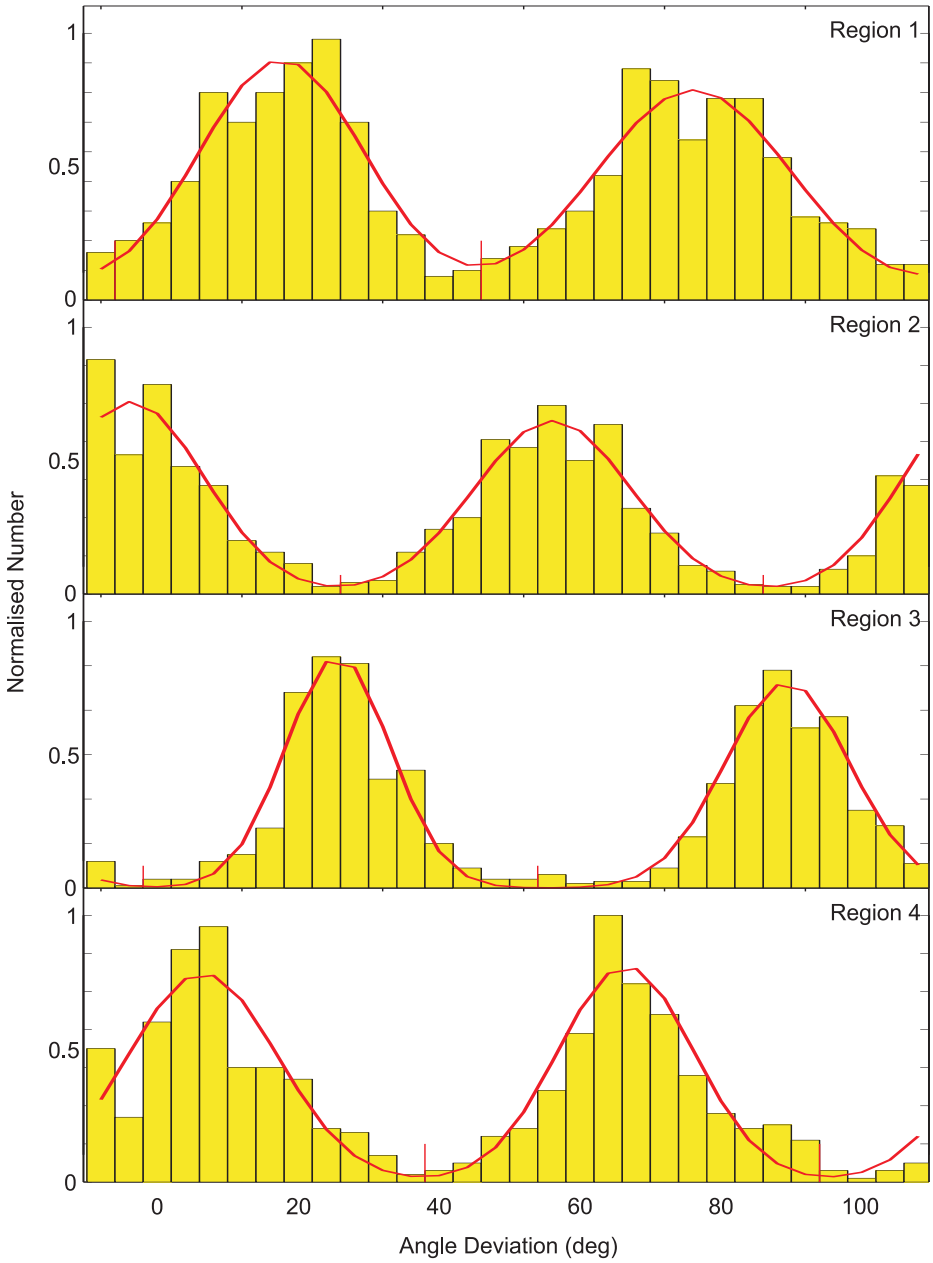


**Figure 4.14** The histogram and mixture model for the frog sartorius muscle regions in Fig. 4.4.

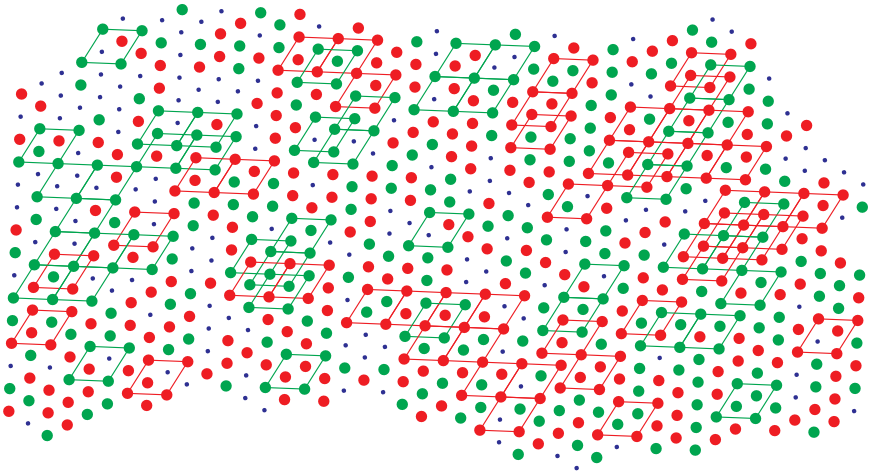

(a)

(b)

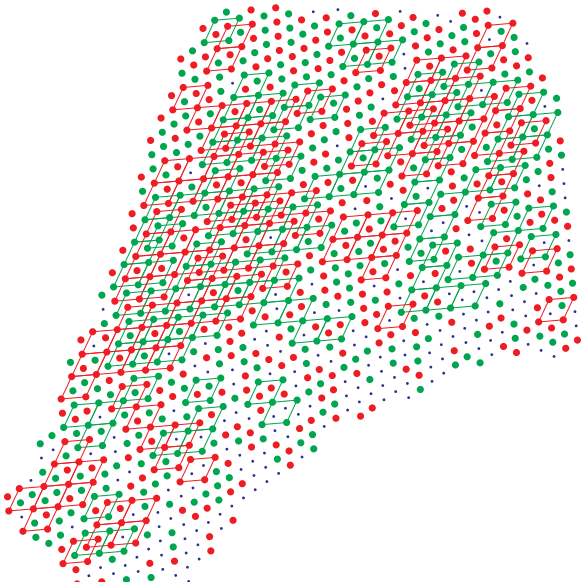

(c)

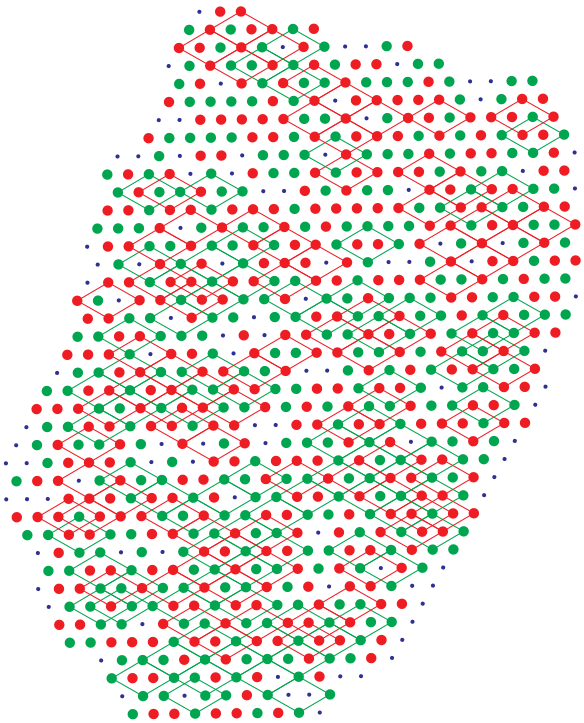

(d)

**Figure 4.15** Myosin lattice disorder in the A-band of frog sartorius muscle of shown in Fig. 4.4. The up and down filaments are shown as light and dark circles and undetermined filament orientations are shown as black dots. Superlattice formations are shown as rhombi. (a) Region 1, (b) region 2, (c) region 3, and (d) region 4.

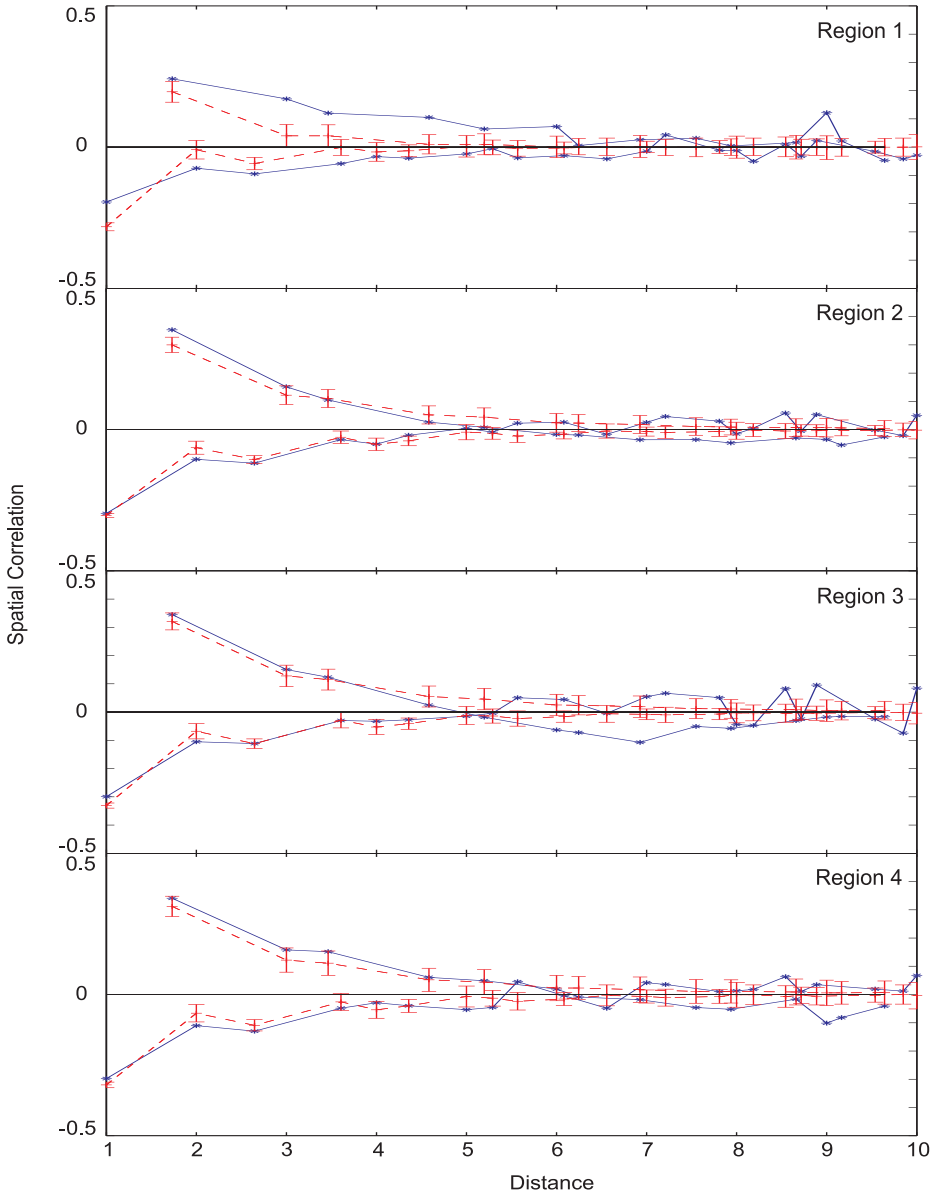


**Figure 4.16** Spatial correlation of the regions (solid) shown in Fig. 4.4 with Monte Carlo simulations (dashed) at the effective temperatures. The error bars are one standard deviation from the mean.

### 4.5.2 Shark

A shark myotomal muscle micrograph shown in Fig. 4.5 was analysed in the same way. The results are summarised in Table 4.6 and the orientation histogram, distribution of orientations and correlation function are shown in Figs. 4.17, 4.18 and 4.21, respectively.

**Table 4.6** Myosin lattice disorder parameters in the A-band of various vertebrate muscles in Fig. 4.5.

| Species | Shark | Turtle | Polypterus 1 | Polypterus 2 | Polypterus 3 |
|---|---|---|---|---|---|
| $N$ | 2215 | 338 | 675 | 377 | 704 |
| $\overline{r}$ | 0.89 | 0.80 | 0.83 | 0.79 | 0.81 |
| $f_u$ | 0.00 | 0.15 | 0.05 | 0.21 | 0.05 |
| $\triangle\mu$ (°) | 60 | 63 | 56 | 59 | 57 |
| $\sigma_{up}$ (°) | 13 | 16 | 12 | 11 | 13 |
| $\sigma_{down}$ (°) | 13 | 14 | 12 | 13 | 11 |
| $p_{up}$ | 0.50 | 0.55 | 0.44 | 0.50 | 0.53 |
| $f_{rv1}$ | 0.06 | 0.05 | 0.08 | 0.09 | 0.06 |
| $f_{rv2}$ | 0.12 | 0.10 | 0.10 | 0.12 | 0.11 |
| $f_s$ | 0.30 | 0.38 | 0.36 | 0.30 | 0.30 |
| $\sigma$ | -0.25 | -0.27 | -0.24 | -0.24 | -0.26 |
| $RMSE_{min}$ | 0.22 | 0.22 | 0.18 | 0.24 | 0.16 |
| $T_{\text{eff}}$ | 0.40 | 0.40 | 0.54 | 0.44 | 0.69 |

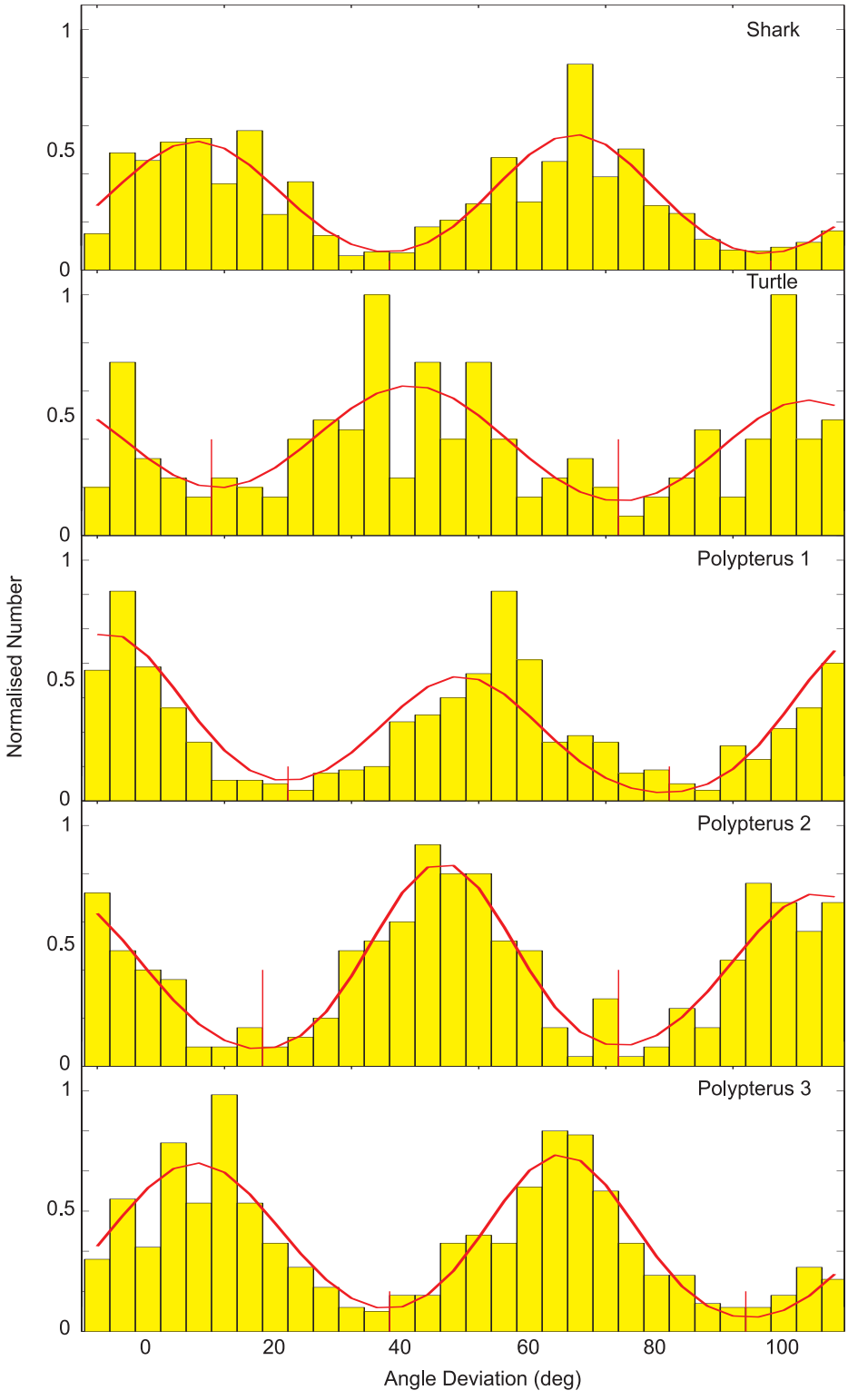


**Figure 4.17** The histogram and mixture model for various muscle regions in Fig. 4.5.

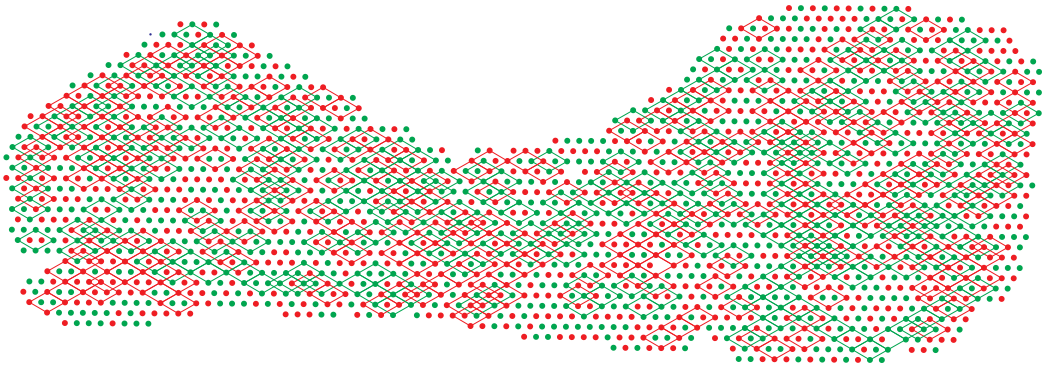

**Figure 4.18** Myosin lattice disorder in the A-band of shark white muscle in Fig. 4.5 Region 1. The up and down filaments are shown as light and dark circles and undetermined filament orientations are shown as black dots. Superlattice clumps are shown as rhombi.

### 4.5.3 Turtle

A turtle leg muscle micrograph shown in Fig. 4.5 was analysed in the same way. The results are summarised in Table 4.6 and the orientation histogram, distribution of orientations and correlation function are shown in Figs. 4.17, 4.19 and 4.21, respectively.

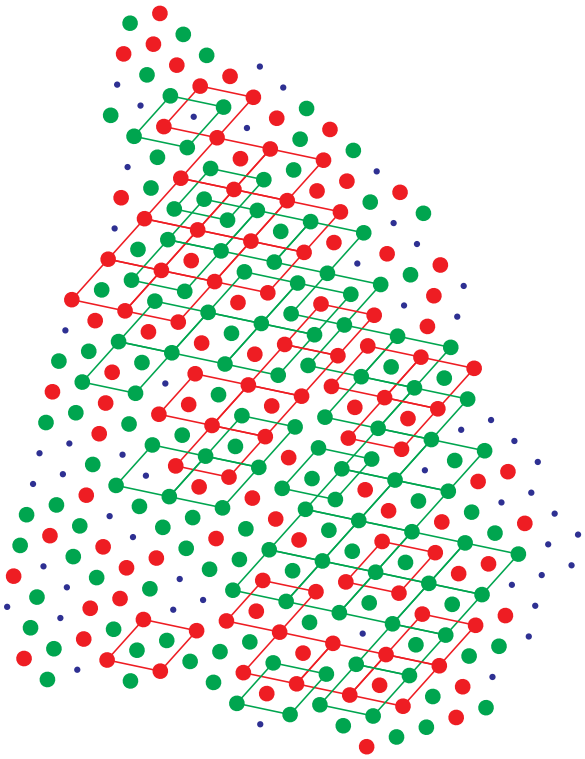

**Figure 4.19** Myosin lattice disorder in the A-band of turtle leg muscle in Fig. 4.5 Region 2. The up and down filaments are shown as light and dark circles and undetermined filament orientations are shown as black dots. Superlattice clumps are shown as rhombi.

### 4.5.4 Polypterus

Three Polypterus muscle micrographs shown in Fig. 4.5 were analysed in the same way. The results are summarised in Table 4.6 and the orientation histograms, distribution of orientations and correlation functions are shown in Figs. 4.17, 4.20 and 4.21, respectively.

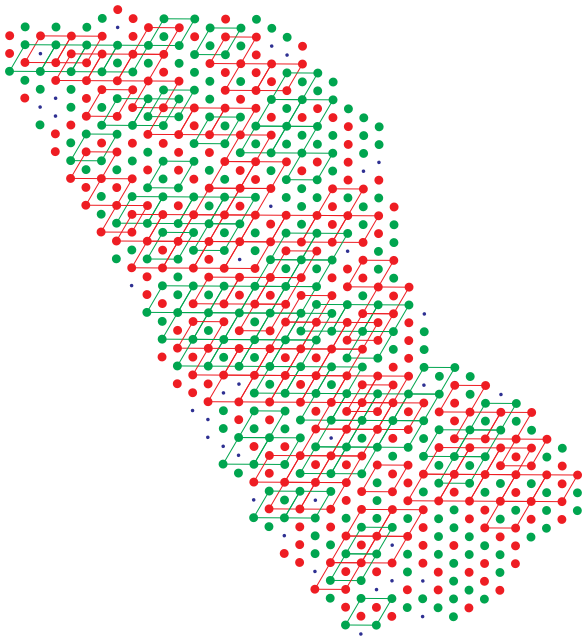

(a)

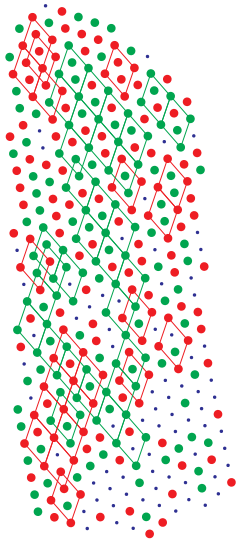

(b)

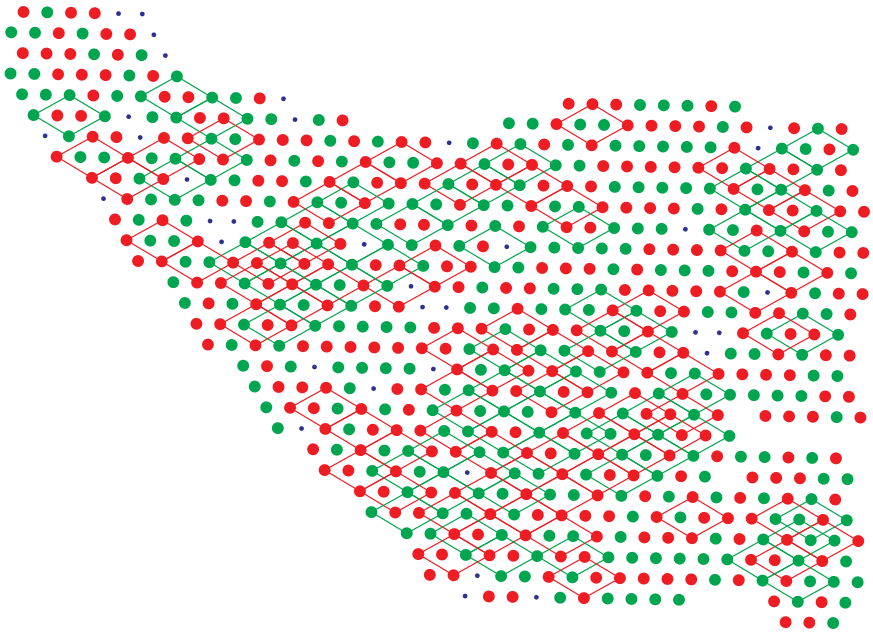

(c)

**Figure 4.20** Myosin lattice disorder in the A-band of polypterus white muscle in Fig. 4.5 Region 3. The up and down filaments are shown as light and dark circles and undetermined filament orientations are shown as black dots. Superlattice clumps are shown as rhombi.

## 4.6 Discussion

Overall, the results presented here show a good fit of the distribution of the myosin filament orientations to the TIA. This indicated by RMSE $< 0.3$ in most cases. Effective temperature are consistent, being the range 0.47 to 0.68.

In order to assess the myosin lattice disorder in vertebrate muscles, some general questions need to be answered. Does the degree of disorder differ significantly for neighbouring myofibrils in the same muscle fiber? How much does the disorder vary within a single species and between different species? These questions are addressed below.

### 4.6.1 Simple Lattice Muscle

The simple lattices of mudskipper muscle were analysed from a single micrograph. In regions 1 and 2, single Gaussian models fitted well to the orientation histograms confirming the existence of only a single orientation in these myofibrils as reported in [LC84]. In regions 3, 4 and 5, it was evident that the filaments did not adopt a single orientation, but two orientations spaced by approximately $30°$. This may be due to the micrograph depicting a slanting transverse cut across the M-band showing myosin filaments on each side of the M-band. Rotational offsets of about $30°$ have been observed either side of the M-band (P. K. Luther, Private communication).

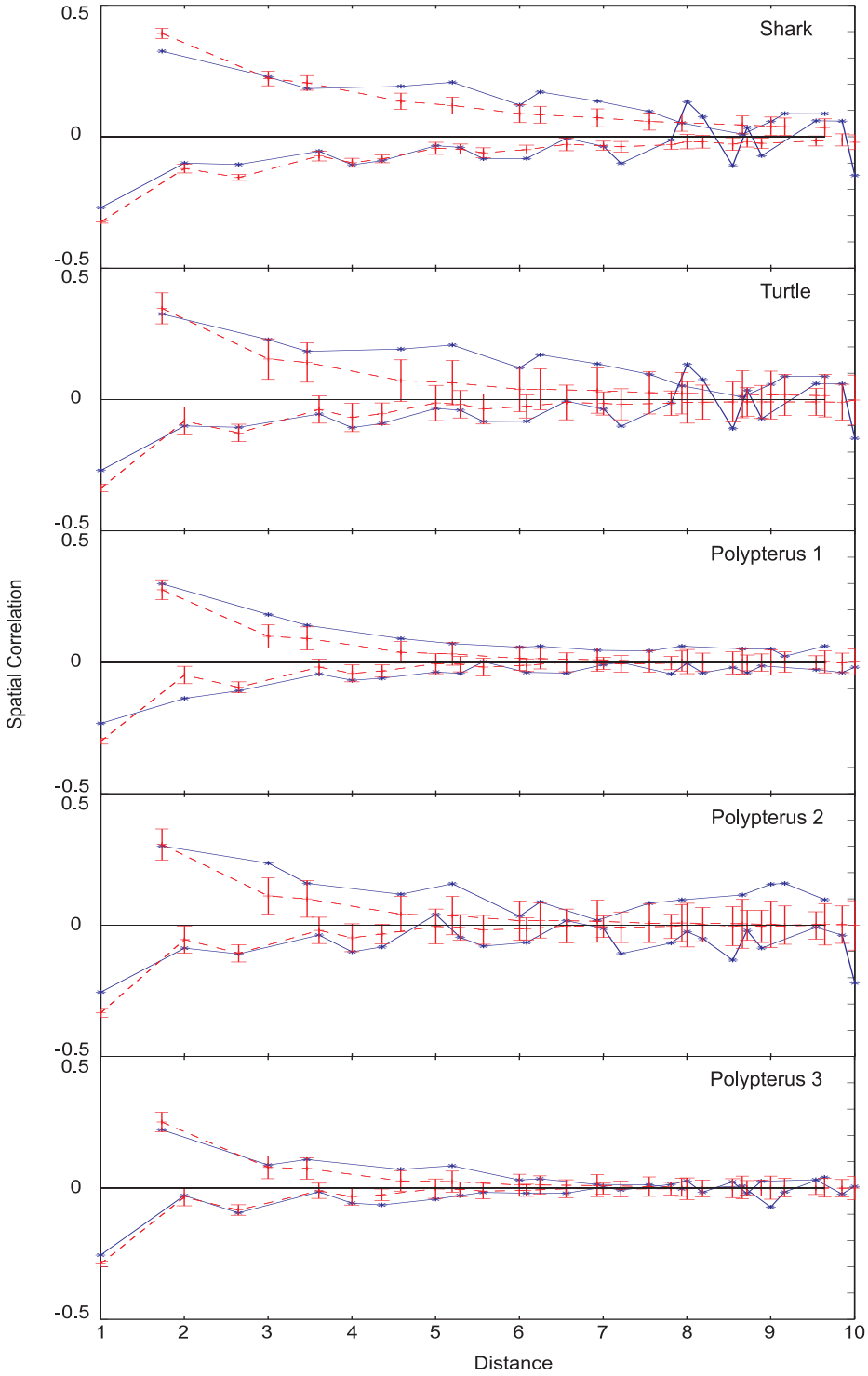


**Figure 4.21** Spatial correlation functions of the regions (solid lines) shown in Fig. 4.5 with Monte Carlo simulations (dashed lines) at the effective temperatures. The error bars are one standard deviation from the mean.

### 4.6.2 Superlattice Muscle

#### 4.6.2.1 Comparison of Myofibrils within a Micrograph

The degree of disorder in different myofibrils within a micrograph is examined with regard to the parameter deviations from the average value for the micrograph. For frog sartorius muscle, the frequency of the rule violations ($f_{rv1}$ and $f_{rv2}$), the fractional superlattice content ($f_s$) and the bond order ($\sigma$) are almost identical for the 5 regions shown in Table 4.3. The effective temperatures of the myofibrils vary by a maximum of 0.13 within micrographs. Similar variations are seen between myofibrils in the other two frog muscles (Tables 4.4 and 4.5). In summary, therefore, the myosin lattice disorder appears to be very similar within a micrograph or a fiber.

#### 4.6.2.2 Comparison within Species

Comparison of the results for the three frog micrographs studied shows similar variations in $f_{rv1}$, $f_{rv2}$ and $\sigma$ to those within micrographs except for 2 of the myofibrils. The average values for each micrograph are very similar. The variation in effective temperature over the 3 micrographs is no larger than that within micrographs.

The variations in $f_{rv1}$, $f_{rv2}$, $f_s$ and $\sigma$ for the three Polypterus micrographs are similar to those for the frog muscle. The range of the effective temperature of the myofibrils vary by 0.14, also very similar to that for the frog muscle.

#### 4.6.2.3 Comparison between Species

Referring to Table 4.6, the disorder parameters for shark myotomal muscle, turtle leg muscle and Polypterus muscle are similar to those for the frog muscle although the frequency of rule violations is somewhat higher. This could be due in part to the slightly lower quality of these micrographs. There is more variability in the effective temperatures between species than within species. With the limited data available, shark and turtle muscles appear to have the lowest effective temperatures, and frog and Polypterus having similar and larger effective temperatures.

## 4.7 Conclusions

Analysis of myofibrils from a variety of fibers and species show that the results described in Chapters 2 and 3 are a general phenomenon of the vertebrate myosin lattice disorder. Good agreement in all cases, and very good agreement in most cases, is obtained between the TIA correlation functions and the myosin lattice correlation functions. This indicates

that the TIA is a good model of the disorder in superlattice muscle in general, and suggests a universal mechanism for the development of this kind of muscle structure. The degree of disorder as described by the various parameters used are fairly constant within a species. A little more variability is observed between species. The effective temperature ranges between 0.40 and 0.69 for the different micrographs analysed. This is a relatively small range and one could use an average effective temperature of 0.55 for modelling purposes, or attempt to refine a temperature parameter as part of the modelling, depending on the number and precision of the data being used.

# Chapter 5

# Diffraction by the Triangular Ising Antiferromagnet

## 5.1 Introduction

The vertebrate skeletal muscle fiber is a polycrystalline fiber where the myofibrils are the crystalline domains, or crystallites, that aggregate parallel to the fiber axis, but are otherwise randomly positioned in the lateral plane and randomly rotated about the fiber axis. The myofibrils exhibit translational disorder along the fiber axis. Inspection of a longitudinal section of the muscle fiber (Fig. 5.1) indicates some axial regularity between myofibrils, although this regularity probably does not extend over a whole fiber. Hence the intensity diffracted by the muscle fiber is the cylindrical average of the intensity diffracted by an individual myofibril. As described in Section 1.6.3, the primary components that contribute to the fiber diffraction pattern are myosin and actin filaments. Since the myosin and actin filaments have different repeat distances, many of their individual layer lines can be separately observed in X-ray fiber diffraction patterns as described in Section 1.6.3. The concern here is with the diffraction due to the myosin lattice.

The myosin lattice exhibits correlated substitutional disorder as described in Chapter 3 which influences the X-ray fiber diffraction pattern. A quantitative description of this effect has not previously been developed, preventing rigorous interpretation of X-ray fiber diffraction data from the myosin component of superlattice muscle. Such an interpretation would be a significant contribution to the study of muscle structure. In this chapter, theory is developed for calculating cylindrically averaged diffraction by lattices with the TIA type of disorder as described in Chapter 3 and simulation results are presented.

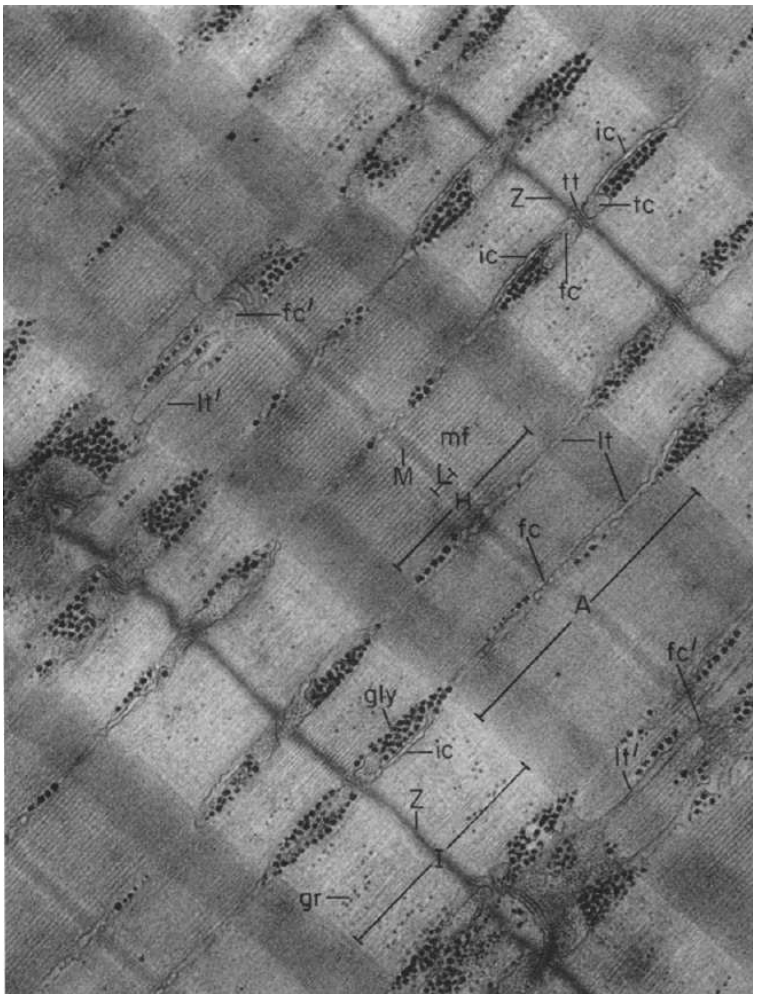


**Figure 5.1** Longitudinal section of frog muscle fiber [Pea65].

Optical transform methods have been used to study diffraction from superlattice lattices [LS80]. The optical transform method involves preparing a mask by punching out apertures and then using a laser to obtain the diffraction pattern of the mask [HTW75, WJ80]. These methods provide some information but are not suitable for the detailed numerical calculations that are required.

The key to calculating the diffraction is the spatial correlation function derived in Chapter 3. Calculation of the full fiber diffraction pattern from the myosin lattices requires considering the full three-dimensional structure of myosin. The superlattice disorder however is a two-dimensional phenomenon and the analysis considered here is restricted to diffraction by disordered two-dimensional lattices. This captures the key effects of this kind of disorder and extension to full myosin lattice would be relatively straightforward.

This chapter is organised as follows. Section 5.2 briefly reviews diffraction by an ordered lattice with triangular scatterers. In Section 5.3 the discrete Fourier transform (DFT) is used to calculate two-dimensional diffraction patterns from disordered lattices by numerical averaging over an ensemble of disordered lattices. The primary objective of this chapter is to reduce the ensemble averaging to an analytic form that allows much faster computation and more insight, for both two-dimensional and cylindrically averaged (one-dimensional) diffraction patterns. Theory and simulations for two-dimensional diffraction are presented in Sections 5.4 and 5.5, respectively, and for cylindrically averaged diffraction in Sections 5.6 and 5.7. Concluding remarks are made in Section 5.8.

## 5.2 Diffraction by an Ordered Lattice

Some basic properties of diffraction by hexagonal lattices and triangular scatterers are presented in this section. A sampled binary mask representing the lattice is calculated on a square array and set to zero outside a circular "crystallite". The edges of the crystallite are tapered to reduce ripples in the diffraction pattern that can obscure details of interest. The diffraction patterns are calculated using the discrete Fourier transform and presented as their amplitudes thresholded typically by 0.8 of the maximum value so that the weak diffuse intensities are clearly visible.

A hexagonal lattice of points is shown in Fig. 5.2(a) and the calculated diffraction pattern in Fig. 5.2(b). The hexagonal reciprocal lattice is evident. The reciprocal lattice axes are perpendicular to the axes in real space, and the lattice spacing on the reciprocal lattice is $1/d$ where $d$ is the spacing between the planes (Fig. 1.28).

Placing circular scatterers at each lattice site gives the diffraction pattern shown in Fig. 5.3. This system can be represented as the hexagonal lattice convolved with the circular scatterer. In the Fourier domain, the diffraction pattern is therefore the reciprocal lattice multiplied by the Fourier transform of the circular scatterer, since

$$f(x,y) \otimes l(x,y) \Leftrightarrow F(u,v)L(u,v), \tag{5.1}$$

where $f(x,y)$ is the scatterer, $l(x,y)$ is the lattice, $F(u,v)$ is the Fourier transform of the scatterer and $L(u,v)$ is the reciprocal lattice. The diffraction pattern of the circular scatterer therefore modulates the overall reciprocal lattice. This is evident in Fig. 5.3(b) where the amplitudes of the reciprocal lattice points vary in accordance with the diffraction pattern of the circular scatterer.

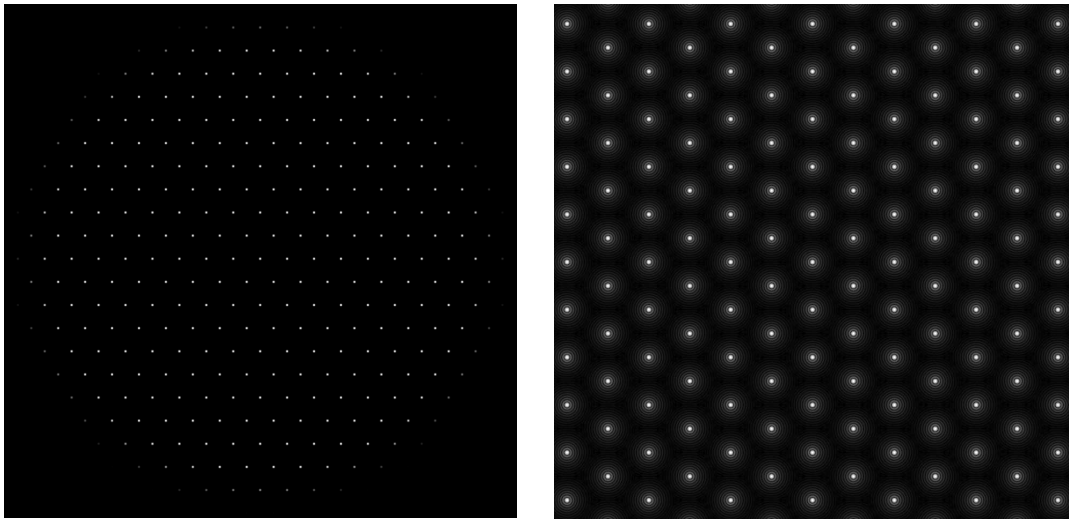

(a) (b)

**Figure 5.2** (a) A hexagonal lattice and (b) its diffraction pattern.

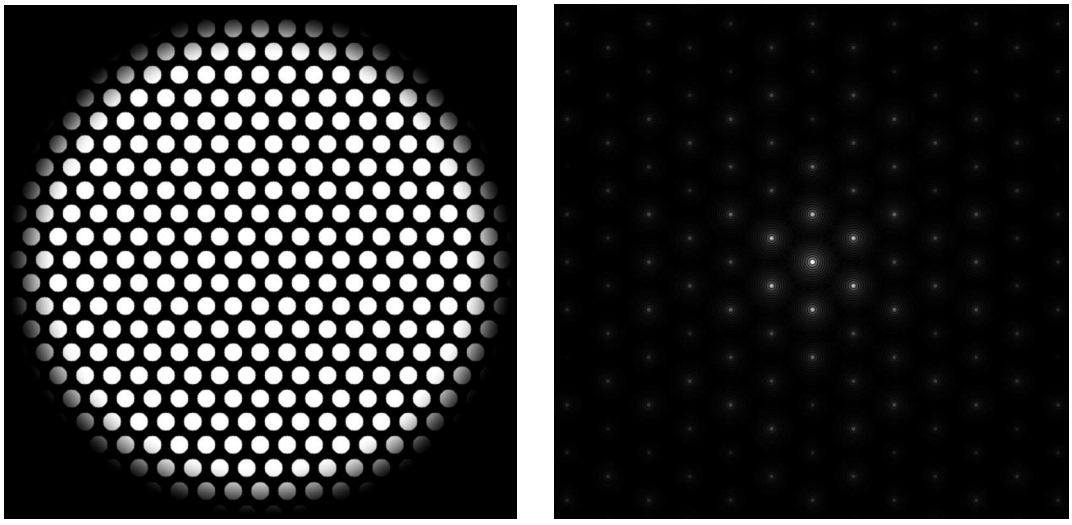

(a) (b)

**Figure 5.3** (a) A hexagonal lattice with a circular scatter on each lattice site and (b) its diffraction pattern.

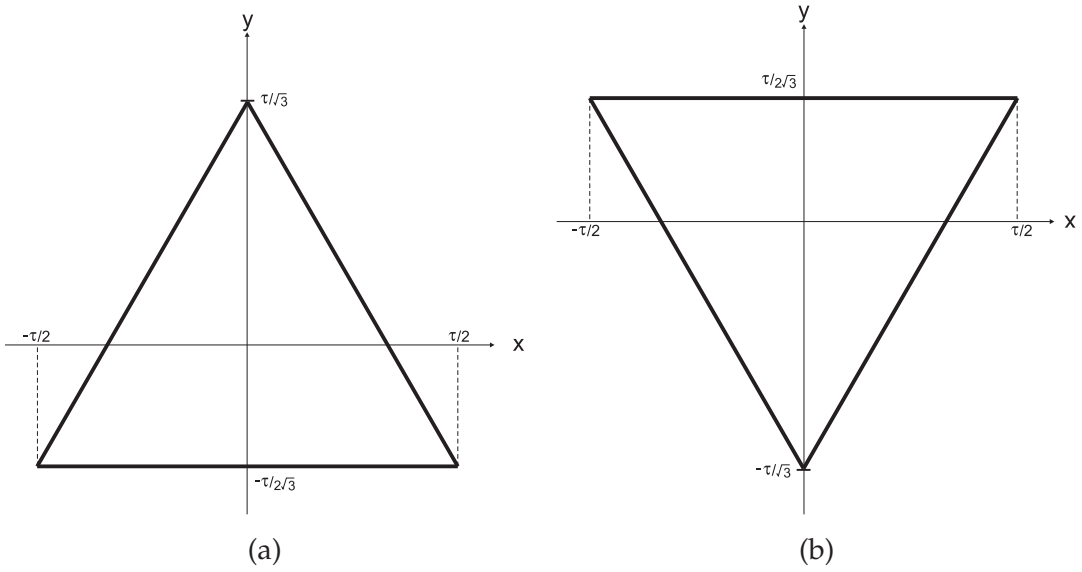


**Figure 5.4** Geometry of (a) up and (b) down triangles.

### 5.2.1 Diffraction by a Triangle

Since the myosin filaments profiles can be approximated by a triangle, the diffraction by an equilateral triangle is considered. A triangle with sidelength $\tau$ is positioned as shown in Fig. 5.4(a) with its centroid at the origin. This is referred to as an "up" triangle. A "down" triangle is shown in Fig. 5.4(b).

Discretised up and down triangles are shown in Fig. 5.5(a) and (b) and their corresponding diffraction patterns calculated by the DFT are shown in Fig. 5.5(c) and (d), respectively. The diffracted intensity is star-shaped, with six-fold symmetry. The diffracted complex amplitude has 3-fold symmetry, the same as that for the triangle. Friedel symmetry [Appendix A.3] for the amplitude then gives 6-fold symmetry. The diffracted intensities are the same for both triangles, since reflection of the triangle in the x-axis corresponds to reflection of the diffraction pattern in the u-axis.

### 5.2.2 Diffraction by an Array of Triangles

The diffraction by a hexagonal array of triangles is now considered. The crystallite shape is circular with a radius $r_c = 400$ pixels. The lattice edges ($> 4r_c/5$) are tapered with a raised cosine to reduce ripples as described previously. The lattice spacing is set to 42 pixels and the sidelength of the triangles is 28 pixels. The crystallite radius is thus 10 lattice spacings. A lattice with up triangles is shown in Fig. 5.6(a) and the diffraction pattern is shown in Fig. 5.6(b). Inspection of the figure shows modulation of the reciprocal lattice by

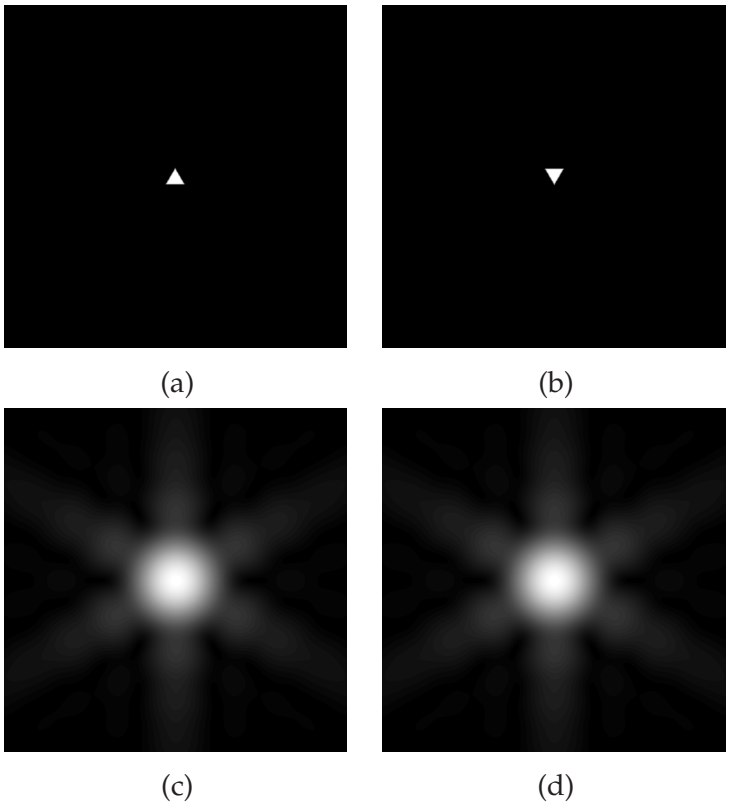


**Figure 5.5** (a) Up and (b) down triangles and their diffraction patterns (c and d).

the six-fold star shape of the diffraction pattern of the triangle.

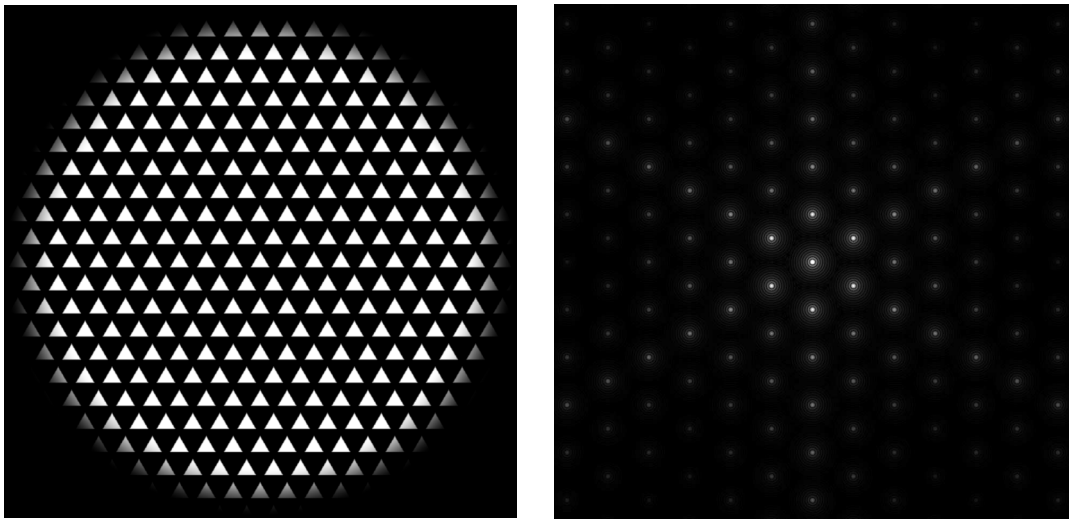

(a) (b)

**Figure 5.6** (a) A hexagonal lattice with an up triangle on each lattice site and (b) its diffraction pattern.

The lattice in Fig. 5.6 is an idealised model of the simple lattice of fish muscle. A section of a mudskipper muscle (which has a simple lattice) micrograph is shown in Fig. 5.7(a), and its diffraction pattern calculated by the DFT is shown in Fig. 5.7(b). Sharp Bragg peaks on the hexagonal reciprocal lattice are evident. The micrograph is noisy and the myosin filament profiles are not perfectly triangular, so that the star-shaped modulation of the diffraction pattern is not particularly evident.

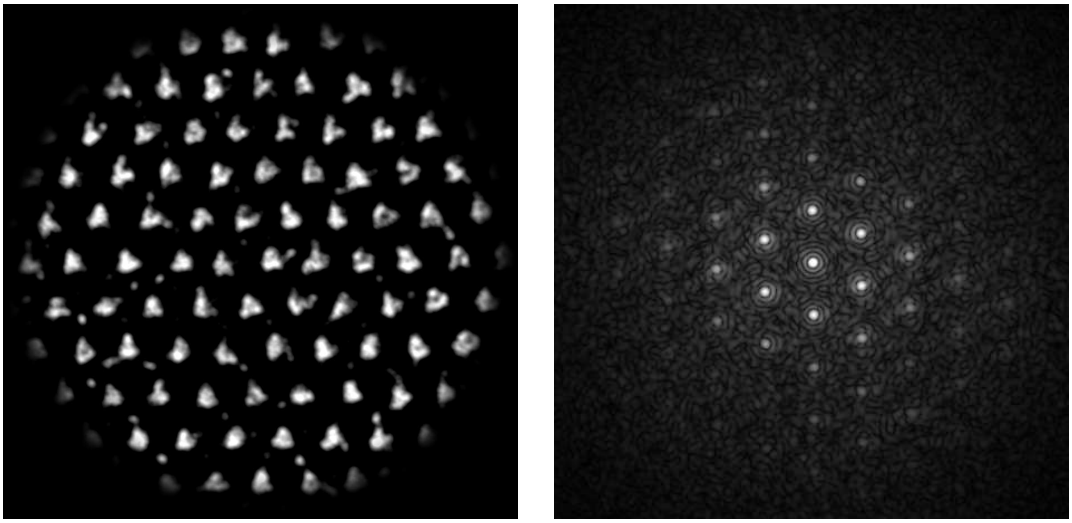

(a) (b)

**Figure 5.7** (a) Electron micrograph of mudskipper muscle and (b) its diffraction pattern calculated using the DFT.

## 5.3 Diffraction in the Presence of Substitution Disorder

In this section the DFT is used to simulate diffraction by disordered lattices by ensemble averaging. This involves calculating the diffraction pattern from many disordered lattices and averaging their intensities. This corresponds to the diffraction from a large number of randomly positioned lattices, i.e. incoherent addition of their diffraction patterns. The process is ergodic so that the diffraction from a large disordered lattice approaches that of the ensemble average.

Substitution disorder encompasses a variety of disorder such as the presence of different kinds of scattering species, or a single species adopting a number of different orientations, at each site. Two cases of substitution disorder are considered; vacancy disorder where triangular scatterers are either present or absent on the lattice sites, and rotational disorder where either up or down triangles are present. Both uncorrelated and correlated disorder are considered.

### 5.3.1 Uncorrelated Substitution Disorder

For uncorrelated substitution disorder, the presence of a particular scatterer at a site is independent of the scatterers present at other sites. A lattice generated in which a triangle is present at each lattice site with probability 0.5 is shown in Fig. 5.8(a). This is uncorrelated disorder with the two scatterers being either a triangle or no scatterer. The diffraction pattern of this lattice calculated by the DFT is shown in Fig. 5.8(b). The diffraction pattern is similar to Fig. 5.6(b), but there is "continuous" diffraction between the Bragg reflections. There is also "noise" due to the random nature of the lattice and the small number of sites. Averaging the intensities of 100 such diffraction patterns over 100 random lattices, gives the diffraction pattern shown in (Fig. 5.8(c)). Inspection of this figure shows that it is similar to that from an ordered lattice but there is some diffuse diffraction and the amplitude of the Bragg reflections decreases with distance from the origin. The "noise" has been smoothed out by the averaging.

A similar calculation in which the two scatterers are up and down triangles is shown in Fig. 5.9. This is similar to Fig. 5.8, the main difference being the different modulation of the diffraction pattern due to the different scatterers.

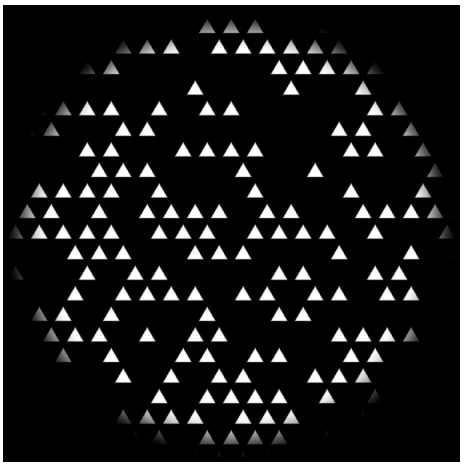

(a)

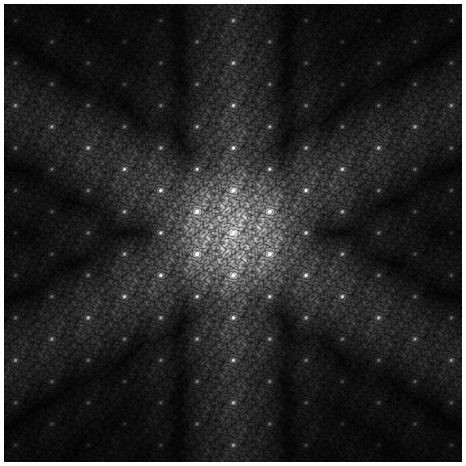

(b)

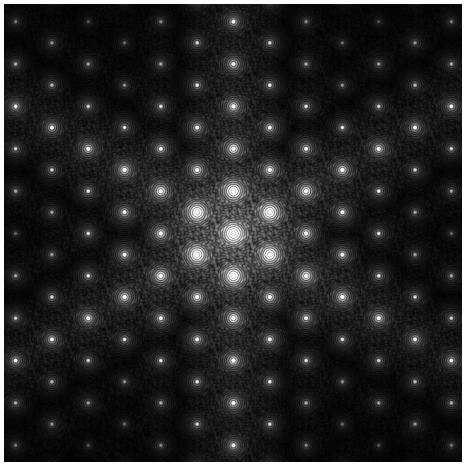

(c)

**Figure 5.8** (a) A hexagonal lattice of randomly distributed triangle scatterers and no scatterers and (b) its diffraction pattern. (c) The diffraction pattern after averaging the intensities of 100 diffraction patterns.

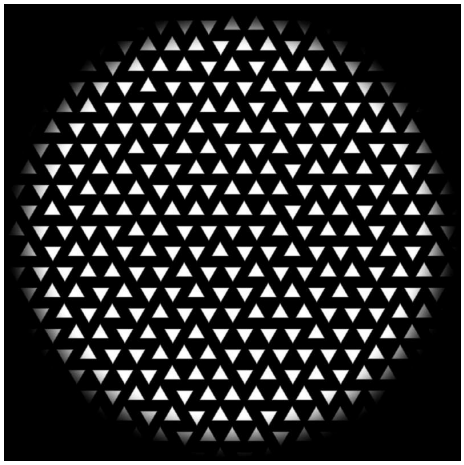

(a)

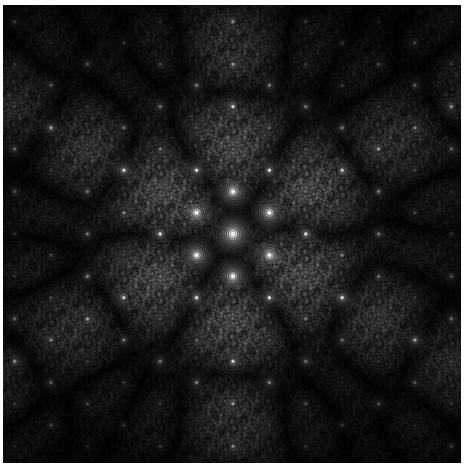

(b)

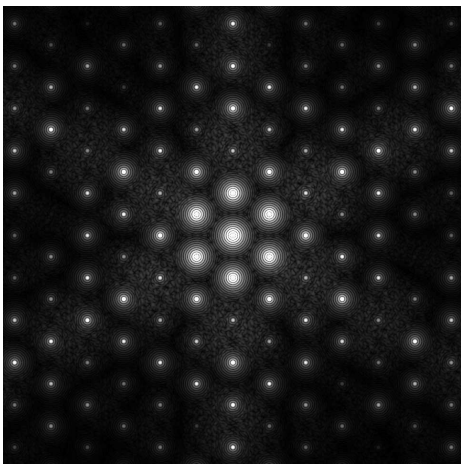

(c)

**Figure 5.9** (a) A hexagonal lattice of randomly distributed up and down triangle scatterers and (b) its diffraction pattern. (c) The averaged diffraction pattern of 100 diffraction patterns.

### 5.3.2 Correlated Substitution Disorder

For correlated substitution disorder the presence of a scatterer at one site depends on the scatterers present at other sites. There are many possible joint densities that can describe these correlations and here only that resulting from the TIA as described in Chapter 3 is considered.

Lattice configurations were generated using Monte Carlo simulations as described in Chapter 3. Lattices containing up triangles and no scatterers and their averaged (over 100 lattices) diffraction patterns are shown in Fig. 5.10 for temperatures, $T = 5, 0.55$ and 0.05. These three temperatures represent almost random disorder, disorder similar to that for muscle, and the disorder very close to the ground state. The diffraction patterns contain Bragg and diffuse diffraction as for the uncorrelated case, $T = \infty$. For correlated disorder, the diffuse intensity forms peaks arranged hexagonally around the Bragg reflections of the basic hexagonal reciprocal lattice. These superlattice reflections are due to the formation of superlattice cells as described in Chapter 1. They are sharper and more prominent at lower temperatures where there are stronger correlations.

Analogous calculations were conducted for up and down triangles and the results are shown in Fig. 5.11. The characteristics of the diffraction patterns are similar to those in Fig. 5.10.

A micrograph of frog muscle is shown in Fig. 5.12, after increasing the contrast and blurring with a psf to make the profiles more triangular. The diffraction pattern calculated by the DFT is shown in Fig. 5.13(a). The pattern is quite noisy but reveals weak superlattice reflections, although not very clearly, as illustrated in Fig. 5.13(b).

## 5.4 Diffraction by a Crystal with Correlated Substitution Disorder: Theory

As shown in the previous section, the averaged diffraction by disordered lattices can be calculated by generating samples of the lattices, calculating the diffraction using the DFT, and averaging over many samples of the disorder. This is computationally very intensive and provides little insight. It also provides information only at the DFT sample points. Here theory is developed to perform the averaging analytically, thus reducing the calculation to a simple form and allowing calculation at any point in reciprocal space.

It was shown in Section 1.5.2 that the average intensity diffracted from an ensemble of crystallites with lattice and substitution disorder, and with identical crystallite shapes and

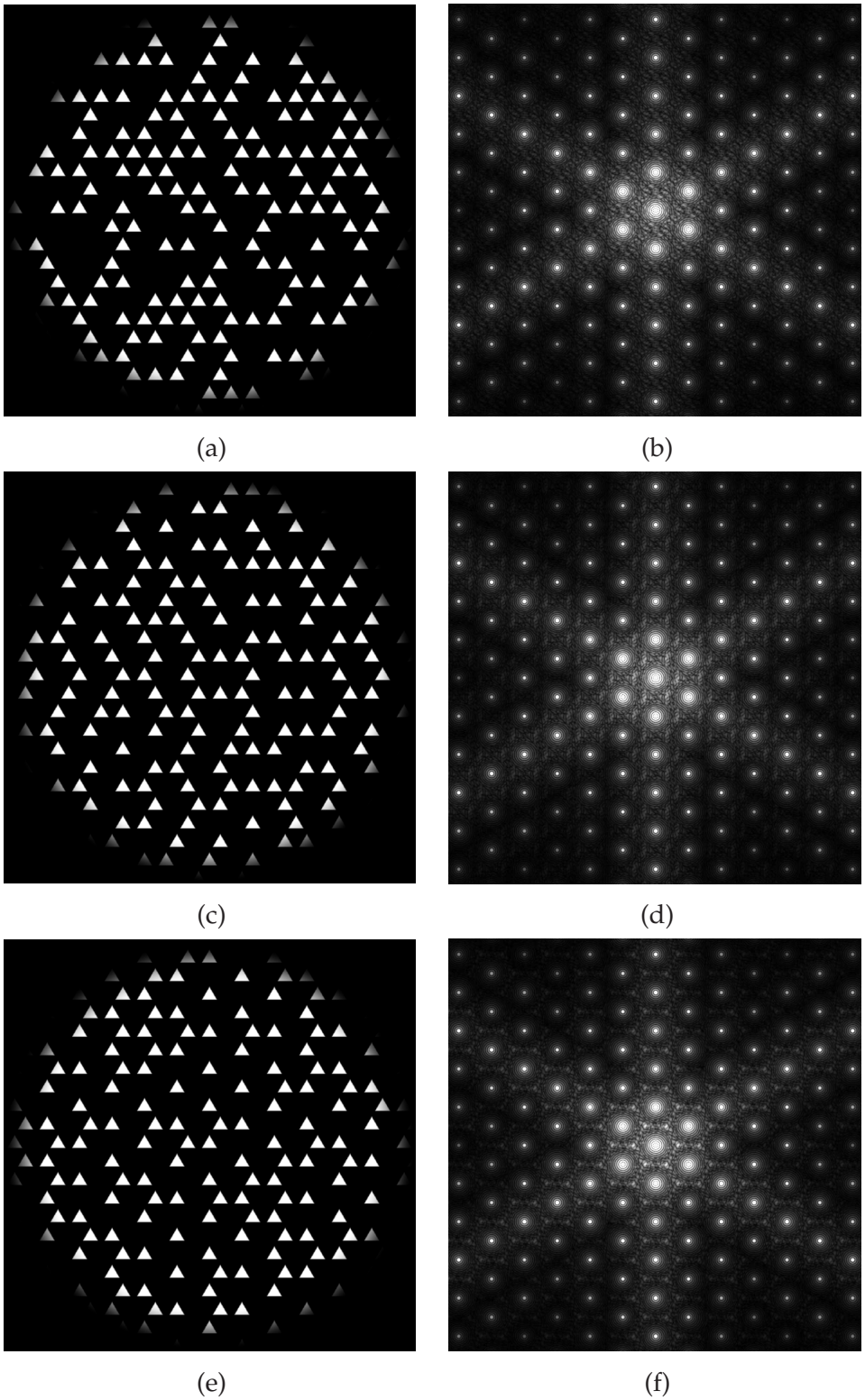


**Figure 5.10** Ising model simulated lattices with either an up triangle or no scatterer (left) and their averaged diffraction patterns (right) for $T = 5$ (top row), $T = 0.55$ (middle row) and T = 0.05 (bottom row).

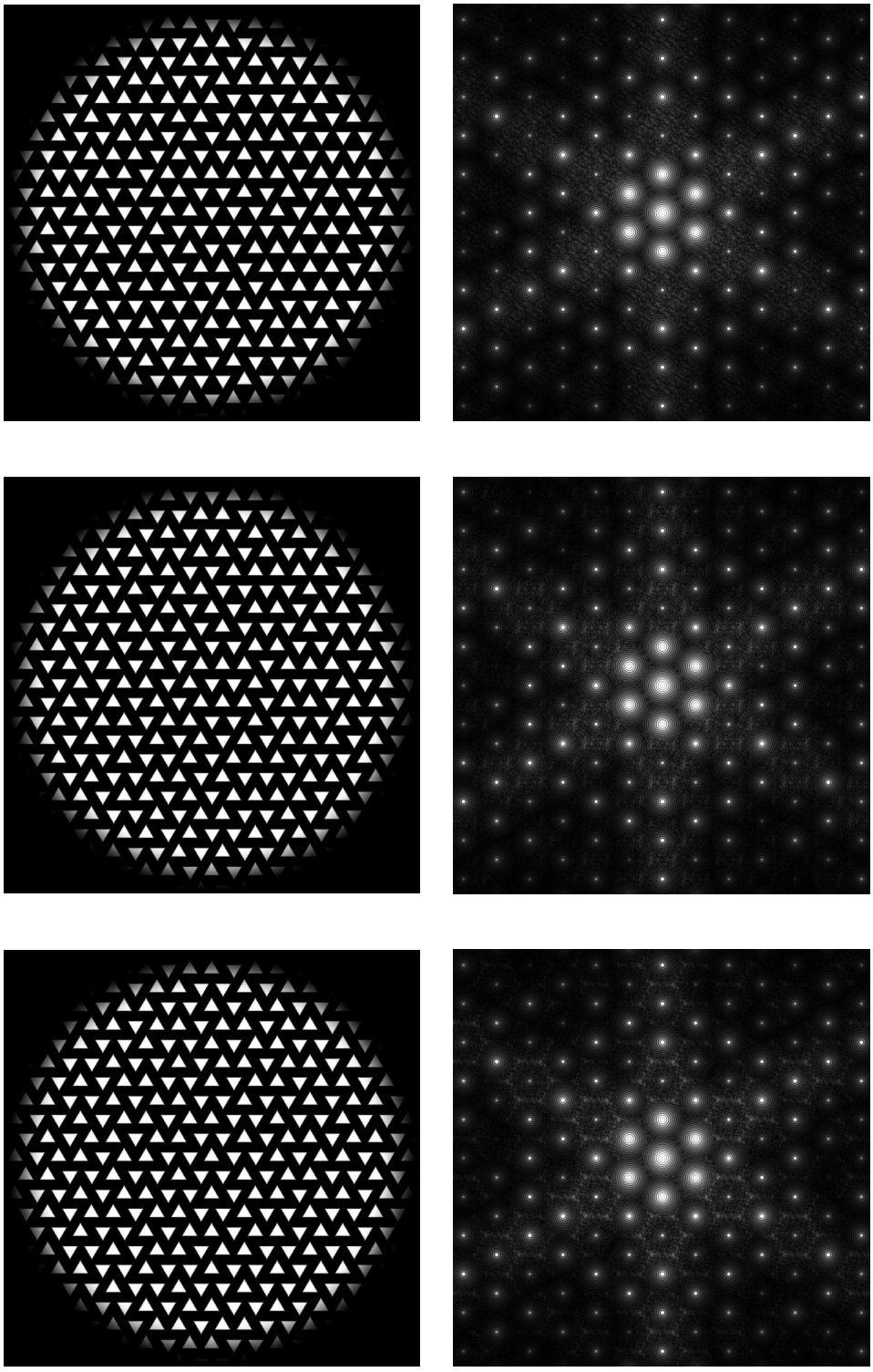

**Figure 5.11** Ising model simulated lattices with either an up or down triangle (left) and their averaged diffraction patterns (right) for $T = 5$ (top row), $T = 0.55$ (middle row) and T = 0.05 (bottom row).

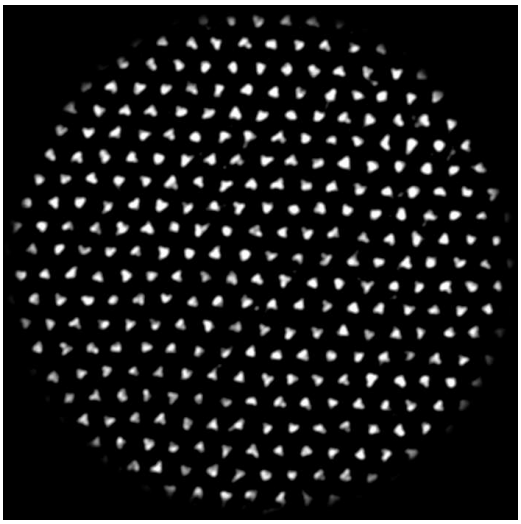

**Figure 5.12** Electron micrograph of a frog muscle.

orientations is given by

$$\begin{aligned}\langle I(\mathbf{R})\rangle_d &= \sum_j \sum_k \sum_{j'} \sum_{k'} \big[s(\mathbf{r}_{jk})s(\mathbf{r}_{j'k'}) \exp(i2\pi\mathbf{R}\cdot[\mathbf{r}_{jk}-\mathbf{r}_{j'k'}]) \\ &\quad \times\langle F_{jk}(\mathbf{R})F^*_{j'k'}(\mathbf{R}) \exp(i2\pi\mathbf{R}\cdot[\mathbf{d}_{jk}-\mathbf{d}_{j'k'}])\rangle_d\big], \end{aligned} \tag{5.2}$$

where $\mathbf{d}_{jk}$ are the lattice distortions at site $(j,k)$ in a two dimensional lattice, the substitution disorder is represented by the diffraction $F_{jk}(\mathbf{R})$ due to the scatterer at site $(j,k)$, $\mathbf{r}_{jk}$ is the position of the site $(j,k)$ in the unperturbed lattice, and $s(\mathbf{r}_{jk})$ is the shape function. If there is no lattice disorder, i.e. only substitution disorder, then

$$\langle F_{jk}(\mathbf{R})F^*_{j'k'}(\mathbf{R}) \exp(i2\pi\mathbf{R}\cdot[\mathbf{d}_{jk}-\mathbf{d}_{j'k'}])\rangle_d = \langle F_{jk}(\mathbf{R})F^*_{j'k'}(\mathbf{R})\rangle_d. \tag{5.3}$$

Substituting Eq. (5.3) into Eq. (5.2) and assuming stationary statistics gives

$$\langle I(\mathbf{R})\rangle_d = \sum_j \sum_k \langle F_{jk}(\mathbf{R})F^*_{00}(\mathbf{R})\rangle_d \exp(i2\pi\mathbf{R}\cdot\mathbf{r}_{jk}) \sum_{j'} \sum_{k'} s(\mathbf{r}_{j'+j,k'+k})s(\mathbf{r}_{j'k'}) \tag{5.4}$$

where

$$\mathbf{r}_{jk} = \mathbf{r}_{j'+j,k'+k} - \mathbf{r}_{j'k'} \tag{5.5}$$

is now interpreted as the intersite vector joining the sites $(j'+j, k'+k)$ and $(j',k')$. The

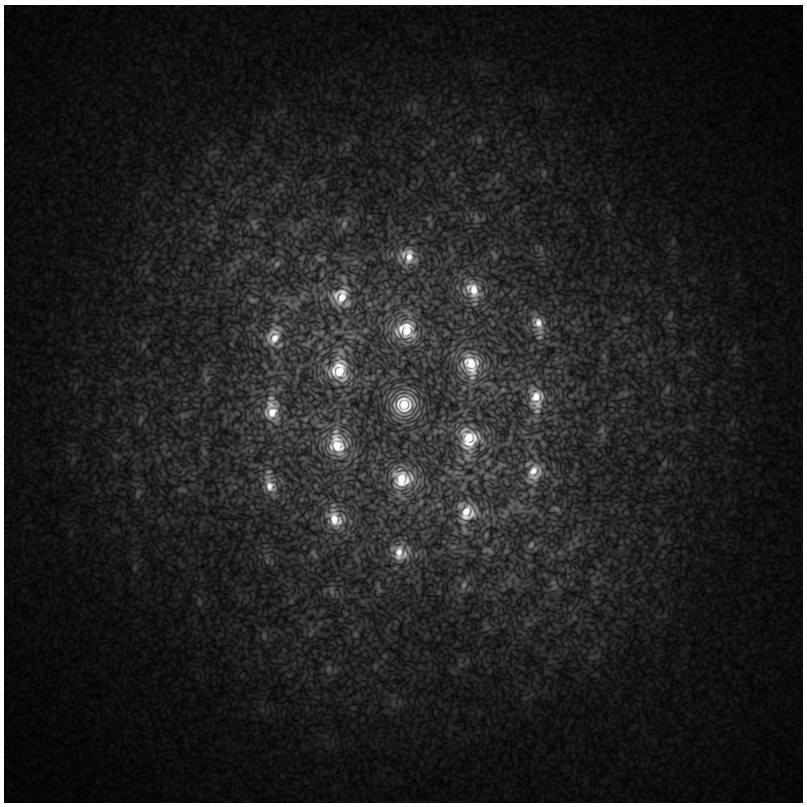

(a)

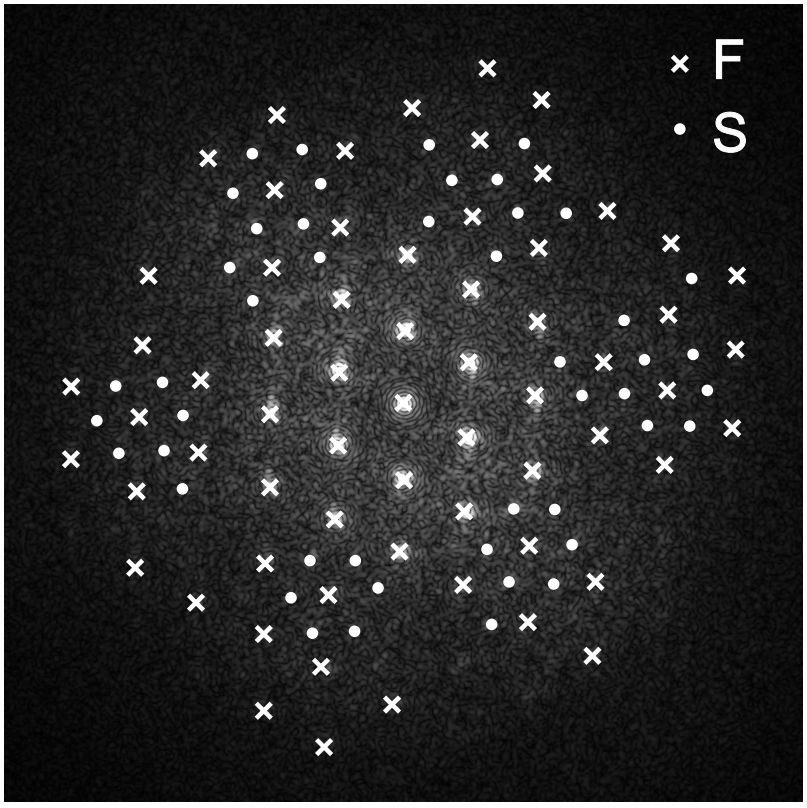


(b)

**Figure 5.13** (a) The diffraction pattern calculated using the DFT of Fig. 5.12 and (b) the diffraction pattern with markers indicating reflections. Six superlattice reflections (S) surrounding a single fundamental lattice reflection (F) are faint but present.

autocorrelation of the shape function $t(\mathbf{r})$ is given by [Str93, SM96a]

$$\frac{t(\mathbf{r}_{jk})}{A_{cell}} = \sum_{j'} \sum_{k'} s(\mathbf{r}_{j'+j,k'+k}) s(\mathbf{r}_{j'k'}), \tag{5.6}$$

and Eq. (5.4) simplifies to

$$\langle I(\mathbf{R}) \rangle_d = \frac{1}{A_{cell}} \sum_{j} \sum_{k} t(\mathbf{r}_{jk}) \langle F_{jk}(\mathbf{R}) F_{00}^*(\mathbf{R}) \rangle_d \exp(i2\pi \mathbf{R} \cdot \mathbf{r}_{jk}). \tag{5.7}$$

If the substitution disorder is correlated and has stationary statistics, then the term $\langle F_{jk}(\mathbf{R}) F_{00}^*(\mathbf{R}) \rangle_d$ can be derived as follows. For convenience, let $s_{jk} = 1$ or $s_{jk} = -1$ denote the site $(j,k)$ being occupied by a scatterer (or molecule) with diffraction $F_1(\mathbf{R})$ or $F_2(\mathbf{R})$, respectively. It is assumed that the two scatterers occur in equal proportions so that $\langle s_{jk} = 0 \rangle$. Then the structure factor at site $(j,k)$ can be written as $F_{jk} = \alpha + \beta s_{jk}$, where

$$\alpha = \frac{F_1(\mathbf{R}) + F_2(\mathbf{R})}{2} \tag{5.8}$$

and

$$\beta = \frac{F_1(\mathbf{R}) - F_2(\mathbf{R})}{2}. \tag{5.9}$$

The product term in Eq. (5.7) can then be expressed in terms of $F_1(\mathbf{R})$ and $F_2(\mathbf{R})$ as

$$\begin{aligned}
\langle F_{jk}(\mathbf{R}) F_{00}^*(\mathbf{R}) \rangle_d &= \langle (\alpha + \beta s_{jk})(\alpha^* + \beta^* s_{00}) \rangle_d \\
&= \langle |\alpha|^2 + \alpha\beta^* s_{00} + \alpha^* \beta s_{jk} + |\beta|^2 s_{jk} s_{00}) \rangle_d \\
&= |\alpha|^2 + \alpha\beta^* \langle s_{00} \rangle_d + \alpha^* \beta \langle s_{jk} \rangle_d + |\beta|^2 \langle s_{jk} s_{00} \rangle_d \\
&= |\alpha|^2 + |\beta|^2 \rho_{jk} \\
&= \left| \frac{F_1(\mathbf{R}) + F_2(\mathbf{R})}{2} \right|^2 + \left| \frac{F_1(\mathbf{R}) - F_2(\mathbf{R})}{2} \right|^2 \rho_{jk},
\end{aligned} \tag{5.10}$$

where $\rho_{jk}$ is the correlation coefficient between the sites $(0,0)$ and $(j,k)$.

It is convenient to write the diffraction in terms of the square of the average structure factor $|\langle F(\mathbf{R}) \rangle_d|^2$ and the average of the squared structure factors $\langle |F(\mathbf{R})|^2 \rangle_d$. For two kinds of scatterers, these quantities are given by

$$|\langle F(\mathbf{R}) \rangle_d|^2 = \left| \frac{F_1(\mathbf{R}) + F_2(\mathbf{R})}{2} \right|^2 \tag{5.11}$$

and

$$\langle |F(\mathbf{R})|^2 \rangle_d = \frac{|F_1(\mathbf{R})|^2 + |F_2(\mathbf{R})|^2}{2}. \tag{5.12}$$

Using Eq. (5.11) and Eq. (5.12), Eq. (5.10) can be written as

$$\begin{aligned}
\langle F_{jk}(\mathbf{R})F_{00}^{*}(\mathbf{R})\rangle_d &= |\langle F(\mathbf{R})\rangle_d|^2 + \frac{\rho_{jk}}{4}\Big[\Big(F_1(\mathbf{R}) - F_2(\mathbf{R})\Big)\Big(F_1^{*}(\mathbf{R}) - F_2^{*}(\mathbf{R})\Big)\Big] \\
&= |\langle F(\mathbf{R})\rangle_d|^2 + \frac{\rho_{jk}}{4}\Big(\,|F_1(\mathbf{R})|^2 + |F_2(\mathbf{R})|^2 - F_1(\mathbf{R})F_2^{*}(\mathbf{R}) - F_1^{*}(\mathbf{R})F_2(\mathbf{R})\Big) \\
&= |\langle F(\mathbf{R})\rangle_d|^2 + \rho_{jk}\Big(\frac{|F_1(\mathbf{R})|^2 + |F_2(\mathbf{R})|^2}{2} - \Big|\frac{F_1(\mathbf{R}) + F_2(\mathbf{R})}{2}\Big|^2\Big) \\
&= |\langle F(\mathbf{R})\rangle_d|^2 + \rho_{jk}\Big[\langle|F(\mathbf{R})|^2\rangle_d - |\langle F(\mathbf{R})\rangle_d|^2\,\Big]. \qquad (5.13)
\end{aligned}$$

Substituting Eq. (5.13) into Eq. (5.7) gives,

$$\begin{aligned}
\langle I(\mathbf{R})\rangle_d &= \frac{1}{A_{cell}}\sum_j\sum_k t(\mathbf{r}_{jk})\exp(i2\pi\mathbf{R}\cdot\mathbf{r}_{jk}) \\
&\quad\times\Big\{\,|\langle F(\mathbf{R})\rangle_d|^2 + \rho_{jk}\Big[\langle|F(\mathbf{R})|^2\rangle_d - |\langle F(\mathbf{R})\rangle_d|^2\,\Big]\Big\}. \qquad (5.14)
\end{aligned}$$

This is the expression for the diffraction by an ensemble of crystallites with correlated substitution disorder, identical shapes and with their lattice identically oriented. Evaluation of this expression involves summing over the lattice points within autocorrelation of the crystallite. It does not require realisations of the lattice configurations and averaging as in the previous section and is thus computationally much more efficient.

To provide some insight, Eq. (5.14) can be separated into two terms containing the Bragg term and the diffuse term as

$$\langle I(\mathbf{R})\rangle_d = I^B(\mathbf{R}) + I^D(\mathbf{R}), \qquad (5.15)$$

where $I^B(\mathbf{R})$ is the Bragg intensity given by

$$\begin{aligned}
I^B(\mathbf{R}) &= \frac{1}{A_{cell}}\,|\langle F(\mathbf{R})\rangle_d|^2\sum_j\sum_k t(\mathbf{r}_{jk})\exp(i2\pi\mathbf{R}\cdot\mathbf{r}_{jk}) \\
&= |\langle F(\mathbf{R})\rangle_d|^2\,\mathcal{Z}(\mathbf{R}), \qquad (5.16)
\end{aligned}$$

where

$$\begin{aligned}
\mathcal{Z}(\mathbf{R}) &= \frac{1}{A_{cell}}\sum_j\sum_k t(\mathbf{r}_{jk})\exp(i2\pi\mathbf{R}\cdot\mathbf{r}_{jk}) \\
&= \left|\sum_j\sum_k s(\mathbf{r}_{jk})\exp(i2\pi\mathbf{R}\cdot\mathbf{r}_{jk})\right|^2 \qquad (5.17)
\end{aligned}$$

is the interference function of the two dimensional lattice [Str93] and

$$I^D(\mathbf{R}) = \frac{1}{A_{cell}}\Big[\langle|F(\mathbf{R})|^2\rangle_d - |\langle F(\mathbf{R})\rangle_d|^2\Big]\sum_j\sum_k \rho_{jk}t(\mathbf{r}_{jk})\exp(i2\pi\mathbf{R}\cdot\mathbf{r}_{jk}). \quad (5.18)$$

It is convenient to define the Bragg term separately as it is independent of the correlation function, hence remains constant for all degree of disorder. The diffuse intensity depends on the disorder. Note that $\mathcal{Z}(\mathbf{R})$ increases as $N^2$ whereas the diffuse diffraction tends to increase as $N$ [Str93], where $N$ is the number of sites, so that the significance of the disorder decreases as the crystallite size increases.

For uncorrelated substitution disorder, i.e. $\rho_{00} = 1$ and $\rho_{jk} = 0$ otherwise, Eq. (5.14) simplifies to

$$\begin{aligned}\langle I(\mathbf{R})\rangle_d &= \frac{1}{A_{cell}}|\langle F(\mathbf{R})\rangle_d|^2\sum_{j\neq 0}\sum_{k\neq 0}t(\mathbf{r}_{jk})\exp(i2\pi\mathbf{R}\cdot\mathbf{r}_{jk}) + N\langle|F(\mathbf{R})|^2\rangle_d \\ &= |\langle F(\mathbf{R})\rangle_d|^2\,\mathcal{Z}(\mathbf{R}) + N\Big\{\langle|F(\mathbf{R})|^2\rangle_d - |\langle F(\mathbf{R})\rangle_d|^2\Big\} \\ &= I^B(\mathbf{R}) + N\Big\{\langle|F(\mathbf{R})|^2\rangle_d - |\langle F(\mathbf{R})\rangle_d|^2\Big\}. \quad (5.19)\end{aligned}$$

The Bragg term is the same as for correlated disorder (and proportional to $N^2$) and the diffuse intensity is $\langle|F(\mathbf{R})|^2\rangle_d - |\langle F(\mathbf{R})\rangle_d|^2$ scaled by the number of lattice sites.

## 5.5 Diffraction by a Crystal with Correlated Substitution Disorder: Simulations

The expression derived in the previous section is used here to calculate 2D diffraction patterns of crystals with TIA disorder. It is convenient to write Eq. (5.15) in Cartesian coordinates as

$$\begin{aligned}\langle I(u,v)\rangle_d &= \frac{1}{A_{cell}}|\langle F(u,v)\rangle_d|^2\sum_j\sum_k t(\mathbf{r}_{jk})\exp(i2\pi ux_{jk}+vy_{jk}) \\ &\quad + \frac{1}{A_{cell}}\Big[\langle|F(u,v)|^2\rangle_d - |\langle F(u,v)\rangle_d|^2\Big]\sum_j\sum_k \rho_{jk}t(\mathbf{r}_{jk})\exp(i2\pi ux_{jk}+vy_{jk}) \\ &= I^B(u,v) + I^D(u,v), \quad (5.20)\end{aligned}$$

where $\mathbf{r}_{jk} = (x_{jk}, y_{jk})$. Calculations are made for hexagonal lattices with circular crystallites with radius $r_c = 8$ pixels ($\sim 200$ sites). The lattice spacing is unity and the diffraction pattern is calculated at intervals $\Delta u = \Delta v = 0.1$. Making use of the symmetry of the diffraction patterns, only the first quadrant of the diffraction image needs to be calculated. Calculations were made for the TIA correlation function at $T = \infty$ ($\rho_{00} = 1$ and $\rho_{jk} = 0$

otherwise), $T = 0.55$ (using Eq. (3.35)) and $T = 0$ (using Eq. (3.23)).

### 5.5.1 Point Scatterers

The case of point scatterers and no scatterers, is considered first, i.e. $f_1(x, y) = \delta(x, y)$ and $f_2(x, y) = 0$. The diffraction is calculated by substituting $F_1(u, v) = 1$ and $F_2(u, v) = 0$ into Eq. (5.20) giving

$$\begin{aligned}\langle I(u,v)\rangle_d &= \frac{1}{4A_{cell}}\sum_j\sum_k t(\mathbf{r}_{jk})\exp(i2\pi ux_{jk}+vy_{jk}) \\ &\quad +\frac{1}{4A_{cell}}\sum_j\sum_k \rho_{jk}t(\mathbf{r}_{jk})\exp(i2\pi ux_{jk}+vy_{jk}).\end{aligned} \tag{5.21}$$

The diffraction patterns for the three cases ($T = \infty$, 0.55 and 0) are shown in Fig. 5.14. In the case of random disorder ($T = \infty$), the fundamental reflections are observed in addition to a weak continuous background. Note that because the averaging has been done analytically there is no "noise" in the diffraction pattern.

For clarity, the Bragg and the diffuse components are calculated separately and are shown in Fig. 5.15. As the temperature reduces and the disorder becomes more correlated and the diffuse component peaks at the superlattice points. Since the superlattice lies on a hexagonal lattice, its reciprocal lattice should in principle form a hexagonal lattice. However, the diffuse intensity peaks are absent at the Bragg peak positions resulting in a honeycomb lattice. This phenomenon is due to the correlation function (Eq. (3.23)) used where the sign changes from $+1$ when the separation is on the same sublattice to $-1/2$ otherwise. It appears that the sign changes cancel out the diffuse diffraction at the Bragg peak positions.

### 5.5.2 Triangle Scatterers

In order to use Eq. (5.61) to calculate diffraction by a disordered lattice containing triangles, an expression for diffraction by a triangle is required. This is derived here. Denote the density of the up triangle by $f_1(x, y)$, i.e. equal to unity inside the triangle and zero outside. The density of the down triangle is denoted $f_2(x, y)$. The diffraction pattern of the up

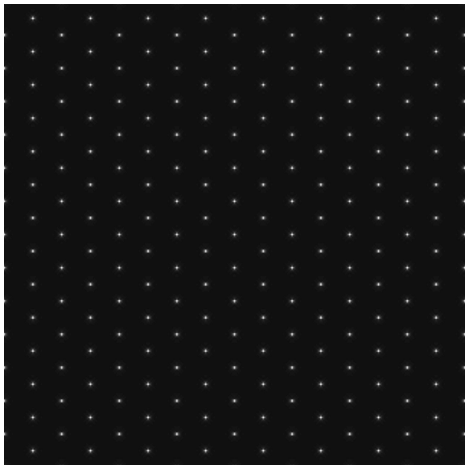

(a)

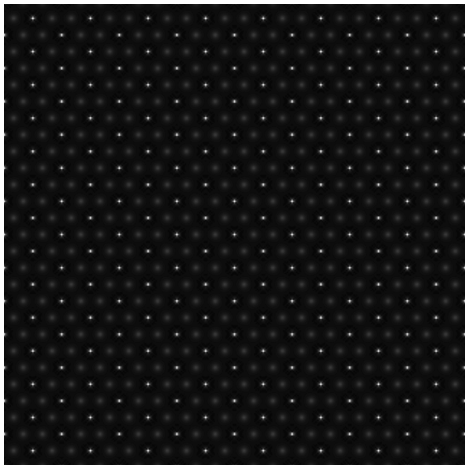

(b)

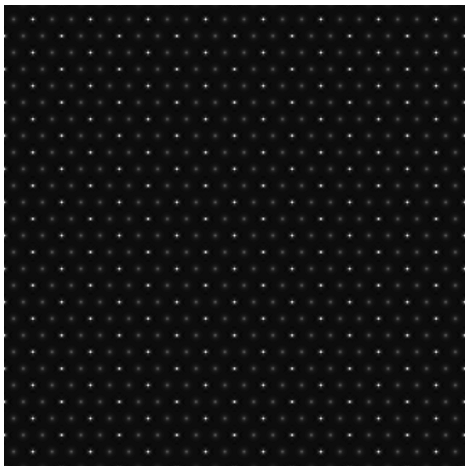

(c)

**Figure 5.14** Diffraction pattern from a hexagonal lattice for the TIA with point scatterers and $r_c = 8$ for (a) $T = \infty$, (b) $T = 0.55$, and (c) $T = 0$.

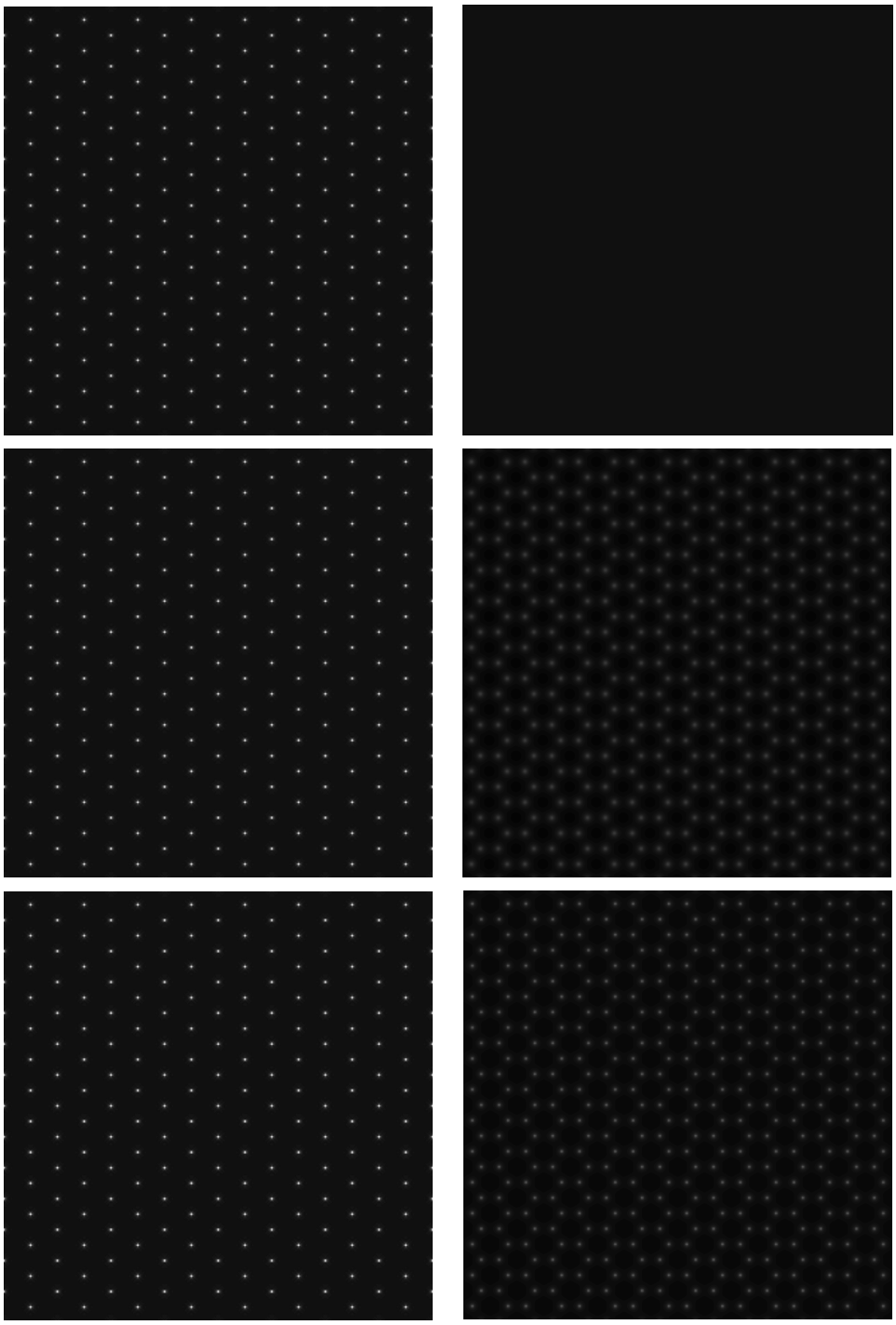

**Figure 5.15** Two contributing terms for the diffraction pattern (Fig. 5.14). Bragg components (left) and diffuse components (right) for $T = \infty$ (top row), $T = 0.55$ (middle row) and $T = 0$ (bottom row).

triangle is then

$$\begin{aligned} F_1(u,v) &= \int_{-\frac{\tau}{2\sqrt{3}}}^{\frac{\tau}{\sqrt{3}}} \int_{-\frac{\tau}{2}}^{\frac{\tau}{2}} f_1(x,y)\exp(i2\pi(ux+vy))dxdy \\ &= \int_{-\frac{\tau}{2\sqrt{3}}}^{\frac{\tau}{\sqrt{3}}} \int_{0}^{\frac{\tau}{3}-\frac{y}{\sqrt{3}}} \exp(i2\pi(ux+vy))dxdy \\ &\quad + \int_{-\frac{\tau}{2\sqrt{3}}}^{\frac{\tau}{\sqrt{3}}} \int_{\frac{y}{\sqrt{3}}-\frac{\tau}{3}}^{0} \exp(i2\pi(ux+vy))dxdy \\ &= \frac{\exp(i\pi\tau(u-v/\sqrt{3}))-\exp(i2\pi\tau v/\sqrt{3})}{4\pi^2 u(v-u/\sqrt{3})} \\ &\quad + \frac{\exp(i2\pi\tau v/\sqrt{3})-\exp(-i\pi\tau(u+v/\sqrt{3}))}{4\pi^2 u(v+u/\sqrt{3})}, \end{aligned} \tag{5.22}$$

The amplitude $|F_1(u,v)|$ is shown in Fig. 5.16 and comparison with Fig. 5.5 shows good agreement.

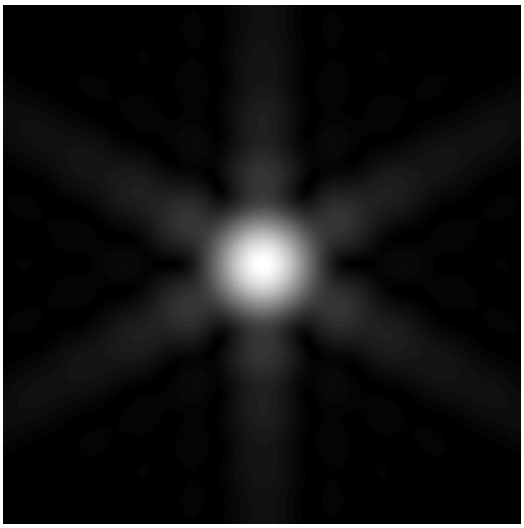

**Figure 5.16** Fourier transform of an equilateral triangle given in Eq. (5.22).

The diffraction pattern for the down triangle is $F_2(u,v) = F_1(u,-v)$, i.e.

$$\begin{aligned} F_2(u,v) &= \frac{\exp(i\pi\tau(u+v/\sqrt{3}))-\exp(-i2\pi\tau v/\sqrt{3})}{4\pi^2 u(-v-u/\sqrt{3})} \\ &\quad + \frac{\exp(-i2\pi\tau v/\sqrt{3})-\exp(-i\pi\tau(u-v/\sqrt{3}))}{4\pi^2 u(-v+u/\sqrt{3})}. \end{aligned} \tag{5.23}$$

Diffraction patterns calculated for up and down triangular scatterers are shown in Fig. 5.17. Modulation of the diffraction pattern by that of an average triangle is evident. The Bragg

and diffuse components are shown in Fig. 5.18 and strengthening of the diffuse intensity at the superlattice points with decreasing temperature is evident.

Computation of the analytical expression took less than 3 minutes on a PC and the computation time for averaging of 100 DFT images took approximately 9 minutes. Comparison of the diffraction patterns with those calculated using the DFT (Fig. 5.11) shows good agreement and validates the analytical expressions. The inherent speed of the FFT helps the direct calculation but note that more than 100 patterns are required for good averaging.

## 5.6 Cylindrically Averaged Diffraction in the Presence of Correlated Substitution Disorder: Theory

In polycrystalline fibers, the individual crystallites are randomly oriented about the fiber axis, as in the case of muscle. The resulting X-ray diffraction is the cylindrical average of the diffracted intensity of a single crystallite. In the 2D dimensional case this corresponds to circular averaging and the diffracted intensity $I(R)$ is given by

$$I(R) = \langle\langle I(\mathbf{R})\rangle_d\rangle_\psi \quad = \quad \frac{1}{2\pi}\int_0^{2\pi} \langle I(R,\psi)\rangle_d \, \mathrm{d}\psi. \tag{5.24}$$

For simplicity, the crystallites are assumed to be circular so that $t(\mathbf{r})$ depends only on $r$. Changing Eq. (5.14) to polar coordinates gives,

$$\begin{aligned}\langle I(R,\psi)\rangle_d \quad &= \quad \frac{1}{A_{cell}}\sum_j\sum_k t(\mathbf{r}_{jk})\exp(i2\pi R r_{jk}\cos(\psi-\phi_{jk})) \\ &\quad \times\Big\{\,|\langle F(R,\psi)\rangle_d|^2 + \rho_{jk}\Big[\langle|F(R,\psi)|^2\rangle_d - |\langle F(R,\psi)\rangle_d|^2\,\Big]\Big\}. \end{aligned}\tag{5.25}$$

As an aside, note that the cylindrically averaged Bragg intensity can be written as

$$\begin{aligned} I^B(R) = \langle I^B(R,\psi)\rangle_\psi \quad &= \quad \langle |\langle F(R,\psi)\rangle_d|^2 \, \mathcal{Z}(R,\psi)\rangle_\psi \\ &= \quad \sum_{h,k} \frac{\mathcal{P}_{hk}(R)}{A_{cell}^2}\,|\langle F(R)\rangle_d|^2 \end{aligned}\tag{5.26}$$

where the sum is over the contributing reflections and $\mathcal{P}_{hk}(R)$ is the radial profile of the $(h,k)$ reflection given by [Str93]

$$\mathcal{P}_{hk}(R) = \frac{1}{2\pi}\int_0^{2\pi} |S(R-R_{hk},\psi-\psi_{hk})| \, \mathrm{d}\psi, \tag{5.27}$$

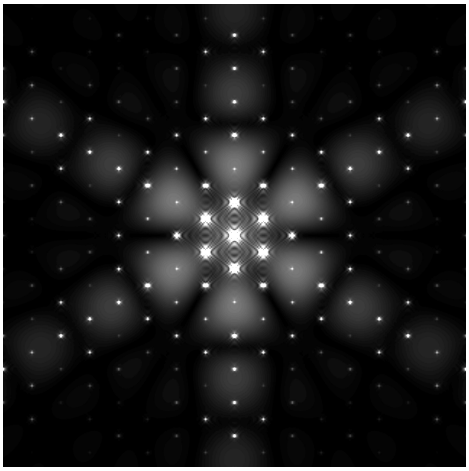

(a)

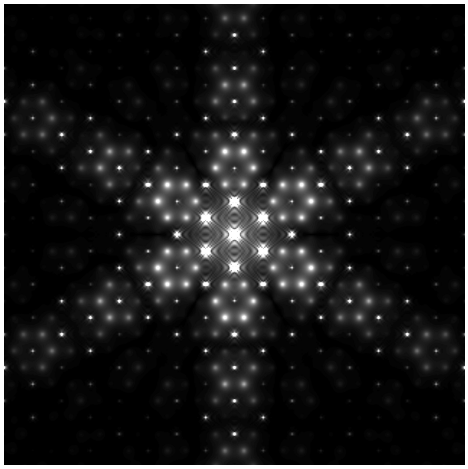

(b)

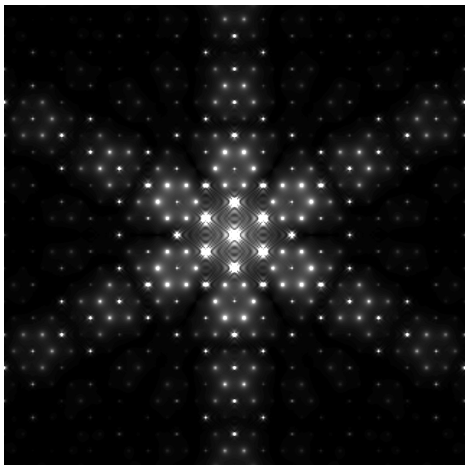

(c)

**Figure 5.17** Diffraction pattern from a hexagonal lattice for the TIA with up and down triangle scatterers and $r_c = 8$ for (a) $T = \infty$, (b) $T = 0.55$, and (c) $T = 0$.

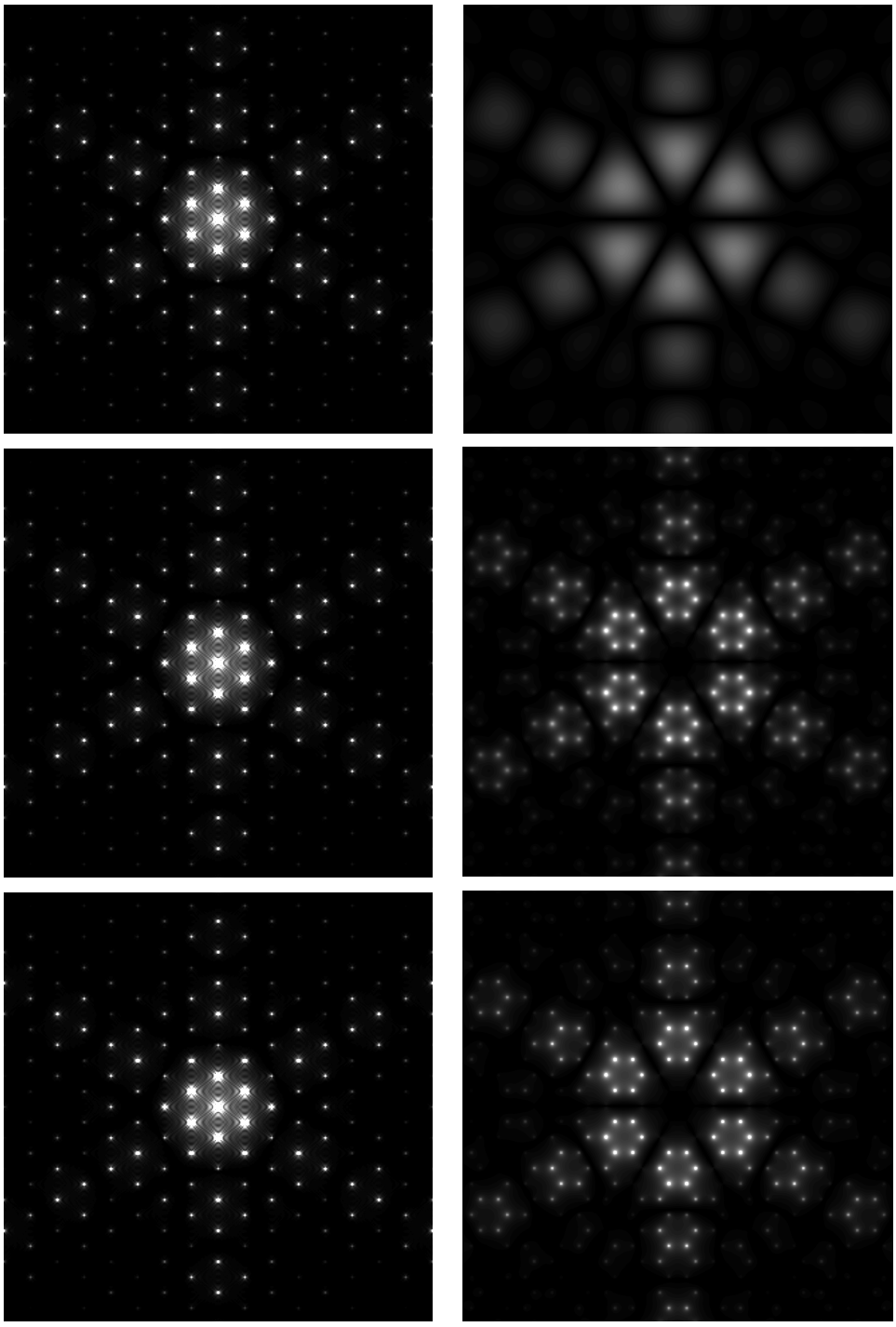

**Figure 5.18** Two contributing terms for the diffraction pattern (Fig. 5.17). Bragg components (left) and diffuse components (right) for $T = \infty$ (top row), $T = 0.55$ (middle row) and $T = 0$ (bottom row).

where

$$S(R-R_{hk},\psi-\psi_{hk}) = r_c \frac{J_1(2\pi r_c[R^2+R_{hk}^2-2RR_{hk}\cos(\psi-\psi_{hk})]^{1/2})}{[R^2+R_{hk}^2-2RR_{hk}\cos(\psi-\psi_{hk})]^{1/2}}. \tag{5.28}$$

It is more convenient here, however, to treat the Bragg intensity as continuous.

To evaluate the angular integral, the scattering factors are expanded in angular Fourier series as

$$F_1(R,\psi) = \sum_{n=-\infty}^{\infty} C_n(R)\exp(in\psi) \tag{5.29}$$

and

$$F_2(R,\psi) = \sum_{m=-\infty}^{\infty} D_m(R)\exp(im\psi). \tag{5.30}$$

Combining Eq. (5.29) and Eq. (5.30) in Eq. (5.11) and Eq. (5.12) gives

$$\begin{aligned}
\langle|F(R,\psi)|^2\rangle_d &= \frac{|F_1(R,\psi)|^2+|F_2(R,\psi)|^2}{2} \\
&= \frac{1}{2}\sum_n\sum_m C_n(R)C_m^*(R)\exp(i[n-m]\psi) \\
&\quad +\frac{1}{2}\sum_n\sum_m D_n(R)D_m^*(R)\exp(i[n-m]\psi) \\
&= \frac{1}{2}\sum_n\sum_m \exp(i[n-m]\psi)\{C_n(R)C_m^*(R)+D_n(R)D_m^*(R)\}
\end{aligned} \tag{5.31}$$

and

$$\begin{aligned}
|\langle F(R,\psi)\rangle_d|^2 &= \left|\frac{F_1(R,\psi)+F_2(R,\psi)}{2}\right|^2 \\
&= \frac{1}{2}\Big(\sum_n C_n(R)\exp(in\psi)+\sum_n D_n(R)\exp(in\psi)\Big) \\
&\quad \times\frac{1}{2}\Big(\sum_m C_m^*(R)\exp(-im\psi)+\sum_m D_m^*(R)\exp(-im\psi)\Big) \\
&= \frac{1}{4}\Big(\sum_n[C_n(R)+D_n(R)]\exp(in\psi)\Big)\Big(\sum_m[C_m^*(R)+D_m^*(R)]\exp(-im\psi)\Big) \\
&= \frac{1}{4}\sum_n\sum_m \exp(i[n-m]\psi)\{[C_n(R)+D_n(R)][C_m^*(R)+D_m^*(R)]\}.
\end{aligned} \tag{5.32}$$

Subtracting Eq. (5.32) from Eq. (5.31) gives

$$\begin{aligned}\langle|F(R,\psi)|^2\rangle_d - |\langle F(R,\psi)\rangle_d|^2 \\ = \frac{1}{4}\sum_n\sum_m \exp(i[n-m]\psi)\big\{[C_n(R)-D_n(R)][C_m^*(R)-D_m^*(R)]\big\}.\end{aligned} \tag{5.33}$$

Let

$$g_{nm}(R) = \frac{1}{4}[C_n(R)+D_n(R)][C_m^*(R)+D_m^*(R)] \tag{5.34}$$

and

$$h_{nm}(R) = \frac{1}{4}[C_n(R)-D_n(R)][C_m^*(R)-D_m^*(R)]. \tag{5.35}$$

Substituting Eq. (5.25) into Eq. (5.24) then gives

$$\begin{aligned} I(R) &= \frac{1}{A_{cell}}\sum_j\sum_k t(r_{jk}) \\ &\quad \times\sum_n\sum_m g_{nm}(R)\cdot\frac{1}{2\pi}\int_0^{2\pi}\exp(i2\pi R r_{jk}\cos(\psi-\phi_{jk}))\exp(i[n-m]\psi)\mathrm{d}\psi \\ &\quad +\frac{1}{A_{cell}}\sum_j\sum_k t(r_{jk})\rho_{jk} \\ &\quad \times\sum_n\sum_m h_{nm}(R)\cdot\frac{1}{2\pi}\int_0^{2\pi}\exp(i2\pi R r_{jk}\cos(\psi-\phi_{jk}))\exp(i[n-m]\psi)\mathrm{d}\psi \\ &= \frac{1}{A_{cell}}\sum_j\sum_k t(r_{jk})\sum_n\sum_m g_{nm}(R)f_{jkmn}(R) \\ &\quad +\frac{1}{A_{cell}}\sum_j\sum_k t(r_{jk})\rho_{jk}\sum_n\sum_m h_{nm}(R)f_{jkmn}(R), \end{aligned} \tag{5.36}$$

where $f_{jkmn}(R)$ denotes the integral

$$f_{jkmn}(R) = \frac{1}{2\pi}\int_0^{2\pi}\exp(i2\pi R r_{jk}\cos(\psi-\phi_{jk}))\exp(i[n-m]\psi)\mathrm{d}\psi. \tag{5.37}$$

A change of variables, $\psi' = \psi - \phi_{jk}$ and referring to Appendix A.1 gives

$$\begin{aligned} f_{jkmn}(R) &= \frac{1}{2\pi}\int_0^{2\pi}\exp(i2\pi R r_{jk}\cos\psi')\exp(i[n-m][\psi'+\phi_{jk}])\mathrm{d}\psi' \\ &= \frac{1}{2\pi}\exp(i[n-m]\phi_{jk})\int_0^{2\pi}\exp(i2\pi R r_{jk}\cos\psi')\exp(i[n-m]\psi')\mathrm{d}\psi' \\ &= i^{n-m}J_{n-m}(2\pi R r_{jk})\exp(i[n-m]\phi_{jk}) \\ &= J_{n-m}(2\pi R r_{jk})\exp(i[n-m][\phi_{jk}+\pi/2]). \end{aligned} \tag{5.38}$$

Substituting Eq. (5.38) into Eq. (5.36) gives

$$\begin{aligned} I(R) &= \frac{1}{A_{cell}} \sum_j \sum_k t(r_{jk}) \\ &\times \sum_n \sum_m g_{nm}(R) J_{n-m}(2\pi R r_{jk}) \exp(i[n-m][\phi_{jk}+\pi/2]) \\ &+ \frac{1}{A_{cell}} \sum_j \sum_k t(r_{jk}) \rho_{jk} \\ &\times \sum_n \sum_m h_{nm}(R) J_{n-m}(2\pi R r_{jk}) \exp(i[n-m][\phi_{jk}+\pi/2]). \end{aligned} \tag{5.39}$$

The diffracted intensity is real and so the imaginary terms in Eq. (5.39) must cancel, giving

$$\begin{aligned} I(R) &= \frac{1}{4A_{cell}} \sum_j \sum_k t(r_{jk}) \\ &\times \sum_n \sum_m J_{n-m}(2\pi R r_{jk}) \mathbb{R}\Big\{ g_{nm}(R) \exp(i[n-m][\phi_{jk}+\pi/2]) \Big\} \\ &+ \frac{1}{4A_{cell}} \sum_j \sum_k t(r_{jk}) \rho_{jk} \\ &\times \sum_n \sum_m J_{n-m}(2\pi R r_{jk}) \mathbb{R}\Big\{ h_{nm}(R) \exp(i[n-m][\phi_{jk}+\pi/2]) \Big\}. \end{aligned} \tag{5.40}$$

Eq. (5.40) is a general expression for the cylindrically averaged intensity diffracted from an ensemble of crystallites in the presence of correlated substitution disorder.

### 5.6.1 Symmetry Considerations for a Hexagonal Lattice

For a hexagonal lattice, the number of calculations in Eq. (5.40) can be reduced using symmetry as follows [Str93]. Note that the correlation function must possess the same symmetry of the underlying lattice, which is the case since, as shown in Chapter 3, the correlation function is, to an excellent approximation, circularly symmetric.

For an unperturbed hexagonal lattice for each lattice vector $\mathbf{r}_{jk}$ at an angle $\phi_{jk}$ to the $a$ axis (Fig. 1.28), such that $0 \leq \phi_{jk} < \pi/3$, there are 5 other vectors of the same length, that are related by six-fold symmetry. The terms in Eq. (5.40) that correspond to these vectors can

be grouped together giving

$$\begin{aligned} I(R) &= \frac{1}{A_{cell}} \sum_{j\geq 0} \sum_{k\geq 0} t(r_{jk}) \\ &\times \sum_n \sum_m J_{n-m}(2\pi R r_{jk}) \mathbb{R}\Big\{ g_{nm}(R) \sum_{p=0}^{5} \exp(i[n-m]([\phi_{jk}+\pi/2]+p\pi/3)) \Big\} \\ &+ \frac{1}{A_{cell}} \sum_{j\geq 0} \sum_{k\geq 0} t(r_{jk}) \rho_{jk} \\ &\times \sum_n \sum_m J_{n-m}(2\pi R r_{jk}) \mathbb{R}\Big\{ h_{nm}(R) \sum_{p=0}^{5} \exp(i[n-m]([\phi_{jk}+\pi/2]+p\pi/3)) \Big\}, \end{aligned} \tag{5.41}$$

where the indices $j$ and $k$ are restricted to values corresponding to vectors with angles in the range $0 \leq \phi_{jk} < \pi/3$. Since

$$\sum_{p=0}^{5} \exp(i[n-m]p\pi/3) = \begin{cases} 6 & \text{if } n-m \text{ is divisible by 6} \\ 0 & \text{otherwise} \end{cases}$$

all of the terms in Eq. (5.41) for which $n-m$ is not divisible by six vanish. Introducing the notation

$$\sum_n \sum_m^{(i)}$$

to denote a double summation over pairs of indices $n$ and $m$ for which $n-m$ is divisible by the integer $i$ allows Eq. (5.41) to be written as

$$\begin{aligned} I(R) &= \frac{6}{A_{cell}} \sum_{j\geq 0} \sum_{k\geq 0} t(r_{jk}) \\ &\times \sum_n \sum_m^{(6)} J_{n-m}(2\pi R r_{jk}) \mathbb{R}\Big\{ g_{nm}(R) \exp(i[n-m][\phi_{jk}+\pi/2]) \Big\} \\ &+ \frac{6}{A_{cell}} \sum_{j\geq 0} \sum_{k\geq 0} t(r_{jk}) \rho_{jk} \\ &\times \sum_n \sum_m^{(6)} J_{n-m}(2\pi R r_{jk}) \mathbb{R}\Big\{ h_{nm}(R) \exp(i[n-m][\phi_{jk}+\pi/2]) \Big\}. \end{aligned} \tag{5.42}$$

The number of calculations can be further reduced by making use of the reflection symmetry in the line $k = j$. Noting that $r_{kj} = r_{jk}$ and $\phi_{kj} = \frac{\pi}{3} - \phi_{jk}$ and introducing the

multiplicity factor, $b_{jk}$,

$$b_{jk} = \begin{cases} 1 & \text{if } j = k = 0 \\ 6 & \text{if } j > 0 \text{ and either } k = 0 \text{ or } k = j \\ 12 & \text{otherwise,} \end{cases}$$

and the phase factor, $\Theta_p(\phi_{jk})$,

$$\Theta_p(\phi_{jk}) = \begin{cases} 1 & \phi_{jk} = 0 \\ (-1)^{p/6} & \phi_{jk} = \pi/6 \\ \cos(p\phi_{jk}) & 0 < \phi_{jk} < \pi/6, \end{cases}$$

Eq. (5.42) reduces to

$$\begin{aligned} \langle\langle I(R)\rangle_d\rangle_\psi &= \frac{1}{A_{cell}} \sum_{j\geq 0} \sum_{k=0}^{j} b_{jk} t(r_{jk}) \\ &\quad \times \sum_n \sum_m{}^{(6)} \Theta_{n-m}(\phi_{jk}) J_{n-m}(2\pi R r_{jk}) \mathbb{R}\Big\{ g_{nm}(R) \exp(i[n-m]\pi/2) \Big\} \\ &\quad + \frac{1}{A_{cell}} \sum_{j\geq 0} \sum_{k=0}^{j} b_{jk} t(r_{jk}) \rho_{jk} \\ &\quad \times \sum_n \sum_m{}^{(6)} \Theta_{n-m}(\phi_{jk}) J_{n-m}(2\pi R r_{jk}) \mathbb{R}\Big\{ h_{nm}(R) \exp(i[n-m]\pi/2) \Big\}. \end{aligned} \tag{5.43}$$

The phase factor $\Theta_{n-m}(\phi_{jk})$ is symmetric with respect to $n$ and $m$ while $J_{n-m}(2\pi R r_{jk})$ changes sign with an interchange of $m$ and $n$ according to Appendix A.1. Since only terms for which $n - m$ are divisible by 6 are included in Eq. (5.43), $n - m$ is even, so that

$$J_{-2n}(x) = J_{2n}(x). \tag{5.44}$$

Therefore the terms in Eq. (5.43) corresponding to interchanging $n$ and $m$ are identical and

can be combined, further reducing the number of required calculations, giving

$$\begin{aligned} I(R) &= \frac{1}{A_{cell}} \sum_{j\geq 0} \sum_{k=0}^{j} b_{jk} t(r_{jk}) \\ &\times \sum_{n} \sum_{m\leq n}^{(6)} \epsilon_{n-m} \Theta_{n-m}(\phi_{jk}) J_{n-m}(2\pi R r_{jk}) \mathbb{R}\Big\{ g_{nm}(R) \exp(i[n-m]\pi/2) \Big\} \\ &+ \frac{1}{A_{cell}} \sum_{j\geq 0} \sum_{k=0}^{j} b_{jk} t(r_{jk}) \rho_{jk} \\ &\times \sum_{n} \sum_{m\leq n}^{(6)} \epsilon_{n-m} \Theta_{n-m}(\phi_{jk}) J_{n-m}(2\pi R r_{jk}) \mathbb{R}\Big\{ h_{nm}(R) \exp(i[n-m]\pi/2) \Big\}, \end{aligned} \tag{5.45}$$

where $\epsilon_n$ is defined by

$$\epsilon_n = \begin{cases} 1 & n = 0 \\ 2 & n \neq 0. \end{cases}$$

Noting that $\exp(i[n-m]\pi/2) = i^{n-m}$ gives

$$\begin{aligned} I(R) &= \frac{1}{A_{cell}} \sum_{j\geq 0} \sum_{k=0}^{j} b_{jk} t(r_{jk}) \\ &\times \sum_{n} \sum_{m\leq n}^{(6)} (-1)^{(n-m)/2} \epsilon_{n-m} \Theta_{n-m}(\phi_{jk}) J_{n-m}(2\pi R r_{jk}) \mathbb{R}\Big\{ g_{nm}(R) \Big\} \\ &+ \frac{1}{A_{cell}} \sum_{j\geq 0} \sum_{k=0}^{j} b_{jk} t(r_{jk}) \rho_{jk} \\ &\times \sum_{n} \sum_{m\leq n}^{(6)} (-1)^{(n-m)/2} \epsilon_{n-m} \Theta_{n-m}(\phi_{jk}) J_{n-m}(2\pi R r_{jk}) \mathbb{R}\Big\{ h_{nm}(R) \Big\}, \end{aligned} \tag{5.46}$$

Equation 5.46 is an alternative for a hexagonal lattice to Eq. (5.40) that significantly reduces the amount of computation.

### 5.6.2 Point Scatterers

If the two scatterers are a point and no scatterer, then the Fourier coefficients of their diffraction are

$$C_n(R) = \begin{cases} 1 & \text{if } n = 0 \\ 0 & \text{otherwise} \end{cases}$$

and

$$D_n(R) = 0.$$

Substitution into the above equations then gives

$$\begin{aligned} I(R) &= \frac{1}{A_{cell}} \sum_{j\geq 0} \sum_{k=0}^{j} b_{jk} t(r_{jk}) J_0(2\pi R r_{jk}) + \frac{1}{A_{cell}} \sum_{j\geq 0} \sum_{k=0}^{j} \rho_{jk} b_{jk} t(r_{jk}) J_0(2\pi R r_{jk}) \\ &= I^B(R) + I^D(R). \end{aligned} \tag{5.47}$$

### 5.6.3 Fourier Coefficients for Diffraction by a Triangle

Calculation of diffraction by a disordered lattice containing triangles using Eq. (5.46) requires first calculating the angular Fourier coefficients $C_n(R)$ and $D_n(R)$ of diffraction by triangles. These coefficients are calculated in this Section.

The Fourier coefficients of the diffraction are obtained via the Fourier coefficients of the triangle as follows. The Fourier transform in polar coordinates is given by

$$F(R,\psi) = \int_0^\infty \int_0^{2\pi} f(r,\phi) \exp(i2\pi R r \cos(\psi - \phi)) r \mathrm{d}r \mathrm{d}\phi. \tag{5.48}$$

where $f(r,\phi)$ represents the triangle in polar coordinates. Expanding $f(r,\phi)$ in an angular Fourier series as

$$f_1(r,\phi) = \sum_n c_n(r) \exp(in\phi), \tag{5.49}$$

using Eq. (5.29) and substituting into Eq. (5.48) gives

$$\begin{aligned} \sum_n C_n(R) \exp(in\psi) &= \int_0^\infty \int_0^{2\pi} \sum_n c_n(r) \exp(in\phi) \exp(i2\pi R r \cos(\psi - \phi)) r \mathrm{d}r \mathrm{d}\phi \\ &= \sum_n \int_0^\infty c_n(r) \int_0^{2\pi} \exp(in\phi) \exp(i2\pi R r \cos(\psi - \phi)) r \mathrm{d}\phi \mathrm{d}r \end{aligned} \tag{5.50}$$

Substituting $\phi' = \psi - \phi$,

$$\begin{aligned} \sum_n C_n(R) \exp(in\psi) &= \sum_n \int_0^\infty c_n(r) \int_0^{2\pi} \exp(in(\psi - \phi')) \exp(i2\pi R r \cos\phi') r \mathrm{d}r \mathrm{d}\phi \\ &= \sum_n \exp(in\psi) \int_0^\infty c_n(r) \int_0^{2\pi} \exp(i(-n)\phi) \exp(i2\pi R r \cos\phi) r \mathrm{d}r \mathrm{d}\phi. \end{aligned} \tag{5.51}$$

Referring to Appendix A.1, Eq. (5.51) simplifies to

$$\sum_n C_n(R)\exp(in\psi) \quad = \quad \sum_n \exp(in\psi)\int_0^\infty c_n(r)\cdot 2\pi i^{-n}J_{-n}(2\pi Rr)r\mathrm{d}r. \tag{5.52}$$

Using the relations in Appendix A.1 and substituting Eq. (A.2) into Eq. (5.53),

$$\sum_n C_n(R)\exp(in\psi) \quad = \quad \sum_n \exp(in\psi)\int_0^\infty c_n(r)\cdot 2\pi i^{n}J_{n}(2\pi Rr)r\mathrm{d}r. \tag{5.53}$$

From Eq. (5.53), $C_n(R)$ is equivalent to

$$C_n(R) \quad = \quad 2\pi i^n\int_0^\infty c_n(r)J_n(2\pi Rr)r\mathrm{d}r. \tag{5.54}$$

Equation 5.54 gives the Fourier coefficients of the diffraction in terms of the coefficients of the scatterer. The Fourier coefficients of the triangle are evaluated below.

The Fourier coefficients for the up triangle are

$$c_n(r) = \frac{1}{2\pi}\int_0^{2\pi} f_1(r,\phi)\exp(-in\phi)\mathrm{d}\phi, \tag{5.55}$$

and the integral is evaluated as follows. The radial coordinate is divided into two intervals; $0 \le r < r_{min}$ and $r_{min} \le r \le r_{max}$ where $r_{min}$ is the distance between the centroid and an edge and $r_{max}$ is the distance between the centroid and a vertex as shown in Fig. 5.19. Note that $r_{max} = 2r_{min} = 2\tau/3$.

Referring to Eq. (5.55) and Fig. 5.19, it is clear that in the interval $0 \le r < r_{min}$,

$$c_n(r) = \begin{cases} 1 & \text{for } n = 0 \text{ and } r < r_{min} \\ 0 & \text{for } n \neq 0 \text{ and } r < r_{min}. \end{cases} \tag{5.56}$$

In the interval $r_{min} \le r \le r_{max}$, the integrand is unity in the interval $(\phi_1(r), \phi_2(r)), (\phi_3(r), \phi_4(r))$

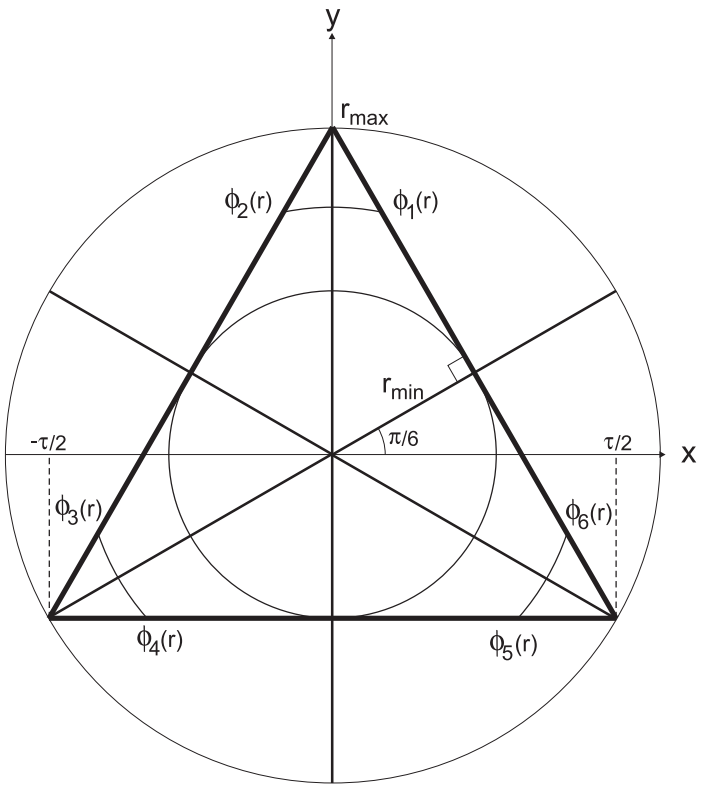


(a)

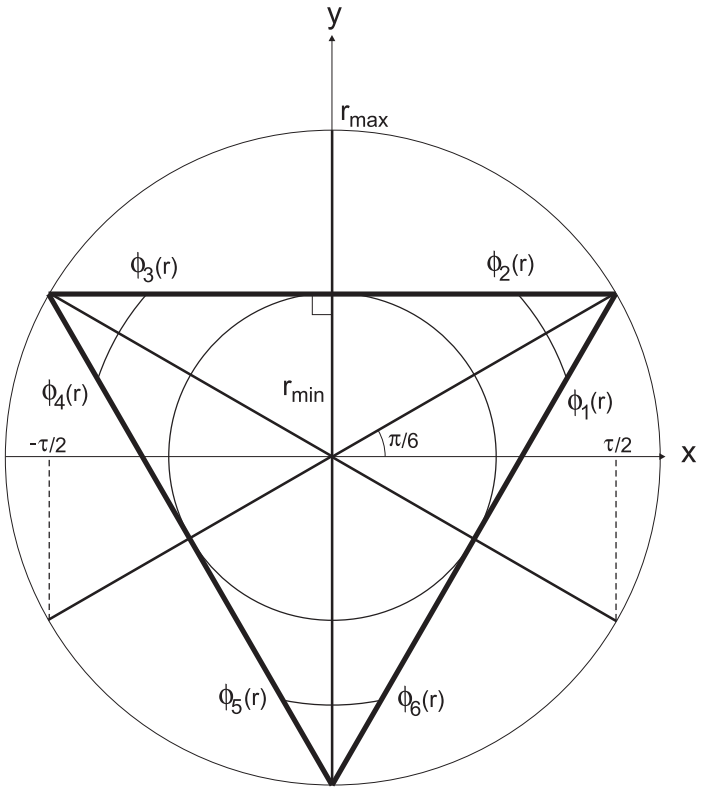


(b)

**Figure 5.19** Geometry and integrating intervals of (a) triangle scatterer oriented upwards and (b) downwards.

and $(\phi_5(r), \phi_6(r))$ where

$$\begin{aligned}
\phi_1(r) &= \frac{\pi}{6} + \epsilon(r), \\
\phi_2(r) &= \frac{5\pi}{6} - \epsilon(r), \\
\phi_3(r) &= \frac{5\pi}{6} + \epsilon(r), \\
\phi_4(r) &= \frac{3\pi}{2} - \epsilon(r), \\
\phi_5(r) &= \frac{3\pi}{2} + \epsilon(r), \\
\phi_6(r) &= 2\pi + \frac{\pi}{6} - \epsilon(r), \\
\epsilon(r) &= \cos^{-1}\Big(\frac{r_{min}}{r}\Big).
\end{aligned} \tag{5.57}$$

For $n = 0$, Eq. (5.55) gives

$$\begin{aligned}
c_0(r) &= \frac{1}{2\pi}\int_0^{2\pi} f_1(r,\phi)\mathrm{d}\phi \\
&= \frac{1}{2\pi}\int_{\phi_1(r)}^{\phi_2(r)} 1\mathrm{d}\phi + \frac{1}{2\pi}\int_{\phi_3(r)}^{\phi_4(r)} 1\mathrm{d}\phi + \frac{1}{2\pi}\int_{\phi_5(r)}^{\phi_6(r)} 1\mathrm{d}\phi \\
&= 1 - \frac{3}{\pi}\epsilon(r) \qquad \text{for } n = 0 \text{ and } r_{min} \le r \le r_{max}.
\end{aligned} \tag{5.58}$$

For $n \neq 0$, substituting the intervals in Eq. (5.57) into Eq. (5.55), the Fourier coefficients are then given by

$$\begin{aligned}
c_n(r) &= \frac{1}{2\pi}\int_{\phi_1(r)}^{\phi_2(r)} \exp(-in\phi)\mathrm{d}\phi + \frac{1}{2\pi}\int_{\phi_3(r)}^{\phi_4(r)} \exp(-in\phi)\mathrm{d}\phi + \frac{1}{2\pi}\int_{\phi_5(r)}^{\phi_6(r)} \exp(-in\phi)\mathrm{d}\phi \\
&= \{\exp(-in\phi_6(r)) - \exp(-in\phi_5(r)) + \exp(-in\phi_4(r)) - \exp(-in\phi_3(r)) \\
&\quad + \exp(-in\phi_2(r)) - \exp(-in\phi_1(r))\}/(-i2\pi n).
\end{aligned} \tag{5.59}$$

Substituting in values and factorising gives

$$\begin{aligned}
c_n(r) &= \Big\{\exp\Big(-in\Big(\frac{\pi}{6} - \epsilon(r)\Big)\Big) - \exp\Big(-in\Big(\frac{3\pi}{2} + \epsilon(r)\Big)\Big) \\
&\quad + \exp\Big(-in\Big(\frac{3\pi}{2} - \epsilon(r)\Big)\Big) - \exp\Big(-in\Big(\frac{5\pi}{6} + \epsilon(r)\Big)\Big) \\
&\quad + \exp\Big(-in\Big(\frac{5\pi}{6} - \epsilon(r)\Big)\Big) - \exp\Big(-in\Big(2\pi + \frac{\pi}{6} + \epsilon(r)\Big)\Big)\Big\}/(-i2\pi n) \\
&= \frac{[\exp(in\epsilon(r)) - \exp(-in\epsilon(r))]\Big[\exp\Big(-in\frac{5\pi}{6}\Big) + \exp\Big(-in\frac{\pi}{6}\Big) + \exp\Big(-in\frac{3\pi}{2}\Big)\Big]}{-i2\pi n} \\
&= -\frac{1}{n\pi}\sin(n\epsilon(r))\Big[\exp\Big(-in\frac{5\pi}{6}\Big) + \exp\Big(-in\frac{\pi}{6}\Big) + \exp\Big(-in\frac{3\pi}{2}\Big)\Big].
\end{aligned} \tag{5.60}$$

Note that the exponential terms in Eq. (5.60) cancel exactly when $n \neq 3m$ and are exactly in phase when $n = 3m$, i.e.

$$\Big[\exp\Big(-in\frac{5\pi}{6}\Big) + \exp\Big(-in\frac{\pi}{6}\Big) + \exp\Big(-in\frac{3\pi}{2}\Big)\Big] = 3\exp\Big(-im\frac{\pi}{2}\Big) \quad \text{for } n = 3m, \tag{5.61}$$

where $m$ is a non-zero integer. Eq. (5.60) then simplifies to

$$c_n(r) \;=\; -\frac{3i^n}{n\pi}\sin(n\epsilon(r)) \quad \text{for } n = 3m \text{ and } r_{min} \leq r \leq r_{max}. \tag{5.62}$$

This can be written as

$$c_n(r) \;=\; -\frac{3i^n}{n\pi}\sqrt{1-\Big(\frac{r_{min}}{r}\Big)^2}\,U_{n-1}\Big(\frac{r_{min}}{r}\Big) \quad \text{for } n = 3m \text{ and } r_{min} \leq r \leq r_{max}, \tag{5.63}$$

where $U_n(\cdot)$ is the $n$-th order Chebyshev polynomial of the second kind (Appendix A.2). The Fourier coefficients for an up triangle, $C_n(R)$ are now derived by substituting Equations (5.56), (5.58) and (5.62) into Eq. (5.54).

For $n = 0$, substituting Eq. (5.56) and Eq. (5.58) into Eq. (5.54) gives

$$\begin{aligned} C_0(R) &= 2\pi\int_0^{r_{min}} J_0(2\pi Rr)r\mathrm{d}r + 2\pi\int_{r_{min}}^{r_{max}}(1-\frac{3}{\pi}\epsilon(r))J_0(2\pi Rr)r\mathrm{d}r \\ &= \frac{r_{max}}{2R}J_1(\pi R r_{max}) + 2\pi\int_{r_{min}}^{r_{max}}(1-\frac{3}{\pi}\epsilon(r))J_0(2\pi Rr)r\mathrm{d}r. \end{aligned} \tag{5.64}$$

For $n = 3m$, substituting Eq. (5.62) into Eq. (5.54) gives

$$C_n(R) \;=\; \frac{6(-1)^{n+1}}{n}\int_{r_{min}}^{r_{max}}\sqrt{1-\Big(\frac{r_{min}}{r}\Big)^2}\,U_{n-1}\Big(\frac{r_{min}}{r}\Big)J_n(2\pi Rr)r\mathrm{d}r. \tag{5.65}$$

The integrals in Eqs. 5.64 and 5.65 do not have a simple analytical solutions and are evaluated numerically.

Consider an up triangle rotated by an angle, $\alpha$. Using the Fourier shift theorem (Appendix A.3) in Eq. (5.49), the Fourier transform of the rotated triangle, denoted $C_n^\alpha(R)$, is given by

$$C_0^\alpha(R) \;=\; C_0(R), \tag{5.66}$$

and

$$C_n^\alpha(R) \;=\; C_n(R)\exp(-in\alpha) \quad \text{for } n \neq 0. \tag{5.67}$$

For the down triangle, $\alpha = \pi$ giving

$$D_0(R) \;=\; C_0(R), \tag{5.68}$$

and

$$D_n(R) \;=\; (-1)^n C_n(R) \quad \text{for } n \neq 0. \tag{5.69}$$

## 5.7 Cylindrically Averaged Diffraction in the Presence of Correlated Substitution Disorder: Simulations

Cylindrically averaged diffraction patterns of lattices with correlated substitution disorder were calculated using the equations derived in the previous section. Calculations were run on a 2.8GHz Pentium 4 PC with 1GB of RAM. As the radius of the crystallites $r_c$ increases, the number of terms to be evaluated increases as $\mathcal{O}(r_c^2)$. The values related to the structure factors of the triangles, $C_n(R)$, $D_m(R)$, $g_{nm}(R)$ and $h_{nm}(R)$, were calculated and stored prior to running the simulations. For the substitution disorder of point- and non-scatterers, computation time took less than 8 seconds even for a large crystallite with $r_c = 40$ ($\sim 5000$ sites). For the substitution disorder of up and down triangles, a typical crystallite with $r_c = 15$ ($\sim 700$ sites) used in the following, simulations took approximately 2 minutes.

The diffraction patterns are represented as plots of amplitude verses $R$ and are normalised to the peak amplitude of the first sharp reflection. The sample interval used in the calculations was $\Delta R = 0.01$ which is small enough to ensure that sharp peaks are adequately sampled. For the following simulations, the correlation function Eq. (3.23) is used for $T = 0$ and the simplified correlation function Eq. (3.35) is used for $T > 0$.

### 5.7.1 Point Scatterers

First, cylindrically averaged diffraction patterns for point scatterers on a hexagonal lattice with no disorder is presented to illustrate some of the essential features that are independent of the disorder and the scatterers. Secondly, substitution disorder with point- and non-scatterers are presented. The effects of temperature and lattice size on the diffraction pattern are examined.

The normalised diffraction amplitude of point scatterers with no disorder is shown in Fig. 5.20. The diffraction pattern consists of a set of discrete sharp Bragg peaks positioned at the reciprocal lattice sites collapsed onto $R$. The variation in the heights of the Bragg peaks is due to the variations in the different number of reciprocal lattice sites that project

onto the same cylindrical radius, i.e. the height of the peaks are weighted by the multiplicity factor, $b_{jk}$. The fall-off with $R$ is due to the cylindrical averaging [SM96a]. Note that the reciprocal lattice shares the same symmetry of the real space lattice. Consider the unit spacing of the reciprocal lattice $R \simeq 1.15$ which is the inverse of the plane spacing, $\cos(\pi/6)$ (refer to Fig. 1.24). The first set of peaks at $R = 1.15n$ ($\bigcirc$) where $n$ is an integer share the same decay envelop due to the symmetry of the lattice, $b_{jk} = 6$. Also, a second set of peaks at $R = 2n$ ($\square$) share the same decay envelop. Now consider the set of peaks situated at $R = 3.06n$ ($\times$) which have a higher decay envelop because there are twelve points collapsing down to $R$, i.e. $b_{jk} = 12$ (Fig. 5.21).

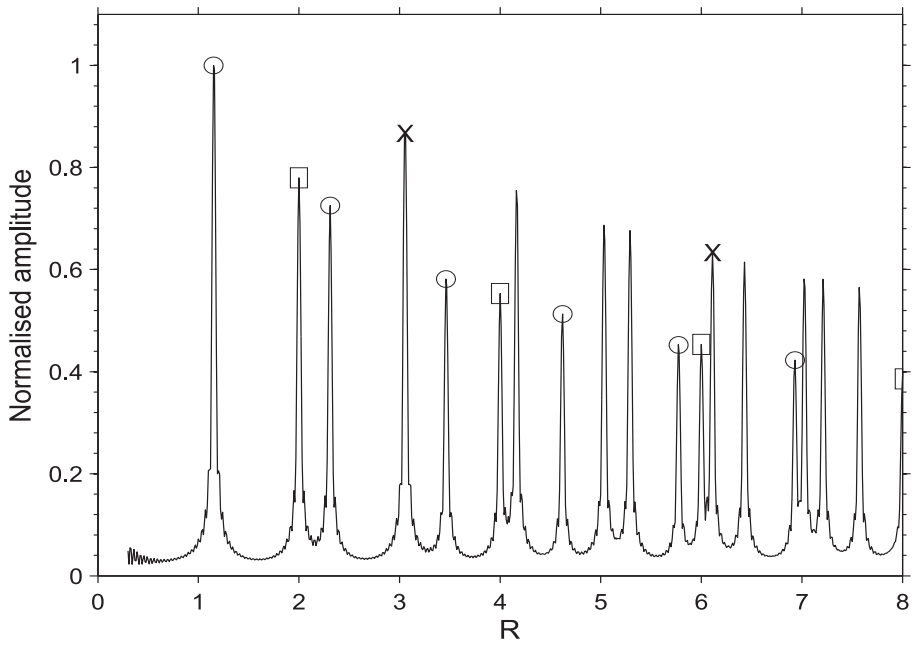


**Figure 5.20** Cylindrically averaged amplitude diffracted from a hexagonal lattice with $r_c = 15$ of point scatterers with no disorder. Variations in the height of the peaks are highlighted for $R = 1.15n$ ($\bigcirc$), $R = 2n$ ($\square$) and $R = 3.06n$ ($\times$).

The normalised diffraction pattern of a hexagonal lattice with substitution disorder of point scatterers and no scatterers with $r_c = 15$ and $T = 0$ is shown in Fig. 5.22. Fig. 5.22(a) shows the first term in Eq. (5.47) that is independent of the correlation function, i.e. the Bragg term. Notice that this is identical to the diffraction pattern shown in Fig. 5.20. Fig. 5.22(b) shows the second term in Eq. (5.47) that depends on the correlation function, i.e. the diffuse term. The diffuse term contains relatively weak peaks amongst the continuous background amplitude. The weak peaks correspond to pseudo-unit cell spacings (such as the superlattice) that are unique to the type of substitutional disorder. Similarly, these peaks also exhibit variations in height due to the symmetry of the lattice. Fig. 5.22(c) is the full diffraction pattern, i.e. the sum of the Bragg and diffuse terms.

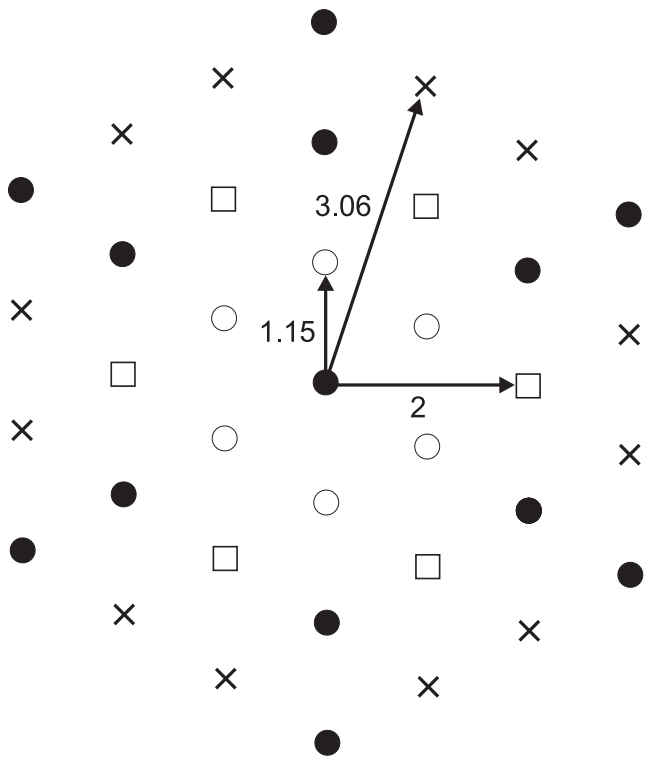


**Figure 5.21** Reciprocal lattice illustrating the number of sites that collapse down to $R = 1.15$ (◯), $R = 2$ (□) and $R = 3.04$ (×).

The normalised diffraction patterns of correlated point- and non-scatterer substitution disorder at various temperatures with $r_c = 15$ are shown in Fig. 5.23. As the temperature increases, the diffuse peaks become less pronounced as the diffuse intensity gradually approaches a constant value of $N/4A_{cell}$.

The cylindrically averaged diffraction amplitude of correlated point- and non-scatterer substitution disorder with various crystallite sizes with $T = 0.55$ are shown in Fig. 5.24. For small $r_c$, all the peaks are broad and the diffuse amplitude is relatively large compared to the Bragg peaks. For large $r_c$, the Bragg peaks are sharp and dominant. The diffuse amplitude is less significant and resembles the diffraction pattern observed for high temperatures as in Fig. 5.23(d).

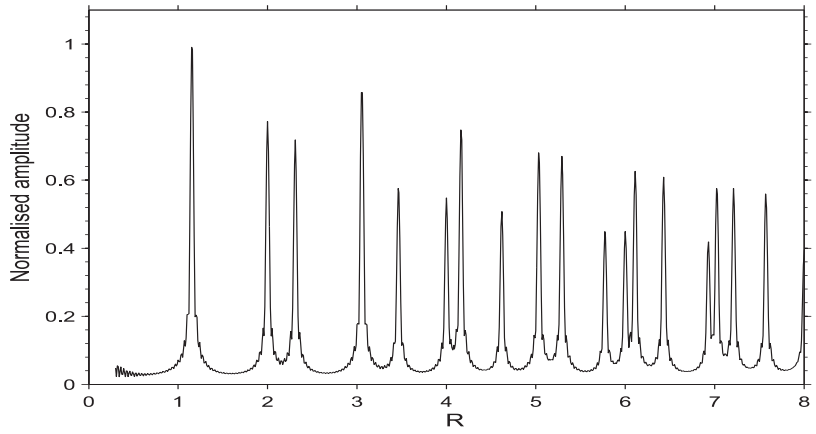


(a)

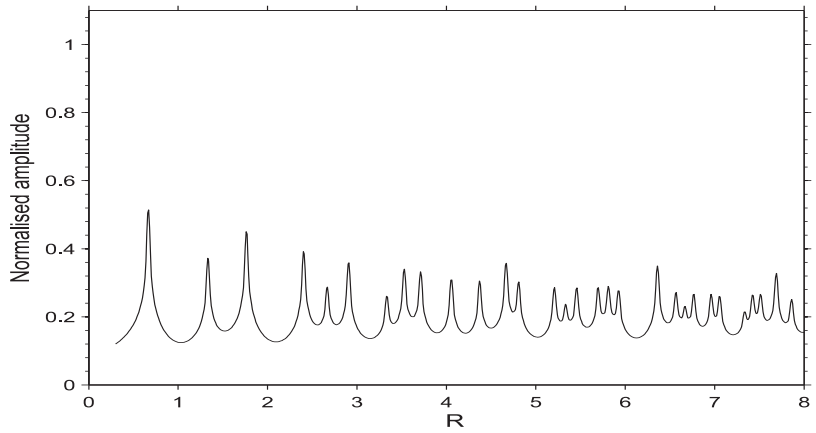


(b)

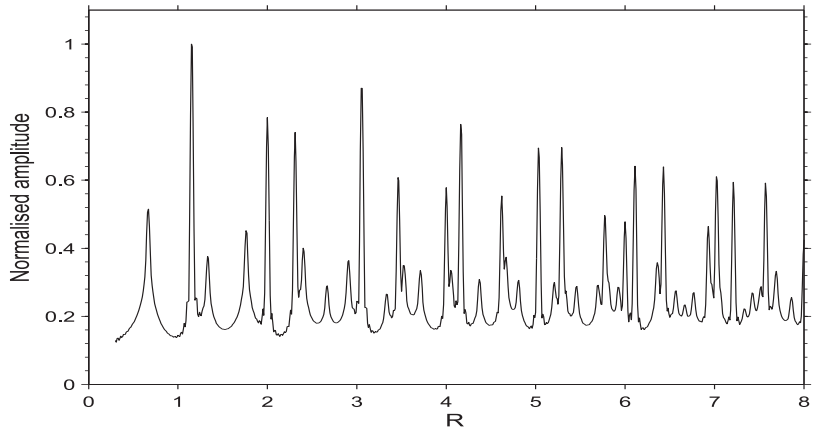


(c)

**Figure 5.22** Amplitude diffracted from a hexagonal lattice with substitution disorder of point scatterers and non-scatterers with $r_c = 15$ and $T = 0$. (a) Bragg and (b) diffuse components, and (c) the total diffracted amplitude.

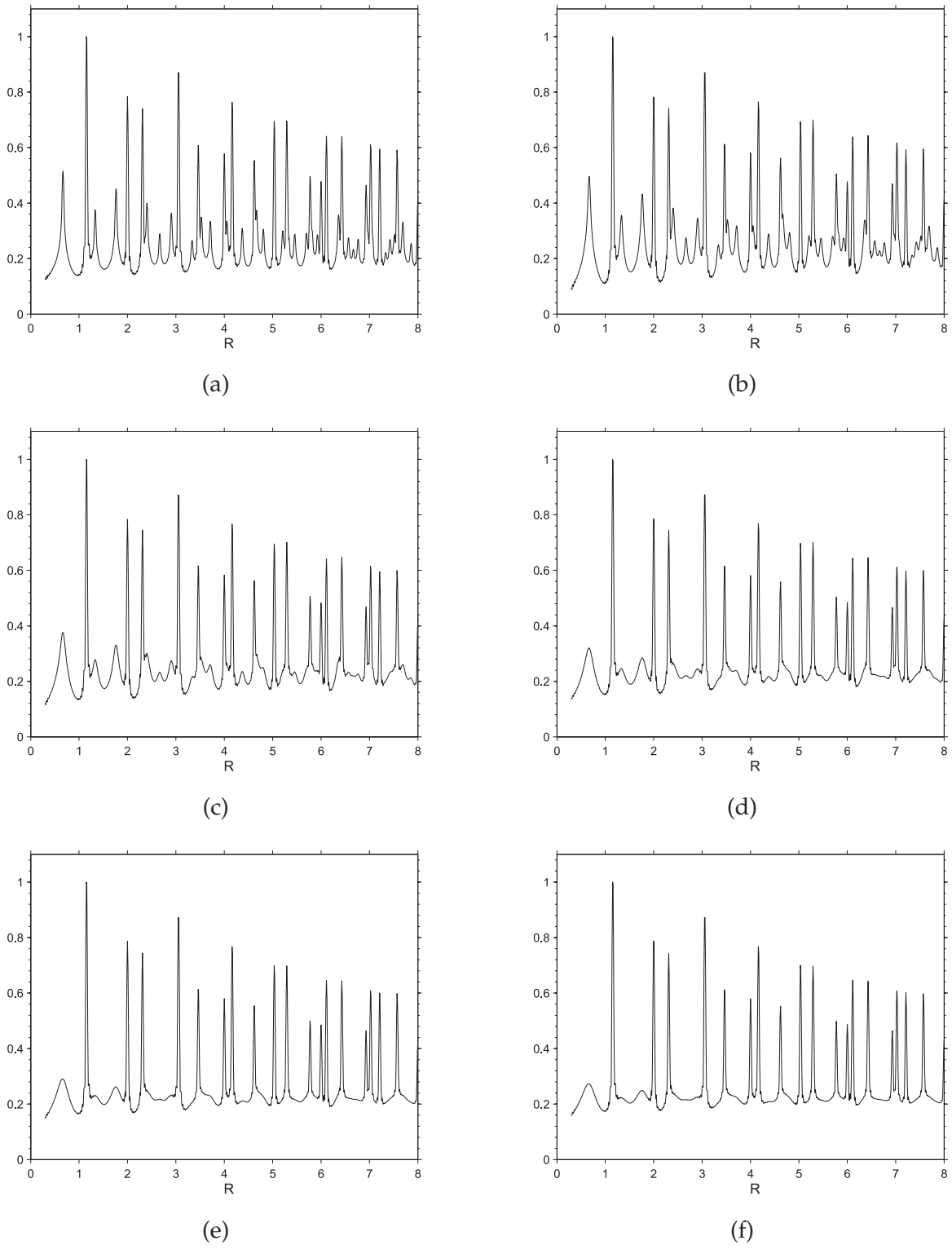


**Figure 5.23** Cylindrically averaged amplitude diffracted from a hexagonal lattice with substitution disorder of point scatterers and non-scatterers with $r_c = 15$ and varying temperature. (a) $T = 0$, (b) $T = 0.3$, (c) $T = 0.5$, (d) $T = 0.7$, (e) $T = 0.9$ and (c) $T = 1.1$.

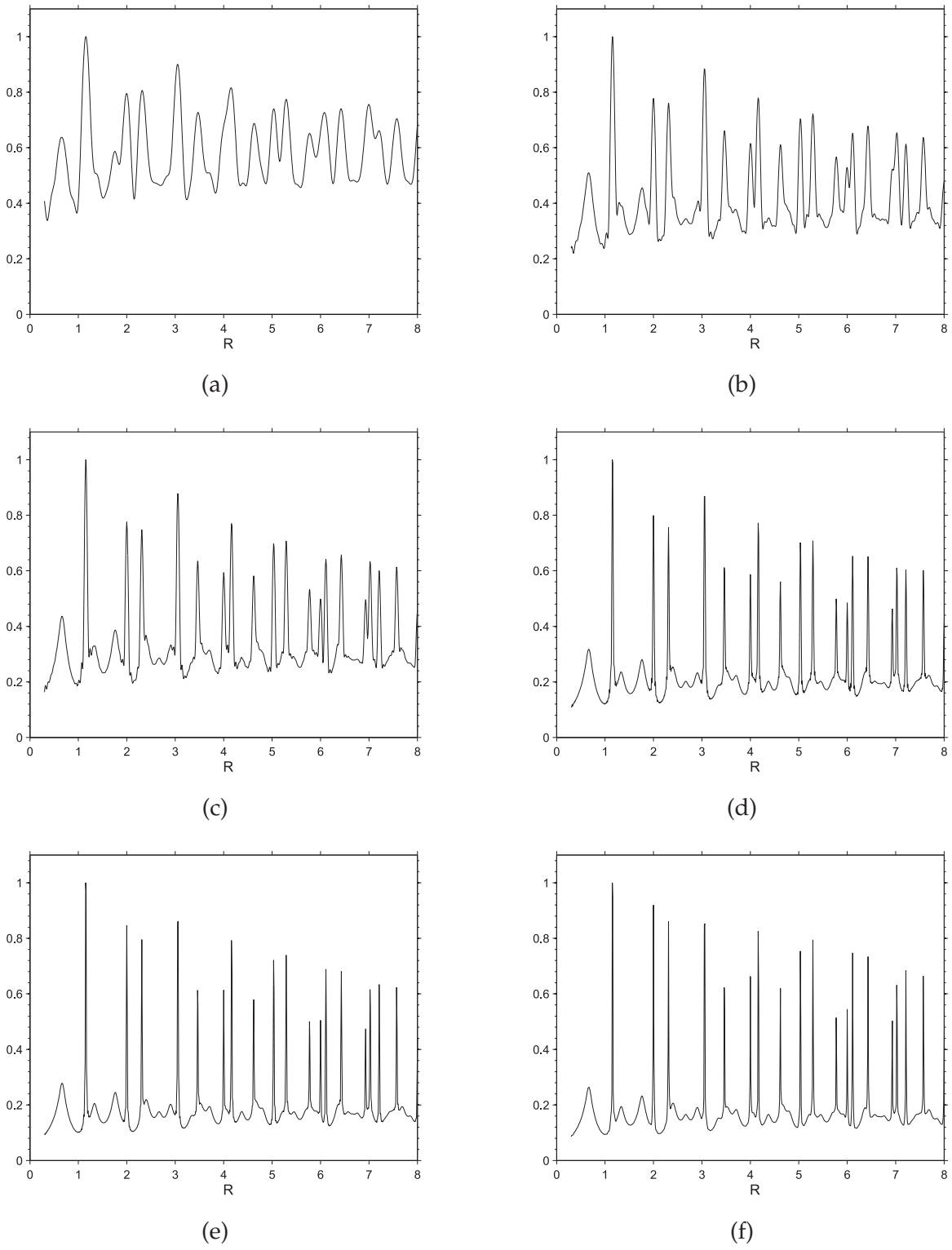


**Figure 5.24** Cylindrically averaged amplitude diffracted from a hexagonal lattice with substitution disorder of point scatterers and non-scatterers with $T = 0.55$ and varying crystallite sizes. (a) $r_c = 3$, (b) $r_c = 6$, (c) $r_c = 9$, (d) $r_c = 20$, (e) $r_c = 30$ and (c) $r_c = 40$.

### 5.7.2 Triangle Scatterers

Cylindrically averaged diffraction by a hexagonal lattice with substitution disorder with up and down triangular scatterers with $r_c = 15$ and $T = 0, 0.55$ and $\infty$ are shown in Figs. 5.25, 5.26 and 5.27, respectively. The Bragg and diffuse components are shown in these plots. Diffraction amplitudes are normalised with respect to the first peak $(R = 1.15)$ and saturated at 0.3 in the plots in order to show the relatively weak diffuse amplitude. The peaks decay with increasing $R$ due to modulation by the Fourier transform of the triangle. The Bragg term is independent of temperature and some peaks are missing as a result of zeros in the molecular transform.

The diffuse amplitude peaks that correspond to multiplicity of $b_{jk} = 6$ are suppressed for triangle scatterers. To elaborate, the point scatterer diffuse intensity and its decay envelope corresponding to multiplicity $b_{jk} = 6$ (Fig. 5.22(b)) are also shown in Fig. 5.25(b). It is evident that the peaks that are on the decay envelope are suppressed in the diffuse amplitude peaks of triangle scatterers.

The most important feature is that some of the diffuse peaks are larger than the neighbouring Bragg peaks. This illustrates that the diffuse term should be included for a more accurate structure determination and justifies the need for modelling the effect of the disorder on the diffraction. The diffuse diffraction is similar for $T = 0.55$ but shows less structure. At $T = \infty$ the diffuse term is smoothly varying, reflecting the molecular transform. This gives the characteristic appearance in the presence of uncorrelated disorder with the Bragg reflections "sitting on top of" the diffuse diffraction [SM96a]. Note that the diffuse term in Eq. (5.46) simplifies to

$$I^D(R) = \frac{\pi r_c^2}{4A_{cell}} \sum_n \mathbb{R}\{h_n(R)\}, \tag{5.70}$$

where

$$\begin{aligned} h_n(R) &= [C_n(R) - D_n(R)][C_n^*(R) - D_n^*(R)] \\ &= |C_n(R) - D_n(R)|^2 . \end{aligned} \tag{5.71}$$

The effect of temperature is shown in Fig. 5.28. As temperature increases, the diffraction pattern approaches that of the uncorrelated case in Fig. 5.27. However, it can be seen that the diffuse intensity is still significant for the effective temperature of the myosin lattice which lies in between $T = 0.35 \sim 0.65$.

The effect of crystallite size at $T = 0.55$ is shown in Fig. 5.29. For small $r_c$, all the peaks are broad and the diffuse term is relatively large. For large $r_c$, the Bragg reflections are sharper and increase in height relative to the diffuse term. The effect of the disorder thus decreases

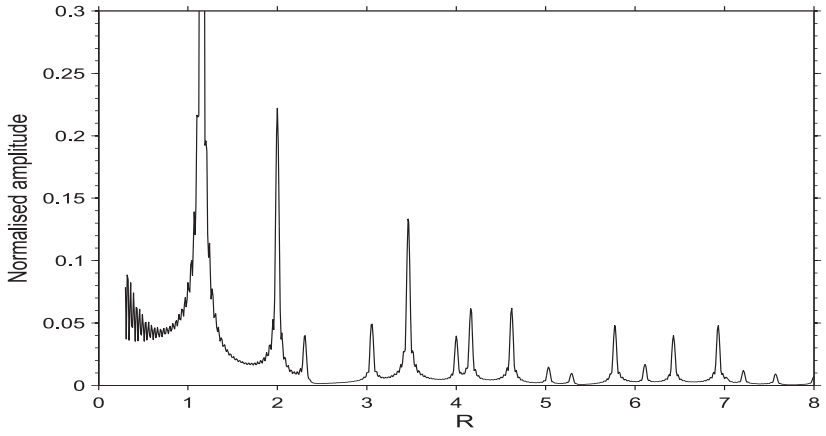


(a)

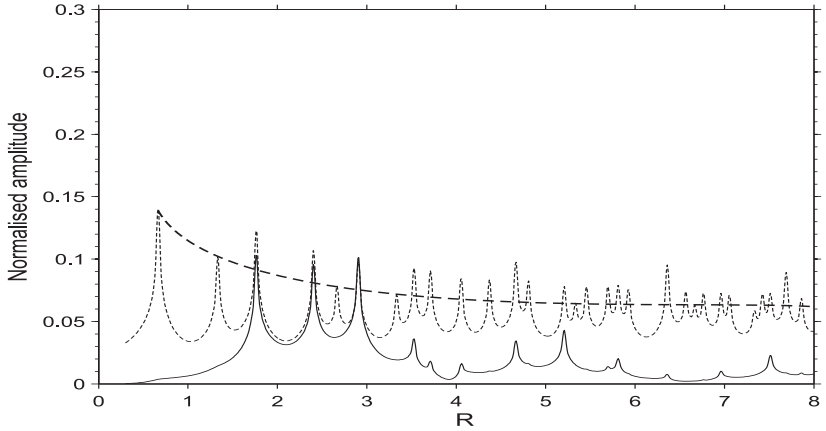


(b)

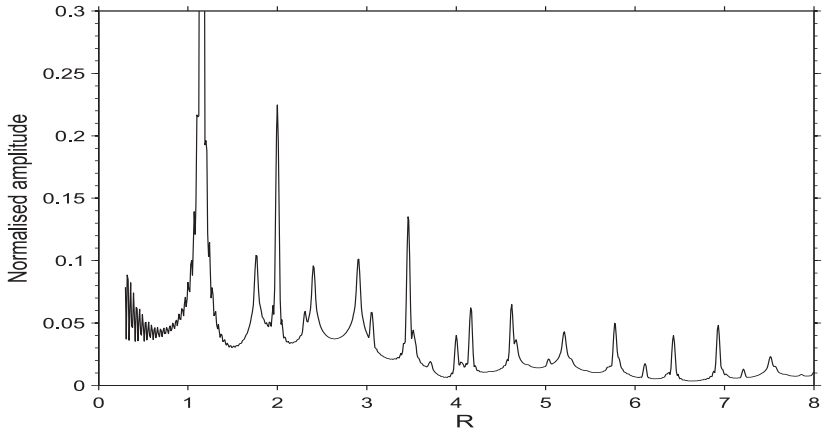


(c)

**Figure 5.25** Cylindrically averaged amplitude diffracted from a hexagonal lattice with substitution disorder of up and down triangle scatterers with $r_c = 15$ and $T = 0$. (a) Bragg and (b) diffuse components. The diffuse components from point scatterers in Fig. 5.22(b) and its decay envelope $b_{jk} = 6$ are also shown as dashed lines (not to scale). (c) The total diffracted amplitude.

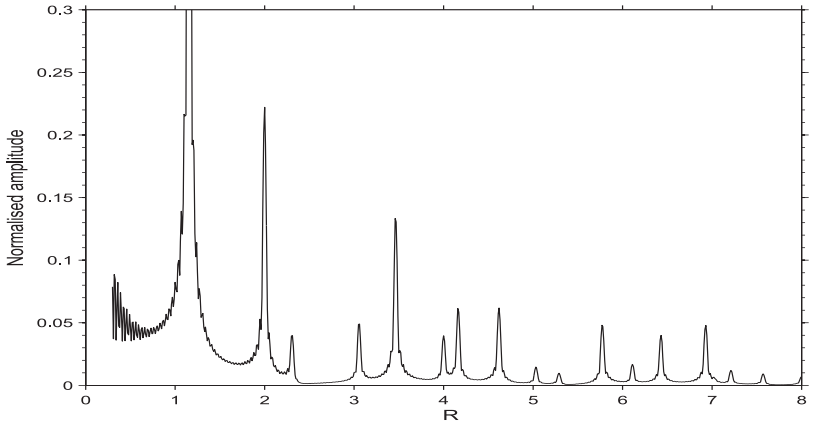


(a)

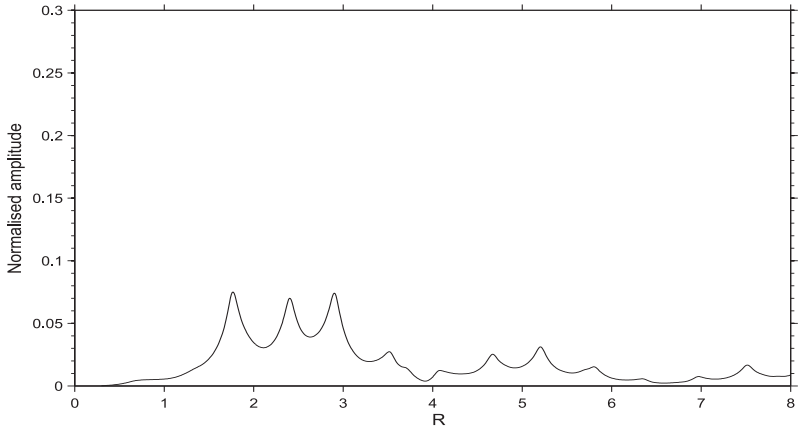


(b)

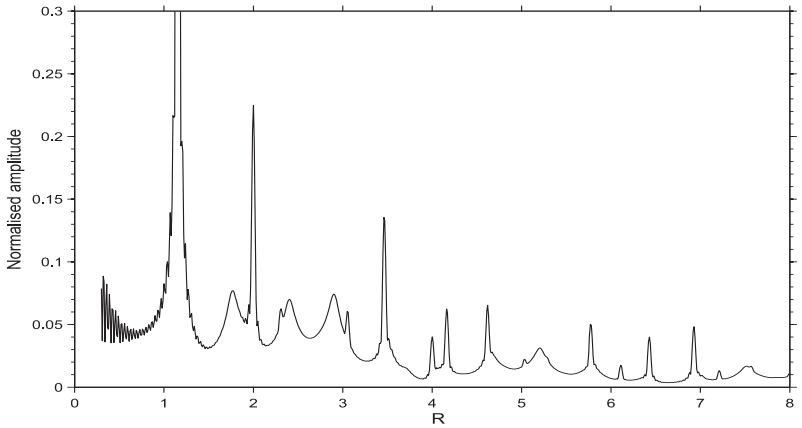


(c)

**Figure 5.26** Cylindrically averaged amplitude diffracted from a hexagonal lattice with substitution disorder of up and down triangle scatterers with $r_c = 15$ and $T = 0.55$. (a) Bragg and (b) diffuse components, and (c) the total diffracted amplitude.

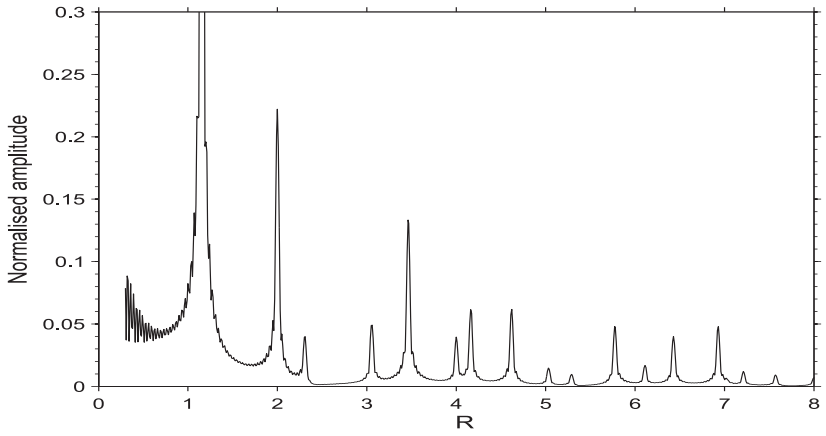


(a)

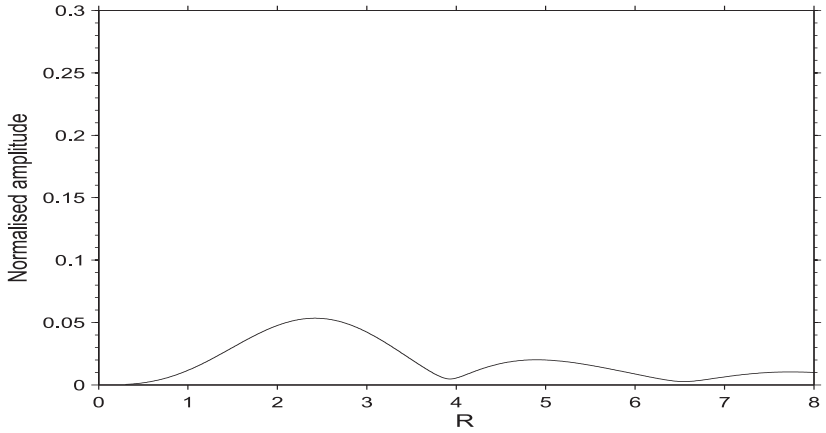


(b)

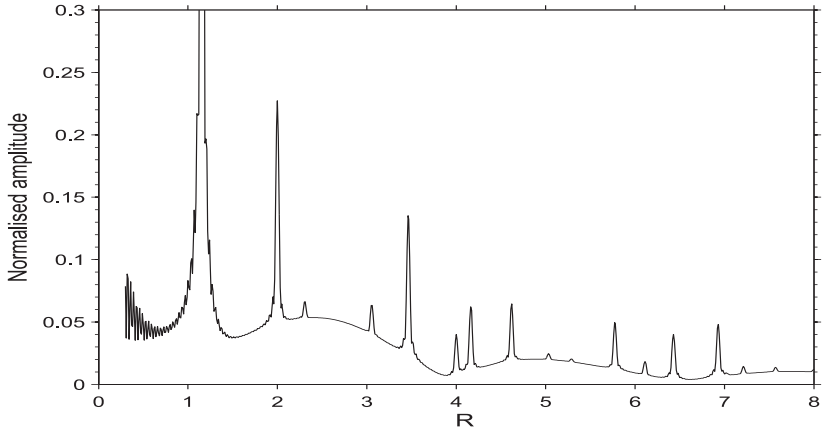


(c)

**Figure 5.27** Cylindrically averaged amplitude diffracted from a hexagonal lattice with uncorrelated substitution disorder ($T = \infty$) of up and down triangle scatterers with $r_c = 15$. (a) Amplitude due to the regular term and (b) amplitude due to the disorder term and (c) the total amplitude diffracted.

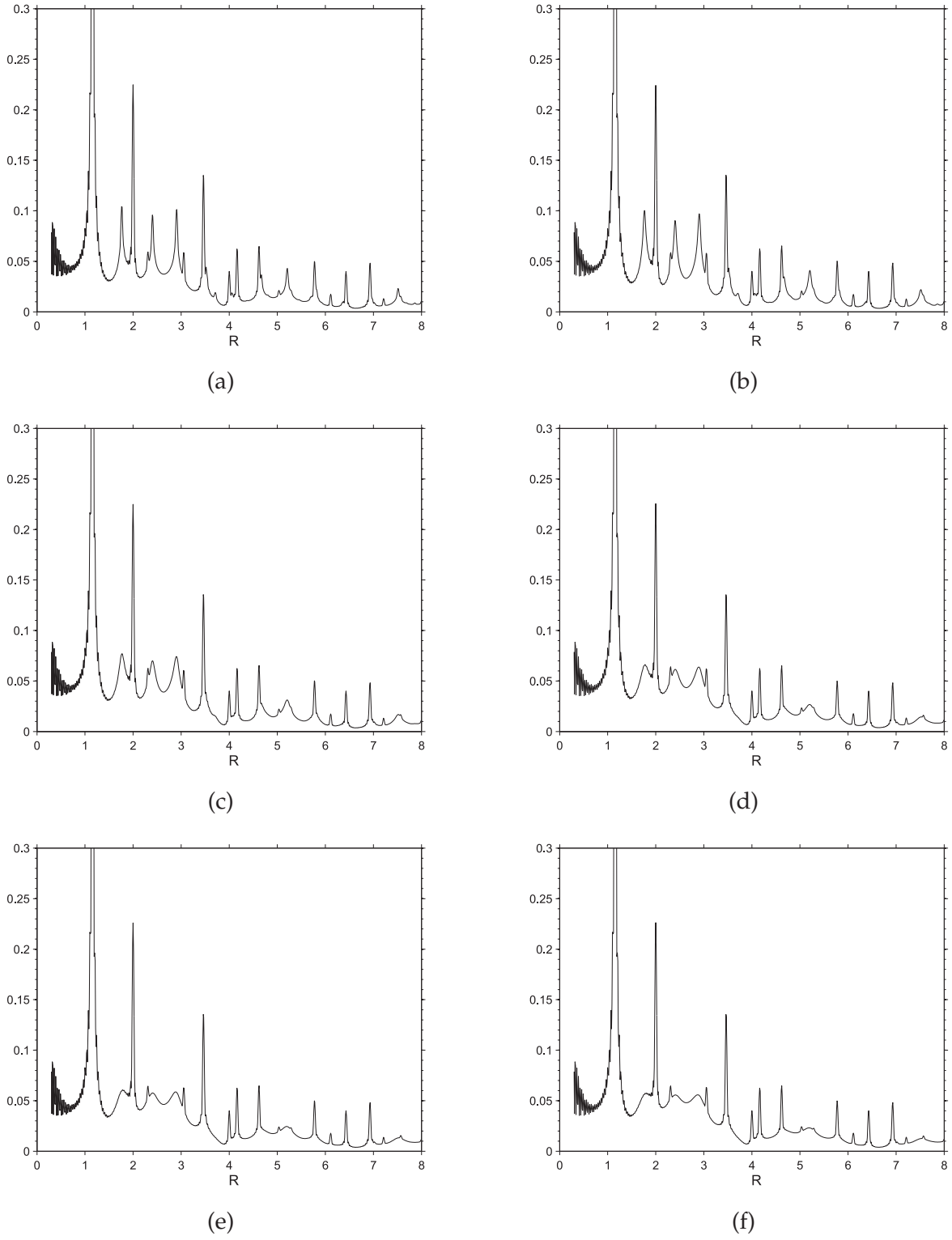


**Figure 5.28** Cylindrically averaged amplitude diffracted from a hexagonal lattice with substitution disorder of up and down triangle scatterers with $r_c = 15$ and varying temperature. (a) $T = 0$, (b) $T = 0.3$, (c) $T = 0.5$, (d) $T = 0.7$, (e) $T = 0.9$ and (c) $T = 1.1$.

for large crystallites.

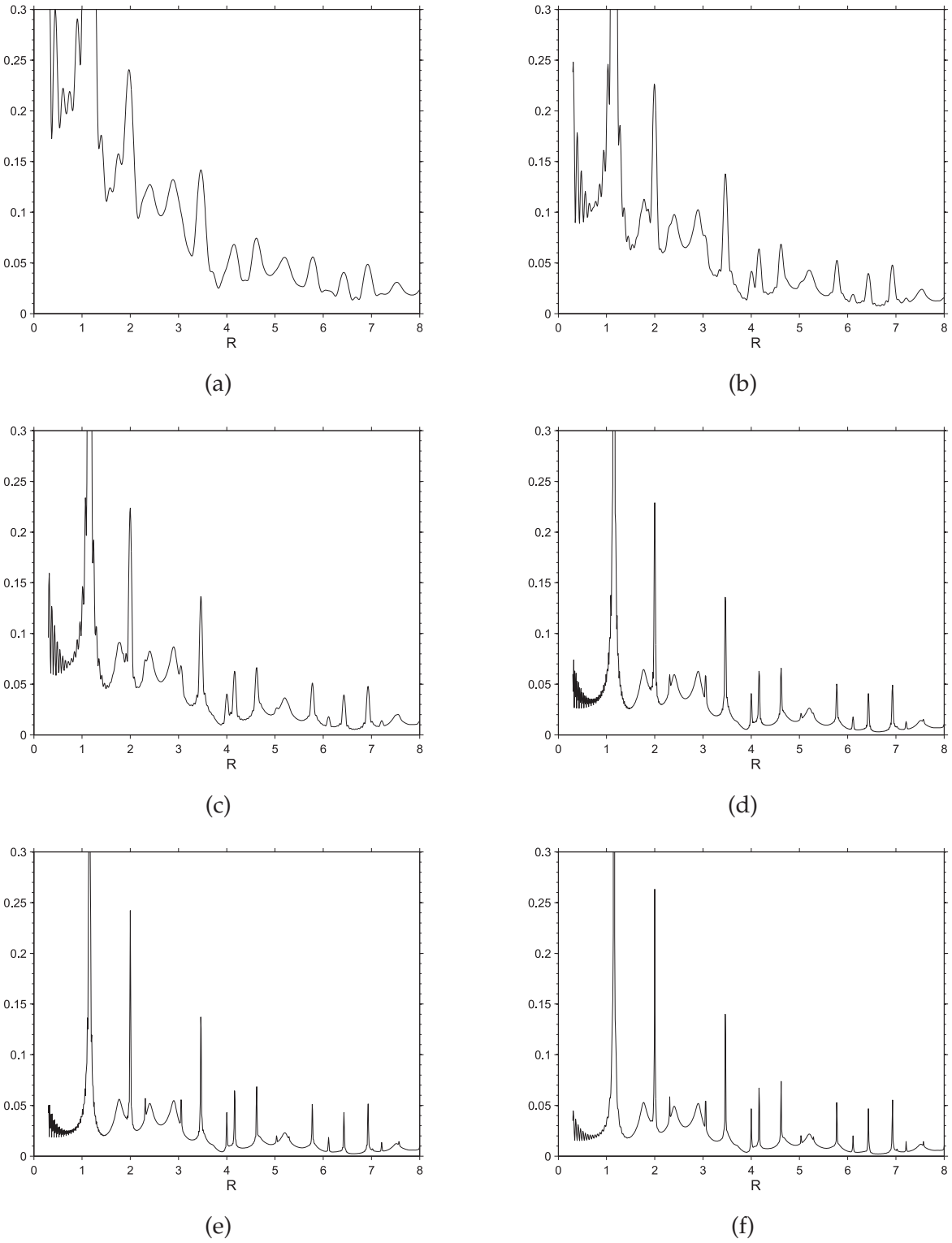


**Figure 5.29** Cylindrically averaged amplitude diffracted from a hexagonal lattice with substitution disorder of up and down triangle scatterers with $T = 0.55$ and varying crystallite sizes. (a) $r_c = 3$, (b) $r_c = 6$, (c) $r_c = 9$, (d) $r_c = 20$, (e) $r_c = 30$ and (c) $r_c = 40$.

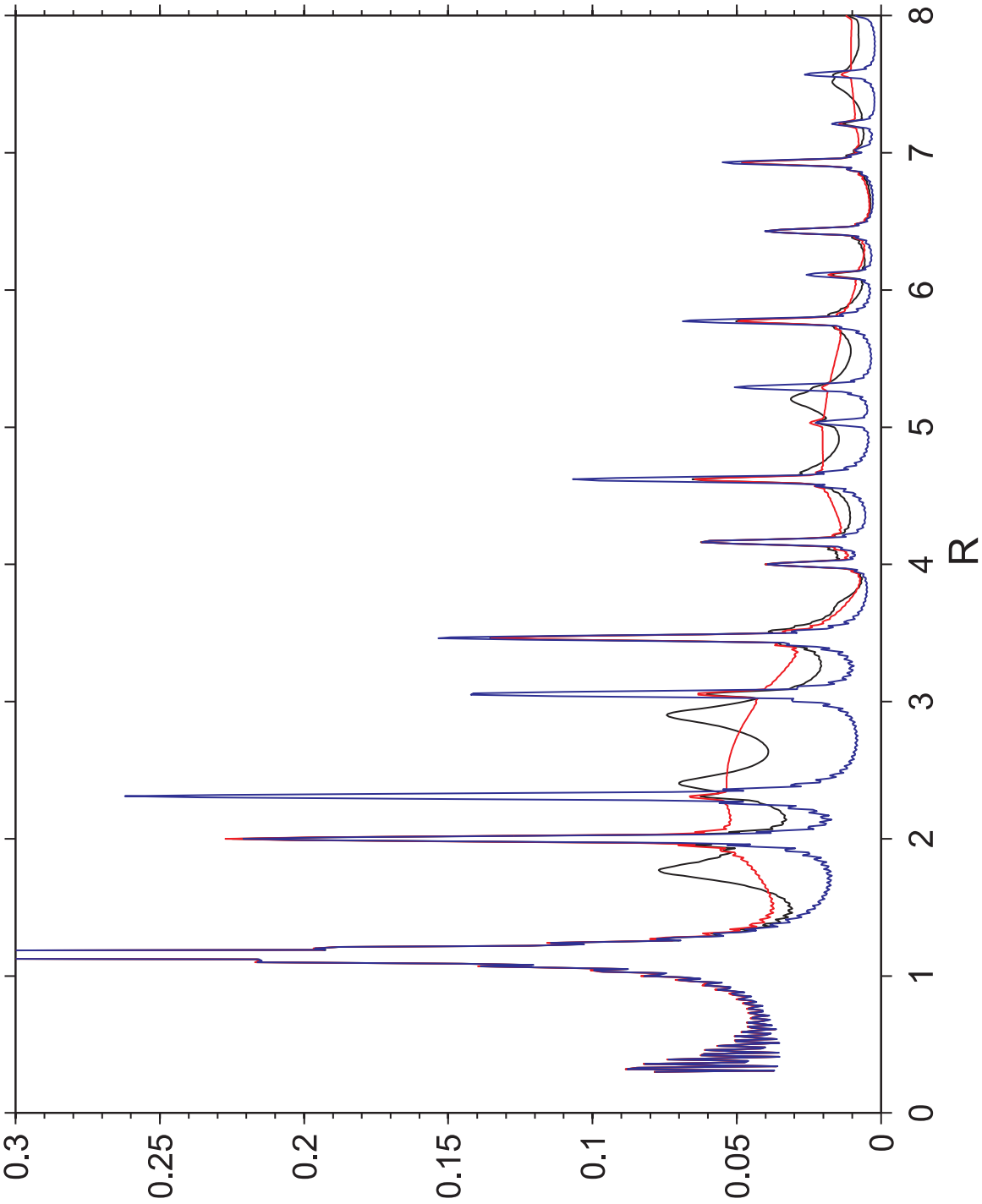


**Figure 5.30** Cylindrically averaged diffraction amplitude from a hexagonal lattice with substitution disorder of up and down triangle scatterers with $r_c = 15$ for uncorrelated disorder (red), correlated disorder at $T = 0.55$ (black), and no disorder (blue).

## 5.8 Discussion

Correlated substitution disorder introduces diffuse diffraction in addition to the Bragg diffraction by a non-disordered lattice. The Bragg and diffuse diffraction can be separated into two separate terms.

Calculation of diffraction using the DFT and ensemble averaging can be used to calculate average diffraction patterns and shows the characteristics of the diffuse diffraction. Calculations for the TIA disorder shows that the diffuse diffraction peaks at the superlattice sites of the reciprocal lattice as the temperature decreases and the correlations increase. The relative magnitude of the diffuse component decreases as the crystallite size increases. Theory is developed that allows the ensemble averaged diffraction pattern to be calculated directly by summing over the lattice sites. This allows a faster calculation and shows the separation into Bragg and diffuse components.

The cylindrically averaged diffraction is determined analytically by expanding the diffraction of the scatterers in an angular Fourier series. This allows fast calculation of the cylindrically averaged diffraction. Calculation of the cylindrically averaged diffraction for the TIA consisting of up and down triangles shows the effect of diffuse diffraction on the diffraction pattern.

The main effect of substitution disorder on the cylindrically averaged diffraction from muscle is to introduce diffuse intensity modulated by a function related to the difference between the scattering factors of the two myosin filament orientations. If the disorder in the muscle is ignored, then it can be approximated either by one with no disorder or with random disorder. Either of these simplifications introduces errors into the calculated diffraction, and the level of these errors is important in assessing the significance of the disorder when performing structure determination from muscle fiber diffraction patterns. To assess these effects, the cylindrically averaged diffraction amplitudes for a simple lattice (no disorder), uncorrelated disorder, and TIA at the effective temperature of muscle, $T = 0.55$, are calculated and shown in Fig. 5.30. For the case of no disorder, the diffuse intensity is not accounted for and there are also large errors in the amplitudes of the Bragg reflections. If random disorder is assumed, then the Bragg reflections are correct but the peaks in the diffuse intensity are not represented. The effect of the disorder is therefore significant and needs to be taken into account when analysing superlattice muscle fiber diffraction patterns. Furthermore, there is a substantial amount of information in the diffuse diffraction that can provide important constraints in determining the structure, packing and interactions of myosin.

To apply the theory developed here to prediction and interpretation of muscle fiber diffrac-

tion patterns, the analysis needs to be extended into three dimensions. This is not expected to be particularly difficult since there is no disorder in the axial direction.

# Chapter 6

# Summary and Suggestions for Future Research

In this thesis, image analysis and modeling of the vertebrate muscle A-band and its effects on X-ray diffraction were investigated. An automated image processing method was developed for rapidly and accurately classifying the filament orientations and extracting statistical information about the collective ordering of the myosin filaments from electron micrographs of muscle cross-sections. Comparison with manual analyses of the micrographs showed that the automated method gave as reliable classification as a human.

The myosin lattice disorder was successfully modeled as an antiferromagnetic Ising model by demonstrating that it is possible to generate statistically equivalent lattices by conducting Monte Carlo simulations at an effective temperature of $T \sim 0.55$. Application of the methods described above showed that different vertebrate species all possess similar degree of disorder and compelling evidence was presented that the crossbridge environment in the vertebrate muscle A-band is a direct result of an antiferromagnetic type of interaction between neighbouring myosin filaments resulting in a frustrated system.

The intensity diffracted by a 2D lattice with TIA disorder was evaluated using numerical and analytical-numerical schemes and triangular scatterers. Analytic expressions were derived to calculate the cylindrically averaged X-ray diffraction intensity for 2D lattices in a computationally efficient manner. Simulations show the kinds of effects to be expected in muscle X-ray fiber diffraction patterns.

A number of extensions to the work described here would be useful.

1. The most important is that of extending the calculation of the cylindrically averaged

diffraction to three dimensions. This should be relatively straight forward and would allow direct application to muscle X-ray fiber diffraction patterns. Helical symmetry could easily be incorporated. Some investigation and consideration of possible axial order between myofibrils should also be conducted.

2. Application of the 3D calculation of fiber diffraction patterns could potentially be incorporated into muscle structure refinement programs. It may be possible to estimate the effective temperature from the diffraction data without *a priori* knowledge of degree of disorder in the specimen. This could be done by including the temperature as a parameter along with the molecular parameters as part of the iterative refinement process.

3. Results from the micrograph analysis program could be used to analyse the lattice disorder in the myofibrils. The lattice disorder may be modelled using a perturbed lattice or a paracrystal. The effects of the lattice disorder are probably small but would be worthwhile quantitating. This could be followed by the development of an analytical expression for the combined effects of correlated lattice disorder and correlated substitution disorder on the diffraction pattern which should be straight forward.

4. It is suggested that the disorder evenly distributes the myosin heads among neighbouring actin filaments, allowing the muscle to produce more tension during contraction. More study, probably by biologists, is needed to interpret the consequences of the disorder in terms of muscle function.

5. By carrying out quantitative analysis on the muscle micrographs, rotation of the myosin filaments, by approximately $30^\circ$ (see Fig. 2.12 and Fig. 4.7), across the M-band, in both simple and superlattice muscles, was observed. It is not clear whether this is caused by a non-transverse cut through the M-band or whether it is some intrinsic property of the disorder. This is worthy of more study.

6. A more complete survey of the vertebrate muscles would be worth while. The automated micrograph analyser described in this thesis makes this a more feasible task. This will provide a better understanding of the muscle disorder and may provide some insight into muscle evolution and structure/function relationship.

# Appendix A

# Appendix A: Mathematics

## A.1 Bessel Functions

The $n$-th order Bessel function of the first kind is defined as [Bow38]

$$J_n(z) = \frac{1}{2\pi i^n}\int_0^{2\pi} \exp(iz\cos\psi)\exp(in\psi)\mathrm{d}\psi. \tag{A.1}$$

$J_0(0) = 1$ and $J_n(0) = 1$ for $n \neq 0$. The positive and the negative orders are related by

$$J_{-n}(z) = (-1)^n J_n(z) = i^{2n} J_n(z). \tag{A.2}$$

## A.2 Chebyshev Polynomials

Chebyshev polynomials of the first kind is defined by [AS65]

$$\begin{aligned} T_n(x) &= \frac{(x+\sqrt{x^2-1})^n + (x-\sqrt{x^2-1})^n}{2} \\ &= \frac{n}{2}\sum_{k=0}^{\lfloor n/2\rfloor}(-1)^k \frac{(n-k-1)!}{k!(n-2k)!}(2x)^{n-2k}. \end{aligned} \tag{A.3}$$

Chebyshev polynomials of the second kind are given by

$$\begin{aligned} U_n(x) &= \frac{(x+\sqrt{x^2-1})^{n+1}-(x-\sqrt{x^2-1})^{n+1}}{2\sqrt{x^2-1}} \\ &= \sum_{k=0}^{\lfloor n/2 \rfloor}(-1)^k \frac{(n-k)!}{k!(n-2k)!}(2x)^{n-2k}. \end{aligned} \tag{A.4}$$

## A.3 Fourier Transform

The Fourier transform of a continuous one dimensional function $f(x)$ is defined as [Bra78]

$$\mathcal{F}\{f(x)\} = F(u) = \int_{-\infty}^{\infty} f(x)\exp(-i2\pi ux)\,\mathrm{d}x, \tag{A.5}$$

where $\mathcal{F}\{\cdot\}$ denotes the Fourier transform operation. In this thesis the upper-case letter is generally used to denote the Fourier transform of a function denoted by the corresponding lower-case letter. Given $F(u)$, the original function is recovered by the inverse Fourier transform defined as

$$\mathcal{F}^{-1}\{F(u)\} = f(x) = \int_{-\infty}^{\infty} F(u)\exp(i2\pi ux)\,\mathrm{d}u, \tag{A.6}$$

where $\mathcal{F}\{\cdot\}$ denotes the inverse Fourier transform. The Fourier transform operation is defined for any square-integrable function $f(x)$.

The two-dimensional Fourier transform pair is defined as

$$F(u,v) = \int_{-\infty}^{\infty}\int_{-\infty}^{\infty} f(x,y)\exp(-i2\pi(ux+vy))\,\mathrm{d}x\,\mathrm{d}y \tag{A.7}$$

and

$$f(x,y) = \int_{-\infty}^{\infty}\int_{-\infty}^{\infty} F(u,v)\exp(i2\pi(ux+vy))\,\mathrm{d}u\,\mathrm{d}v, \tag{A.8}$$

where $(x,y)$ and $(u,v)$ denote Cartesian coordinates in real and reciprocal space, respectively. Using the polar coordinate notations $(r,\phi)$ and $(R,\psi)$, the two-dimensional Fourier transform pair is given by

$$F(R,\psi) = \int_{0}^{\infty}\int_{0}^{2\pi} f(r,\phi)\exp(-i2\pi Rr\cos(\psi-\phi))r\,\mathrm{d}r\,\mathrm{d}\phi \tag{A.9}$$

and

$$f(r,\phi) = \int_{0}^{\infty}\int_{0}^{2\pi} F(R,\psi)\exp(i2\pi Rr\cos(\psi-\phi))R\,\mathrm{d}R\,\mathrm{d}\psi. \tag{A.10}$$

The two-dimensional Fourier transform of a circularly symmetric function denoted $f(r)$

(also known as the Hankel transform) can be determined by integrating over $\phi$ in Eq. (A.9) giving

$$F(R) = \int_0^\infty f(r) J_0(2\pi Rr) r \, \mathrm{d}r, \tag{A.11}$$

where $J_0(\cdot)$ is zero order Bessel function of the first kind (Section A.1).

Using cylindrical-polar coordinates $(r, \phi, z)$ and $(R, \psi, Z)$ for real space and Fourier space where the $z$ and $Z$ axes are aligned, and the axes $\phi = 0$ and $\psi = 0$ are aligned, the three-dimensional Fourier transform pair is given by

$$F(R, \psi, Z) = \int_{-\infty}^\infty \int_0^{2\pi} \int_0^\infty f(r, \phi, z) \exp(-i2\pi[Rr\cos(\psi - \phi) + zZ]) r \, \mathrm{d}r \, \mathrm{d}\phi \, \mathrm{d}z \tag{A.12}$$

and

$$f(r, \phi, z) = \int_{-\infty}^\infty \int_0^{2\pi} \int_0^\infty F(R, \psi, Z) \exp(i2\pi[Rr\cos(\psi - \phi) + zZ]) R \, \mathrm{d}R \, \mathrm{d}\psi \, \mathrm{d}Z. \tag{A.13}$$

A Fourier transform pair is denoted by

$$f(\mathbf{r}) \Leftrightarrow F(\mathbf{R}), \tag{A.14}$$

where **r** and **R** are vectors in real and Fourier space, respectively. For any constant vector **t**,

$$f(\mathbf{r} - \mathbf{t}) \Leftrightarrow F(\mathbf{R}) \exp(i2\pi \mathbf{R} \cdot \mathbf{t}). \tag{A.15}$$

The convolution of $f(\mathbf{r})$ and $g(\mathbf{r})$ is defined as

$$f(\mathbf{r}) \otimes g(\mathbf{r}) = \int_0^\infty f(\mathbf{r}) g(\mathbf{r} - \mathbf{t}) \, \mathrm{d}\mathbf{t} \tag{A.16}$$

and the convolution theorem for Fourier transforms states that

$$f(\mathbf{r}) \otimes g(\mathbf{r}) \Leftrightarrow F(\mathbf{R}) G(\mathbf{R}). \tag{A.17}$$

Friedel's law is a property of Fourier transforms of real functions. For a real function $f(\mathbf{r})$, its Fourier transform satisfies

$$F(\mathbf{R}) = F^*(-\mathbf{R}) \tag{A.18}$$

where $F^*$ is the complex conjugate of $F$. $F(\mathbf{R})$ and $F(-\mathbf{R})$ are called Friedel's pairs. The squared amplitude $|F|^2$ is centrosymmetric

$$|F(\mathbf{R})|^2 = |F^*(-\mathbf{R})|^2 \tag{A.19}$$

and the phase $\phi$ of $F$ is antisymmetric

$$\phi(\mathbf{R}) = -\phi(-\mathbf{R}). \tag{A.20}$$

The discrete Fourier transform (DFT) pair for an $N \times M$ grid in $x$ and $y$ is defined by

$$F(u,v) = \frac{1}{NM} \sum_{x=0}^{N-1} \sum_{y=0}^{M-1} f(x,y) \exp(-i2\pi(ux/N + vy/M)) \tag{A.21}$$

and

$$f(x,y) = \sum_{u=0}^{N-1} \sum_{v=0}^{M-1} F(u,v) \exp(i2\pi(ux/N + vy/M)). \tag{A.22}$$

# Appendix B

## Appendix B: Micrographs

The images that are used in this thesis are electron micrographs of 50 nm thick transverse sections through the bare region of muscles, where the filaments are roughly triangular in cross-section. Details of specimen preparation and microscopy are given in Section 2.5. The images were provided by Dr. Pradeep Luther, Imperial College London. The images are:

| Image name | Dimensions (pixels) | Bits per pixel | Muscle |
|---|---|---|---|
| FROG370.TIF | $3742 \times 3030$ | 8 | *Frog* |
| FROG375.TIF | $3823 \times 3091$ | 8 | *Frog* |
| FROG410.TIF | $3549 \times 3081$ | 8 | *Frog* |
| THE384.TIF | $3841 \times 3122$ | 8 | *Frog* |
| PLP2774.TIF | $1050 \times 1050$ | 8 | *Polypterus* |
| 10462-MUDSKIPP.TIF | $3291 \times 2240$ | 16 | *Mudskipper* |
| 27779-SHARKW.TIF | $3295 \times 2240$ | 16 | *Shark* |
| TURT13465.TIF | $3200 \times 2800$ | 8 | *Turtle* |
| SHKW27781.TIF | $3200 \times 2800$ | 8 | *Shark* |
| PLPW27765.TIF | $3200 \times 2800$ | 8 | *Polypterus* |

## FROG370

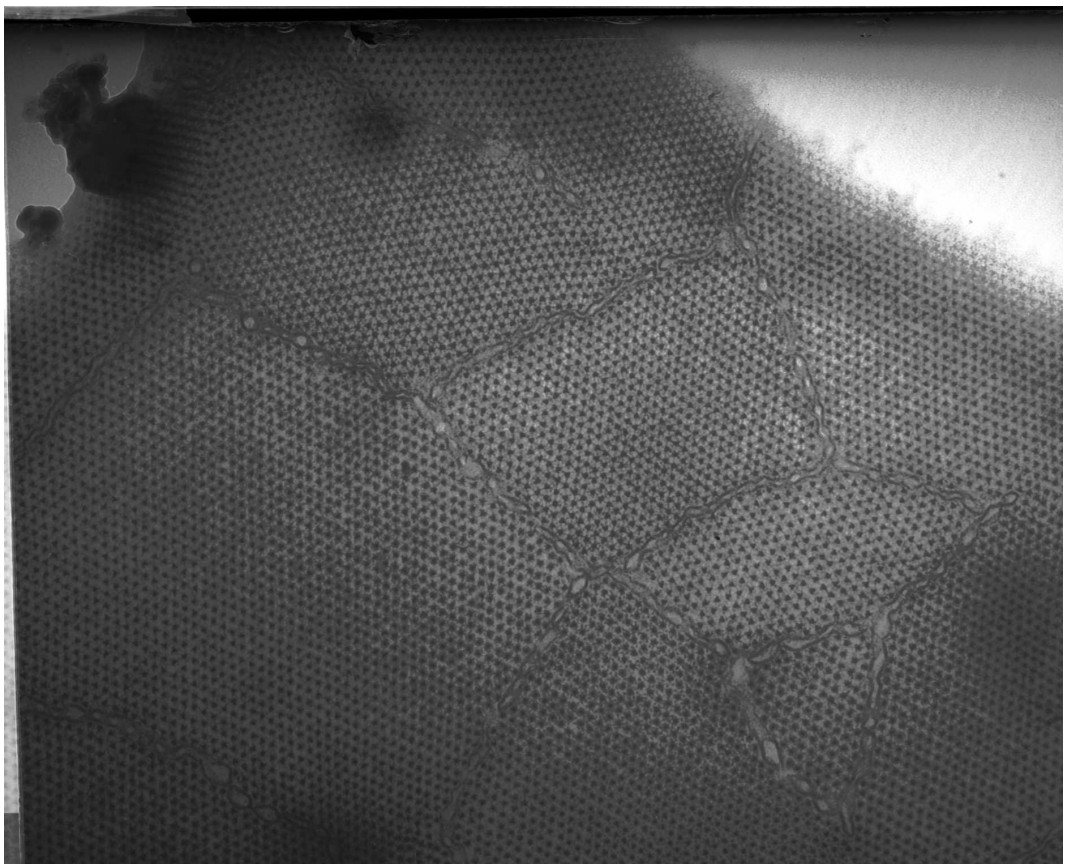

**Figure B.1** FROG370.tif - 3742 × 3030 pixels.

# FROG375

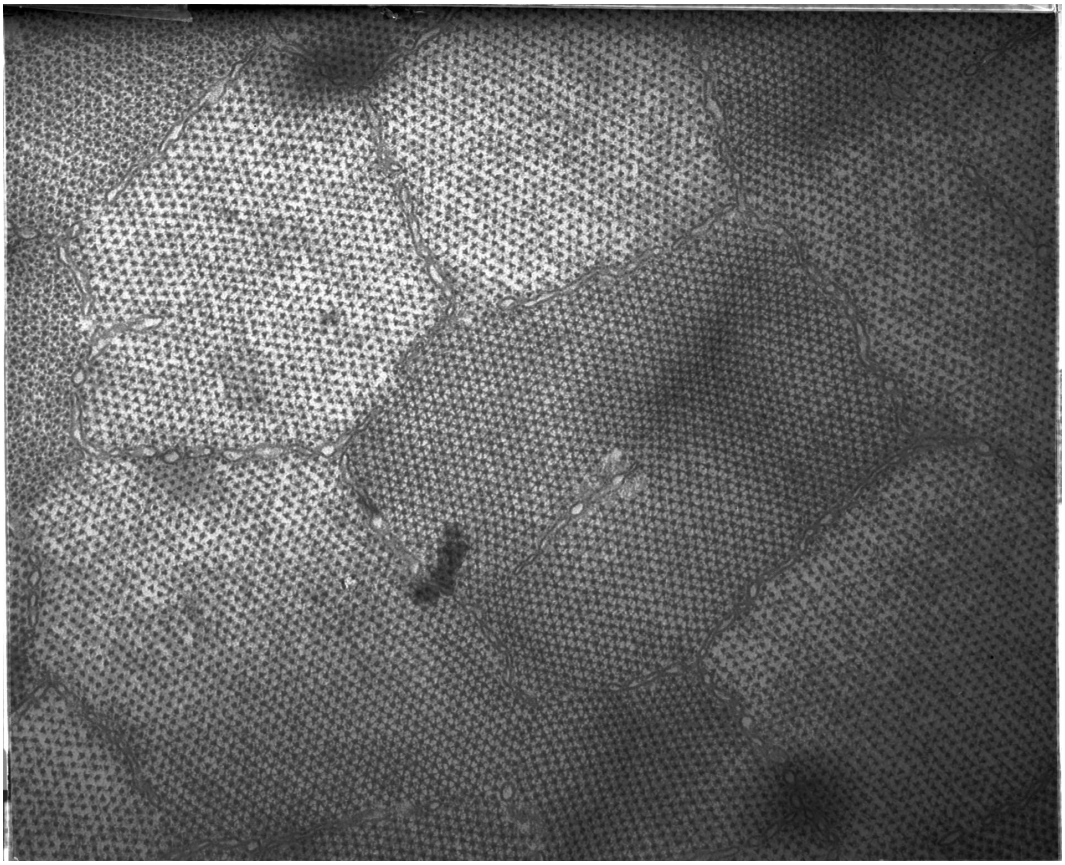

**Figure B.2** FROG375.tif - 3823 $\times$ 3091 pixels.

## FROG410

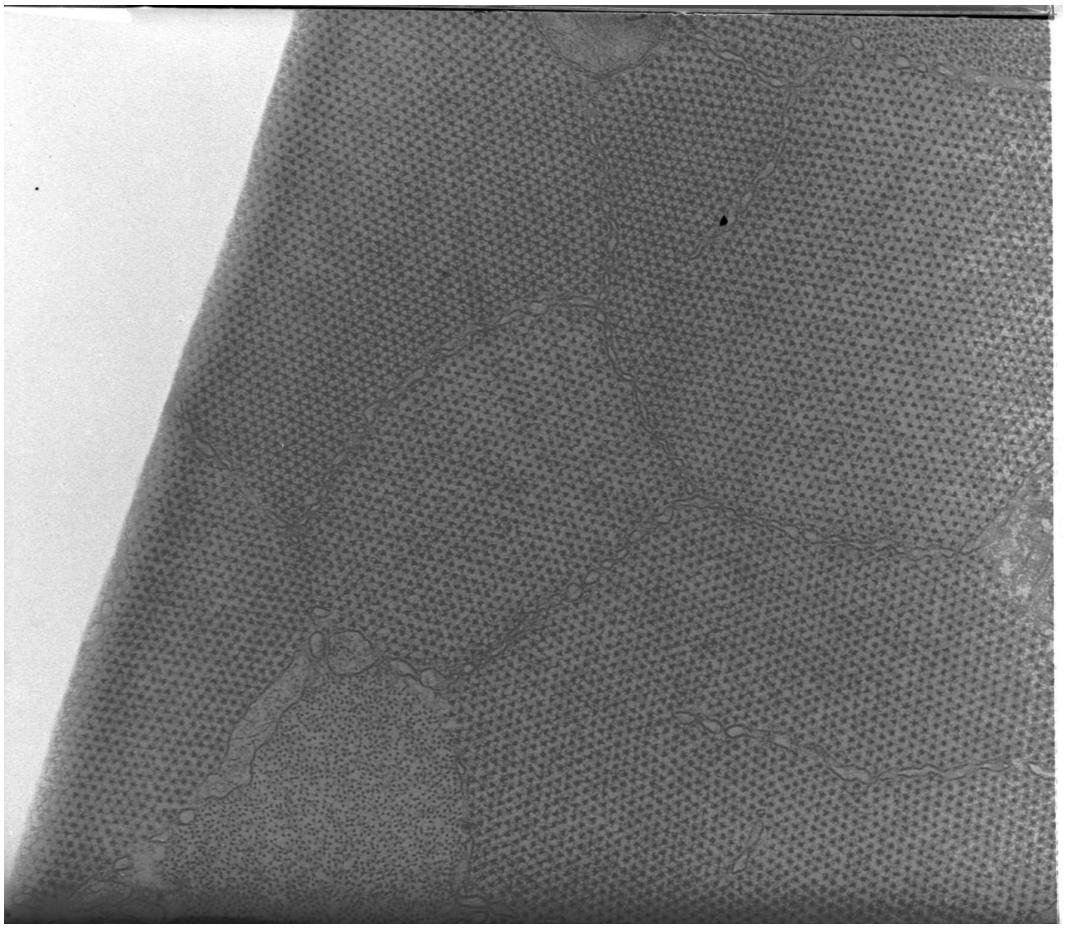

**Figure B.3** FROG410.tif - 3549 × 3081 pixels.

## THE384

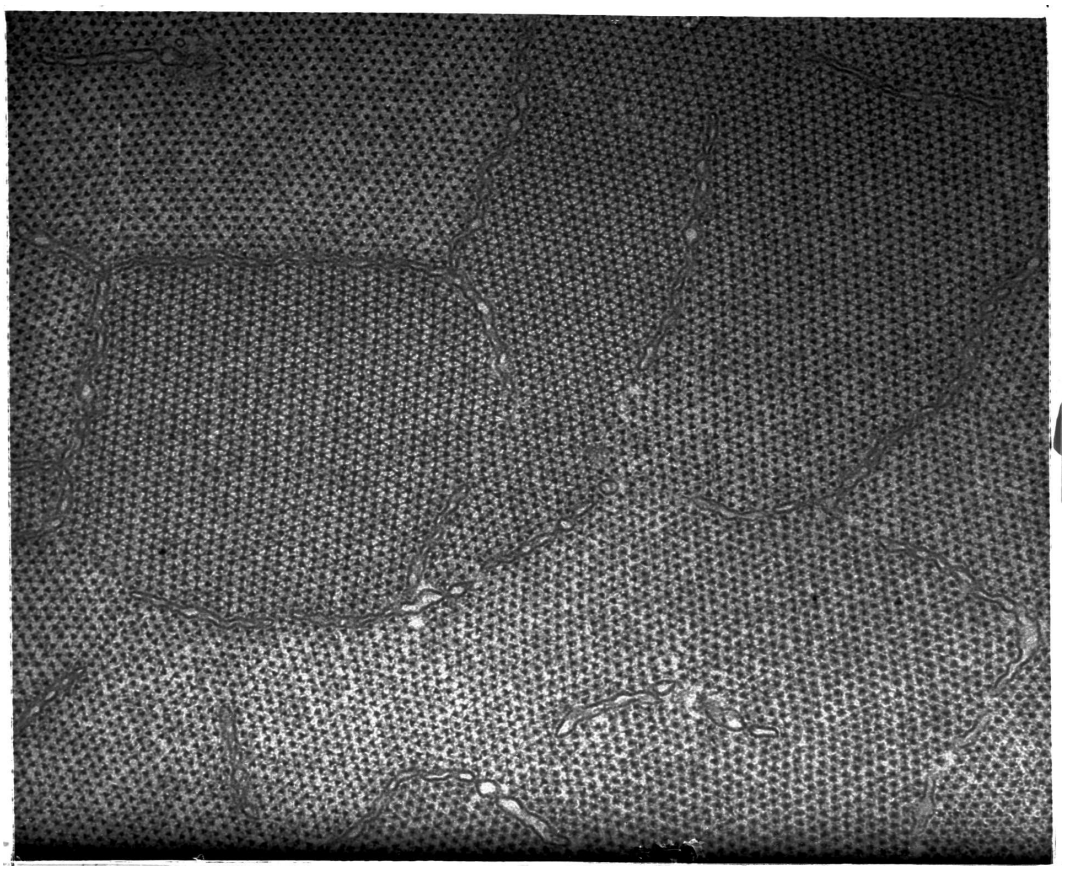

**Figure B.4** the384.tif - 3841 × 3122 pixels.

## PLP27774-BOX

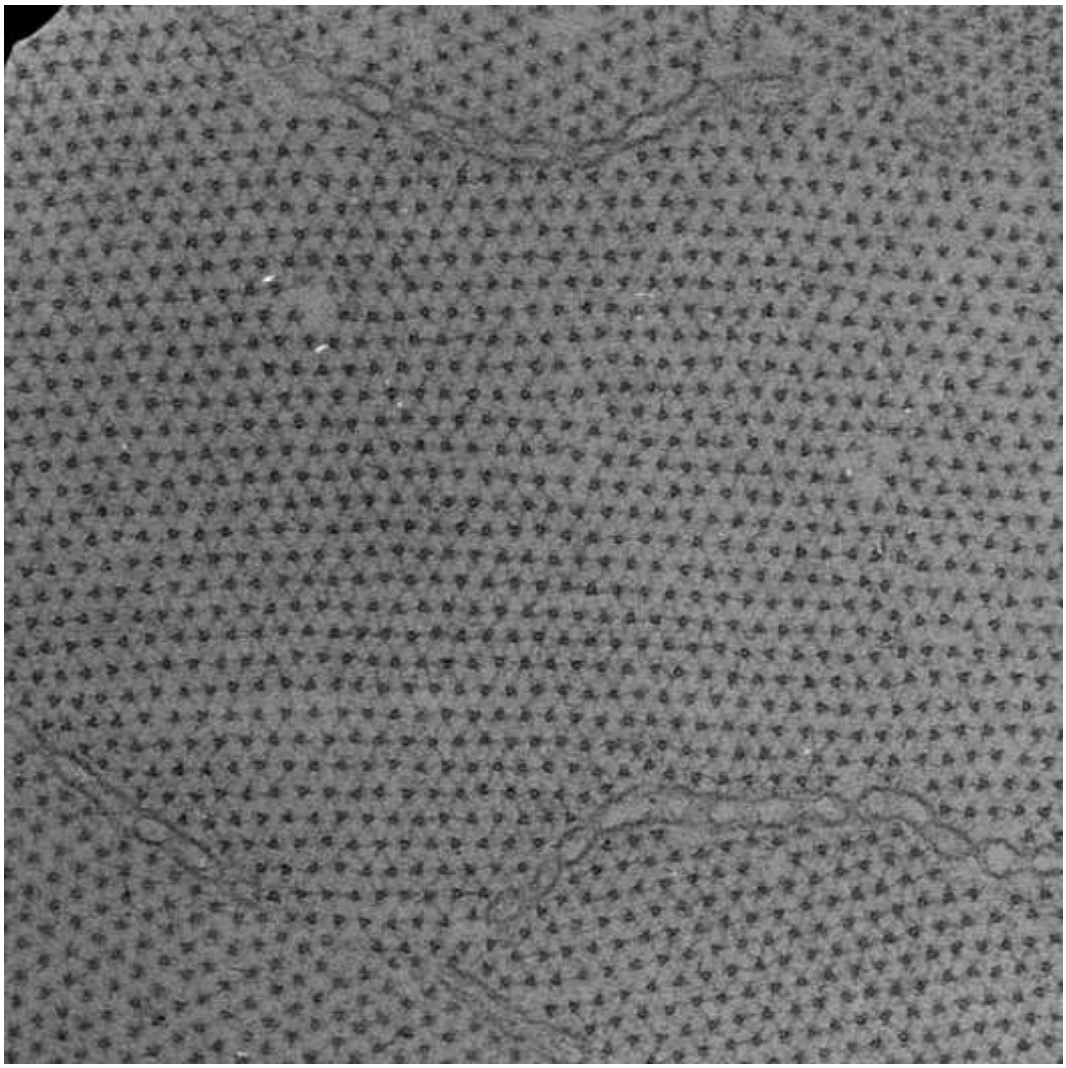

**Figure B.5** plp27774-box.tif - $1050 \times 1050$ pixels.

## 10462-MUDSKIP

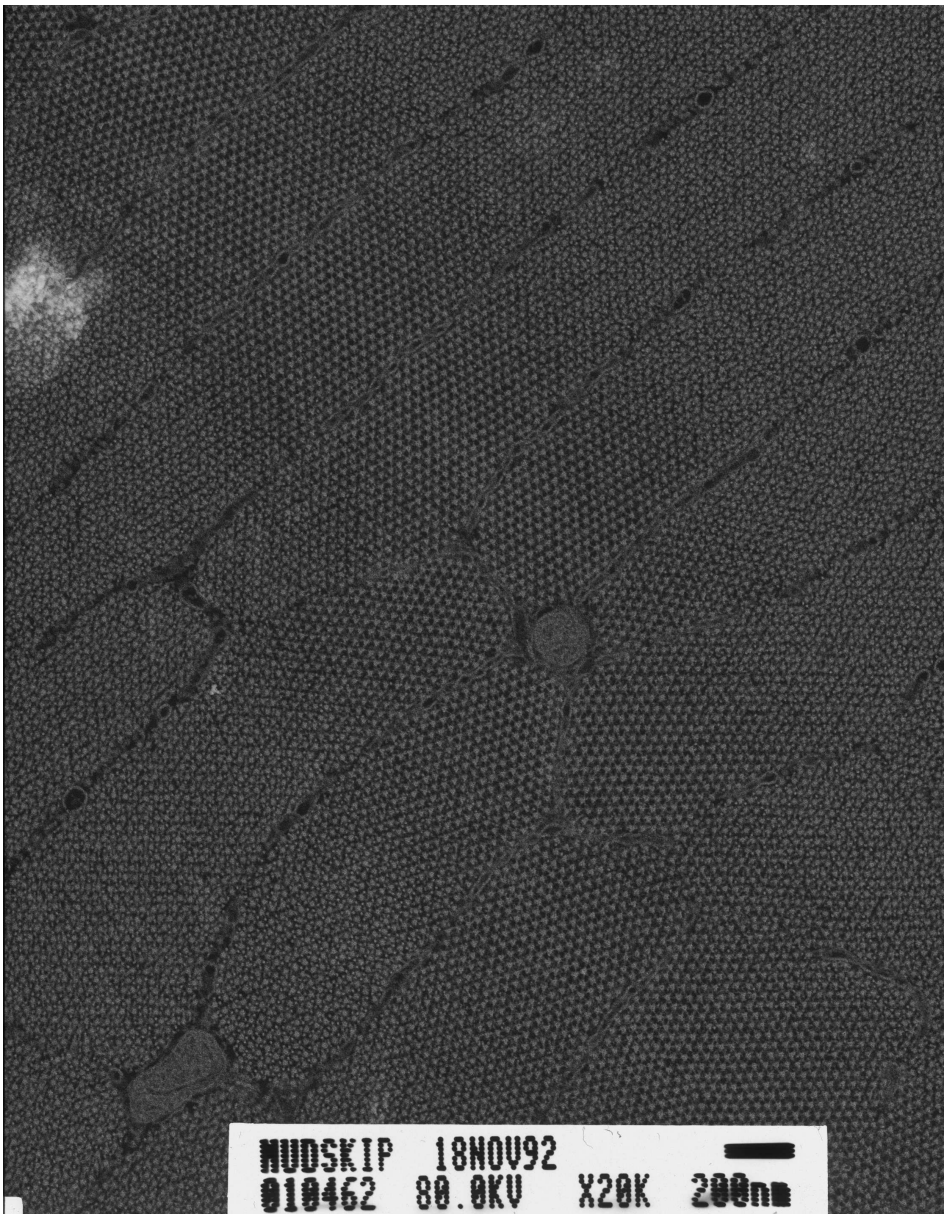


**Figure B.6** 10462-MUDSKIP.tif - 3291 × 2240 pixels.

## 27779-SHARKW

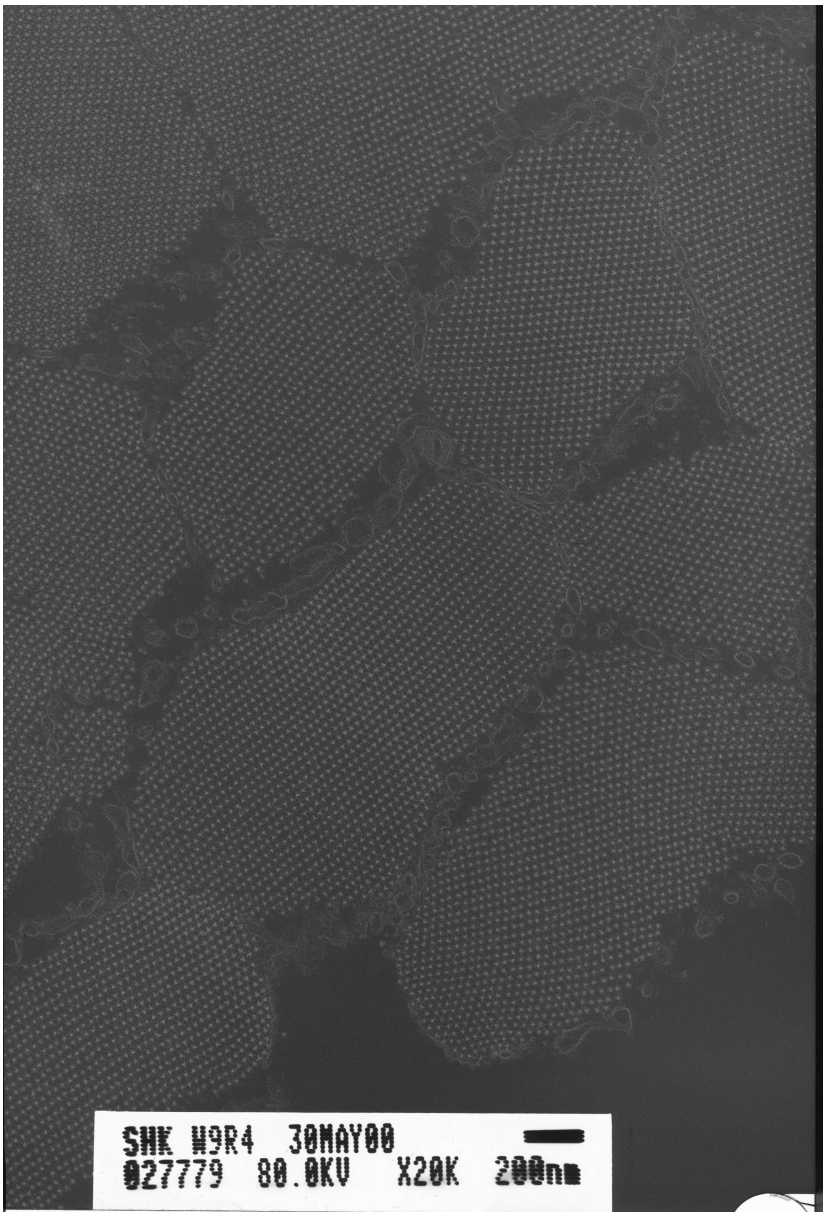


**Figure B.7** 27779-SHARKW.tif - 3295 × 2240 pixels.

## TURT13465

**Figure B.8** TURT13465.tif - 3200 × 2800 pixels.

## SHKW27781

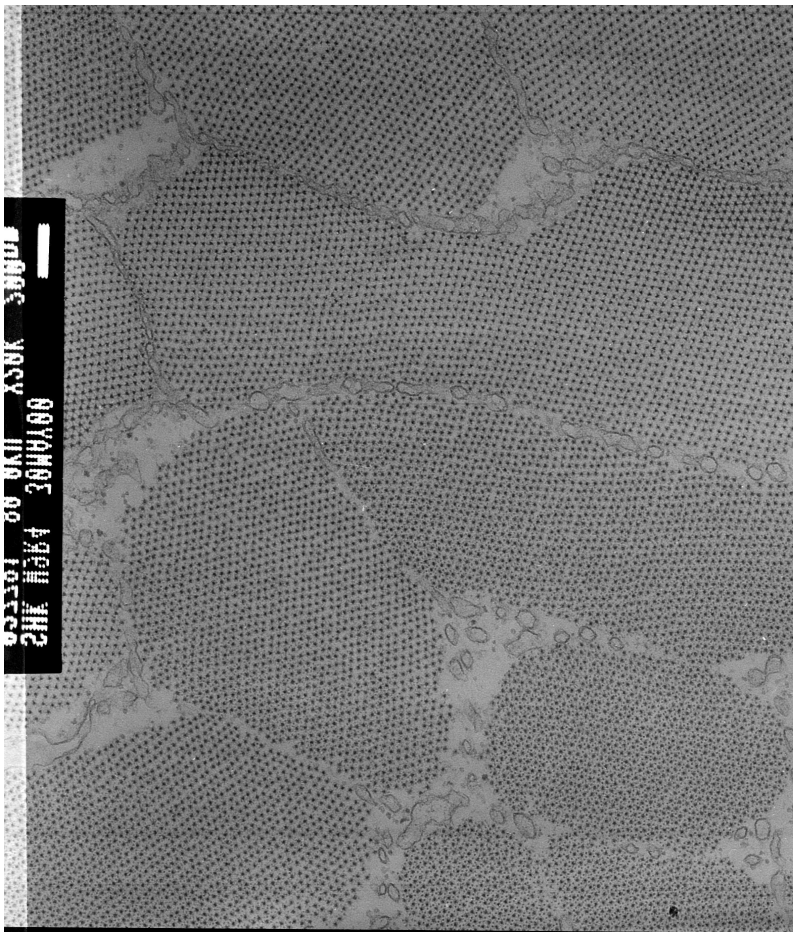

**Figure B.9** SHKW27781.tif - 3200 × 2800 pixels.

## PLPW27765

**Figure B.10** PLPW27765.tif - 3200 × 2800 pixels.

# Bibliography


[AC97] G. Aeppli and P. Chandra. "Seeking a simple complex system," *Science*, vol. 275, no. 5297, pp. 177–178, 1997. 19

[ARDS03] P-O. Astrand, K. Rodahl, H. A. Dahl, and S. B. Stromme. *Textbook of work physiology: physiological bases of exercise*. Human Kinetics, London, UK, 4th edition, 2003. 7

[AS65] M. Abramowitz and I. A. Stegun. *Handbook of mathematical functions: with formulas, graphs, and mathematical tables*. Dover Publications, New York, USA, 1965. 185

[Bag82] C. R. Bagshaw. *Muscle Contraction*. London, UK, 1982. 5, 9, 40

[Bal71] C. J. Ball. *An introduction to the theory of diffraction*. Pergamon Press, New York, USA, 1971. 34

[Bax82] R. J. Baxter. *Exactly solved models in statistical mechanics*. Academic Press, London, UK, 1982. 17

[BKM+08] B. Bödvarsson, S. Klim, M. Mørkebjerg, S. Mortensen, C. H. Yoon, J. Chen, J. R. Maclaren, P. K. Luther, J. M. Squire, P. J. Bones, and R. P. Millane. "A morphological image processing method for locating myosin filaments in muscle electron micrographs," *Image and Vision Computing*, vol. 26, pp. 1073–1080, 2008. 49

[Bow38] F. Bowman. *Introduction to Bessel functions*. Longmans, London, UK, 1938. 185

[Bra78] R. N. Bracewell. *The Fourier transform and its applications*. McGraw-Hill, 1978. 186

[BS96] R. Bowley and M. Sánchez. *Introductory Statistical Mechanics*. Clarendon Press, Oxford, UK, 1996. 16

[CCV52] W. Cochran, F. H. C. Crick, and V. Vand. "The Structure of Synthetic Polypetides. I. The Transform of Atoms on a Helix," *Acta Crystallographica*, vol. 5, pp. 581–586, 1952. 42

[CDK70] R. A. Crowther, D. J. DeRosier, and A. Klug. "The reconstruction of a three-dimensional structure from projections and its application to electron microscopy," *Proceedings of Royal Society of London. A.*, vol. 317, pp. 319–340, 1970. 43

[Cha87] D. Chandler. *Introduction to modern statistical mechanics*. Oxford University Press, 1987. 14

[Cip00] B. Cipra. "Revealing Uncertainties in Computer Models," *Science*, vol. 287, no. 5455, pp. 960–961, 2000. 14

[CP04] R. W. Craig and R. Padrón. "Molecular Structure of the Sarcomere," in *Myology*, A. G. Engel, Ed., pp. 129–166. McGraw-Hill, 3rd edition, 2004. 2

[CW74] F. D. Carlson and D. R. Wilkie. *Muscle Physiology*. Prentice Hall, New Jersey, USA, 1974. 9

[DKR+97] Dragomir Davidović, Suman Kumar, Daniel H. Reich, Jeffrey Siegel, S. B. Field, R. C. Tiberio, R. Hey, and K. Ploog. "Magnetic correlations, geometrical frustration, and tunable disorder in arrays of superconducting rings," *Physical Review B*, vol. 55, no. 10, pp. 6518–6540, 1997. 68

[Dre94] J. Drenth. *Principles of Protein X-Ray Crystallography*. Springer-Verlag, 1994. 34

[DUdVW00] W. L. DeLano, M. H. Ultsch, A. M. de Vos, and J. A Wells. "Convergent solutions to binding at a protein-protein interface," *Science*, vol. 287, pp. 1279–1283, 2000. 82

[Ead01] J. L. Eads. *Diffraction by disordered crystalline materials*. Ph.D. thesis, Purdue University, 2001. 31, 37

[EM01] J.L. Eads and R.P. Millane. "Diffraction by the ideal paracrystal," *Acta Crystallographica*, vol. A57, pp. 507–517, 2001. 37

[GH05] M. A. Geeves and K. C. Holmes. "The molecular mechanism of muscle contraction," *Advances in Protein Chemistry*, vol. 71, pp. 161–193, 2005. 2, 8

[Gib02] J. W. Gibbs. *Elementary Principles of Statistical Mechanics*. Yale University Press, 1902. 15

[Gre01] J. E. Greedan. "Geometrically frustrated magnetic materials," *Journal of Materials Chemistry*, vol. 11, pp. 37–53, 2001. 21

[GRS96] W. R. Gilks, S. Richardson, and D. J. Spiegelhalter. *Markov Chain Monte Carlo in Practice*. CRC Press, 1996. 27

[Gui63] A. Guinier. *X-ray Diffraction in Crystals, Imperfect Crystals and Amorphous Bodies*. W. H. Freeman and Company, 1963. 31

[Han75] R. J. Hanson. "Stably Updating Mean and Standard Deviation of Data," *Journal of Association for Computing Machinery*, vol. 18, pp. 57–58, 1975. 71

[HB62] R. Hosemann and S. N. Bagchi. *Direct Analysis of Diffraction by Matter*. North-Holland Publishing, 1962. 37

[HB67] H. E. Huxley and W. Brown. "The low-angle x-ray diagram of vertebrate striated muscle and its behaviour during contraction and rigor," *Journal of Molecular Biology*, vol. 30, pp. 383–434, 1967. 13

[HH95] R. Hosemann and A. Hindeleh. "Structure of crystalline and paracrystalline condensed matter," *Journal of Macromolecular Science*, vol. B34, pp. 327–356, 1995. 37

[Hou50] R. M. F. Houtappel. "Order-disorder in hexagonal lattices," *Physica*, vol. 16, pp. 425–455, 1950. 21

[HTW75] G. Harburn, C. A. Taylor, and T. R. Welberry. *Atlas of Optical Transforms*. Cornell University Press, New York, USA, 1975. 132

[Hua63] K. Huang. *Statistical mechanics*. Wiley-Interscience Publication, 1963. 17

[Hux57] H. E. Huxley. "The double array of filaments in cross-striated muscle," *Journal of Biophysical and Biochemical Cytology*, vol. 3, pp. 631–648, 1957. 6

[Hux71] H. E. Huxley. "The croonian lecture, 1970: The structural basis of muscular contraction," *Proceedings of the Royal Society of London. Series B, Biological Sciences*, vol. 178, no. 1051, pp. 131–149, 1971. 9

[Hux74] A. F. Huxley. "Muscular contraction," *Journal of Physiology (London)*, vol. 243, pp. 1–43, 1974. 6, 13

[Isi24] E. Ising. *Beitrag zur Theorie des Ferro- und Paramagnetismus*. Ph.D. thesis, University of Hamburg, 1924. 14

[Ist00] S. Istrail. "Statistical mechanics, three-dimensionality and NP-completeness: I. Universality of intracatability for the partition function of the Ising model

across non-planar surfaces," *Proceedings of the ACM Symposium on Theory of Computing*, pp. 87–96, 2000. 14

[JF97] J. L. Jacobsen and H. C. Fogedby. "Monte Carlo Study of Correlations Near the Ground State of the Triangular Antiferromagnetic Ising Model," *Physica A*, vol. 246, pp. 563, 1997. 23

[Kau49] B. Kaufman. "Crystal Statistics. II. Partition Function Evaluated by Spinor Analysis," *Physical Review*, vol. 76, pp. 1232, 1949. 23

[KCW58] A. Klug, F. H. C. Crick, and H. W. Wyckoff. "Diffraction from helical structures," *Acta Crystallographica*, vol. 11, pp. 199–212, 1958. 42

[KK05] N. Kasai and M. Kakudo. *X-Ray Diffraction by Macromolecules*. Springer-Verlag, Berlin, Germany, 2005. 36

[KW41] H. A. Kramers and G. H. Wannier. "Statistics of the Two-Dimensional Ferromagnet. Part i," *Physical Review*, vol. 60, pp. 252–262, 1941. 18

[LC84] P. K. Luther and R. A. Crowther. "Three-dimensional reconstruction from tilted sections of fish muscle M-band," *Nature*, vol. 307, pp. 566–568, 1984. 127

[Lie86] R. Liebmann. *Statistical Mechanics of Periodic Frustrated Ising Systems*. Springer-Verlag, Berlin, Germany, 1986. 21

[LK02] R. J. C. Levine and R. W. Kensler. "The thick filament of vertebrate striated muscle," in *Molecular control mechanisms in striated muscle contraction*, R. John Solaro and R. L. Moss, Eds., pp. 91–141. Kluwer Academic Publishers, Boston, Massachusetts, USA, 2002. 44

[LS80] P. K. Luther and J. M. Squire. "Three-dimensional structure of the vertebrate muscle A-band. II. The myosin filament superlattice," *Journal of Molecular Biology*, vol. 141, pp. 409–439, 1980. xiii, 4, 12, 13, 40, 66, 82, 132

[LSF96] P. K. Luther, J. M. Squire, and P. L. Forey. "Evolution of myosin filament arrangements in vertebrate skeletal muscle," *Journal of Morphology*, vol. 229, pp. 325–335, 1996. 13, 82, 99, 100

[Mak82] L. Makowski. "The use of continuous diffraction data as a phase constraint. II. Application to fiber diffraction data," *Journal of Applied Crystallography*, vol. 15, pp. 546–557, 1982. 43

[MC06] R. P. Millane and R. M. Clare. "Triangular Ising antiferromagnet: Boundary conditions, ground state entropy, and vortices," *Physical Review E*, vol. 74, pp. 051101, 2006. 23

[MD01] R. P. Millane and D. L. Dorset. "Polymer crystallography," in *International Tables for Crystallography*, U. Shmueli, Ed., vol. B, pp. 466–485. IUCr, 2001. 41, 44

[ME02] R. P. Millane and J. L. Eads. "Structure determination from screw-disordered fibres," *Fibre Diffraction Review*, vol. 10, pp. 57–62, 2002. 13

[MG00] R. P. Millane and A. Goyal. "Analysis of the disordered myosin lattice in muscle," *Fibre Diffraction Review*, vol. 9, pp. 6–11, 2000. xiii

[MGP03] R. P. Millane, A. Goyal, and R. C. Penney. "Ground states of the antiferromagnetic Ising model on finite triangular lattices of simple shape," *Physics Letters A*, vol. 311, pp. 347–352, 2003. 21

[Mil90] R. P. Millane. "Phase Retrieval in Crystallography and Optics," *Journal of the Optical Society of America A*, vol. 7, pp. 394–411, 1990. 32

[MNE01] G. Morandi, F. Napoli, and E. Ercolesi. *Statistical Mechanics. An Intermediate Course*. World Scientific, Singapore, 2001. 14, 21

[MPW63] E. W. Montroll, R. B. Potts, and J. C. Ward. "Correlations and Spontaneous Magnetization of the Two-Dimensional Ising Model," *Journal of Mathematical Physics*, vol. 4, pp. 308, 1963. 23

[MRR$^+$] N. Metropolis, A. W. Rosenbluth, M. N. Rosenbluth, A. H. Teller, and E. Teller. "Equation of state calculations by fast computing machines," *Journal of Chemical Physics*, vol. 21, no. 6, pp. 1087–1092. 27

[MS01] R. Moessner and S. L. Sondhi. "Ising models of quantum frustration," *Physical Review B*, vol. 63, pp. 224401, 2001. 21

[MU] N. Metropolis and S. Ulam. "The Monte Carlo Method," *Journal of the American Statistical Association*, vol. 44, no. 247, pp. 335–341. 27

[NB99] M. E. J. Newman and G. T. Barkema. *Monte Carlo Methods in Statistical Physics*. Oxford University Press, Oxford, UK, 1999. 16, 27, 28, 29, 30, 71

[NHB84] B. Nienhuis, H. J. Hilhorst, and H. W. Blöte. "Triangular SOS models and cubic-crystal shapes," *Journal of Physics A: Mathematical and General*, vol. 17, pp. 3559–3581, 1984. 25

[Nie88] F. Niedermayer. "General Cluster Updating Method for Monte Carlo Simulations," *Physical Review*, vol. 61, no. 18, pp. 2026–2029, 1988. 29

[Off74] G. Offer. "The Molecular Basis of Muscular Contraction," in *Companion to Biochemistry*, A. T. Bull, J. R. Lagnado, J. O. Thomas, and K. F. Tipton, Eds., chapter 21, pp. 623–671. London, UK, 1974. 2

[OGWF97] W. M. Obermann, M. Gautel, K. Weber, and D. O. Furst. "Molecular structure of the sarcomeric M band: mapping of titin and myosin binding domains in myomesin and the identification of a potential regulartory phosphorylation site in myomesin," *EMBO Journal*, vol. 16, pp. 211–220, 1997. 87

[Ons44] L. Onsager. "Crystal statistics I. A two-dimensional model with an order-disorder transition," *Physical Review*, 1944. 14, 23

[OTS+07] K. Oshima, Y. Takezawa, Y. Sugimoto, T. Kobayashi, T. C. Irving, and K. Wakabayashi. "Axial Disposition and Conformations of Myosin Crossbridges Along Thick Filaments in Relaxed and Contracting States of Vertebrate Striated Muscles by X-ray Fiber Diffraction," *Journal of Molecular Biology*, vol. 367, pp. 275–301, 2007. 45

[Pat96] R. K. Pathria. *Statistical Mechanics*. Butterworth-Heinemann, Oxford, UK, 2nd edition, 1996. 16

[Pau35] L. Pauling. "The structure and entropy of ice and of other crystals with some randomness of atomic arrangement," *Journal of American Chemistry Society*, vol. 57(12), pp. 2680–2684, 1935. 21

[Pea65] L. D. Peachey. "The sarcoplasmic reticulum and transverse tubules of the frog's sartorius," *Journal of Cell Biology*, vol. 25, pp. 209–231, 1965. 8, 132

[PJLS94] H. Pask, K. L. Jones, P. K. Luther, and J. M. Squire. "M-band Structure, M-bridge interactions and contraction speed in vertebrate cardiac muscles," *Journal of Muscle Research and Cell Motility*, vol. 15, pp. 633–645, 1994. 87

[Ram03] A. P. Ramirez. "Geometric frustration: Magic moments," *Nature*, vol. 421, no. 6922, pp. 483, 2003. 21

[Ram05] A. P. Ramirez. "Geometrically frustrated matter - magnets to molecules," *MRS Bulletin*, vol. 30, pp. 447–451, 2005. 21

[RHC+99] A. P. Ramirez, A. Hayashi, R. J. Cava, R. Siddharthan, and B. S. Shastry. "Zero-point entropy in 'spin ice'," *Nature*, vol. 399, pp. 333–335, 1999. 21

[SAKKL05] J. M. Squire, H. A. Al-Khayat, C. Knupp, and P. K. Luther. "Molecular architecture in muscle contractile assemblies," *Advances in Protein Chemistry*, vol. 71, pp. 17–87, 2005. 2, 5, 6, 7, 10, 87

[SEO69] M. Endo S. Ebashi and I. Otsuki. "Control of muscle contraction," *Quarterly reviews of biophysics*, vol. 2, pp. 351–384, 1969. 44

[SLM90] J. M. Squire, P. K. Luther, and P. Morris. "Organisation and Properties of the Striated Muscle Sarcomere," in *Molecular mechanisms in muscular contraction*, J. M. Squire, Ed., pp. 1–48. CRC Press, Boca Raton, Florida, USA, 1990. 2

[SM95a] W. J. Stroud and R. P. Millane. "Analysis of disorder in biopolymer fibers," *Acta Crystallographica*, vol. A51, pp. 790–800, 1995. 13

[SM95b] W. J. Stroud and R. P. Millane. "Diffraction by disordered polycrystalline fibers," *Acta Crystallographica*, vol. A51, pp. 771–790, 1995. 37

[SM96a] W. J. Stroud and R. P. Millane. "Cylindrically averaged diffraction by distorted lattices," *Proceedings of the Royal Society London A*, vol. 452, pp. 151–173, 1996. 146, 168, 173

[SM96b] W. J. Stroud and R. P. Millane. "Diffraction by polycrystalline fibers with correlated disorder," *Acta Crystallographica*, vol. A52, pp. 812–829, 1996. 37

[Squ72] J. M. Squire. "General model of myosin filament structure. II. Myosin filaments and cross-bridge interactions in vertebrate striated and insect flight muscles," *Journal of Molecular Biology*, vol. 72, pp. 125–138, 1972. 44

[Squ81] J. M. Squire. *The Structural Basis of Molecular Contraction*. Plenum, New York, USA, 1981. 4, 6, 7, 13

[Squ97] J. M. Squire. "Architecture and function in the muscle sarcomere," *Current Opinions in Structural Biology*, vol. 7, pp. 247–257, 1997. 2

[SS77] M. Sjostrom and J. M. Squire. "Fine structure of the a-band in cryo-sections I: the structure of the A-band of human skeletal muscle from ultrathin cryo-sections negatively stained," *Journal of Molecular Biology*, vol. 109, pp. 49–68, 1977. 87

[Ste64] J. Stephenson. "Ising-Model Spin Correlations on the Triangular Lattice," *Journal of Mathematical Physics*, vol. 5(8), pp. 1009–1024, 1964. 23

[Ste70] J. Stephenson. "Ising-Model Spin Correlations on the Triangular Lattice. III. Isotropic Antiferromagnetic Lattice," *Journal of Mathematical Physics*, vol. 11(2), pp. 413–419, 1970. 25, 89

[Str93] W. J. Stroud. *Theory and simulation of diffraction by disordered polycrystalline fibers*. Ph.D. thesis, Purdue University, 1993. 37, 39, 44, 146, 148, 153, 158

[SW87] R. H. Swendsen and J. S. Wang. "Nonuniversal Critical Dynamics in Monte Carlo Simulations," *Physical Review*, vol. 58, no. 2, pp. 86–88, 1987. 29

[Vin93] L. Vincent. "Morphological grayscale reconstruction in image analysis: Applications and efficient algorithms," *IEEE, Trans. on Image Process.*, vol. 2, no. 2, pp. 176–201, 1993. 49, 51

[Wan50] G. H. Wannier. "Antiferromagnetism: The triangular Ising net," *Physical Review*, vol. 79, pp. 357–364, 1950. 21, 23, 24

[WB95] T. R. Welberry and B. D. Butler. "Diffuse X-ray Scattering from Disordered Crystals," *Chemical Reviews*, vol. 95, pp. 2369–2403, 1995. 37

[Wel04] T. R. Welberry. *Diffuse X-Rray Scattering and Models of Disorder*. Oxford University Press, 2004. 37

[WH81] J. S. Wray and K. C. Holmes. "X-ray diffraction studies of muscle," *Annual Review of Physiology*, vol. 43, pp. 553–565, 1981. 9

[WHf95] M. Woolfson and F. Hai-fu. *Physical and non-physical methods of solving crystal structures*. Cambridge University Press, 1995. 31

[WJ80] T. R. Welberry and R. D. G. Jones. "Optical transforms of disordered molecular crystals," *Journal of Applied Crystallography*, vol. 13, pp. 244–251, 1980. 132

[WM08] D. H. Wojtas and R. P. Millane. "The two-point correlation function for the triangular Ising antiferromagnet," *submitted to Phys. Rev. E*, 2008. 25

[WMC80] T. R. Welberry, G. H. Miller, and C. E. Carroll. "Paracrystal and Growth-Disorder models," *Acta Crystallographica*, vol. A36, pp. 921–929, 1980. 18, 37

[Wol89] U. Wolff. "Collective Monte Carlo Updating for Spin Systems," *Physical Review*, vol. 62, no. 4, pp. 361–364, 1989. 29

[WS98] R. E. Wilde and S. Singh. *Statistical Mechanics: Fundamentals and Modern Applications*. Wiley-Interscience Publication, 1998. 14

[Wu66] T. T. Wu. "Theory of Toeplitz Determinants and the Spin Correlations of the Two-Dimensional Ising Model. I," *Physical Review*, vol. 149, pp. 380–401, 1966. 25

[YBK+08] C. H. Yoon, B. Bödvarsson, S. Klim, S. Mortensen, M. Mørkebjerg, J. Chen, J. R. Maclaren, P. K. Luther, J. M. Squire, P. J. Bones, and R. P. Millane. "Determination of myosin filament orientations in electron micrographs of muscle cross-sections," *IEEE Transactions on Image Processing, in press*, 2008. 49

[Yeo92] J. M. Yeomans. *Statistical mechanics of phase transitions*. Oxford University Press, Oxford, UK, 1992. 16, 18

[Zim79] John M. Ziman. *Models of disorder*, p. 17. Cambridge University Press, Cambridge, UK, 1979. 68